Terahertz Reflectarrays

by

Tiaoming Niu

B. Science (Electronic Science and Technology)
Lanzhou University, China, 2003

M. Science (Radio Physics)
Lanzhou University, China, 2011

Thesis submitted for the degree of

Doctor of Philosophy

in

School of Electrical and Electronic Engineering,
Faculty of Engineering, Computer and Mathematical Sciences
The University of Adelaide, Australia

2015

Supervisors:

Prof. Christophe Fumeaux, School of Electrical & Electronic Engineering

Dr. Withawat Withayachumnankul, School of Electrical & Electronic Engineering

THE UNIVERSITY of ADELAIDE

Contents

Abstract

REFLECTARRAY, the concept combining the principles of phased arrays and geometrical optics, can produce predesigned radiation characteristics without requiring a complicated feeding network. A free-space excitation is used to illuminate reflectarrays with passive resonant elements made of metal and dielectric structures, whose individual reflection phase is dependent on the size and geometry of a radiating resonator. Reflectarrays offer the advantages of flat profile and high efficiency, and therefore various reflectarray structures have been intensively realised in the microwave region. With the development of integrated circuit lithography processes, the application of the reflectarrays has been extended to the infrared and even to the visible light regions. However, the realisation of the reflectarrays that can manipulate beams in the terahertz regime still remains largely under-explored, because of the high intrinsic material loss and due to the challenges associated with measurement technology in this frequency range. In recent years, owing to emerging solid-state sources and detectors in the terahertz spectrum, high-gain antennas have become intensively required for constructing terahertz wireless networking or imaging systems. Low-loss terahertz reflectarray antennas thus promise attractive potential for enabling the manipulation of terahertz radiation. This thesis will first introduce the background of terahertz technology, approaches for manipulating terahertz radiation, and fundamental theories for reflectarray design. Following the introductory chapters, the core of the thesis shows how several terahertz reflectarrays have been designed, fabricated, measured and analysed for the aim of (**Part I**) beam deflection with polarisation independence, (**Part II**) beam splitting with polarisation dependence, and (**Part III**) broadband operation:

Part I involves a terahertz reflectarray that is composed of resonant microstrip gold patches on a dielectric substrate. The relation between the patch size and the reflection phase is analysed for a realisation at 1 THz. A subarray is then configured based

on a progressive and cyclic phase distribution to deflect an incident beam into a predesigned angle off the specular direction. Both the numerical simulation and the experimental measurement verify that the proposed reflectarray can efficiently deflect the incident TM and TE polarised waves into the same desired direction at an operation frequency.

Part II focuses on reflectarray designs that can split an incident beam into two different directions with polarisation dependence. In the first realisation, two sets of orthogonal strip dipoles are arranged into interlaced triangular lattices, whereas the second realisation is based on metallic wire grids patterned into square layout with variable lengths backed with wire-grid ground layer. Both configurations of reflectarrays can separate the two polarisation components into different designed directions by deflection or transmission. The designs are realised for experimental validation, and the corresponding measurements are performed in a terahertz time-domain spectroscopy system. The measurement results verify the designs and show acceptable efficiency and high polarisation purity of these polarisation beam-splitters.

Part III concerns the design of novel radiating resonators for broadband reflectarrays. Three parallel elliptical dipoles with variable lengths are proposed to enable broadband operation. A reasonably linear phase response with a wide enough range is obtained by the proposed configuration while the phase curves for different frequencies are nearly parallel each other over a wide frequency range. The simulated field distributions and radiation patterns at different frequencies in the terahertz range demonstrate that the designed reflectarray can perform as expected in a wide frequency band.

These original designs along with corresponding experimental validations offer a first demonstration of reflectarray in the terahertz regime, with antennas composed of metal-dielectric resonators. This is an important progress in expanding approaches for terahertz wave manipulation. The designed reflectarrays with different structures can be utilised as high-efficiency components for advancing the technologies of high-speed communications and high-resolution imaging in the terahertz range.

Statement of Originality

I certify that this work contains no material that has been accepted for the award of any other degree or diploma in my name, in any university or other tertiary institution and, to the best of my knowledge and belief, contains no material previously published or written by another person, except where due reference has been made in the text.

I give consent to this copy of the thesis, when deposited in the University Library, being available for loan, photocopying, and dissemination through the library digital thesis collection, subject to the provisions of the Copyright Act 1968.

I also give permission for the digital version of my thesis to be made available on the web, via the Universitys digital research repository, the Library catalogue, the Australasian Digital Thesis Program (ADTP) and also through web search engines, unless permission has been granted by the University to restrict access for a period of time.

Signed

09/11/2015

Date

Acknowledgments

I would like to take the opportunity to express my gratitude to all those people whose support, skills, friendship and encouragement has helped me to complete this thesis successfully.

First of all, I would like to convey my special thanks to my principal supervisor **Prof Christophe Fumeaux** for accepting me as a Ph.D candidate in 2011 and guiding me throughout my candidature. His extensive experience and comprehensive knowledge in the antenna area have offered me invaluable advice in my research. Reviewing manuscripts with his enlightening questions and critical comments always challenged me. However, these hard times eventually turned out as a productive Ph.D journey. I am grateful to have meetings with him every week from where many creative ideas were inspired, revised and realised. Dear Christophe, I am so appreciated to have your time, concerns, contributions, passions, and quick replies on each publication including this thesis. It was your warm encouragement that kept me going when times were tough.

My sincere gratitude definitely goes to my co-supervisor and supportive colleague **Dr Withawat Withayachumnankul**, an outstanding scholar with passionate personalities at the University of Adelaide. He was very generous with his time and knowledge and assisted me in each step to complete the thesis. I still remember some words from his email saying "trust me that everything is going to be fine" just before my departure from Beijing to Adelaide in 2011. Since my first day of this journey, his generous patience and extensive knowledge in the terahertz area have made me feel free to knock his office door or just write an email for intellectual supervision at any time. Long-hours discussion with him on different research issues, inspirations from him on our weekly meetings, and his constructive comments on each publication guaranteed the completion of the thesis.

In particular, I would like to take the opportunity to express my deep gratitude to **Prof Zhonglei Mei**, an outstanding professor of the Lanzhou University. He was a passionate and humorous teacher during my Bachelor study, and the great supervisor of my Master research. He has been not only my spiritual mentor, but also a dear friend.

I must show my gratitude to Functional Materials and Microsystems Research Group of RMIT University. All prototypes presented in the thesis were fabricated by this group. Sincere thanks to Dr Madhu Bhaskaran, Dr Sharath Sriram, Hakan Menekse, Aditi Upadhyay, and Philipp Gutruf for providing me these delicate samples with excellent performance.

During the time of my Ph.D study I received plentiful support and help from my friends and colleagues in the Applied Electromagnetics Group at the University of Adelaide, Dr Thomas Kaufmann, Dr Longfang Zou, Dr Shifu Zhao, Dr Zhi Xu, Dr Ali Karami Horestani, Dr Pouria Yaghmaee, Dr Zahra Shaterian, Weixun Wu, Amir Ebrahimi, Shengjian (Jammy) Chen, Chengjun Zou, Nghia Nguyen, Sree Pinapati, Wendy Suk Ling Lee, Andrew Udina, and Fengxue Liu. I enjoyed the time of our group meetings with critical questions, which has made me more professional in presenting my work. Great thanks also go to people at the Adelaide T-ray Group, Prof Derek Abbott, Daniel Headland, Dr Benjamin S.-Y. Ung, Dr Jining (Andrew) Li and Mr Henry Ho for their lab training and experimental support to my measurements.

I am grateful to the School of Electrical and Electronic Engineering whose financial support for attending several high-quality international conferences in which I presented my papers and built up connections with the participants. I also gratefully acknowledge the staff of the school, IT officers, and Workshop colleagues for giving me all necessary assistance during my studies. My appreciation is also given to the University of Adelaide for Adelaide University China Fee Scholarship (AUCFS) covering my international tuition fees and to China Scholarship Council (CSC) for the State Scholarship covering my living stipend here. These scholarships have set me free from financial pressures and made the thesis possible. My heartfelt gratitude especially to the Lanzhou University where my Bachelor and Master degrees were issued in 2003 and 2011, respectively. Fundamental knowledge in various subjects and basically electromagnetic theories I learned in the Lanzhou University have been the solid basement of the thesis and also of my future research career.

I cannot go without mentioning my pastor Mr Chris Ambrose along with his lovely wife Mary Ambrose. Blessed by the God with grace and mercy, I was welcomed and loved by this spiritual family since the moment I stepped into the Maylands Church of Christ for the first time. Blessings from the God and loves from my Christian siblings supported me to go through these tough time. Sincere thanks also go to my friends.

Their patience, tolerance and friendship can always make me relaxed from my work, either through enjoying a meal together and a calling chat, or even a long-trip travel.

And finally, but not least, my warmest thanks goes to my whole family, who have been an important and indispensable source of spiritual support. Endless love, continuous encouragement, and spiritual support from my parents always accompany me in my ups and downs. Love and support from my dear brothers and sister always comfort me. I have learned so much from them about how to fulfill a life with passion, love and kindness. My endless appreciation goes to my dear husband Mr Yuming Zhu. His unconditional love and infinite support provided me the energy to attain my study.

Thesis Conventions

The following conventions have been adopted in this Thesis:

Typesetting

This document was compiled using LaTeX2e. TeXnicCenter was used as text editor interfaced to LaTeX2e. Adobe Illustrator CS2 was used to produce schematic diagrams and other drawings.

Spelling

Australian English spelling conventions have been used, as defined in the Macquarie English Dictionary (A. Delbridge (Ed.), Macquarie Library, North Ryde, NSW, Australia, 2001).

Referencing

The Harvard style is used for referencing and citation in this thesis.

System of Units

The units comply with the international system of units recommended in an Australian Standard: AS ISO 1000-1998 (Standards Australia Committee ME/71, Quantities, Units and Conversions 1998).

Publications

Journal Articles

Niu T. M., Withayachumnankul W., Ung B. S.-Y, Menekse H., Bhaskaran M., Sriram S., & Fumeaux C. (2013). Experimental demonstration of reflectarray antennas at terahertz frequencies, *Optics Express*, **21**(3), pp. 2875–2889.

Niu T. M., Withayachumnankul W., Upadhyay A., Gutruf P., Abbott D., Bhaskaran M., Sriram S., & Fumeaux C. (2014). Terahertz reflectarray as a polarizing beam splitter, *Optics Express*, **22**(13), pp. 16148–16160.

Niu T. M., Upadhyay A., Withayachumnankul W., Headland D., Abbott D., Bhaskaran M., Sriram S., & Fumeaux C. (2015). Polarization-dependent thin-film wire-grid reflectarray for terahertz waves, *Applied Physics Letters*, **107**(3), 031111.

Conference Articles

Niu T. M., Withayachumnankul W., Ung B. S.-Y, Menekse H., Bhaskaran M., Sriram S., & Fumeaux C. (2012). Design and implementation of terahertz reflectarray, *2012 37th International Conference on Infrared, Millimeter, and Terahertz Waves (IRMMW-THz)*, Wollongong, Australia, pp. 1–2.

Niu T. M., Withayachumnankul W., Abbott D., & Fumeaux C. (2014). Design of polarization-dependent reflectarray for terahertz waves, *2014 International Workshop on Antenna Technology: "Small Antennas, Novel EM Structures and Materials, and Applications"(iWAT)*, Sydney, Australia, pp. 205–207. (Best Student Paper Award)

Niu T. M., Withayachumnankul W., Abbott D., & Fumeaux C. (2014). Terahertz reflectarray for bidirectional beam splitting, *2014 39th International Conference on Infrared, Millimeter, and Terahertz Waves (IRMMW-THz)*, Tucson, AZ, USA, pp. 1–2.

Niu T. M., Withayachumnankul W., & Fumeaux C. (2015). Terahertz broadband reflectarray with parallel elliptical dipoles, *2015 IEEE 4th Asia-Pacific Conference on Antennas and Propagation (APCAP)*, Bali Island, Indonesia, pp. 102–104.

List of Figures

List of Tables

Chapter 1

Introduction

As one of the relatively un-tapped regions of the electromagnetic spectrum, the terahertz frequency range sandwiched between the traditional microwave and infrared ranges has attractive properties and thus unique potential for various applications. This introductory chapter gives a general definition of the terahertz radiation range as well as the techniques for generating terahertz waves. The background knowledge on terahertz radiation, including its advantages and applications, is introduced here. With an aim to control the propagation of the terahertz radiation, a type of antenna with high efficiency and flat profile is introduced. At the end of the chapter, the outline of the thesis is included.

1.1 Definition of the terahertz radiation

Generally, terahertz (THz) radiation or T-rays refers to the frequency range from 0.1 THz to 10 THz, which lies between the domains of electronics and optics in the electromagnetic spectrum as shown in Fig. 1.1(a) (Siegel 2002, Abbott 2000). In the broad view of the spectrum, the terahertz range overlaps with microwaves on its lower frequency side and infrared on its higher frequency side. More specifically as shown in Fig. 1.1(b), from the lower side to upper side of the frequency range, the terahertz radiation starts at 100 GHz or 0.1 THz, i.e. at a frequency point belonging to the extremely high frequency (EHF) band defined between 30 GHz and 300 GHz. After covering the whole range of sub-millimetre waves (SMMW) from 300 GHz to 3 THz, the upper boundary of the terahertz radiation goes up to the frequency point of 10 THz while the conventional definition for the far infrared (FIR) starts at 1 THz. Although the border between SMMW and FIR is not clearly defined (Siegel 2002), it is obvious that the terahertz band overlaps with these two frequency bands.

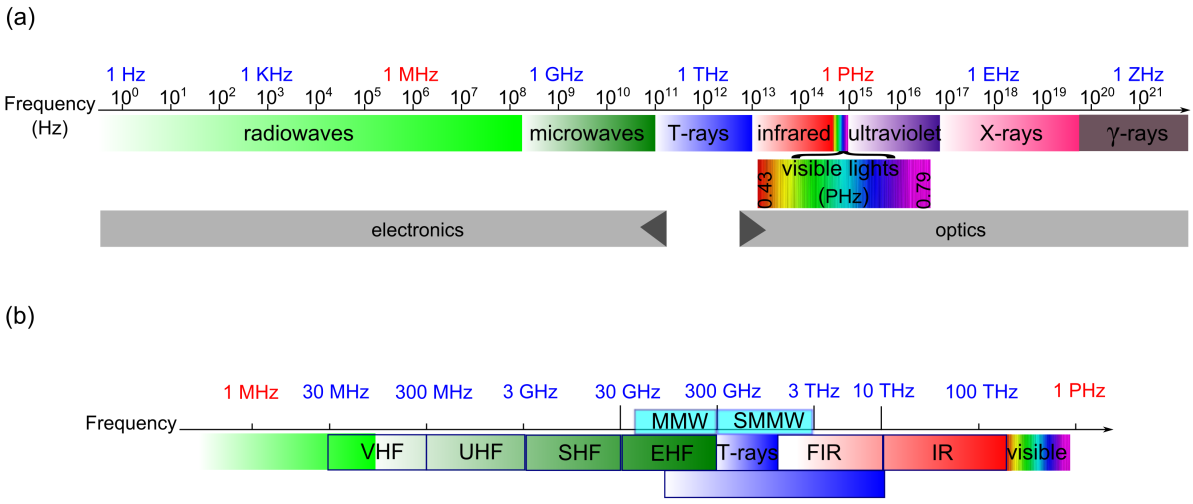

Figure 1.1. Electromagnetic spectrum. (a) The terahertz frequency region in the broad view of the electromagnetic spectrum is loosely defined from 0.1 THz to 10 THz, i.e. between the borders of electronics and optics. It overlaps with the upper side of the microwave range and the lower side of the infrared regime. (b) The terahertz frequency region with its spectrum neighbours in a closeup view of the electromagnetic spectrum. The terahertz radiation covers the range of the upper part of millimetre waves, then the whole range of sub-millimetre waves, and the lower part of the infrared.

For a long time, the terahertz frequency range was known as 'terahertz gap', because the technologies for generating, propagating and detecting terahertz radiation were not well developed, because of inherent challenges. There is no media that can radiate terahertz rays in nature, and the generation of terahertz radiation has to resort to laser excitation. On the other hand, propagating terahertz waves either with conventional devices or in air suffers high attenuation due to significant loss from the transporting materials. Therefore, it was critically required to develop advanced materials and new techniques for generating terahertz radiation (Ferguson and Zhang 2002).

In the last decades, with the development of the new materials providing higher-power sources, terahertz technology has seen a rapid revolution in the methods of generating terahertz radiation. The techniques of exciting different materials such as photoconductive antennas based on semiconductor (Matsuura *et al.* 1997, Dreyhaupt *et al.* 2005) and organic nonlinear crystals (Brunner *et al.* 2008) with ultrafast lasers are used for generating broadband terahertz radiation, while the narrow band terahertz radiation are usually obtained through upconversion of lower-frequency microwave oscillators (Siegel 2002). Recently, the evolutional progress of the terahertz time-domain spectroscopy (THz-TDS) technology has offered remarkable capability in generating and detecting broadband coherent terahertz radiation. As an example, Fig. 1.2 shows a THz-TDS system, TERA K15 from Menlo Systems. The key components of the setup are the mode-locked femtosecond fibre laser and the fibre-coupled THz emitter and detector antenna modules. The terahertz radiation of the system is obtained from excitation of photoconductive antennas, and the ultrafast pulses from the laser are utilised for both generation and detection. A time-domain terahertz radiation pulse from the system is shown in Fig. 1.3(a) and the corresponding spectrum is demonstrated in Fig. 1.3(b). By using vibrational or rotational transitions of molecules in gas phase matching the radiation frequencies that lead to sharp characteristic absorption lines, i.e. "fingerprints" of materials, the system can be used for chemical identification. As the system is phase and magnitude sensitive, it allows measuring the refractive index or the thickness of a sample. In terahertz imaging, the amplitude and phase of a terahertz pulse can reveal the internal structure of a sample.

1.2 Applications of terahertz radiation

In the past, terahertz spectroscopy has been mainly used by chemists and astronomers to spectrally characterize the thermal-emission lines of simple molecules due to the

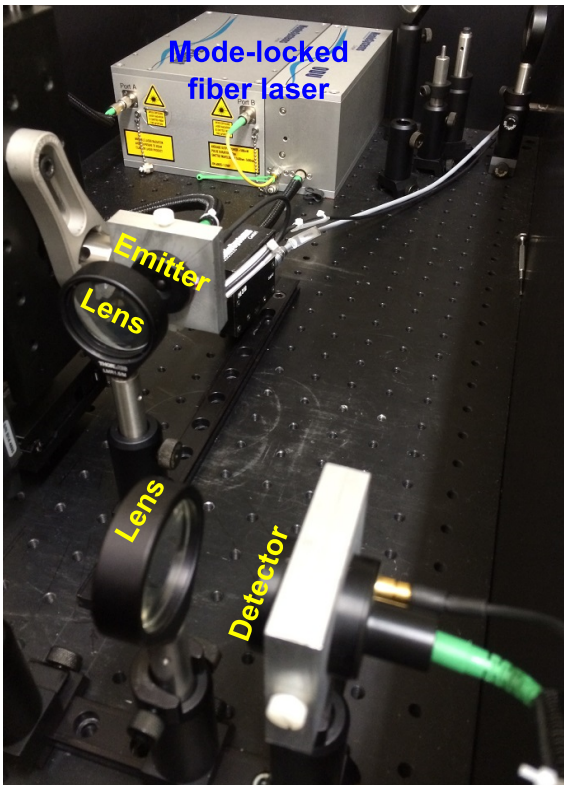

Figure 1.2. Terahertz time-domain spectroscopy system (THz-TDS) TERA K15 from Menlo Systems. The system contains a mode-locked femtosecond fibre laser, an emitter antenna, a detector antenna, and lenses for collimating and focusing terahertz beams.

fact that many materials of interest have unique spectroscopic "fingerprints" lines in the terahertz region (Ferguson and Zhang 2002). In the past decades, benefiting from development of the technology of THz-TDS, terahertz radiation along with the devices operating in this frequency band has been playing an increasingly important role in a very diverse range of applications.

Sensing and analysing

Owing to the fact that many materials, in particular crystalline substances and polar gases, have their unique absorption spectra, i.e. spectral fingerprints, in the terahertz range, terahertz radiation can be used to scan substrate and then extract material's characteristics. This application was initially processed by astronomy and space researchers to identify, catalog and map molecules and thermal emission and absorption of lightweight gases in planetary atmospheres as well as information of the earth (Siegel 2007, de Maagt 2007). By now, the range of materials that can be sensed and

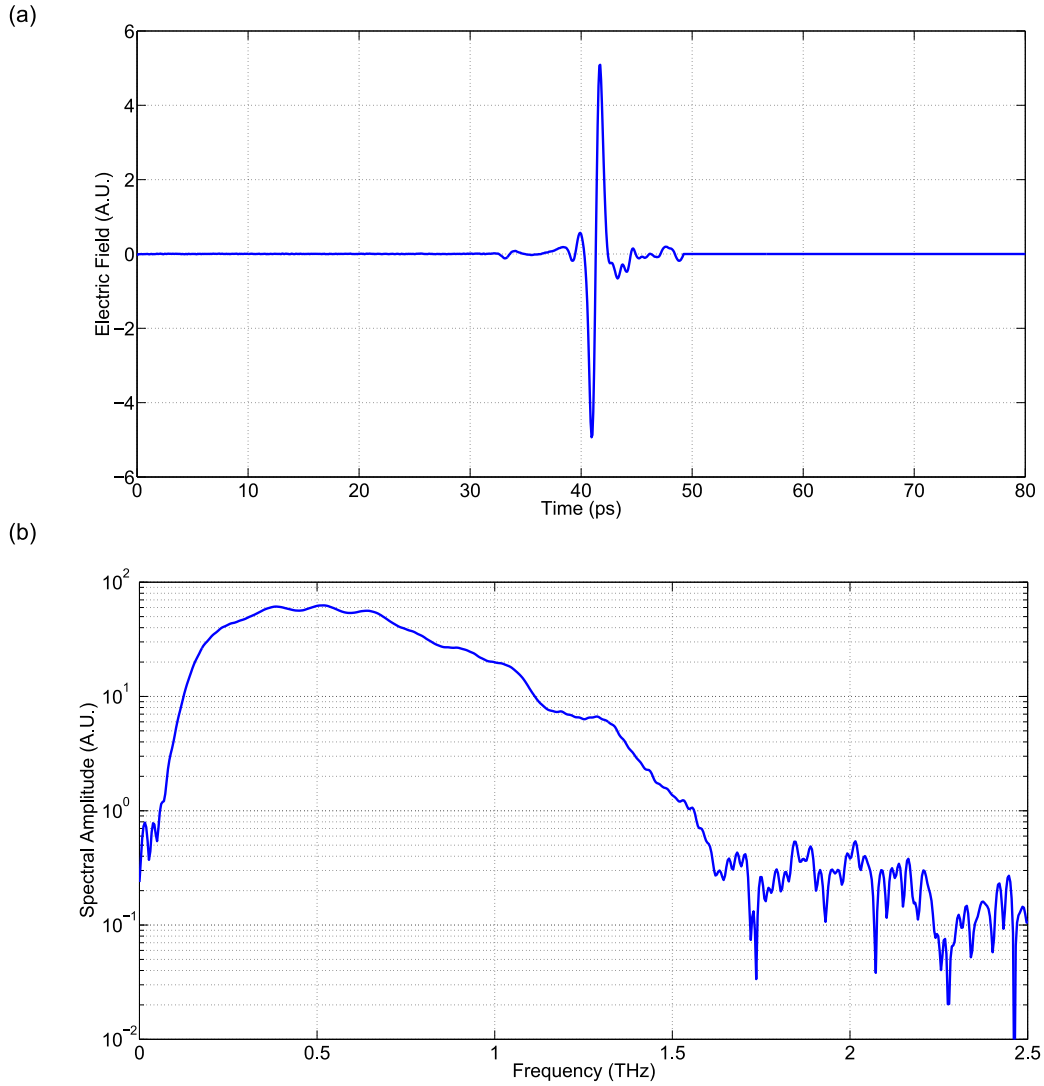

Figure 1.3. Terahertz pulse from THz-TDS TERA K15. (a) Electrical field of the pulse as a function of time. (b) The corresponding spectrum of the terahertz pulse.

analysed by terahertz radiation has been expanded to chemical, medical, and biological areas (Tonouchi 2007, Federici *et al.* 2005, Yoshida *et al.* 2007). In addition, because the terahertz radiation can penetrate a wide variety of dry, nonmetallic and nonpolar materials such as polymers, paper, textiles, ceramics, composite materials, chemical powders and so on, it can be applied for sensing and identifying the objects covered by the solid dry nonmetallic materials that are opaque to optical scanning. For example, in airport security scanning application, the terahertz sensing and diagnosing can offer an alternative stand-off inspection method for accurate surveillance by detecting the concealed weapons and drugs (Hübers *et al.* 2007, Weg *et al.* 2008, Pawar *et al.* 2013, Kawase *et al.* 2003).

Imaging

The response of matter to terahertz radiation, when exploited for imaging applications, can reveal the inner composition of optical opaque materials. Furthermore, terahertz radiation exhibits the properties of low photon energies, and therefore it has been widely and successfully applied in medicine and biological imaging without damaging tissues and DNAs (Mittleman *et al.* 1996, Woodward *et al.* 2003). Due to the wavelength-dependent diffraction limit, terahertz radiation offers better imaging resolution than microwave radiation. On the other hand, it provides worse imaging resolution than optical imaging techniques, but suffers lower scattering (Han *et al.* 2000). Thus, terahertz radiation can be used to visualise internal contents and improve the accuracy of diagnosis for treating diseases. Although the terahertz radiation suffers very severe attenuation when it propagates in the media with high water content, it can still penetrate several millimetres of fatty tissue with low water content and then be reflected back. In addition, when the water content and density of a tissue changes, the dielectric spectral properties of the tissues will exhibit distinctive variation in terahertz reflectivity. Some database recording variations of water content in different tissue types (i.e. cancerous and healthy tissues) have been built. Based on the database, detectable changes of hydration in the tissue can be identified when scanning tissue with terahertz waves, and informative results can help doctors in their diagnosis. Such applications have been demonstrated in cases of imaging skin cancer, breast cancer and other tumours (Mittleman *et al.* 1999, Wallace *et al.* 2004, Nishizawa *et al.* 2005, Taylor *et al.* 2011, Fitzgerald *et al.* 2012, Fitzgerald *et al.* 2014). Some frequencies of terahertz radiation have been used for establishing the characteristic spectroscopic properties of the enamel and dentine with 3D imaging showing various types of tooth decay (Zinov'ev *et al.* 2003, Pickwell *et al.* 2007, Churchley *et al.* 2011).

Communications

With the increasing demand for ultrafast wireless communications over the last few years, terahertz technology has attracted intensive interest due to the fact that the terahertz radiation can support ultrabroadband communication networks with ultrafast data rates (Bird *et al.* 2008, Jacob *et al.* 2009). By now, the main carrier frequency range for wireless links at millimetre waves is around 60 GHz providing data rates of around 1.5 Gbps (Nagatsuma *et al.* 2013). In this frequency band, current WLAN

and WPAN systems have shown the feasibility of the transmission of video signals. Future wireless systems with data rates of 10 Gbps or even higher have been proposed for operation in the unallocated frequency band over 275 GHz. Terahertz radiation with its huge spectral resources have been reported to show the potential for such a wireless communication environment (Song and Nagatsuma 2011). In order to control the terahertz carrier, the available photonic-based high-frequency components such as lasers, modulators, filters and photodiodes can be employed for terahertz communications. Moreover, terahertz systems can be compatible with existing optical networks (Bird *et al.* 2008). However, due to strong water vapour absorption in air, the limited transmission distance restricts the wireless terahertz radiation to indoor communications. In space, atmospheric absorption is not a problem, and the terahertz radiation can be applied to wireless communications between satellites and spacecrafts (Fitch and Osiander 2004, Grant *et al.* 2009).

1.3 Challenges in terahertz technology

As mentioned in previous sections, the significant progress in laser technology has provided the terahertz community with both photonic solid-state sources and vacuum electronic devices. Especially, the advanced development of generating and detecting technologies based on photonic solid-state sources have enabled terahertz radiation to be widely used in various applications (Booske 2008, Booske *et al.* 2011, Clough *et al.* 2012, Berry *et al.* 2014, Yardimci *et al.* 2015). However, challenges are still remaining in this rapidly evolving field. Firstly, it suffers from the lack of compact high-power-density sources at room temperature. Several kinds of terahertz sources, such as solid-state electronic sources based on frequency multiplier, quantum cascade lasers and compact vacuum electronic devices, are all useful but have limitations in output power, operation stability, spectral purity, size, cost, or complexity (Chattopadhyay 2011). On the other hand, terahertz sources based on vacuum electronic devices requires precision electromagnetic circuit fabrication and high-vacuum packaging, although the approach is intrinsically superior at high power density (Booske *et al.* 2011). These factors limit potential of the terahertz radiation for commercial, industrial and military applications. Secondly, because of high water-vapour absorption, terahertz wave suffers severe attenuation when it propagates in the atmosphere with high water content. As illustrated in Fig. 1.4, the time-domain terahertz pulse propagating in the air with water

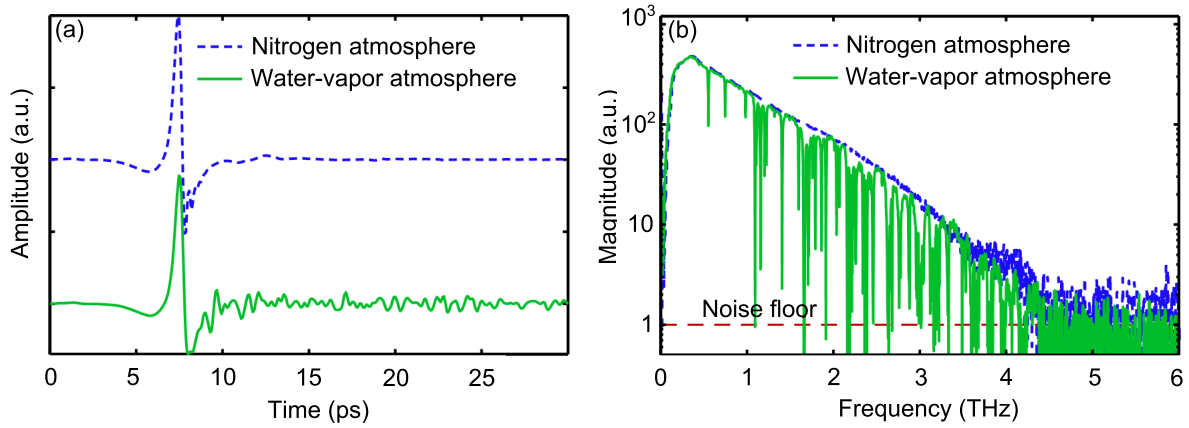

Figure 1.4. Terahertz radiation suffering severe attenuation due to water-vapour absorption. (a) Terahertz pulses recorded in nitrogen (blue dash line) and water-vapour (green solid line) atmospheres. (b) The corresponding spectra of the terahertz pulses in (a). Adapted from Withayachumnankul *et al.* (2008).

vapour undergoes long fluctuations caused by energy re-emission of rotational transitions of water molecules. The strong attenuation is represented in the corresponding spectrum by these sharp resonances at discrete frequencies (Withayachumnankul *et al.* 2008). The characteristic of water-vapour absorption restricts terahertz radiation within low-water content or even dry atmosphere. The property endows terahertz radiation with the potential for short-distance high-capacity communications with high security that is particularly attractive to military applications (Juarez *et al.* 2006). However, applications of long distance communications along with penetrating through water-content objects with acceptable transmission quality still requires high-efficiency terahertz radiation components. Additional challenges range from the development of efficient ultra-broadband antennas, and building database for characterization of common materials at the terahertz band, to the development of portable and affordable terahertz devices, communication protocols tailored to the peculiarities of this paradigm (Akyildiz *et al.* 2014, Robin *et al.* 2014).

Beyond the approaches aiming to create high-power, low-cost and portable room-temperature sources for terahertz radiation, researches targeting the realisation of functional terahertz antennas with high efficiency and broad bandwidth have attracted intensive interest in the terahertz community. Various terahertz antenna components and beamforming networks have been developed with different principles and structures, and each has its relative advantages (Jepsen and Keiding 1995, Deibel *et al.* 2005, Matsuura *et al.* 1997, Tamagnone *et al.* 2012). Due to the fact that the propagation of

terahertz radiation suffers significant attenuation in the media with high humidity, high-efficiency low-profile antennas that can manipulate terahertz radiation hold the potentials for the applications in terahertz indoor communications, terahertz imaging, terahertz detecting, etc. In this thesis, the concept of reflectarray that has been successfully applied in the microwave regime is investigated for terahertz waves, i.e. terahertz reflectarray antenna as a promising candidate for manipulating terahertz radiation.

Reflectarray can be regarded as the combination of parabolic reflectors and phased arrays (Huang and Encinar 2008), and possess the characteristics of high efficiency, flat profile, easy design, easy manufacturing, low-cost, low cross polarisation, directive gain, and low loss. The antenna technology of reflectarrays has become very mature, and has been adopted widely in the microwave and millimetre-wave regions (Huang and Encinar 2008, Tamminen *et al.* 2013b, Tamminen *et al.* 2013a). By now, its implementations have been extended across the electromagnetic spectrum to the terahertz (Nayeri *et al.* 2014, Carrasco and Perruisseau-Carrier 2013) and optical regimes (Memarzadeh and Mosallaei 2011, Pors *et al.* 2011, Zou *et al.* 2013, Yifat *et al.* 2014) with various functionalities such as beam deflection, focussing and beam shaping. At the terahertz frequency range, low-loss reflectarray antennas thus promise attractive advantages in manipulating the terahertz radiation, and can be designed and realised for versatile applications in different fields such as terahertz imaging, sensing, detecting and communications.

1.4 Outline of the thesis

As outlined in Fig. 1.5, the thesis is composed of 8 chapters in total. The first three chapters give the introduction and background of the thesis, and the following 4 chapters constitute the three major parts of original contributions, including (**Part I**) the terahertz reflectarray with resonant microstrip gold patches for beam deflection with polarisation-independence, (**Part II**) the terahertz reflectarrays with orthogonal strip dipoles arranged into interlaced triangular lattices and with thin parallel strips patterned into square lattice for beam splitting with polarisation-dependence, and (**Part III**) radiating resonators with three parallel elliptical dipoles for broadband operation. The last chapter includes the thesis summary and conclusions. The detailed description for each part is as follows:

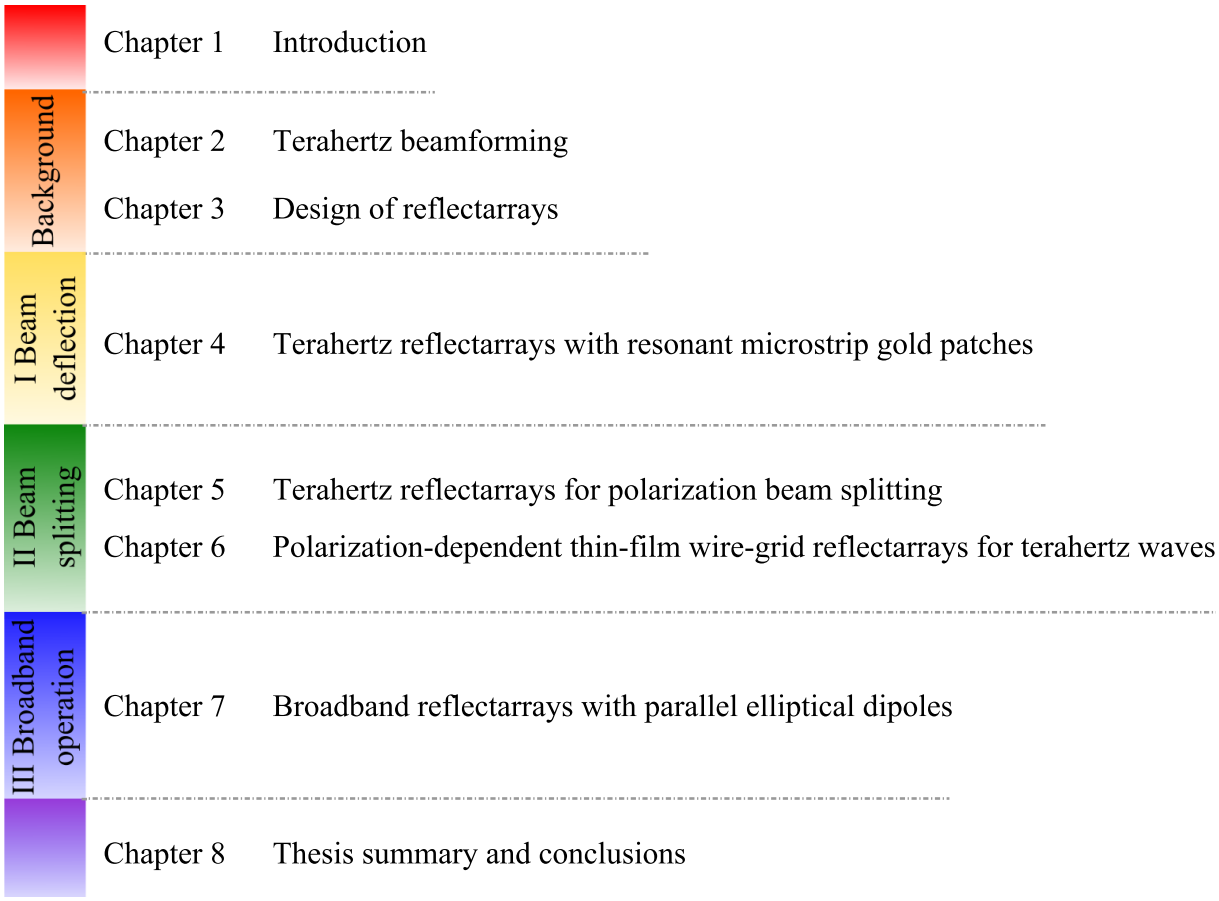

Figure 1.5. Thesis outline and original contributions. The thesis is composed of 8 chapters in total including introduction and summary, and is sub-divided into 4 major parts. The first part gives the background of the thesis, while original contributions of the thesis are distributed in three parts, from I to III. All chapters are virtually self-contained.

Background provides the background of terahertz reflectarrays in three aspects. Chapter 1 introduces the terahertz radiation including its definition, characteristics, applications and challenges. Chapter 2 presents a general review of the approaches that have been proposed and applied for terahertz beam manipulating, including the devices for free-space terahertz radiation. Chapter 3 reviews various resonators for reflectarrays, and then focuses on the analysis of rectangular dipoles. Resonance modes, fringing effects, and design procedures for the rectangular resonator are described. For the design of terahertz reflectarrays, array theory along with material modelling and beam manipulating principles are presented.

Part I— Reflectarrays for terahertz beam deflection with polarisation independence demonstrates reflectarrays made of square resonant microstrip gold patches. The

details are presented in Chapter 4. The characteristics of the radiating element are numerically studied. Based on the phase and magnitude responses of the unit element, a reflectarray with periodically arranged subarrays with a progressive phase distribution is configured and then fabricated. The simulated far field distributions and the measured radiation patterns verify that the designed structure can deflect the both incident TE and TM polarised terahertz beams onto the same predesigned direction with reasonable efficiency and high polarisation purity.

Part II— Reflectarrays for terahertz beam splitting with polarisation dependence shows two types of reflectarrays that can separate the orthogonal polarisation components of an incident beam into different directions. The first type of reflectarray, presented in Chapter 5, follows the conventional configuration with a solid metal ground plane, but the radiating resonators with orthogonally orientated metal dipoles are arranged into a triangularly interlaced lattice. This arrangement offers the structure with the ability of deflecting the orthogonal incident components backwards into two different directions. The second reflectarray shown in Chapter 6 utilises the thin-film wire grids for both the radiating resonators and ground plane. The structure combines the functionalities of conventional reflectarray and polariser, which reflectively deflects one polarisation component and normally transmits the other orthogonal polarisation.

Part III— Broadband reflectarrays with three parallel elliptical dipoles concerns the approaches for broadening bandwidth of reflectarrays. Chapter 7 proposes a radiating element composed of three parallel elliptical dipoles for broadband operation. Both the simulated phase response of the single element and radiation patterns of the reflectarray at different frequencies verify that the proposed structure can perform as expected in a wide frequency band.

1.5 Summary of original contributions

This thesis presents several original contributions in advancing the technology of terahertz reflectarrays, as discussed in the following.

Successful realisation and measurement of reflectarrays at a frequency as high as 1 THz are main contributions of this thesis (Niu *et al.* 2012, Niu *et al.* 2013). There are specific technological challenges that need to be addressed to achieve a functional 1 THz reflectarray. The micro-scale manufacturability, the available materials, and the fabrication

tolerances are factors that are accounted for in the design. Furthermore, the experimental validation in the terahertz range is not trivial, since it involves an unconventional setup for radiation pattern measurements.

In the design of the radiating resonators for reflectarrays, various structures have been proposed for different functions across the electromagnetic spectrum. In this thesis for the first time, two sets of orthogonal strip dipoles arranged in a triangularly interlaced lattice are used to construct the reflectarrays for bidirectional deflections as a beam splitter with high efficiency and high polarisation purity in the terahertz regime (Niu *et al.* 2014a, Niu *et al.* 2014b, Niu *et al.* 2014c). The dipoles arranged in both sparse and compact layouts are investigated in terms of phase and magnitude responses and deflection efficiency. The fabricated reflectarray verifies the validity of the proposed functionality, efficiently separating the two polarisation components of a normally incident wave towards different predesigned directions with high polarisation purity.

Conventionally, reflectarrays are mostly used for beamforming when the incident electric field interacts with the structures. Due to the presence of the reflecting full ground plane, fields are only re-radiated backwards into free space, and cannot be transmitted through the reflectarray. Another original contribution of the thesis is to introduce thin-film wire grids into the design of the structure for combing the functionalities of a reflectarray for the TE polarisation and polariser for the TM polarisation, which has not been previously proposed and realised in any frequency range (Niu *et al.* 2015a). This novelty is based on the novel implementation of thin-film wire grids for both the radiating resonators and ground plane. Because this reflectarray is fabricated on a free-standing flexible polymer substrate, the structure is flexible and stretchable and can be conformed onto curved surfaces to achieve a desired radiation pattern provided that the radius of the curved surface is large compared with the operation wavelength.

Another contribution of this thesis is to utilise the multi-resonance effect of three parallel elliptical dipoles in a single layer to achieve a broadband operation (Niu *et al.* 2015b). By numerically optimising the length ratio of these three dipoles, nearly linear phase response with acceptable resonance loss is obtained when varying the length of the elliptical dipoles. Simulated field distributions and radiation patterns of the designed reflectarrays shows that the structure with the proposed radiating elements can offer a bandwidth of over 20%. This bandwidth is dramatically improved from conventional reflectarrays with a bandwidth of around 5%. This design method can be adopted to other frequency ranges for broadband reflectarrays.

Chapter 2

Terahertz beamforming

IN the field of electromagnetic engineering, beamforming refers to a technique used to create particular radiation patterns via constructive interference towards specific directions in the wavefront while other directions experience destructive interference. The interferences are achieved by locally controlling the phase and magnitude of the waves radiated from a beamforming device. Beamforming has been applied extensively in wireless communications, imaging, and biomedicine. In the terahertz regime, different principles along with corresponding devices have been developed to form desired patterns. This chapter reviews several approaches and devices for terahertz beamforming.

2.1 Introduction

In scientific history, various natural materials were discovered, and, by forming particular geometries such as lenses and prisms, they can be used to observe and manipulate visible light. When light propagates from one medium to the other, it is refracted away from the original direction due to the contrast of the media parameters at the interface. Thus, when incident light impinges on these structures, the visible light can be focused or collimated. After Maxwell thoroughly formulated electromagnetic equations, the principle of electromagnetics have been widely adopted in various fields. Electromagnetically inhomogeneous materials or newly developed metamaterials can direct electromagnetic waves by introducing specific gradients in the equivalent refractive index of the materials (Pendry *et al.* 2006). In recent times, arbitrarily and actively forming the wavefronts of the electromagnetic fields has been one of the most attractive topics in the field of electromagnetic engineering. From the classical optical lenses based on geometrical optics to the novel beamforming devices designed with advanced techniques, researchers have gradually introduced more degrees of freedom to control the wavefronts of propagating electromagnetic fields for various applications.

Beamforming, one aim of controlling wavefronts of electromagnetic fields, is based on the Huygens-Fresnel principle. For a structure performing electromagnetic beamforming, each point of the structure can be considered as a point source radiating a spherical wave with its local phase and magnitude. Controlling the phase and magnitude layout is generally achieved by specifically designing the configuration of the structure, and thereby constructive interference at the desired angles and destructive interference at other directions can be arbitrarily tailored to form a desired far-field pattern. Advanced structures for controlling wavefronts range from diffraction gratings (Schermer *et al.* 2011, Blanchard *et al.* 1999) and leaky-wave antennas (Jackson and Oliner 2008) to phased arrays (Sun *et al.* 2013) and reflectarrays (Huang and Encinar 2008). For diffraction gratings, each slit in the grating acts as a quasi point-source from which light propagates in all directions. The electromagnetic waves after interacting with all slits of the grating then additively and destructively interfere in the far field to form a diffraction pattern. A leaky-wave antenna uses a guiding structure with leaky slits or radiating stubs that can leak or radiate waves continuously along the length of the structure. Phased arrays and reflectarrays shape the wavefront by controlling a specifically designed phase-delay arrangement.

The functionality of electromagnetic beamforming plays an important role in various applications such as smart antennas in wireless communications, radar systems, medical imaging and diagnosis, and security screening. The terahertz regime holds the prospects of increased bandwidth and data rate for wireless communications, more directional beams for radars, high sensitivity for stand-off security scanning, and higher resolution for imaging comparing to the millimetre waves. Therefore, developing efficient terahertz beamforming components is critical for the rapidly evolving terahertz industry. Theoretically, the principle for beamforming techniques used in microwaves can be adopted to design the components for shaping the wavefront of terahertz radiation. However, due to high loss and dispersions in conventional materials and the severe attenuation in atmosphere, specific materials and structures as well as mathematical material models are required for constructing the corresponding terahertz counterparts. Diffraction gratings, leaky-wave antennas, phased arrays and reflectarrays based on new design strategies have been reported for terahertz frequencies. In this chapter, these terahertz devices along with corresponding techniques for terahertz polarisation control and beamforming are non-exhaustively reviewed.

2.2 Polariser

Polarisers are not strictly speaking beamforming structures, as they act on the amplitude of the waves rather than their phase. Nevertheless, they are important components for the polarisation selection of an incident beam and thus are described in this sub-section as a first type of discrete beam manipulating structure.

Wire-grid polarisers are composed of metallic narrow wires arranged in parallel with a regular grating spacing. The grating spacing or the gap between the adjacent strips is much smaller than the wavelength of interest. If the incident electromagnetic waves have a polarisation component parallel to the wires, electric currents arising from the free movement of electrons along the length of the wires are induced, and the polariser behaves in a similar manner to the surface of a metal for reflection. If the polarisation component is perpendicular to the wires, the electrons cannot move very far across the width of each wire, and therefore the incident wave is able to pass through the grid nearly unaffected. Across the whole electromagnetic spectrum, structures based on the concept of the polariser are fundamental components in polarisation-sensitive applications.

In the terahertz regime, polariser structures are highly demanded in applications such as imaging with high extinction ratio, beam filtering, polarisation conversion, and beam splitting. Towards improving performance, different materials and structures have been utilised to realise terahertz polarisers with high efficiency and high extinction ratio. A grid with parallel arranged metallic narrow wires is one of most economical alternatives for constructing terahertz polarisers, by which the waves with the polarisation perpendicular to the length of the wires can be transmitted with high efficiency, while the parallel polarisation is reflected, resulting in a high extinction ratio. According to whether the thin-film wire grids are supported by a substrate or not, polarisers are classified into two typical types: free-standing polarisers and substrate-based polarisers. By mechanically winding thin metallic strings on a rigid frame under physical tension, free-standing terahertz polarisers exhibit high extinction ratio and transmission efficiency. However, the structure are extremely fragile and easily deformed due to mechanical fragility of the micro-width thin-film wires (Costley *et al.* 1977). Because of improved robustness, substrate-based polarisers with metals such as aluminium (Yamada *et al.* 2009, Huang *et al.* 2013) and gold (Deng *et al.* 2012) have been widely developed for terahertz systems. As shown in Fig. 2.1, in the structures of the substrate-based polarisers, metallic grids are normally deposited on the surface of a substrate by photolithography. The substrate functions as a supporting platform to enhance the mechanical robustness of the polarisers. Further mechanical enhancement can be achieved by adding a protecting cover layer with low relative permittivity and low absorption loss polymer as shown in Fig. 2.1(a). For the substrate, materials such as Si and SiO_2 are preferred for higher efficiency and extinction ratio. With the given materials, the performance of the polariser, i.e. the extinction ratio is mainly determined by the spacing period. Smaller period results in higher extinction ratio, and this holds the potential challenges for fabricating high extinction ratio polarisers in the terahertz regime. Moreover, a configuration with double-layer self-complementarily aligned grids as shown in Fig. 2.1(d) has been demonstrated with an outstanding extinction ratio of 69.9 dB in a broad spectral range from 0.6 to 3 THz and the highest value 84.9 dB happens at 1.67 THz (Deng *et al.* 2012).

Besides the polarisers with grids for polarisation-sensitive transmission, some other structures can be integrated with wire grids for polarisation conversion and beam manipulation as shown in Fig. 2.2 (Grady *et al.* 2013). In this classic demonstration, two layers of gold-wire grids are deposited on each side of a substrate, and the orientations of grids on the two sides of the substrate are orthogonal to each other as shown

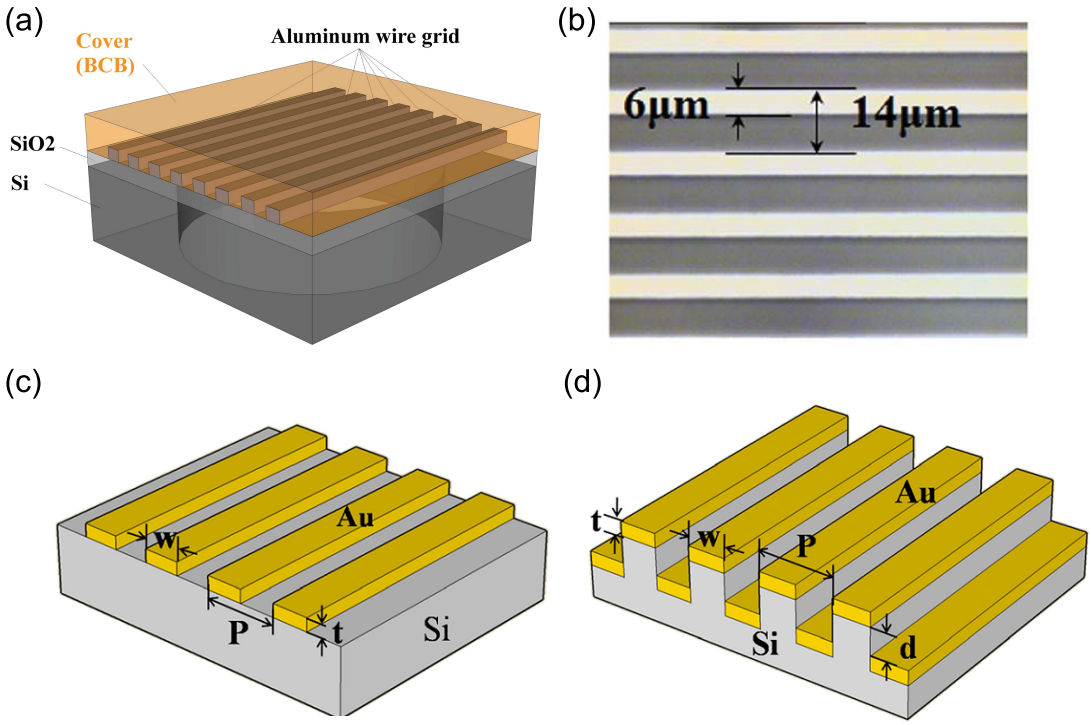

Figure 2.1. Terahertz polarisers with metallic wire gratings. (a) The schematic diagram of a terahertz polariser consisting of four parts: an aluminium (Al) wire grating, cover layer with polymer benzocyclobutene (BCB) for preventing the aluminium grating from further oxidizing after patterning, SiO_2 thin film for sustaining the shape of the wire grating, and Si substrate for enhancing the mechanical strength of the entire polariser. (b) Microscopy image of the polariser from top side of (a). (a) and (b) are adapted from Huang *et al.* (2013). (c) The schematic diagram of the terahertz polariser made of a single layer of gold grating deposited on the surface of a Si substrate. (d) The schematic diagram of the terahertz polariser made of two layers of gold grating deposited on the Si substrate. (c) and (d) are adapted from Deng *et al.* (2012).

in Fig. 2.2(b). Between the two layers of grids, an array of gold cut-wires is adopted for polarisation conversion. When an incident wave propagates in the z axis, and is linearly polarised in the direction perpendicular to the grid on the left side, the wave can penetrate into the substrate and then interacts with the array composed of gold cut-wires as shown in Fig. 2.2(a). The angle between the polarisation and the cut-wires is 45°, which results in polarisation conversion. The grid on the right side enhances the polarisation purity of transmitted wave. As an extension, the cut-wire array can be replaced with a layer of metamaterial structures as investigated in (Yu *et al.* 2011). The transmitted terahertz wave deviates away from normal direction with an angle of θ as shown in Fig. 2.2(c), and therefore an anomalous refraction is observed. In this

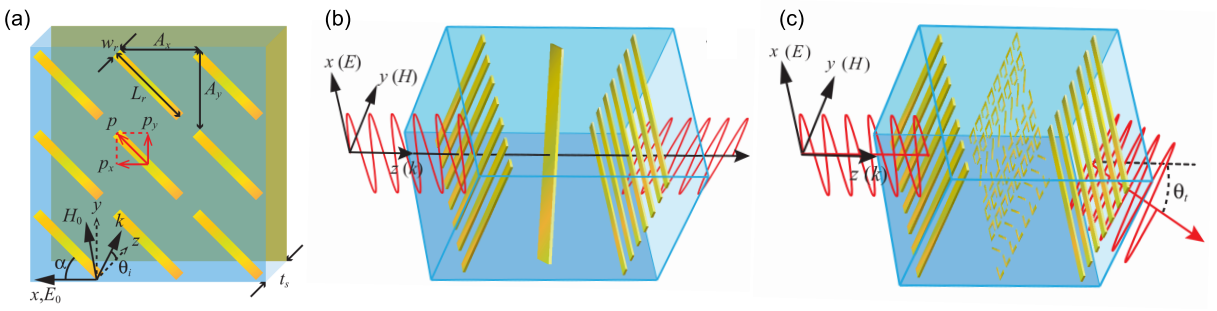

Figure 2.2. Terahertz wire grids integrated with a layer of metamaterial structure for polarisation conversion and anomalous refraction. (a) Schematic diagram of a gold cut-wire array with a solid ground plane for polarisation conversion in reflection. (b) Schematic diagram of a unit cell for a polarisation converter in transmission with two layers of orthogonally arranged wire grids. (b) A layer of metamaterial structure investigated in (Yu *et al.* 2011) is inserted between the two layers of wire grids shown in (b) for anomalous refraction. Adapted from Grady *et al.* (2013).

case, the grid on the front side relative to the incident wave plays the role of beam filter while the grid on the back side functions as both the ground plane and beam filter.

2.3 Diffraction gratings

Diffraction gratings are typically composed of a series of closely arranged slits or grooves that have been engraved or etched into the grating's surface for beam transmission or reflection. For diffraction gratings, the grating spacing is of the same order or larger compared to the operation wavelength. The incident field interacts with the slits or the grooves as separated quasi line sources resulting in diffraction effects. Moreover, diffraction gratings can be integrated with other structures for beamforming. As an example, gratings can be used as a coupler to couple free-space photons to surface plasmon polaritons (SPPs) for surface-wave radiation (O'Hara *et al.* 2004). In this section, the different application scenarios of diffraction gratings for terahertz beamforming are reviewed as follows.

For the diffraction grating shown in Fig. 2.3, the relationship between the angles of incident and diffracted waves is determined by the configuration of the grating following the well-known grating formula (Wise *et al.* 2005)

$$d(\sin\theta_{\mathrm{i}} + \sin\theta_{\mathrm{d}}) = m\lambda, \tag{2.1}$$

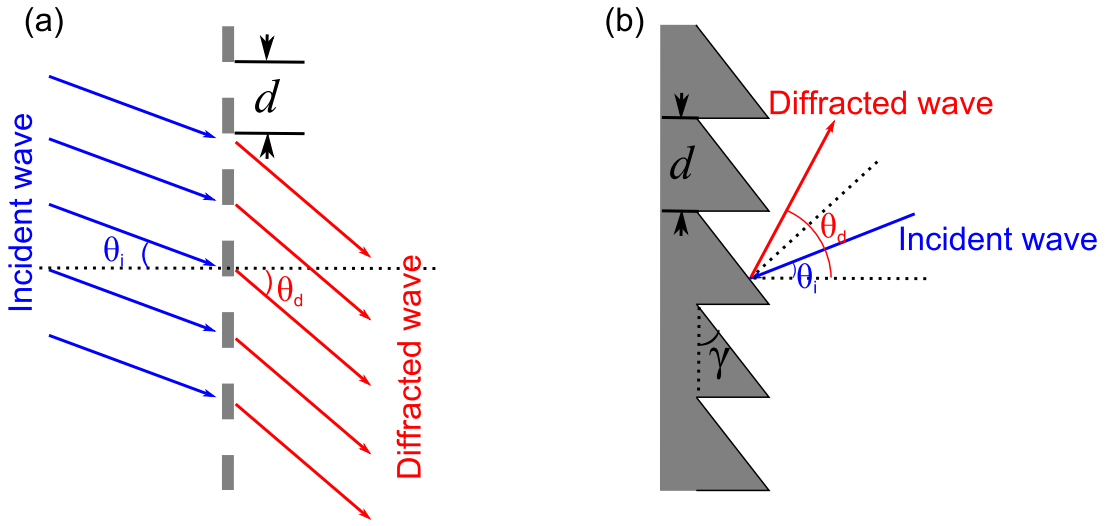

Figure 2.3. Schematic diagram illustrating periodic diffraction gratings in transmission and reflection mode. (a) Diffraction grating with slits in transmission mode. (b) Diffraction grating with grooves in reflection mode. For both cases, the incident and diffraction angles are θ_i and θ_d, respectively, while the grating period is d.

where θ_i and θ_d are the incident and diffracted angles relative to the grating normal, while d is the grating period and λ the operation wavelength. The number m is the order of the diffraction. A value of $m = 0$ corresponds to normal transmission and specular reflection in transmission mode and reflection mode, respectively, which occurs to most of the incident waves. A value of $m = 1$ refers to the first-order diffraction and $m = 2$ corresponds to the second-order diffraction, etc. Based on the grating formula, directions of the diffracted beams for different orders can be arbitrarily controlled by tailoring the grating period for the particular incident waves. If the grating period is a constant, the grating is called periodic grating. When the grating period varies with the position of the strips or grooves, the grating is chirped and can be used to create convergent wavefronts for beam focusing.

In the terahertz regime, periodic and chirped gratings have been frequently utilised for beamforming in both the transmission and reflection mode (Stolarek *et al.* 2013, Monnai *et al.* 2013, Chatzakis *et al.* 2013, Squires *et al.* 2014). In (Squires *et al.* 2014), 3D printing technology was used to fabricate a transmissive diffraction grating with periodically arranged plastic grids and a blazed grating by engraving wedge-shaped grooves on a plastic base. By suppressing other orders of diffraction through optimising the heights of the plastic bars and wedges, both gratings diffract the incident terahertz beams into the designed first-order diffraction direction with high efficiency. A more

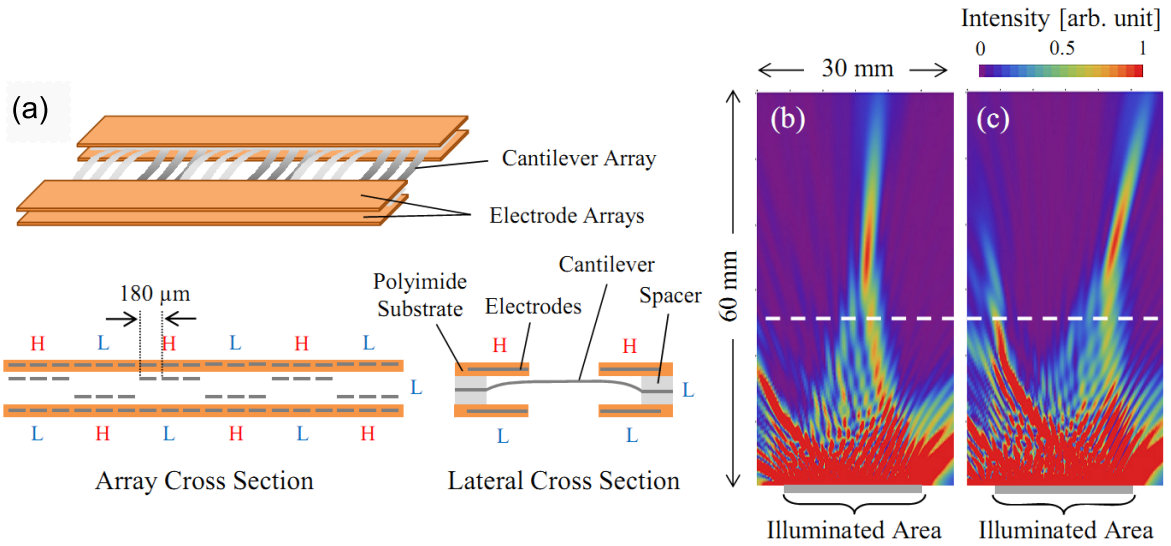

Figure 2.4. Switchable diffraction grating for terahertz beamforming. (a) Schematic diagram showing the diffraction grating with metallic cantilevers sandwiched between programmable electrode arrays. (b) and (c) Theoretically calculated intensity map of focused diffraction of two chipped gratings with different pattern. The colour bar is valid above the white dashed line. Adopted from Monnai *et al.* (2013).

sophisticated demonstration for terahertz radiation has been presented by Monnai *et al.* (2013) as shown in Fig. 2.4(a). A free-standing array of metallic cantilevers is connected to a frame and then sandwiched between electrode arrays. By switching the bias voltage between the metallic cantilever and the electrodes from off to on, each cantilever is individually addressed and displaced in the vertical direction, and therefore different grating patterns such as a periodic or a chirped grating enable tailoring profiles of wavefronts of the first order diffraction. Two different chirped grating patterns have been designed for verification, and their theoretically calculated intensity map for focused diffraction are shown in Figures 2.4(b) and (c). This kind of programmable gratings offer a reconfigurable functionality for stand-off scanning and indoor communications at terahertz frequencies.

Furthermore, diffraction gratings can be used as beam splitters by diffracting the incident beams into different directions with different diffraction orders (Park *et al.* 2003, Lin *et al.* 2008). A sophisticated terahertz diffraction grating for beam splitting has been demonstrate based on a structure with liquid crystals (Lin *et al.* 2008). The diffracted beam can be magnetically switchable by changing the effective refractive index of nematic liquid crystals.

2.4 Leaky-wave antennas

The definition of the leaky-wave antenna (LWA) is given by *IEEE Standard Definitions of Terms for Antennas* as "an antenna that couples power in small increments per unit length, either continuously or discretely, from a traveling wave structure to free-space" (Elliott and Gillespie 1983). The LWA is one type of traveling wave antennas, and most realisations are fast wave structures where the phase constant is smaller than the free-space wave number. In order to continuously radiate energy along the length of the traveling wave structure to free space, increments such as continuous slit and a series of closely spaced holes cut along one side of a rectangular waveguide, are basically applied to leak power along the length of the waveguide (Oliner and Jackson 1993). Depending on the geometry of the waveguiding structure, LWAs can be categorized into two types as shown in Fig 2.5: uniform and periodic LWAs. Uniform LWAs radiate energy into the forward quadrant and can provide scanning from broadside direction to forward end-fire direction, while periodic LWAs can achieve a wide radiation range from backward end-fire through broadside direction to a part of the forward quadrant (Xu *et al.* 2010). The "leaking" travelling wave in the waveguide has a complex propagation wave number. The real part of the wave number, i.e. attenuation constant is related to the beamwidth and the radiation efficiency, while the image coefficient, i.e. phase constant determines the beam direction. The characteristics of the leakage radiation, i.e. beam direction, beamwidth, and sidelobes can be tailored according to application requirement. LWAs have the advantages of straight-forward analysis approaches, simplicity of structure, capability of producing narrow beams, and scanning with frequency-dependence. Due to these advantages, various LWAs have been widely used in microwave and millimetre-wave frequencies.

At terahertz frequencies, the LWA technology is in principle still a very promising platform for developing low-cost and high-performance integrated antennas for terahertz beamforming (Wu *et al.* 2012). However, due to high material losses in the terahertz regime, LWAs based on conventional leaky waveguide structures have rarely been demonstrated. On the other hand, by modifying the conventional LWA structures, leaky radiation along a LWA with low-loss material and carefully designed geometrical apertures can be efficiently generated and easily steered. A novel realisation worthy to mention here is a sinusoidally modulated graphene leaky-wave antenna at the frequency of 2 THz demonstrated by Esquius-Morote *et al.* (2014), as shown in Fig. 2.6. Graphene has the tunable characteristics that its complex conductivity can

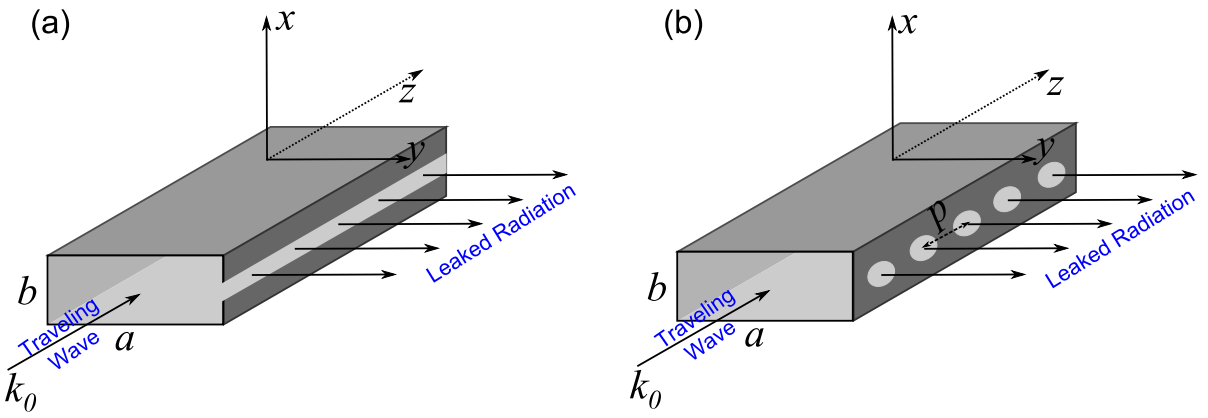

Figure 2.5. Schematic diagrams of leaky-wave antenna. (a) A uniform LWA made of a waveguide with a long longitudinal slot in the narrow wall of the waveguide. (b) A periodic LWA composed of a rectangular waveguide where a periodic array of holes arrange with a periodic center space of p are loaded in the narrow wall of the waveguide.

be controlled by applying a transverse electric field via a biased gating structure, i.e. the polysilicon DC gating pads beneath the graphene sheet transferred onto a back-metallised substrate, as illustrated in Fig. 2.6. When a modulation is applied along the y axis by applying adequate bias voltages to the different pads, the surface reactance of graphene is modulated and can be used to achieve leaky-wave radiation. At the fixed frequency of 2 THz, the graphene LWA offers the characteristic of wide-range electronic beamscanning with a radiation efficiency of over 10%. The graphene terahertz LWA holds very promising potential for beanscanning and constructing graphene-based reconfigurable sensors at terahertz frequencies, but it has not been demonstrated experimentally yet. Moreover, terahertz leaky-wave structures have been proposed to couple the emission from a terahertz source to form a directive pattern. For example, fed by a master oscillator quantum-cascade laser source with terahertz radiation in the surface direction, a LWA composed of a one-dimensional waveguide with compound cavities was used to couple and then tailor the terahertz emission of main beam in one dimension to a directive beam (Tavallaee *et al.* 2011). Llombart *et al.* (2011) have demonstrated a terahertz antenna architecture where a leaky-wave waveguide was integrated into a silicon lens. A couple of leaky-wave modes are excited in the resonant cavity between the lens and the leaky-wave waveguide, and the leaky field radiated into the lens is very directive. The use of such a leaky-wave directive feed can increase the effective F-number of the lens. This strategy also offers the possibility of the fabrication of an array of sub-millimetre height lens antennas directly on a single wafer.

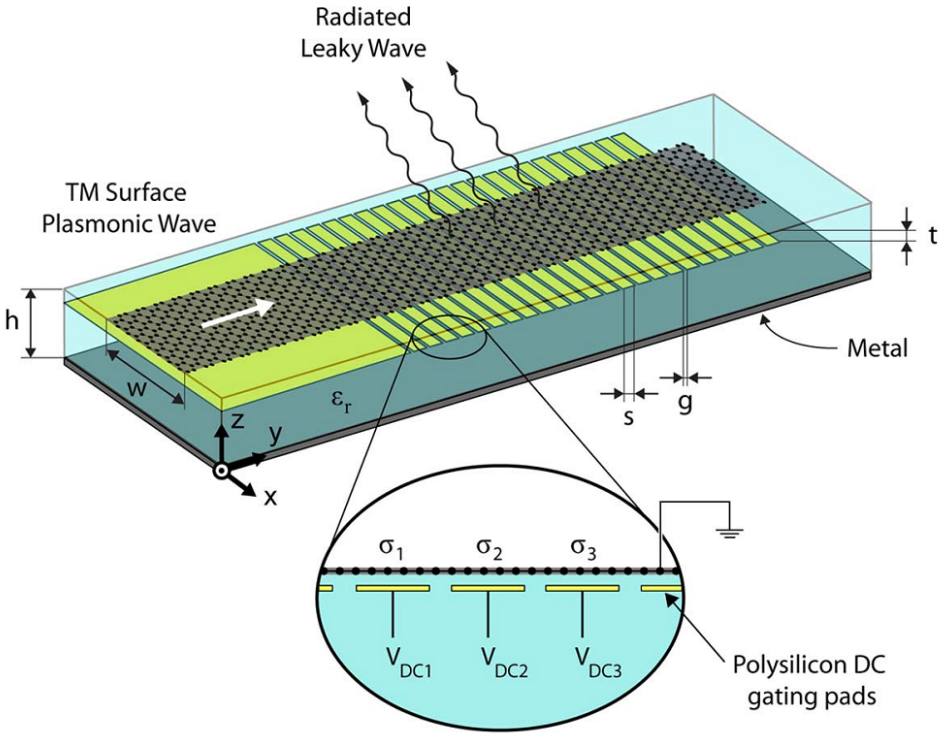

Figure 2.6. Schematic diagram of a terahertz LWA with sinusoidally modulated reactance graphene surface. The polysilicon gating pads beneath the graphene sheet are used to provide bias voltages to modulate the reactance surface for generating terahertz radiation. Adopted from Esquius-Morote *et al.* (2014).

Overall, the concept of conventional LWA technology is an attractive alternative for terahertz beamforming. However, it cannot directly be adopted into terahertz applications due to the challenges such as fabrication tolerance, material losses, structural complexity, and power handing. Also, low-loss substrate-integrated structures holds great potential for developing terahertz LWAs with high gain and wide frequency bandwidth (Wu *et al.* 2012).

2.5 Phased array antennas

A phased array is an array composed of a certain number of antennas where each radiating element is individually excited by a coherent signal with a magnitude and a relative phase shift. Figure 2.7 gives a schematic diagram of a simplified model illustrating the architecture and operation principle of a phased array antenna. The fundamental composition of a conventional phased array includes a feeding network,

phase shifters, and an array of radiators. Each radiator is connected to the feeding network via a phase shifter and emits radiation with specific magnitude A_{mi} and phase $\psi_i (i = 1, 2, 3, ...)$. By programming the magnitude and phase distribution of the array, the effective far-field radiation pattern with the main lobe directed to an angle of θ with respect to the normal of the array can be achieved by reinforcing interference in the desired direction and suppressing interference in undesired directions. With different feeding techniques, phased array antennas can be divided into two types: fixed and dynamic phased array. The former is generally achieved with fixed phase delayers, while the latter is normally based on programmable phase shifters to move the beam direction.

Since the first phased array was used to demonstrate electrical beam scanning, phased array antennas have played a significant role in conventional high-performance radar and communication systems for beam focusing and steering. Phase shifters based on PIN diodes have been widely used in microwaves for obtaining electronically-controlled phase and amplitude for patterning radiation beams in the far field. By now, phased arrays are not only used to replace fixed aperture antennas such as reflectors and lenses due to the advantages of flat profile and more precise control of radiation

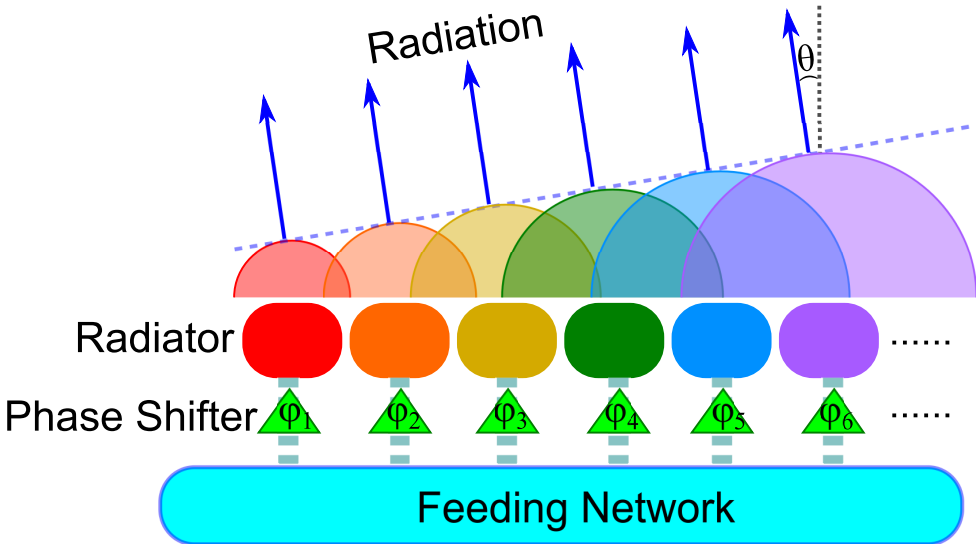

Figure 2.7. Schematic diagram indicating the architecture and operation principle of a phased array. A phased array consists a feeding network and an array of radiating elements. Each radiator is connected to the feeding network and fed by an excitation to radiate a wave with specific magnitude and phase. By controlling the phase delay for each radiating element, a beam directing in the angle of θ can be achieved in the far field.

patterns (Mailloux 1994), but also utilised to pursue large-scale sophisticated structures for generating arbitrary radiation patterns across the electromagnetic spectrum. One outstanding demonstration of a nanophotonic phased array for optical lights by Sun *et al.* (2013) is given in Fig. 2.8. In this nanophotonnic phased array, 64×64 optical nanoantennas are densely integrated on a compact and inexpensive silicon chip. As shown in inset of Fig. 2.8(a), each radiator is composed of two functional parts: a grating-based nanoantenna with 5 grating teeth to radiate the incoming power from laser fibre into space; two optical phase delay lines for adjusting the relative phase shift ϕ_{mn} of the light arriving at the nanoantenna. With the uniform amplitude radiation, the phase of each radiator is determined by the length of the phase delay lines. Based on this configuration, arbitrary far-field radiation pattern can be achieved by synthesising the phase distribution of phased array. As an instance, the authors designed an array to generate the MIT logo in the far field. In this scenario, if the layout of the phased array is configured, the far-field radiation pattern is fixed due to the unchangeable length of the phase delay lines. By connecting a portion of the silicon light path to a resistive heater, the element is converted into a thermally phase-tunable radiator. The thermal effect is electrically controlled by connecting the copper-silicon contacts to a voltage. By applying different voltages on each element, different phase distributions can be achieved in the phased array to generate different radiation patterns therefore a dynamic nanophotonic phased array. This significant work demonstrates that phased array antennas enable generation of arbitrary radiation patterns, while the functionalities of the phased array can be extended to applications such as three-dimensional holography and laser detecting that are beyond the conventional beamforming and beamsteering.

At terahertz frequencies, it is very challenging to directly transfer technology for implementing phase shifters based on conventional techniques, due to the high loss of conventional materials, difficulty of tolerance control, and stability of switching components. As an instance, for the terahertz phased array composed of metal patches fed by microstrip lines based on conventional phase-delayer principle, as shown in Fig. 2.9, the feeding network can become very complicated and is prone to high losses when the number of array elements is large (Islam and Koch 2006). A promising alternative media with fast refractive index tuning ability in a wide range is graphene in

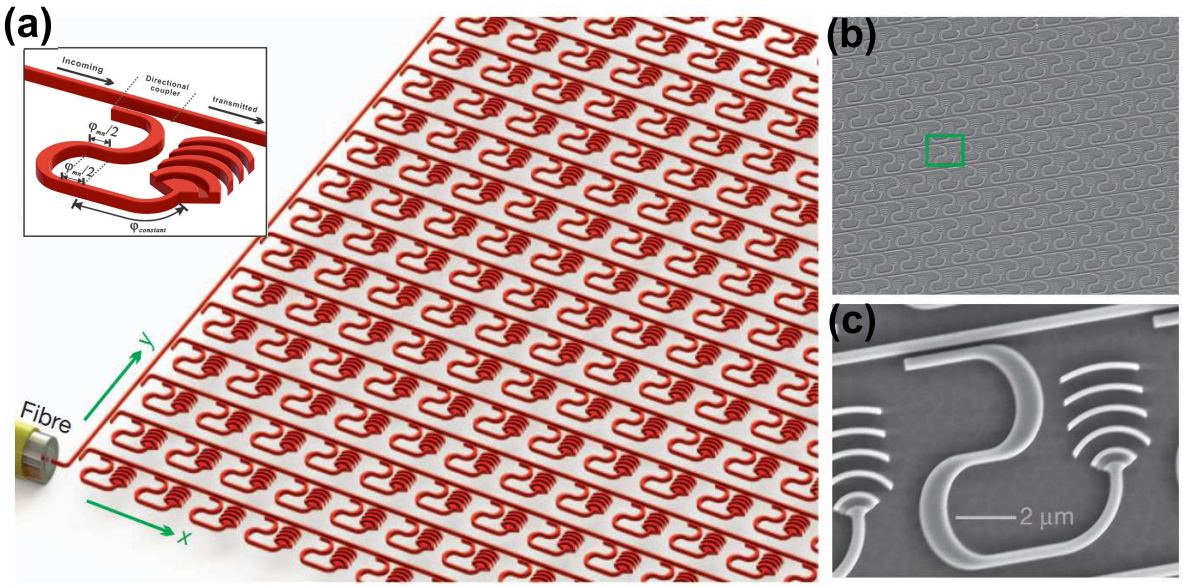

Figure 2.8. Nanophotonic phased arrays for generating arbitrary radiation patterns. (a) Schematic illustration of a 64×64 static nanophotonic phased array system. The input power form a laser is delivered through silicon waveguides to each nanoantenna with uniform amplitude, while the phase of the nanoantenna is controlled by phase delay lines. (b) SEM of part of the fabricated sample. (c) Zoom-in SEM of one element indicated by the green rectangle in (b). Adapted from Sun *et al.* (2013).

which the carbon atoms are formed in two dimensions with an arrangement in honeycomb lattices. In the terahertz band, graphene can be regarded as a low-loss atomic-scale conduction surface. The complex value of surface conductivity and the refractive index of graphene can be significantly changed by externally applied bias such as electric field (Lee *et al.* 2013). With this feature, graphene has become attractive for constructing electrically tunable devices at terahertz frequencies. Chen *et al.* (2013) has proposed a variety of terahertz phase shifters based on graphene parallel-plate waveguide sections integrated with double-gate electrodes. By adjusting the bias voltage, continuously varying phase shifts from the proposed structures can be achieved.

In addition, some other approaches based on the principle of phased array have been applied to control terahertz waves. Froberg *et al.* (1992) have shown a photoconducting antenna array with 64 electrodes by which the generated terahertz radiation is electrically scanned in a angular range of over 40°. Unfortunately, the structure is sensitive to the electric noise, and the complexity of realisation could be a potential limitation of this approach. High-speed and wide angular-range terahertz beam steering have been realised by using an optical method (Maki *et al.* 2009), where a periodically-poled

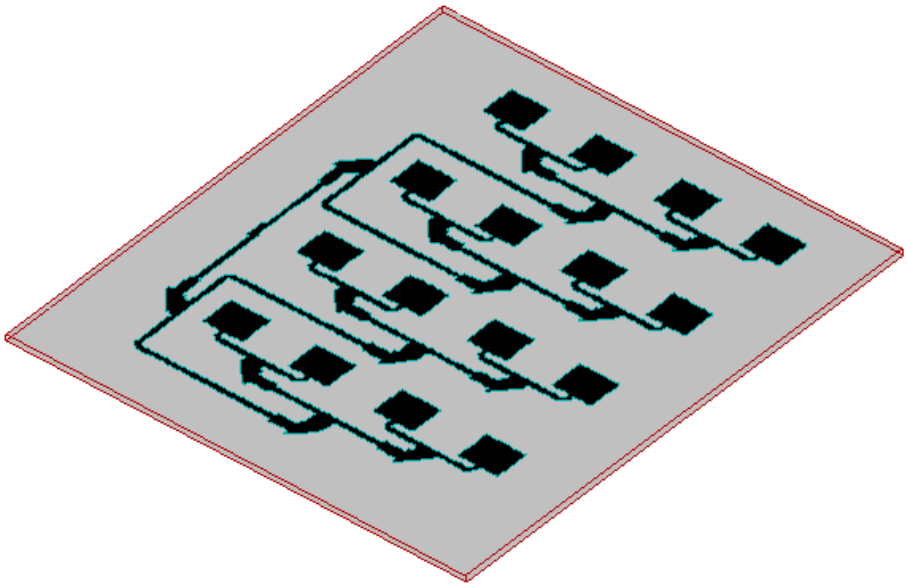

Figure 2.9. Proposed terahertz phased array with 4×4 patches fed by microstrip lines. Feeding the individual patch elements with microstrip lines can become very complicated when the array becomes large. Adapted from Islam and Koch (2006).

lithium niobate (PPLN) crystal is pumped by two laser beams with different wavelengths and the terahertz radiation generated from the crystal can be steered by controlling the incident angle of the pumped beams without using actual phase shifters. The terahertz phased array technology has benefited from these versatile methods and thereby is continuously expending its applications.

2.6 Reflectarray

A reflectarray antenna has a very similar operation principle compared to the phased array antenna described in the previous section, i.e. it is a planar device built as an array of radiating elements where the phase of radiation from each element is individually tailored to form a desired radiation pattern in far-field distance. The main difference between the two structures is the feeding mechanism where a free-space feed, rather than a complicated feeding network, is utilised to spatially illuminate the radiating elements of the reflectarray. The phase of a reflective radiating element is principally determined by its geometrical parameters, and different phases can be obtained by varying the dimensions of the element. The phases introduced by the radiating elements together with the different path lengths from the illuminating source

combine to form a predesigned phase front in the far field. Reflectarray inherits the advantages of planar profile but eliminates the complicated feeding network of phased array. Therefore, reflectarrays possess the superiority of simple feeding mechanism, flat antenna aperture, easy manufacturing, and high efficiency, especially in the applications in large aperture spacecraft antennas. Due to these intrinsic superiorities, reflectarray antennas with printed microstrip elements have been widely applied in microwaves to achieve good antenna performance with low reflecting profile and low manufacturing cost (Huang and Encinar 2008). A typical configuration of a reflectarray is shown in Fig. 2.10 (Encinar 2010). The reflectarray is formed by an array of metal patch radiating elements printed on a spacer backed by a full metal ground plane. The phase and magnitude responses of each radiating element are obtained from the resonance of metal-substrate structure. By varying the geometrical parameters of the element, different phase responses can be achieved for constructing the reflectarray for beamforming. Generally, the radiating elements and ground plane for reflectarrays are made of metals, while the spacer between them is made of dielectric materials. For more sophisticated functionalities such as reconfigurable beam direction, semiconductor diodes and microelectromechanical systems (MEMS) devices have been usually implemented for phase control at microwaves or millimetre-waves (Carrasco *et al.* 2012, Perruisseau-Carrier *et al.* 2010). On the other hand, materials such as liquid crystals whose electromagnetic properties can be tuned by applying an external bias, have been used as substrate for constructing reconfigurable reflectarray elements as demonstrated in Fig. 2.11 (Hu *et al.* 2008, Perez-Palomino *et al.* 2013). The electrically-tunable materials can be utilised for the reflectarrays at higher frequencies where semiconductor diodes and MEMS devices are not suitable due to prohibitive loss and dimensions.

Theoretically speaking, the concept of the reflectarray can be extended to higher frequencies by down scaling the size of microwave counterparts. This prediction has been verified in various realisations of optical reflectarrays with dielectric resonators for beam deflection (Zou *et al.* 2013) and later for optical vortex beam generation (Yang *et al.* 2014), as shown in Fig. 2.12. Without exception, planar-profile reflectarray holds great potential to offer the terahertz regime a high-efficiency antenna alternative for terahertz beamforming. Such attempt for terahertz reflectarrays has been conceptualized mainly by the group of Julien Perruisseau-Carrier (Carrasco *et al.* 2013b, Carrasco and

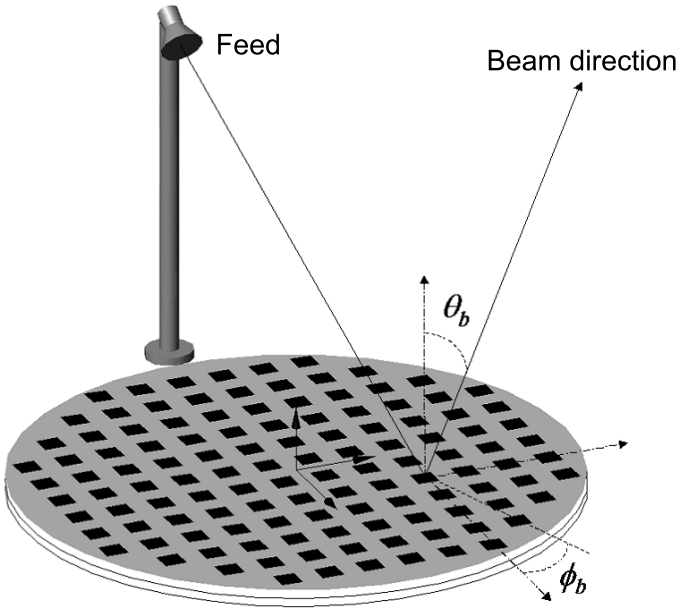

Figure 2.10. The configuration of a typical reflectarray. The reflectarray is composed of an array of metal patch radiating elements, and a primary feed antenna is used to illuminate the reflectarray for reflective beamforming. Adapted from Encinar (2010).

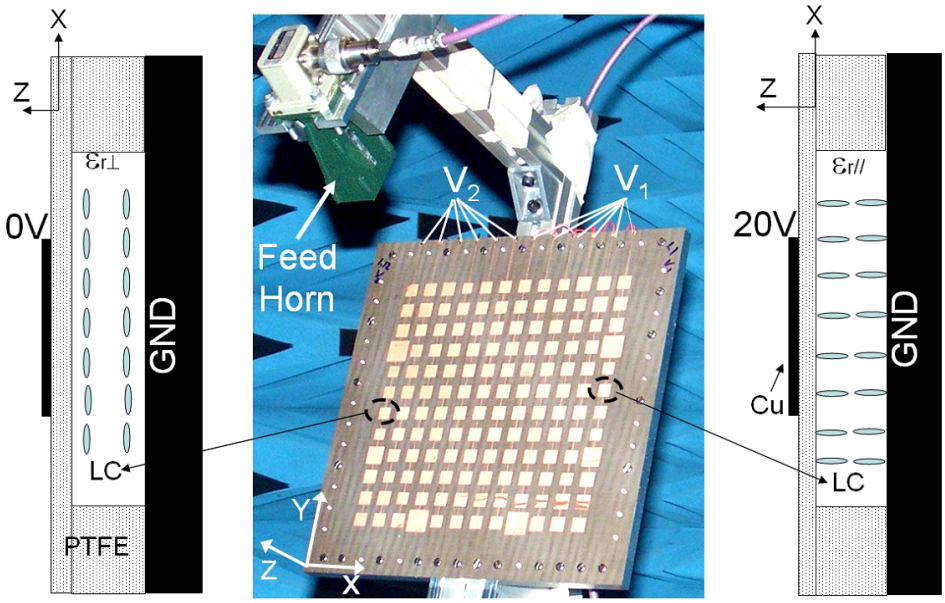

Figure 2.11. Demonstration of a reconfigurable reflectarray with liquid crystal spacer. The orientation of the liquid crystal molecule can be biased into two states, and thereby the effective permittivity of the reflectarray substrate is tuned for a reconfigurable reflection beam. Adapted from Encinar (2010).

Perruisseau-Carrier 2013). In their work, patches made of graphene, rather than metals, on a SiO_2 substrate were proposed, as radiating elements, however without experimental validation. The structure of the radiating element is shown in Fig. 2.13. The graphene can be modelled as an infinitely thin surface with the complex conductivity that can be tuned by an externally applied electric field. This property provides the terahertz reflectarrays with the characteristic of reconfigurability. Moreover, because of the slow-wave propagation associated with the plasmonic mode on the graphene surface, the resonance of the graphene patches occurs at much smaller sizes comparing to the conventional metal-substrate resonators. This advantage can dramatically reduce the size of the reflectarray antenna. However, the material properties of graphene are not only dependent on the external bias, but also determined by the operation temperature and frequencies (Falkovsky and Pershoguba 2007), which leads the performance of such reflectarrays made of graphene-based elements to be narrow-band and not necessarily reliable in all circumstances. Another interesting reflectarray realisation at low terahertz frequencies is a 3D printed reflectarray based on variable height dielectric elements where phase tuning is achieved by varying the height of the dielectric element (Nayeri *et al.* 2013, Nayeri *et al.* 2014). This design strategy could be a promising low-loss and low-cost solution for high gain terahertz antennas.

Except for the terahertz reflectarrays mentioned previously, terahertz reflectarrays remain a underexplored but promising topic of research. In this thesis, robust terahertz reflectarray elements based on conventional metal-substrate resonance will be pursued. The metals used in this thesis are good conductors, and can insure high stability in great temperature fluctuations. Several reflectarrays composed of these elements with different designs will be built up for terahertz beamfoming. These original contributions show on one hand the micro-scale manufacturability with highly demanding tolerances for terahertz reflectarrays and on the other hand the versatility of terahertz beamforming achieved using the reflectarray design framework. For the terahertz range where efficient and effective antenna components are still under developed, these high-efficiency and simple-design reflectarrays are very promising for the future communication and imaging systems.

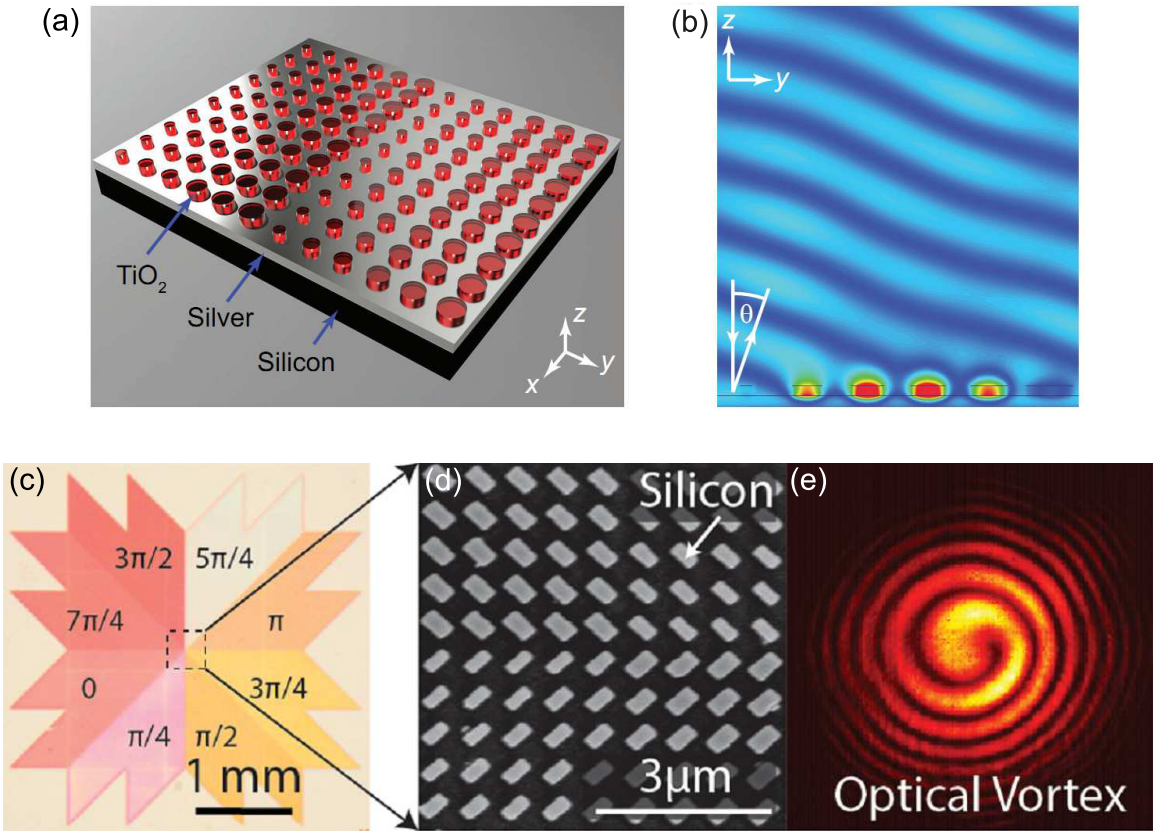

Figure 2.12. Optical reflectarrays with dielectric resonators. (a) A partial view an optical reflectarray for beam deflection. (b) Simulated scattered electric fields of a subarray shown in (a). (c) Phase distribution composed of eight sections for constructing the reflectarray aiming to a optical vortex. (d) SEM image showing a small area at the centre of the reflectarray. (e) Experimentally measured intensity profiles of the generated vortex beam from the reflectarray shown in (d). (a)-(b) are adapted from Zou *et al.* (2013), while (c)-(e) are adapted from Yang *et al.* (2014).

2.7 Summary

In this chapter, terahertz polarisers with wire-grid structures have been first described, followed by a non-exhaustive review of several techniques for terahertz beamforming. Terahertz polarisers have been widely applied in polarisation-sensitive applications. To this end, metallic wire-grid structures where the grating period is much smaller than the wavelength of interest possess the advantages of high extinction ratio, high efficiency and low loss for constructing terahertz polarisers. The terahertz polarisers demonstrated in the literature based on metallic wire grids can be integrated with other functional structures to form a desired radiation pattern with high polarisation purity or high polarisation extinction ratio. In terms of techniques and devices

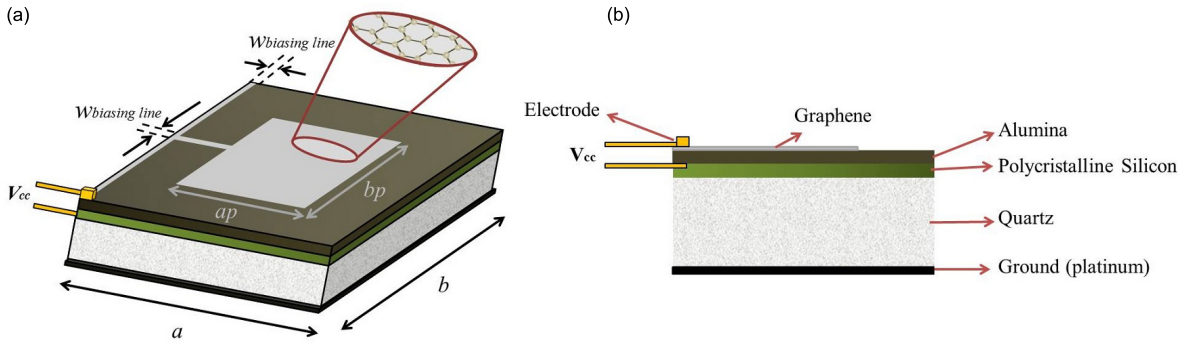

Figure 2.13. Concept of graphene-based radiating element for terahertz reflectarrays. (a) 3D view of the radiating element. A graphene patch is used as radiating resonator, and biased by an external voltage for reconfigurable performance. (b) Side view of the element. Adapted from Carrasco *et al.* (2013b).

for terahertz beamforming, four categories of technologies, namely diffraction gratings, LWAs, phased arrays and reflectarrays, have been reviewed. Diffraction gratings where the grating period is of the same order or larger comparing to the operation wavelength, are generally used for forming the wavefronts in optical devices. The waves can be transmitted through or reflected by the gratings composed of transmissive slits or reflective grooves, respectively. The grating period can be either periodic or chirped, depending on the desired functionalities of beam diffraction or beam convergence. Moreover, the introduction of programmable configurations can result in dynamic terahertz beamforming. Leaky waves along the waveguiding structure can be freely patterned in a wide angular range extending from back end-fire through broadside to front end-fire, and the characteristics of the leaked radiation is determined by the leakage configuration. Challenges for terahertz LWAs range from the fabrication tolerance, power handing to material losses. Suitable design strategies and newly developed materials with low loss are highly demanded for constructing terahertz LWAs. Furthermore, it has been demonstrated that phased arrays are one type of the most versatile beamforming antennas in microwaves. But this antenna technology has rarely been developed for the terahertz regime, due to the lack of efficient phase shifters. Although some unconventional materials such as electrically tunable liquid crystals and graphene have been proposed to design terahertz phased arrays, unaffordable loss introduced by the complicated feeding network and strict fabrication tolerance are still challenging to address. By eliminating the feeding network and therefore offering increased efficiency, reflectarrays hold great potential in applications of terahertz

beamforming. Researchers have postulated that graphene can be a good candidate for constructing terahertz radiating resonators in a specific temperature range.

In this thesis, terahertz reflectarrays with conventional metallic resonators based on metal-substrate resonances will be pursued. Both metals and substrates used in the realisation of these reflectarrays can perform with high stability in a wide temperature range, which insures the robustness of the proposed terahertz reflectarrays. The designed reflectarrays with different configurations can perform beamforming such as beam deflection and beam splitting with polarisation dependence. These functional high-efficiency components can be applied in emerging applications of terahertz communications and imaging.

Chapter 3

Design of reflectarrays

AS a combination of phased array and reflector, a reflectarray antenna shows advantages of high efficiency and planar profile. Reflectarrays can produce predesigned radiation characteristics without requiring a complicated feeding network. Due to these attractive properties, various reflectarrays have been widely implemented for different applications across the electromagnetic spectrum. In this chapter, different resonators as radiation elements of reflectarrays are reviewed. As one type of the mostly commonly used resonator, rectangular dipoles and patches are particularly analysed. Dimensions, materials and the fringe effect of the resonators as radiation elements determine the phase and magnitude of the local reflection responses. In addition, methods for obtaining the desired radiation patterns of a reflectarray are also included in this chapter.

3.1 Introduction

The concept of reflectarrays comes from the combination of the phased array and reflector antenna (Huang and Encinar 2008). On the one hand, phased array antennas reinforce the effective radiation pattern in a given direction by controlling the phase and magnitude of each radiation element, which is individually excited by a feeding source and collectively produce a far-field pattern. Normally, phaser shifters—the devices producing variable phase shifts—along with phase delay lines are crucial components that cooperatively provide beam scanning function. Owing to the variable phase shifts, phased-array antennas can offer the property of dynamic beam scanning, however at the cost of a complicated feeding network (Hansen 2009). On the other hand, based on the geometric properties of an accurately-designed curved surface, traditional reflector antennas can offer very high efficiency in controlling reflection of electromagnetic waves without a complicated feeding network. Both structures however have their weaknesses: for the phased array antennas, the loss introduced by the feeding network can become significant when the number of elements in the array increases to a certain amount, while the reflector antennas with their heavy and bulky structures along with their particularly curved surface have limited applications. Lightweight antennas with flat profile and high efficiency are always demanded in practical applications, especially at higher operation frequencies. In view of this background, the concept of reflectarray becomes an attractive alternative. Taking the advantages of both the phased array and the reflector, low-profile printed reflectarray antennas have attracted intensive interest across the electromagnetic spectrum (Huang and Encinar 2008), from microwave (Carrasco *et al.* 2013a, Bayraktar *et al.* 2012), millimetre-wave (Nayeri *et al.* 2014, Hu *et al.* 2008), to optics (Ahmadi *et al.* 2010, Zou *et al.* 2013, Yifat *et al.* 2014, Carrasco *et al.* 2015). The free-space feeding mechanism of the reflectarray eliminates the loss caused by complicated feeding networks, and therefore significantly improves the efficiency of the antenna. Furthermore, the planar surface with a designed phase configuration offers the ability of producing desired far-field radiation patterns while keeping a flat profile. Especially benefiting from the development of micro- and nano-fabrication technology, reflectarrays with micro- even nano-scale radiation elements have been successfully realised for novel functions.

Generally, a typical reflectarray is composed of three layers as shown in Fig. 3.1(a): a top layer with resonant elements arranged periodically with a beam-forming phase

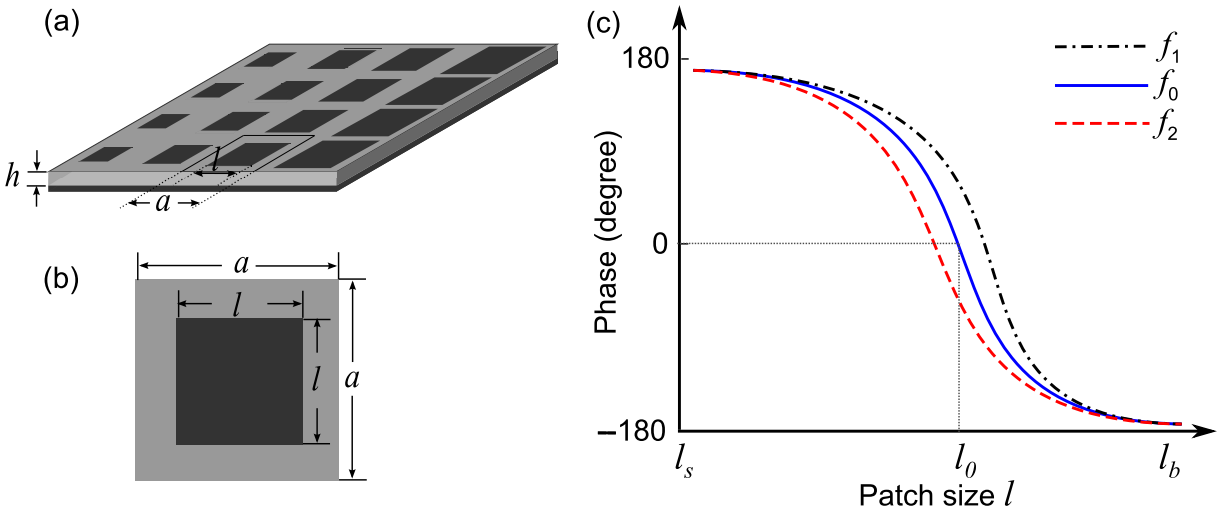

Figure 3.1. Schematic diagram indicating the structure of a typical reflectarray. (a) A typical reflectarray is composed of three layers: a top layer with periodically arranged metal radiating resonators, a dielectric spacer with a thickness of h, and a metal ground plane. (b) A square metal patch with a size of l functions as the radiating resonator of a reflectarray radiation element with size of a. (c) By varying the width of the patch l, different phase responses with a range over 300° can be achieved for constructing a reflectarray for beamforming. The phase responses are frequency-dependent.

distribution, a dielectric spacer, and a solid metal ground plane. A requirement imposed on the resonant elements used for constructing a reflectarray is that the possible phase range for the single element can cover one 360° cycle. This is sufficient for narrowband operation, as the phase can be wrapped to attain larger phase variations. As the reflection phase response is dependent on a critical dimension of the resonant structure, the expected phase range is achieved by varying one or several geometrical parameters of the resonant elements. For instance, a resonant element with a size of a made of square metallic radiating patch can achieve a phase range of over 300° by varying the size of the patch resonator l, as shown in Figs. 3.1(b) and (c). As commonly used resonators, rectangular dipoles and patches with variable dimensions are mostly preferred due to their simple fabrication and analytical models that can be solved by classical electromagnetics theory.

In the design of reflectarrays, several factors should be taken into account. Firstly, the overall size of the radiation element, also denoted as the unit cell, is determined by the operation frequency, and should be around a half of wavelength or less. If the unit cell size is larger than the operation wavelength, diffraction effects will be invoked to interfere with the fundamental resonance. Secondly, the phase range obtained by varying

geometrical dimensions of the chosen radiation element should be large enough for practical design. The thickness of the substrate plays an important role in determining the phase range, and a phase range of over 2π is an ideal value. A thinner thickness results in a wider phase range but a higher Q-factor of the resonance of the element therefore a steeper slope of the phase response. Thirdly, the loss in materials affects the efficiency of the designed reflectarray. Especially in the higher frequency regime, highly lossy substrate and finite conductivity of metals could decrease the radiation efficiency dramatically. Fourthly, the bandwidth of the reflectarrays should be considered for some application scenarios. Some approaches such as multilayered structures have been applied for improving the bandwidth, however at the cost of increasing the complexity in the manufacture process (Encinar 2001, Encinar 2010). Lastly, the coupling effect between the neighboured radiation elements will affect the local phase responses and may require the optimization of the size and layout of the radiation elements in the reflectarray.

In this chapter, several types of unit elements for constructing reflectarrays are reviewed. For the simplicity of analysis and fabrication, rectangular dipoles and patches are the main structures that are used in this thesis. The related theoretical analysis, such as fringing effect (electromagnetic fields extend to the space beyond the edges of the dipoles and patches, which increases the effective areas of the dipoles and patches), resonance modes and the relation between a progressive phase distribution and the resulting deflection angle, is given in this chapter. Based on the properties of the radiating elements, subarrays for constructing a reflectarray yielding desired radiation characteristics can be synthesized by array theory. General synthesis array theory for antenna pattern is included at the end of this chapter.

3.2 Radiating resonators for reflectarrays

The concept of reflectarray as well as the first investigation dates back to the early 1960s, when the device was proposed by Berry *et. al.* (1963). The authors found that elements consisted of a short-ended waveguide can be stacked to form a reflecting surface characterized by the surface impedance. When a feeding source illuminates the surface, the reflection phase and magnitude at any point of the reflectarray is determined by the local surface impedance that can be changed by varying the length of the waveguide at that point. By synthesizing the surface impedance of the reflecting

surface, a variety of radiation patterns can be produced. The fundamental principle of the reflectarray was clearly illustrated in this work. However, most wireless operations at this early stage were based on relatively low microwave frequencies, and therefore the first reflectarray prototype with large waveguide was still significantly bulky and heavy, which made the concept un-pursued for a long time. More than one decade later, Phelan developed a Spiralphase reflectarray that was composed of 4 spiral arms connected with switching diodes for circular polarisation (Phelan 1977). By switching the diodes, different spiral arms are activated, and this operation is equivalent to a angular rotation of the radiation elements. Correspondingly, the radiated phase of the element is adjusted, and the main beam of the reflectarray can be scanned. Due to the thick spiral arms and the diodes, the Spiralphase reflectarray was still bulky and heavy.

Benefiting from the development of printable microstrip antennas, the concept of reflectarray started to regain attention from the academic and engineering communities since its first realisation with microstrip elements (Malagisi 1978, Pozar and Metzler 1993). Compared with the former prototypes with end-shorted waveguides and spiral arms, high-efficiency microstrip reflectarrays significantly reduced the antenna size and mass, and showed huge potential for practical applications. Towards low flat-surface profile, light antenna mass and low manufacturing cost, various printed microstrip radiating elements for reflectarrays have been developed since then as shown in Fig. 3.2. The configuration of metal microstrip patch with loaded stub shown in Figs. 3.2(a) and (b) was the most used structure for constructing reflectarrays at the early stage (Javor *et al.* 1995). The size of the rectangular microstrip patch determines the resonance frequency, while the length of the stub, i.e. an open-circuited microstrip transmission lines, offers an element phase response equal to twice the stub's electrical length. The rectangular patch loaded with the stub only at one edge responded to the polarisation that is parallel to the direction of the stub. By placing two stubs on perpendicular edges of a square patch resonator as shown in Fig. 3.2(b), two orthogonal polarisations can be activated independently. A simplified structure that has been used widely is the microstrip patch without stubs as shown in Fig. 3.2(c). By varying the size of the patch, different phase responses can be obtained for designing a reflectarray with desired far-field radiation patterns (Pozar and Metzler 1993, Targonski and Pozar 1994). The patch resonators are simple to fabricate and can be adopted into different frequency ranges for linear polarisations by scaling their sizes. For circular polarisation, the patch resonators loaded with phase-delay stubs as shown in Fig. 3.2(d)

can be used for achieving desired phase responses by rotating the identical elements with variable angles(Huang and Pogorzelski 1998). Some other resonant elements that have been developed such as double rectangular loops (Memarzadeh and Mosallaei 2011) and circular rings (Sayidmarie and Bialkowski 2008), crossed dipoles (Pozar and Targonski 1998, Li *et al.* 2011) and cross shaped microstrip loop (Perruisseau-Carrier 2010) are shown in Fig. 3.2(e). These two-dimensional microstrip resonators have provided unique properties for constructing various flat reflectarrays with specific functional characteristics. In recent years, some three-dimensional dielectric elements have been also demonstrated to build up reflectarrays with unique proprieties. For example, as shown in Fig. 3.2(f), a dielectric block with variable height has been proposed as a low-loss and low-cost phase-delay radiating element for realising a high gain reflectarray antenna at terahertz frequencies (Nayeri *et al.* 2014). In this design, fabrication process is based on a polymer-jetting 3D printing technology, which makes it possible to realise a terahertz reflectarray prototype composed of non-resonant elements with different heights in a fast and low-cost way.

Reflectarrays based on microstrip radiating resonators have the advantages of flat profile, small mass, high efficiency, low-loss, wide-angle beam scanning capability, accurate and high-directional beam shape, *etc*. However, the intrinsic characteristic of narrow bandwidth is always associated with the operation of the various reflectarrays based on resonant elements. The narrow bandwidth is generally limited by two factors: the narrow bandwidth from the resonant elements and the limitation arising from the differential spatial phase delay resulting from the different lengths from feeding source to each element. For an ideal plane wave or a collimated beam excitation as commonly used at terahertz frequencies, mostly the first factor determines the bandwidth performance of the reflectarray and typically limits the fractional bandwidth to around 5%. For the resonant element, broadening bandwidth corresponds to having a smooth and linear phase response when one or several dimensional parameters are varied. The method of using a thick substrate can make the phase curve smooth but reduces the total phase range achievable by the radiating element. More efficient techniques have been required to overcome the bandwidth limitation of the radiating elements. As shown in Fig. 3.3(a), the strategy of using stacked patches in a multilayered configuration can offer a smooth and linear phase curve with a phase range of several cycles (Encinar 2001, Encinar *et al.* 2006). It has been proved that the use of multilayered stacked patches can significantly improve the bandwidth at least

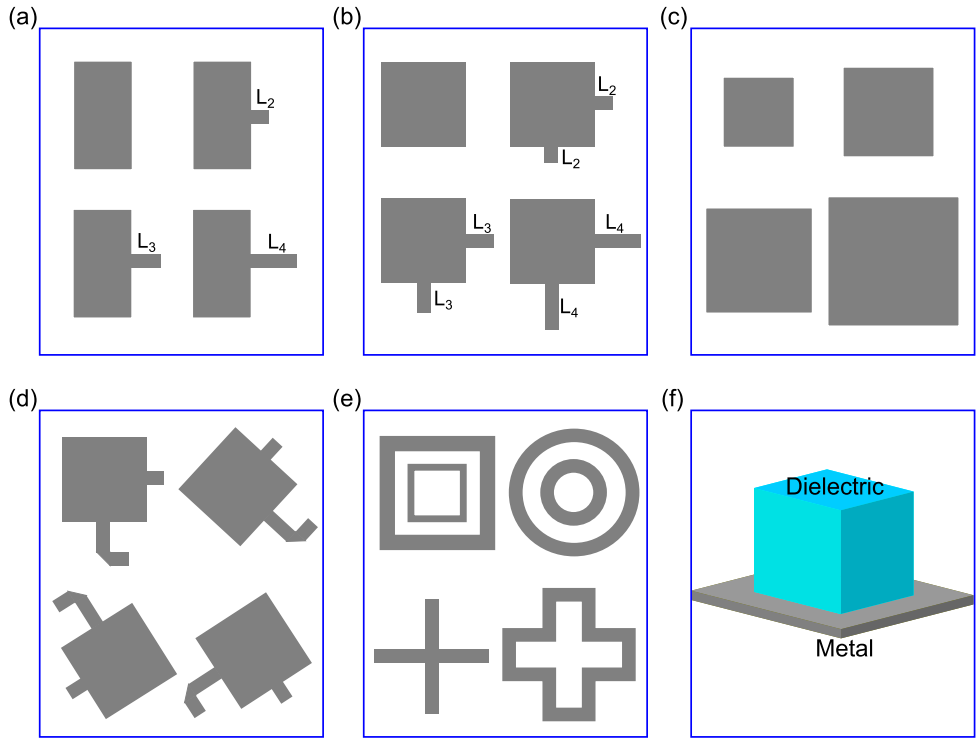

Figure 3.2. A series of resonant elements for reflectarrays. (a) Identical rectangular patches loaded with variable-length stubs at one edge for phase delay response to a specified polarisation. Adapted from Javor *et al.* (1995). (b) Identical square patches loaded with variable-length stubs at two perpendicular edges for phase delay that respond to dual polarisations. Adapted from Javor *et al.* (1995). (c) Square patches with variable lengths for different phase shifts. (d) Identical microstrip structures with variable rotation angles for the circular polarisation. Adapted from Huang and Pogorzelski (1998). (e) Double rectangular loops, double circular rings, crossed dipoles and cross shaped microstrip resonators for reflectarrays. Adapted from Memarzadeh and Mosallaei (2011), Sayidmarie and Bialkowski (2008), Li *et al.* (2011), and Perruisseau-Carrier (2010), respectively. (f) Dielectric block on a metal ground plane for 3D printed reflectarray at the terahertz frequencies. Adapted from Nayeri *et al.* (2014).

in the low microwave frequency range. However, it demands complicated manufacturing process to bond the different reflectarray layers together, and therefore would be very challenging for fabrication with high accuracy particularly at high frequencies beyond the millimetre-wave range. Single-layered structures are thus preferred at higher frequencies due to the advantage of accurately controlled fabrication tolerance. A strategy of three multi-resonant dipoles arranged in a single layer with a linear phase response can be adopted to the design of broadband reflectarrays, as demonstrated in

Fig. 3.3(b) in the microwave range (Li *et al.* 2009, Florencio *et al.* 2014). The corresponding phase response of the element with three parallel multi-resonant dipoles is shown in Fig. 3.3(e). Comparing to the narrow-band phase response for the element made of a square patch shown in Fig. 3.1(c), the strategy for broadband operation offers a nearly linear phase response with a wide enough phase range by properly adjusting the length ratio of the three dipoles. When the operation frequencies specifically deviate from the designed frequency, the phase curves remain nearly linear and are nearly parallel for the different frequencies, which translates into broad bandwidth operation. More sophisticated single-layered structures that can provide smooth and linear phase response as resonant elements include a round disk with attached phase-delay lines (Hasani *et al.* 2010) and a windmill-shaped element with variable length (Li *et al.* 2007), as shown in Figs. 3.3(c) and (d), respectively.

3.3 Analysis of rectangular patch

Among various resonant elements, the rectangular patch with variable size is the most widely used configuration for constructing reflectarrays. There are many methods such as transmission-line model and cavity model that have been used to successfully analyse the characteristics of the rectangular patches mounted on a substrate backed by a ground plane. Based on these analysis, some results i.e. fringing effect, effective dimensions and resonance frequency have been illustrated in textbooks and classical references (Balanis 1982). In this section, some general analysis results are given for the convenience of following sections.

In the classical configuration of resonant element with rectangular patch as shown in Fig. 3.4, the most relevant parameters are: element size a, length of the patch l, width of patch w, thickness of the substrate h, and relative permittivity and loss tangent of the substrate ϵ_r and $\tan\delta$, respectively. For these parameters, the size of the element, also commonly denoted as unit cell size, is mainly determined by the operation frequency. The length and width of the patch can be varied to achieve a desired phase response while the thickness of the substrate affects the obtained phase range. The relative permittivity indicates the relative charge storage capabilities of the substrate. The larger its value, the more electrical energy can be concentrated in the substrate. However, a high relative permittivity leads to narrow bandwidth and high loss and therefore low efficiency. At high frequencies, the loss tangent of the dielectric and ohmic

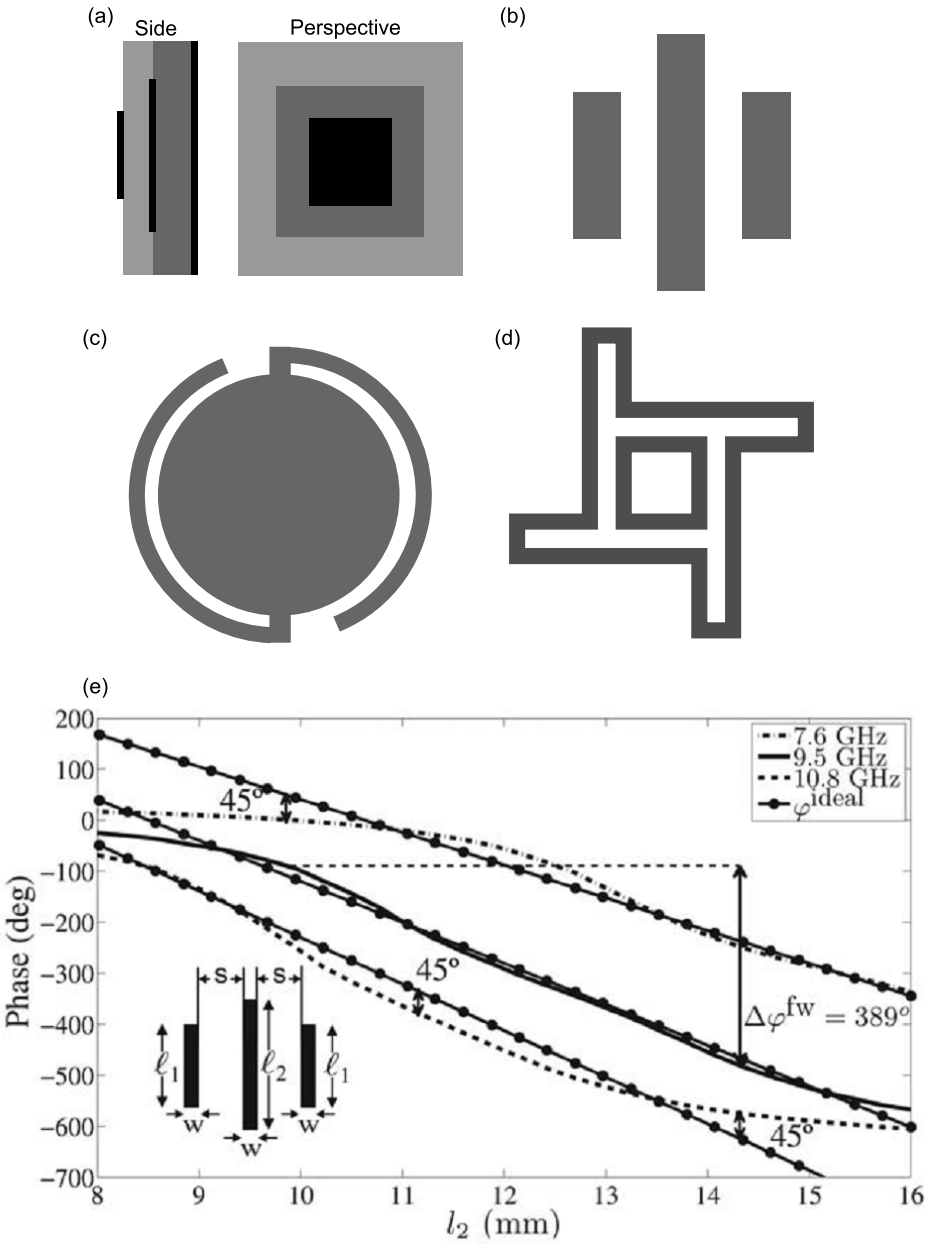

Figure 3.3. Resonant elements for broadband reflectarrays. (a) Stacked multilayered patches with variable size. Adapted from Encinar (2001). (b) Multi-resonant dipoles with variable lengths. Adapted from Florencio *et al.* (2014). (c) A round disk with attached phase-delay lines. Adapted from Hasani *et al.* (2010). (d) A windmill-shaped element with variable length. Adapted from Li *et al.* (2007). (e) Phase response for the broadband radiating element consisting of three parallel dipoles shown in (b). Adapted from Florencio *et al.* (2014).

losses of metal are the main factors that determine the reflection efficiency. The most desirable element for good electrical performance (high efficiency, broad bandwidth, loosely bound fields for radiation into free space) would have a thick substrate with

a low relative permittivity and loss, but at the cost of a narrow phase range and large size. Mode analysis and approaches for determining the parameters of the element at a given operation frequency are presented in the following subsections.

3.3.1 Modes

In order to analyse the modes of the resonant element with rectangular patch, the structure shown in Fig. 3.4 is considered. It can be assumed that the dielectric material under the patch is truncated along the edges of the patch, and the volume under the patch can be treated as a rectangular cavity filled with a material with a relative permittivity

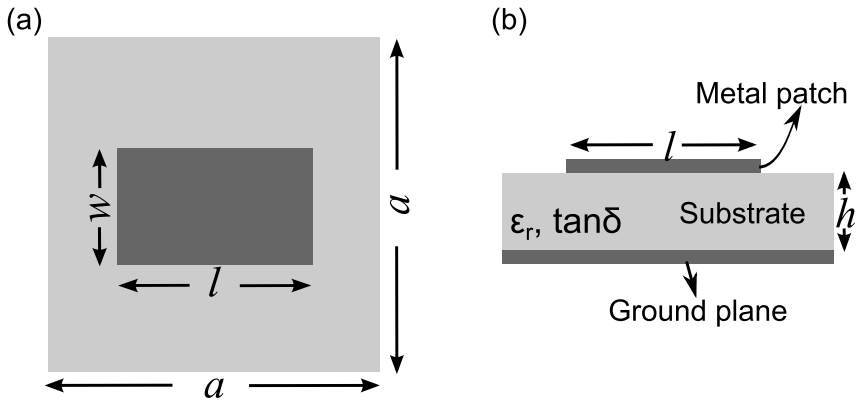

Figure 3.4. Resonant element with rectangular patch. (a) Top view of the element. The size of the square element is a, while the length and width of the rectangular path is l and w, respectively. (b) Side view of the element. Thickness of the substrate with a relative permittivity of ϵ_r is h.

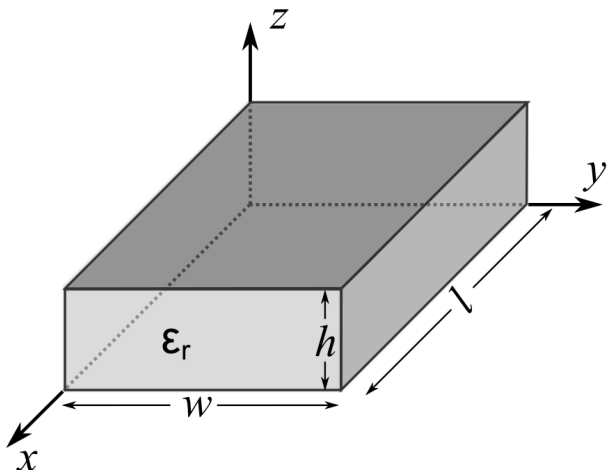

Figure 3.5. Geometry of a rectangular patch for mode analysis. The volume under the patch shown in Fig. 3.4 can be treated as a rectangular cavity filled with a dielectric material.

ϵ_r as shown in Fig. 3.5. In this configuration, the vector potential approach with boundary conditions can be used to obtain the modes of the resonant element (Balanis 1989). Because the thickness of the dielectric spacer is generally very small comparing with the operation wavelength, the fringing of the fields along the edges of the patch is very small, and the electric field is nearly normal to the surface of the patch. Therefore, only the TM field configurations will be considered in the cavity. Assuming that the vector potential along z directions is $\mathbf{A}_z$, the following equation must be satisfied:

$$\bigtriangledown^2 \mathbf{A}_z + \beta^2 \mathbf{A}_z = 0, \tag{3.1}$$

where $\beta = \omega\sqrt{\epsilon\mu}$ is the wave number and $\omega = 2\pi f$ is the angular frequency. Using the method of the separation of variables, and due to the cavity being bounded in x, y, and z directions, i.e. with standing waves in all directions, the solution to Eq. 3.1 can be generally expressed as

$$A_z = [A_1 \cos(\beta_x x) + B_1 \sin(\beta_x x)][A_2 \cos(\beta_y y) + B_2 \sin(\beta_y y)][A_3 \cos(\beta_z z) + B_3 \sin(\beta_z z)], \tag{3.2}$$

where β_x, β_y, and β_z are the wave numbers along the axis x, y, and z, respectively, that can be determined by boundary conditions. The equation

$$\beta^2 = \beta_x^2 + \beta_y^2 + \beta_z^2 \tag{3.3}$$

is referred to as the dispersion equation. Referring to the structure shown in Fig. 3.5, the electric and magnetic fields in terms of the vector potential $\mathbf{A}$ are given by

$$\begin{aligned} E_x &= -j\frac{1}{\omega\epsilon\mu}\frac{\partial^2 A_z}{\partial z \partial x} & H_x &= \frac{1}{\mu}\frac{\partial A_z}{\partial y} \\ E_y &= -j\frac{1}{\omega\epsilon\mu}\frac{\partial^2 A_z}{\partial z \partial y} & H_y &= -\frac{1}{\mu}\frac{\partial A_z}{\partial x}. \\ E_z &= -j\frac{1}{\omega\epsilon\mu}\left(\frac{\partial^2}{\partial z^2} + \beta^2\right) A_z & H_z &= 0 \end{aligned} \tag{3.4}$$

With the boundary conditions of the electric and magnetic fields

$$\begin{aligned} &E_x(0 \le x \le l, 0 \le y \le w, z = 0) = E_x(0 \le x \le l, 0 \le y \le w, z = h) = 0, \\ &H_x(0 \le x \le l, y = 0, 0 \le z \le h) = H_x(0 \le x \le l, y = w, 0 \le z \le h) = 0, \\ &H_y(x = 0, 0 \le y \le w, 0 \le z \le h) = H_y(x = l, 0 \le y \le w, 0 \le z \le h) = 0, \end{aligned} \tag{3.5}$$

the wave numbers β_x, β_y, and β_z can be derived as followings:

$$\begin{aligned}
E_x\Big|_{z=0} &= -j\frac{1}{\omega\epsilon\mu}\frac{\partial^2 A_z}{\partial z\partial x}\Big|_{z=0} \\
&= -j\frac{1}{\omega\epsilon\mu}[-A_1\beta_x\sin(\beta_x x)+B_1\beta_x\cos(\beta_x x)][A_2\cos(\beta_y y)+B_2\sin(\beta_y y)] \\
&\quad \cdot[-A_3\beta_z\sin(\beta_z z)+B_3\beta_z\cos(\beta_z z)]\Big|_{z=0} \\
&= -j\frac{1}{\omega\epsilon\mu}B_3\beta_z[-A_1\beta_x\sin(\beta_x x)+B_1\beta_x\cos(\beta_x x)][A_2\cos(\beta_y y)+B_2\sin(\beta_y y)] \\
&= 0 \qquad \Longrightarrow B_3 = 0 \\
E_x\Big|_{z=h} &= 0 \qquad \Longrightarrow \beta_z = \frac{p\pi}{h}, \qquad p = 0,1,2,.....
\end{aligned} \tag{3.6a}$$

$$\begin{aligned}
H_x\Big|_{y=0} &= \frac{1}{\mu}\frac{\partial A_z}{\partial y}\Big|_{y=0} \\
&= \frac{1}{\mu}[A_1\cos(\beta_x x)+B_1\sin(\beta_x x)][-A_2\beta_y\sin(\beta_y y)+B_2\beta_y\cos(\beta_y y)] \\
&\quad \cdot[A_3\cos(\beta_z z)+B_3\sin(\beta_z z)]\Big|_{y=0} \\
&= \frac{1}{\mu}B_2\beta_y[A_1\cos(\beta_x x)+B_1\sin(\beta_x x)][A_3\cos(\beta_z z)+B_3\sin(\beta_z z)] \\
&= 0 \qquad \Longrightarrow B_2 = 0 \\
H_x\Big|_{y=w} &= 0 \qquad \Longrightarrow \beta_y = \frac{n\pi}{w}, \qquad n = 0,1,2,.....
\end{aligned} \tag{3.6b}$$

$$\begin{aligned}
H_y\Big|_{x=0} &= -\frac{1}{\mu}\frac{\partial A_z}{\partial x}\Big|_{x=0} \\
&= -\frac{1}{\mu}[-A_1\beta_x\sin(\beta_x x)+B_1\beta_x\cos(\beta_x x)][A_2\cos(\beta_y y)+B_2\sin(\beta_y y)] \\
&\quad \cdot[A_3\cos(\beta_z z)+B_3\sin(\beta_z z)]\Big|_{x=0} \\
&= -\frac{1}{\mu}B_1\beta_x[A_2\cos(\beta_y y)+B_2\sin(\beta_y y)][A_3\cos(\beta_z z)+B_3\sin(\beta_z z)] \\
&= 0 \qquad \Longrightarrow B_1 = 0 \\
H_y\Big|_{x=l} &= 0 \qquad \Longrightarrow \beta_x = \frac{m\pi}{l}, \qquad m = 0,1,2,.....
\end{aligned} \tag{3.6c}$$

Therefore, Eq. 3.2 can be rewritten as

$$A_z = A_{mnp}\cos(\beta_x x)\cos(\beta_y y)\cos(\beta_z z), \tag{3.7}$$

where $A_{mnp} = A_1 A_2 A_3$ represents the magnitude coefficients of the potential vector A_z in each mnp mode.

By substituting Eq. 3.7 into Eq. 3.4, the expressions of the electric and magnetic fields are obtained as

$$\begin{aligned}
E_x &= -j\frac{\beta_x\beta_z}{\omega\epsilon\mu}A_{mnp}\sin(\beta_x x)\cos(\beta_y y)\sin(\beta_z z)\\
H_x &= -\frac{\beta_y}{\mu}A_{mnp}\cos(\beta_x x)\sin(\beta_y y)\cos(\beta_z z)\\
E_y &= -j\frac{\beta_y\beta_z}{\omega\epsilon\mu}A_{mnp}\cos(\beta_x x)\sin(\beta_y y)\sin(\beta_z z)\\
H_y &= \frac{\beta_x}{\mu}A_{mnp}\sin(\beta_x x)\cos(\beta_y y)\cos(\beta_z z)\\
E_z &= -j\frac{\beta^2-\beta_z^2}{\omega\epsilon\mu}A_{mnp}\cos(\beta_x x)\cos(\beta_y y)\cos(\beta_z z)\\
H_z &= 0
\end{aligned} \tag{3.8}$$

and the dispersion equation Eq. 3.3 can be represented by

$$\begin{gathered}
\beta_x^2+\beta_y^2+\beta_z^2 = \left(\frac{m\pi}{l}\right)^2+\left(\frac{n\pi}{w}\right)^2+\left(\frac{p\pi}{h}\right)^2 = \beta^2 = \omega^2\epsilon\mu,\\
m,n,p = 0,1,2,..... \quad \text{and} \quad m+n+p \neq 0.
\end{gathered} \tag{3.9}$$

Thus, the resonance frequency in the mnp mode, $(f_r)_{mnp}$, of the structure shown in Fig. 3.5 is

$$(f_r)_{mnp} = \frac{1}{2\pi\sqrt{\epsilon\mu}}\sqrt{\left(\frac{m\pi}{l}\right)^2+\left(\frac{n\pi}{w}\right)^2+\left(\frac{p\pi}{h}\right)^2}. \tag{3.10}$$

Based on Eq. 3.10, resonance frequencies for different modes can be determined. For the structure shown in Fig. 3.5, the addition of $h < w < l$ is satisfied, and therefore the dominant mode, i.e. the mode with the lowest resonance frequency, is the mode TM_{100} with resonance frequency of

$$(f_r)_{100} = \frac{1}{2l\sqrt{\epsilon\mu}} = \frac{c}{2l\sqrt{\epsilon_r}} \tag{3.11}$$

where c is the speed of light in free space. The second high order mode is determined by the difference between $l/2$, w and h. If $w > l/2 > h$, the second high order mode is TM_{010}, and its resonance frequency is

$$(f_r)_{010} = \frac{1}{2w\sqrt{\epsilon\mu}} = \frac{c}{2w\sqrt{\epsilon_r}} \tag{3.12}$$

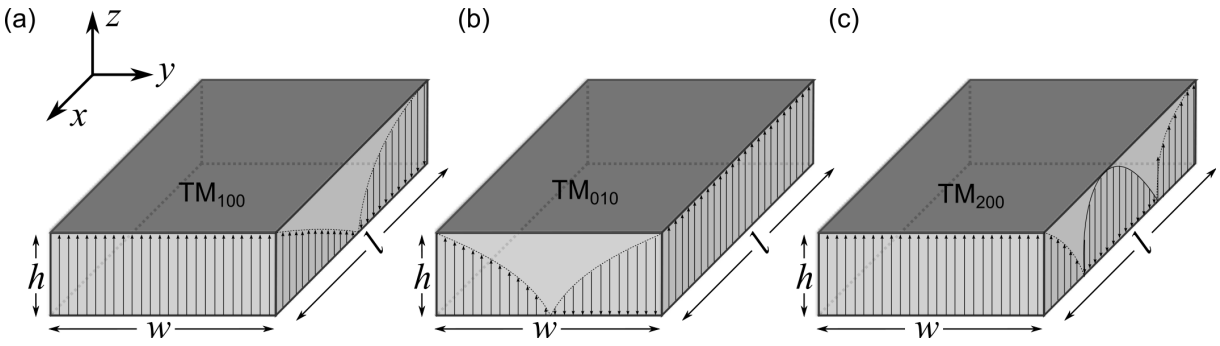

Figure 3.6. Tangential electric field distributions along the side walls of the cavity for the different modes. (a) TM_{100}. (b) TM_{010}. (c) TM_{200}.

However, if $h < w < l/2$, the second high order mode will be TM_{200} rather than TM_{010}. The corresponding resonance frequency is

$$(f_r)_{200} = \frac{1}{l\sqrt{\epsilon\mu}} = \frac{c}{l\sqrt{\epsilon_r}} \tag{3.13}$$

Based on Eq. 3.8, tangential electric field distributions along the side walls of the cavity shown in Fig. 3.5 for the dominant, TM_{010} mode and TM_{200} mode are illustrated in Fig. 3.6, neglecting the fringing effect along the edges.

3.3.2 Fringing effect

As shown in Fig. 3.4, the dimensions of the rectangular patch is finite, therefore fringing effects cannot be avoided for the fields at the edges of the patch. A schematic diagram illustrating the fringing effects at the edges is given in Fig. 3.7. For the polarisation parallel to the long side of the patch, the amount of the fringing effect is determined by the ratio of the patch length to the thickness of the substrate i.e. l/h and the value of relative permittivity ϵ_r of the substrate: The smaller the value of l/h

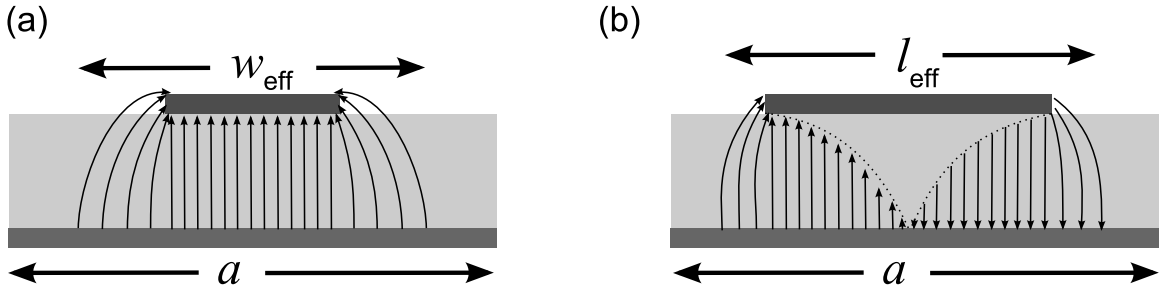

Figure 3.7. Schematic diagram showing the fringing effect at the edges of the rectangular patch. (a) Effective width. (c) Effective length.

and ϵ_r, the stronger the fringing effect. Although in general $l/h \gg 1$, the fringing effect still needs to be taken into account in the design process as it affects the resonance frequency of the element. In order to define the fringing effect, two parameters are needed to be introduced: an effective relative permittivity ϵ_{reff} and an effective length l_{eff}. Generally, the effective relative permittivity is in the range of $1 < \epsilon_{reff} < \epsilon_r$ and its introduction aims to describe the extent of the unbounded fields aroused by the inhomogeneity at the surface between the substrate and air. The effective length is larger than the real length of the rectangular patch ($l_{eff} > l$) and includes the fringing effect around the edges of the patch. The empirical formulations for these two parameters are given as (Balanis 1989)

$$\epsilon_{reff} = \frac{\epsilon_r + 1}{2} + \frac{\epsilon_r - 1}{2}\left[1 + 12\frac{h}{w}\right]^{-\frac{1}{2}}, \tag{3.14}$$

and

$$l_{eff} = l + 2 \times 0.412h\frac{(\epsilon_{reff} + 0.3)\left(\frac{w}{h} + 0.264\right)}{(\epsilon_{reff} - 0.258)\left(\frac{w}{h} + 0.8\right)}. \tag{3.15}$$

For the cases where ϵ_r is much larger than unity while the ratio of thickness of the substrate to the width of the patch h/w is much smaller than unity, the value of the effective relative permittivity ϵ_{reff} is very close to the actual material intrinsic relative permittivity ϵ_r. In most practical designs with the features mentioned above, the actual material intrinsic relative permittivity can be used approximately as effective relative permittivity. The effective length indicates that the resonator patch looks electrically larger comparing to its physical dimensions due to the fringing effect, which should be taken into account in determining the resonance size.

Taking the fringing effects into account, for the dominant TM_{100} mode, the resonance frequency presented by Eq. 3.11 should be adjusted to

$$(f_r)'_{100} = \frac{c}{2l_{eff}\sqrt{\epsilon_{reff}}} \tag{3.16}$$

The fringing effect is then defined by a factor q with

$$q = \frac{(f_r)'_{100}}{(f_r)_{100}} \tag{3.17}$$

In practical design, the fringing effect factor is affected by the thickness of the substrate h. Increasing the substrate thickness h leads to increased fringing effect and reduced Q-factor for the resonance at the designed frequency.

3.3.3 Design procedure

With a given resonance frequency f_r, the dimensions of a rectangular patch for a resonant element can be determined based on the above analysis. Basically, the size of the resonant element (also called unit cell) a is generally fixed to around a half of wavelength, while the thickness h of the given substrate with a relative permittivity ϵ_r is fixed to a value smaller than a tenth of the wavelength as this allows achieving a phase range of over 330° (Huang and Encinar 2008). For determining the width and length of the rectangular patch with consideration of fringing effect, the following design procedure can be taken:

1. For determining the width of the rectangular patch leading to good radiation efficiency, the following formula has been proved to be effective (Bahl and Bhartia 1980):

$$w = \frac{c}{2f_r}\sqrt{\frac{2}{\epsilon_r + 1}}. \tag{3.18}$$

2. Calculate the effective relative permittivity ϵ_{reff} with Eq. 3.14.

3. Calculate the effective length l_{eff} of the rectangular patch for resonance with Eq. 3.15.

4. Then, the actual length of the patch for resonance is solved by

$$l = \frac{1}{2f_r\sqrt{\epsilon_{\text{reff}}}\sqrt{\mu_0\epsilon_0}} - 2 \times 0.412h\frac{(\epsilon_{\text{reff}} + 0.3)\left(\frac{w}{h} + 0.264\right)}{(\epsilon_{\text{reff}} - 0.258)\left(\frac{w}{h} + 0.8\right)}. \tag{3.19}$$

In the practical design of a reflectarray, the ground plane is generally constructed by a layer of solid metal. As a special case where $w = l$, the rectangular patch becomes a square patch, and the dimensions of the square patch for resonance can be obtained by solving the simultaneous solutions of Eq. 3.14 and 3.19. At the target frequency, the length and/or width of the rectangular patch can be varied around the resonance size in a range to achieve the desired phase and magnitude responses. Based on the reflection coefficients, rectangular or square patches with differently configured dimensions can be arranged in a specific lattice to form a reflectarray for realising the desired beamforming functions.

3.4 Array theory

Generally, a single radiating element with sub-wavelength size offers a radiation pattern with wide major lobe and low gain. In the applications that require high gains, antenna arrays composed a number of radiating elements with designed configurations are used to provide the desired radiation patterns. In order to achieve the desired far-field radiation pattern, there are several factors that must be considered: the dimensions of the radiating resonator, the radiation pattern of each individual radiating element, the phase response of the individual element, the relative displacement between the elements, and the geometrical configuration of the overall array. For an array composed of elements excited all with identical magnitude and possibly with a progressive phase, the total field at a specified point in the far field is determined by the vector addition of the field radiated by all the individual elements. This section introduces the array theory, followed by the operation principle of a reflectarray for angular deflection.

3.4.1 Array factor

When the spacing between the edges of adjacent radiating elements is larger than a quarter wavelength, coupling between the elements can be neglected (Jedlicka *et al.* 1981, Javor *et al.* 1995). With this assumption, an array of N radiating elements with identical radiation magnitude is shown in Fig. 3.8. The elements are positioned along the y axis, and the relative displacement between the elements is a. It is assumed that the field amplitude and phase of the n^{th} radiating element are E_0 and ϕ_n, respectively. At the observation point with an angle of θ and radial distance of r_n from the element, the field radiated by the n^{th} element is given by

$$\mathbf{E}_n = \mathbf{E}_0 e^{-j(kr_n - \phi_n)} \tag{3.20}$$

where k is the wave number and its vector indicates the observation direction. With a specified progressive phase change $\Delta\phi = \phi_{n+1} - \phi_n \ \ (n = 1, 2, 3, ...\mathrm{N})$, the following relations are satisfied at the far field of the array:

$$\begin{aligned} r_n &= r_1 - (n-1)a\sin\theta \\ \phi_n &= \phi_1 + (n-1)\Delta\phi \end{aligned} \tag{3.21}$$

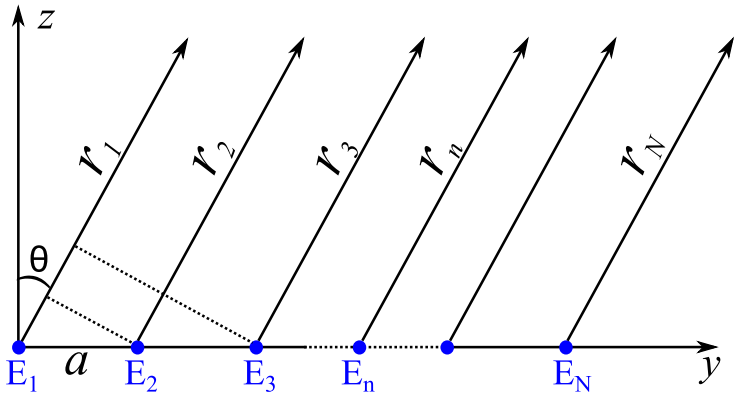

Figure 3.8. Schematic diagram for far-field observation of an uniform array with N elements. The electric fields of all elements have the same magnitude, while the progressive phase change is $\phi_{n+1} - \phi_n = \Delta\phi \ \ (n = 1, 2, 3, ...N)$ for steering the major lobe to the direction of θ. The spacing between the adjacent elements is a.

where r_1 and ϕ_1 are the radial distance and phase of the element located at the coordinate origin, respectively. Thus Eq. 3.20 can be rewritten as

$$\begin{aligned} \mathbf{E}_n &= \mathbf{E}_0 e^{-j\{k[r_1-(n-1)a\sin\theta]-[\phi_1+(n-1)\Delta\phi]\}} \\ &= \mathbf{E}_0 e^{-j(kr_1-\phi_1)} \cdot e^{j(n-1)(ka\sin\theta+\Delta\phi)} \end{aligned} \tag{3.22}$$

The total field of the array at the observation point is equal to the summation of the fields of all N radiating elements as

$$\begin{aligned} \sum_{n=1}^{N} \mathbf{E}_n &= \mathbf{E}_0 e^{-j(kr_1-\phi_1)} \sum_{n=1}^{N} e^{j(n-1)(ka\sin\theta+\Delta\phi)} \\ &= \mathbf{E}_1 \cdot \mathrm{AF} \end{aligned} \tag{3.23}$$

where

$$\mathrm{AF} = \sum_{n=1}^{N} e^{j(n-1)(ka\sin\theta+\Delta\phi)} \tag{3.24}$$

is defined as the array factor. From the definition, the array factor AF is a function of the number of elements, the space between the elements, the progressive phase change and the geometrical arrangement of the array. Equation 3.23 can be more generally expressed as

$$E(\text{total}) = [E(\text{single element at reference point})] \times [\text{array factor}] \tag{3.25}$$

It illustrates that the far field of an array of elements with identical magnitude is equal to the product of the field of a single element at the reference point and the array factor

of the array. By varying the radiation characteristics of the single element, the number n of the elements, the spacing a between the adjacent elements, and the progressive phase change $\Delta\phi$, the characteristics of the far field radiation pattern of the array can be tailored according to practical applications.

3.4.2 Reflectarrray with angular deflection

The diagram shown in Fig. 3.9 illustrates the operation principle of a reflectarray for angular deflection. It shows an array of microstrip patch elements with progressive phase shifts, designed to steer the reflected beam away from the specular direction with an angle of θ. Assuming that each radiating element offers a phase of ϕ_n $(n = 1, 2, 3, 4, ...)$, the progressive phase change is $\Delta\phi = \phi_{n+1} - \phi_n$. Neglecting the coupling effect between the elements, the plane wave incident normal to the surface will be deflected towards an angle of θ, which will depend on the array geometrical configuration and the progressive phase change $\Delta\phi$, regardless of the polarisation of the incident wave. Referring to the array theory, i.e. Eq. 3.24, the first maximum of the array factor, i.e. the major lobe of the radiation pattern of the array, occurs when

$$k_0 a \sin\theta + \Delta\phi = 0 \tag{3.26}$$

where k_0 is the propagation constant of the wave in free space, and $a \sin\theta$ is the optical path difference between the n^{th} and $(n+1)^{\text{th}}$ elements after reflection. Equation (3.26) can be rewritten as

$$\Delta\phi = -k_0 a \sin\theta = -\frac{2\pi}{\lambda_0} \cdot a \cdot \sin\theta \tag{3.27}$$

or

$$\sin\theta = -\frac{\Delta\phi\lambda_0}{2\pi a} \tag{3.28}$$

where λ_0 is the wavelength of the incident wave in free space. The sign in Eqs (3.27) and (3.28) indicates that the phase responses introduced by the corresponding elements is decreased along the y axis, and therefore $\Delta\phi < 0$.

Equations (3.27) and (3.28) describe the inter-dependence between the value of the deflection angle θ and the progressive phase change $\Delta\phi$. If the deflection angle is specified, the progressive phase change can be calculated with the relation shown in Eq. (3.27). For the simplicity of design and fabrication, a strategy with periodically arranged identical linear sub-arrays can be adopted for designing deflecting reflectarrays. Therefore, the progressive phase change becomes an integer fraction of 360°, e.g.

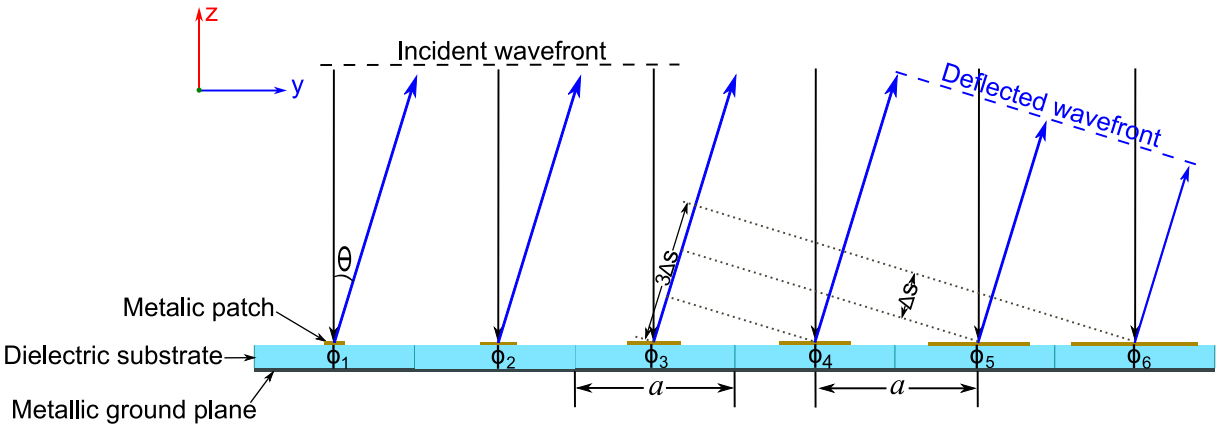

Figure 3.9. Operation principle of a reflectarray for beam deflection. The phase distribution results in deflection of a normally incident plane wave towards a predesigned angle θ. Here, a indicates the spacing between the centre points of two adjacent elements, and $\phi_i (i = 1,2,3,4,5,6)$ indicates the phase change introduced by the corresponding element.

a N-element sub-array will require a progressive phase change of $360^\circ/N$ to satisfy the periodicity condition. With this strategy, it is possible to determine a specified deflection angle θ by using Eq. (3.28).

3.5 Reflectarray in the terahertz regime

In theory, radiating elements that have been applied in the microwave regime can be directly scaled down to micro-scale for terahertz applications. However, a successful realisation of a reflectarray at a frequency in the terahertz regime is practically very challenging to achieve. Besides the strategies for choosing proper resonant elements with specified structures, there are specific technological concerns that need to be addressed to achieve a functional reflectarray at terahertz frequencies. Metals show high loss and dispersion behaviour at terahertz frequencies, while particular dielectric materials with low loss are required for the substrate. In addition, micro-scale manufacturability, fabrication tolerances and experimental validation are further challenges associated with reflectarrays at terahertz frequencies.

3.5.1 Drude's model for metals

In the terahertz range, one concern that should be taken into account in the design process is the the unique features of the employed materials. For the radiating elements

and the ground plane, metals are generally applied, but do not perform as perfect electric conductors particularly at the high frequencies beyond the millimetre-wave range. High loss from finite conductivity and dispersion both require effective models to accurately describe the metals in the high frequency range. There are several modelling strategies that have been used to treat normal metals (Lucyszyn 2007). One classical treatment is Drude's model that describes an ideal system of free electrons having a spherical Fermi surface. For conductor, the classical relaxation-effect model is represented by the following expression for surface impedance, Z_{SR},

$$Z_{SR} = \sqrt{\frac{j\omega\mu_0\mu_r}{\sigma_R + j\omega\epsilon_0}}, \quad \text{with } \sigma_R = \frac{\sigma_0}{1 + j\omega\tau} \tag{3.29}$$

where σ_R is the intrinsic bulk complex conductivity of the metal at the considered frequency, σ_0 the DC-conductivity, $\tau = 1/\gamma_p$ the relaxation time, γ_p the temperature-dependent damping frequency, μ_0 the permeability of free space, μ_r the relative permeability, ϵ_0 the permittivity of free space, $\omega = 2\pi f$ the angular frequency, and f the frequency of the incident wave. At room temperature and sufficiently low frequencies, Eq. 3.29 reduces to classical skin-effect model:

$$Z_{SR} \approx \sqrt{\frac{j\omega\mu_0\mu_r}{\sigma_0}} = R_0(1 + j), \quad \text{when } \omega\tau \ll 1 \tag{3.30}$$

where R_0 is classical skin-effect surface resistance.

For the design of reflectarrays in the terahertz regime, the Drude's model described by Eq. 3.29 is used to calculate surface impedances of metals for radiating resonators and ground plane. The calculated real and image parts of the surface impedance at the designed frequency are imported into the simulation software, Ansys HFSS, as the resistance and reactance, respectively, of the thin metal films.

3.5.2 Material parameters

For the terahertz reflectarrays described in this thesis, gold is used for either the radiating element or the ground plane, while polydimethylsiloxane (PDMS) is adopted as the dielectric spacer due to its low loss at terahertz frequencies and its compatibility with spin-coating. In some cases, platinum is applied as the ground plane because of the requirement of micro-fabrication. Gold and platinum are good conductors, and

are not subject to oxidization in air, whereas PDMS exhibits relatively low loss in the terahertz range. The operation frequency of most designs is set to 1 THz.

For simulations, the used metals are described by the surface impedance model with Eq. 3.29. For gold and platinum, the corresponding parameters are $\sigma_{0,\mathrm{Au}} = 4.10 \times 10^7$ S/m, $\sigma_{0,\mathrm{Pt}} = 9.43 \times 10^6$ S/m, $\gamma_{p,\mathrm{Au}} = 6.48 \times 10^{12}$ Hz, and $\gamma_{p,\mathrm{Pt}} = 16.73 \times 10^{12}$ Hz. At the operation frequency $f = 1$ THz, the surface impedance of gold and platinum can be calculated as

$$\begin{aligned} Z_{SR,\mathrm{Au}} &= 0.287 + j\,0.335 \ \ \Omega/\mathrm{sq} \\ Z_{SR,\mathrm{Pt}} &= 0.628 + j\,0.667 \ \ \Omega/\mathrm{sq} \end{aligned} \tag{3.31}$$

In terms of the substrate, the parameters of PDMS are determined from measurement (Khodasevych *et al.* 2012). At 1 THz, the relative permittivity and loss tangent of PDMS are 2.35 and 0.06 , respectively.

3.6 Summary

As a promising candidate for antennas with high efficiency, low profile, and low cost, the concept of reflectarray was proposed about 5 decades ago. Benefiting from the development of the technology of micro-scale or nano-scale manufacturability, reflectarrays have been realised and applied in many areas such as communications, satellite antennas, sensing and detection. In this chapter, the general background, fundamental operation principle and characteristics of reflectarrays have been briefly introduced. More specifically, several kinds of radiating elements that have been proposed to obtain a desired phase response for constructing reflectarrays have been reviewed. Rectangular patches are the main resonant structure used in this thesis, and therefore the relevant theories, i.e. resonant modes, fringing effects and design procedures have been given in this chapter. In the configuration of a reflectarray with radiating elements offering a required phase distribution, array theories can be conveniently used to design the arrangement of these radiating elements. In the terahertz regime, the dissipation loss in metals caused by their finite conductivity and the dispersion require a realistic metal model to describe its performance, and thus Drude's model has been introduced and used to calculate the surface impedance of the metals for radiating resonators and the ground plane.

This chapter has provided required fundamental knowledge and theories for the following core chapters of the thesis. Based on these general knowledge and theoretical

understanding for the design of reflectarrays, several reflectarrays for different functions are designed, fabricated, and measured at terahertz frequencies. Those designs will be presented in the following chapters of the thesis.

Chapter 4

Terahertz reflectarrays with resonant microstrip patches

REFLECTARRAYS composed of resonant microstrip gold patches on a dielectric substrate are demonstrated for operation at terahertz frequencies. Based on the relation between the patch size and the reflection phase, a progressive phase distribution is implemented on the patch array to create a reflector able to deflect an incident beam towards a predefined angle off the specular direction. In order to confirm the validity of the design, a set of reflectarrays each with periodically distributed 360×360 patch elements are fabricated and measured. The experimental results obtained through terahertz time-domain spectroscopy (THz-TDS) show that up to nearly 80% of the incident amplitude is deflected into the desired direction at an operation frequency close to 1 THz. The radiation patterns of the reflectarray in TM and TE polarisations are also obtained at different frequencies. This work presents an attractive concept for developing components able to efficiently manipulate terahertz radiation for emerging terahertz communications.

4.1 Introduction

Various reflectarray structures have been intensively realised in the microwave region. Since metals perform like nearly ideal conductors in the microwave band, metal patches with variable dimensions are common for building reflectarrays, and can reflect the incident waves with high efficiency (Encinar 2010). As an example of successful applications, a 1.2-metre reflectarray antenna made of three stacked layers containing varying-sized patches has been demonstrated to satisfy the demanding requirements of satellite communication (Huang and Encinar 2008). The structure works in two separate frequency bands of $11.7 - 12.2$ GHz and $13.75 - 14.25$ GHz. Hu *et al.* (2008) proposed a millimetre wave reflectarray with phase agile elements consisting of identical microstrip patches and a liquid crystal layer over the ground plane. By applying two external bias voltages to the liquid crystal, the wide range of the phase change can be obtained with reasonable loss at both 102 GHz and 130 GHz. Beyond the millimetre wave range, the concept of reflectarrays have been extended to the infrared band, where a binary phase reflectarray has been realised using subwavelength metallic patches on a dielectric substrate to act as a reflective Fresnel zone plate (Ginn *et al.* 2008). In addition, nano-sized spherical particles with a core-shell structure have been investigated as concept for an optical reflectarray (Ghadarghadr *et al.* 2009, Ahmadi *et al.* 2010). By independently configuring the material properties or radii of the core and shell structures, the reflected phase change can be controlled. Due to its complexity, the core-shell reflectarray remains a theoretical concept. Recently a reflectarray of dielectric resonators operating in the visible frequency range has been proposed and experimentally validated (Zou *et al.* 2013).

For the terahertz spectrum, driven by emerging solid-state sources and detectors, high-gain antennas are required for the construction of wireless networking or imaging systems. Low-loss terahertz reflectarray antennas thus promise attractive advantages for the manipulation of the terahertz radiation. Up to now, however, no reflectarray has been realised for terahertz radiation at around 1 THz and above. But it is certainly worth mentioning some implementations of terahertz *phased* arrays such as the photoconducting antenna array with 64 electrodes by Froberg *et al.* (1992) and the 4×4 patch antenna array for indoor terahertz communication by Islam and Koch (2006). The former is sensitive to the electric noise, and the complexity of realisation could be a potential limitation of this approach. The latter can become very complicated and is prone to high losses when the number of array elements is large. In addition,

Maki *et al.* (2009) demonstrated a terahertz electro-optic source based on the principle of phased array. It was shown that the terahertz beam radiated from the crystal can be steered by controlling the incident angle of the pumped beams without using actual phase shifters. Recently, a similar approach for terahertz beam steering has been implemented in a photoconductive antenna with interference of two pump beams (Uematsu *et al.* 2012). As components for terahertz communications, tunable terahertz phase shifters for phased arrays have been proposed by Chen *et al.* (2004). The arrays are composed of elements that can be reconfigured to scatter and focus surface waves dynamically. Scherger *et al.* (2012) demonstrated an alternative approach for terahertz beam scanning. A wedge-shaped structure filled with liquid crystals is demonstrated to alter the transmission beam path by applying a dc bias.

Towards improving the flexibility of controlling the direction of terahertz radiation, the realisation of reflectarrays operating at the terahertz band is proposed here. The structures employ square metal patches as resonant phase-controlling elements. Particular attention is paid to the choice of suitable materials at terahertz frequencies, while the tolerances of manufacturing techniques are also taken into account. The single element is optimized by simulations employing a Drude model expression for the metal surface impedance, and the relation between the phase response and the patch size is obtained. Based on this relation, a reflectarray is designed to deflect an incident wave on to a predesigned angle off the specular direction. The wave deflection capability is essential for terahertz communications to alleviate the line-of-sight limitation (Kleine-Ostmann and Nagatsuma 2011). In order to verify the design, the terahertz reflectarrays have been fabricated and the performance of the reflectarrays has been experimentally evaluated by using THz-TDS.

4.2 Specific design of terahertz reflectarrays

The unit cell with a square metal path resonator and the constructed reflectarray are numerically investigated, and the design details along with simulation results are given in this section.

4.2.1 Dimensions of patch radiating element

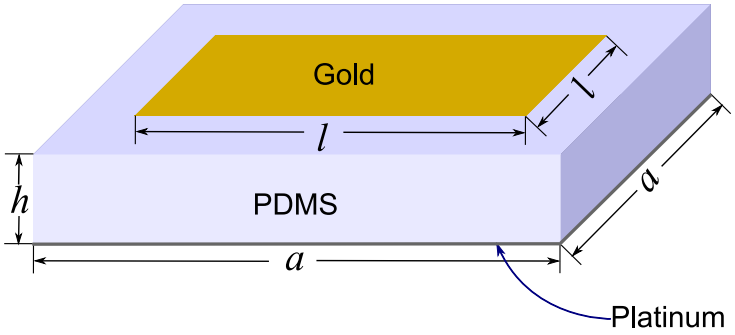

Figure 4.1. Unit cell for the reflectarrays. The dimension of the unit cell is $a = 140\,\mu\text{m}$ and $h = 15\,\mu\text{m}$. The length of the patch l is varied within the range from $10\,\mu\text{m}$ to $136\,\mu\text{m}$ to cover a nearly full cycle of the phase response.

As shown in Fig. 4.1, a unit element for the terahertz reflectarray with square patch resonators is made of three layers, from top to bottom: a gold patch, a polydimethylsiloxane (PDMS) substrate, and a platinum ground plane. Gold and platinum are good conductors, and are not subject to oxidization in air, whereas PDMS exhibits relatively low loss in the terahertz range. Different metals are chosen for the top and ground layer metallisations because of their selectivity for patterning as they react to different etching agents. If the same metal is used, permeation of the etchant through the PDMS will deteriorate the ground layer when patterning the top metallization. Based on the design procedure given in Section 3.3.3, the size of a radiating element a should be approximately half the wavelength. At 1 THz i.e. the wavelength $\lambda = 300\,\mu\text{m}$, the size of the element is fixed at $a = 140\,\mu\text{m}$, while the thickness of the PDMS substrate is $h = 15\,\mu\text{m}$. With the condition of $w = l$, the effective dielectric constant and actual length (also the width) of the square gold patch on resonance at 1 THz are the solutions of Eqs. 3.14 and 3.19, yielding $\epsilon_{\text{reff}} = 2.08$ and $l = 89.5\,\mu\text{m}$, respectively.

4.2.2 Characteristics of patch elements

In the simulation for the operation frequency $f = 1$ THz, the material parameters of the metals are: the surface impedance of gold $Z_{SR,\text{Au}} = 0.287 + j0.335\,\Omega$ and platinum $Z_{SR,\text{Pt}} = 0.628 + j0.667\,\Omega$, the PDMS relative permittivity $\epsilon_r = 2.35$ and loss tangent $\tan\delta = 0.06$, as given in Section 3.5.2. For the wave deflected from the surface of the gold patch, the local phase shift can be controlled by changing one or several parameters of the unit element, such as the size of the square gold patch l or the thickness of the substrate h. By taking the design and fabrication feasibility into account, the side

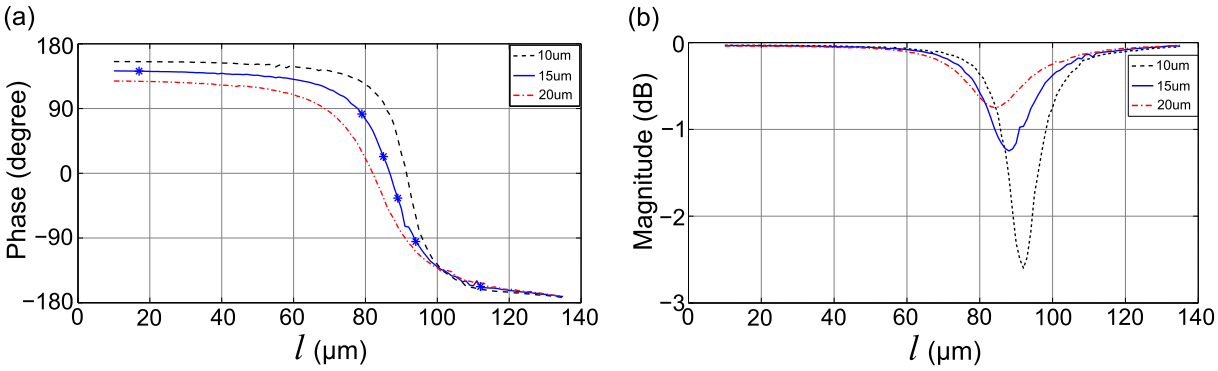

Figure 4.2. Simulated reflection coefficients for 2D uniform infinite patch arrays. Reflection phase response in degree (a) and reflection magnitude in dB (b) at 1 THz as a function of the patch size. The six points on the phase curve of the 15 μm thick substrate indicate the selected patch sizes to define a sub-array that completes one full cycle phase change. The roughness in the magnitude and phase curves is due to the limitation in the numerical accuracy.

length l of the gold patch is chosen as a variable, while the unit cell size and thickness of the PDMS substrate are selected at fixed values $a = 140\,\mu m$ and $h = 15\,\mu m$, respectively. The unit element is optimized at 1 THz by simulations using Ansys HFSS commercial software with master-slave boundary conditions. When the length of the gold patch l is varied within the range from 10 μm to 136 μm, the magnitude and phase of the simulated reflection coefficient for a uniform 2D infinite patch array change as shown in Fig. 4.2. The simulation results show that for the considered geometry and materials, the maximum range of the phase shift covers approximately 330°, which is close to a full cycle and sufficient for the intended operation of a reflectarray. In addition, low-loss reflection is observed for all of the investigated patch sizes with the highest loss of only about -1.2 dB on resonance.

One point to emphasize here is that the total range of the possible phase change shown in Fig. 4.2(a) depends on the thickness of the substrate (Huang and Encinar 2008). Generally, a total phase range of 360° is required for a practical design of reflectarrays, and this demand can be satisfied by using a thin substrate, in practice typically thinner than one tenth of the operational wavelength. This can be physically understood by considering the x-axis limits in Fig. 4.2(a): The case of a zero-size patch or $l = 0\,\mu m$ corresponds to a reflection phase from the lower metal plane covered with a dielectric layer (substrate), whereas the full-size patch corresponds to a reflection phase from a full metallic plane on the top of the substrate. However, as Fig. 4.2(a) implies, the drawback associated with the use of a thinner substrate is that it results in a steeper

phase slope versus a variation of the metal patch size l, particularly around the resonant length. A consequence of a rapid variation in the phase curve is a high sensitivity of the local reflection phase on the patch size. Therefore, the performance of the design employing thinner substrates is more affected by slight inaccuracies of the patch size. In addition, as shown in Fig. 4.2(b), given the same material, the loss of the reflectarray is also mainly influenced by the thickness of the substrate. A thinner substrate corresponds to a higher loss because of a stronger resonance. These trade-offs underpin the choice of thickness $h = 15\,\mu\text{m}$ for the PDMS substrate.

4.2.3 Design and simulations of the reflectarray

Based on the relation between the phase change and the patch size shown in Fig. 4.2, a reflectarray with an off-specular reflection in one plane is designed. The progressive phase change $\Delta\phi$ is fixed at 60°. Therefore the number of elements for one linear subarray amounts to 6 so that it covers one cycle of 360°. The unwrapped phase between the first and last elements of the sub-array also amounts to 60°, so that a periodic arrangement of the subarray fulfils the desired deflection function. According to Eq. 3.27, the deflection angle θ is calculated to be around 21°. As shown in Fig. 4.2(a), the chosen 6 elements in the linear sub-array exhibit the phases decreasing from 142° to -158° in 60° increments. This corresponds to increasing gold patch side lengths of 17 µm, 79 µm, 85 µm, 89 µm, 94 µm, and 112 µm. The configuration of the subarry and the dimension of each patch are shown in Fig. 4.3(c). By the principle of reciprocity of light, if the wave is incident with an angle of 21° away from the normal, the direction of the deflected wave will be perpendicular to the surface of the reflectarray. Therefore, for convenience of observation, the incident wave is set with an angle of 21° in the simulation with HFSS. In the simulations for both the TM and TE polarisation, plane wave with master-slave boundary conditions is applied.

The numerically resolved instantaneous field distributions of the deflected wave for the TM and TE polarisations are shown in Figs. 4.3(a) and 4.3(b), respectively. It is clear that the plane wave incident from an angle of 21° is deflected toward the normal direction, in close accordance with the theory. The field distributions for both the TM and TE polarisations are similar. A slight difference can be observed in the immediate proximity to the surface. This difference can be explained by the orthogonal mode field distributions under the patch elements for the two polarisations. Away from the surface, the slight deviation from a perfect plane wave is explained by the following

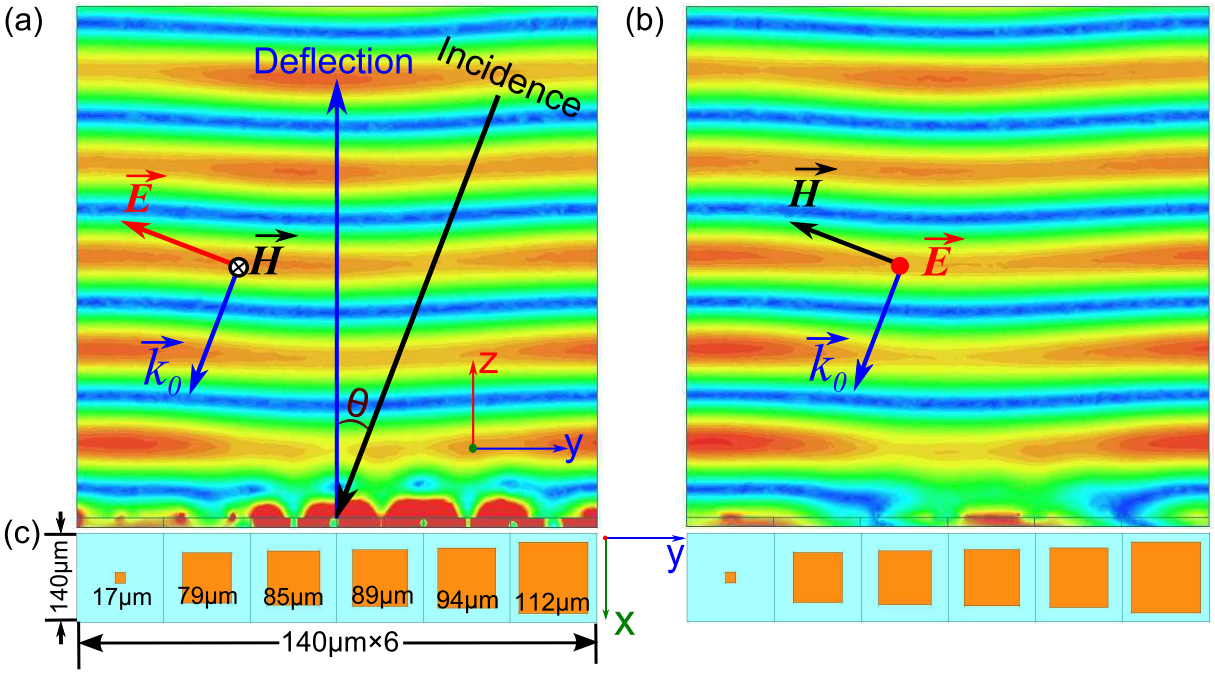

Figure 4.3. Simulated instantaneous scattered fields from the reflectarray in the TM and TE polarisations at 1 THz. (a) Field distribution for the TM polarisation. (b) Field distribution with the same structure and incident direction as in (a) but for the TE polarisation. The incident wave is off normal with $\theta = 21°$. For the TM polarisation, the E field is in the yz plane, and for the TE polarisation, the E field is in parallel with the x axis. (c) Structure of one sub-array made of 6 patch elements depicted at the same scale as those in (a) and (b).

effects. Firstly, inter-element coupling is different in uniform and nonuniform arrays. In the optimisation of a single element, an infinite array with identical elements is considered, and the relation shown in Fig. 4.2 is obtained based on this assumption. In contrast, in the configuration of the sub-array, the dimensions of the neighbouring elements vary in one direction, resulting in a different coupling behaviour. Generally, smaller variations in the reflection phase of successive elements result in a flatter wave front, and therefore a better reflectarray performance. Secondly, the stronger attenuation of the patches near resonance, as illustrated by the magnitude curve in Fig. 4.2(b), affects the uniformity of the deflected wave. Thirdly, the resolution of the patch size in the simulation is limited to 1 μm to reflect the tolerance inherent to the fabrication process. This resolution limitation is relatively coarse and can cause significant error for the required phase response particularly around the resonance. This is clearly observed in Fig. 4.2(a), where the phase response close to resonance is very sensitive to minor inaccuracies of the patch size. A less steep curve of the phase versus the patch

size can decrease the sensitivity to the tolerances, however at the cost of a reduced range of available phases.

4.3 Fabrication and measurement

In order to validate the design, the reflectarray configuration shown in Fig. 4.3(c) has been fabricated and measured. The details of the fabrication process and measurement system are given in this section.

4.3.1 Fabrication

The terahertz reflectarray antennas have been fabricated using microfabrication and polymer processing techniques on 3" silicon substrates. The silicon (100) oriented substrates are cleaned in solvents (acetone and isopropyl alcohol) and dried using high purity compressed nitrogen. A 20 nm layer of titanium serves as an adhesion promoter and a 200 nm thick layer of platinum for the ground plane are deposited from 99.99% pure discs by electron beam evaporation at room temperature following pumpdown to a base pressure of 1×10^{-7} Torr. PDMS, a silicone polymer prepared as a two-part mixture in a 1:10 ratio of hardener and pre-polymer, is spun on to the surface of the platinum coated wafers. This PDMS layer defines the dielectric in the reflectarray antenna. As the PDMS thickness is a critical parameter, the thickness dependence as a function of the spin speed at a fixed acceleration of $1,000\,\mathrm{rpm/s^2}$ and duration of 30 s is experimentally determined. This is defined as an equation that presents a spin speed (r, in rpm) for a desired PDMS thickness (h, in μm) as:

$$r = 0.0001h^4 - 0.0328h^3 + 3.9880h^2 - 238.460h + 7926.4\ . \tag{4.1}$$

For this work, to attain a 15 μm thick PDMS layer, a spin speed of 5,000 rpm is used. The spun on PDMS layer is cured at 72°C for 1 hour. A 200 nm gold layer, with a 20 nm chromium adhesion layer, is then deposited by electron beam evaporation. These metal layers are patterned to define the antenna patches by photolithography and wet etching. The samples are then cleaned with solvents to strip residual photoresist in preparation for terahertz measurements.

4.3.2 Measurement system

The sample shown in Fig. 4.4(a) is made of 360 × 360 patch elements with periodic sub-array arrangement. The microscopy image shown in Fig. 4.4(b) reveals the details of a small area of the sample. The THz-TDs measurement system, Tera K15 developed by Menlo Systems GmbH, is shown in Fig. 4.5(a) with a corresponding schematic representation in Fig. 4.5(b). The emitter and detector antenna models are Tera15-SL25-FC and Tera15-DP25-FC, respectively. The two identical lenses with a diameter of 50 mm are made of a polymer and have an effective focal length of 54 mm and a working distance of 46 mm. A femtosecond optical pulse is guided by a fibre from a near-infrared laser source to the terahertz emitter. The generated broadband terahertz radiation is then guided from the emitter to the reflectarray via Lens 1 that collimates the divergent terahertz beam from the emitter. The parallel beam is either reflected or deflected, depending on the frequency, when it is incident on the surface of the reflectarray sample. The detection part of the system, comprising of Lens 2 and the detector, is mounted on a rotatable arm for scanning the radiation in a wide angular range. On this arm, Lens 2 focuses the scattered radiation into the detector. An incidence angle of 45° is adopted in the measurement, owing to the limitation introduced by the clearance of the two lenses associated with the emitter and the detector. All the reflectarray measurements are normalized by the free-space reference to remove any system dependency. For the reference, a gold-coated mirror substitutes the reflectarray, and the incident and reflection angles are set to 45°. All measurements are performed under ambient temperature in dry atmospheric conditions.

4.4 Results and discussion

The sample is measured for both the TM and TE polarised incident plane waves, and corresponding results are shown in this section.

4.4.1 Measured reflection and deflection spectra

For the TM polarisation, the reference pulse and its spectrum are presented in Figs. 4.6(a) and 4.6(d) (black dashed line), respectively. From 0.5 to 1.5 THz, the reference spectrum curve decreases smoothly without distinct absorption. The mirror is then replaced by the reflectarray sample to register the reflection in the specular direction. A

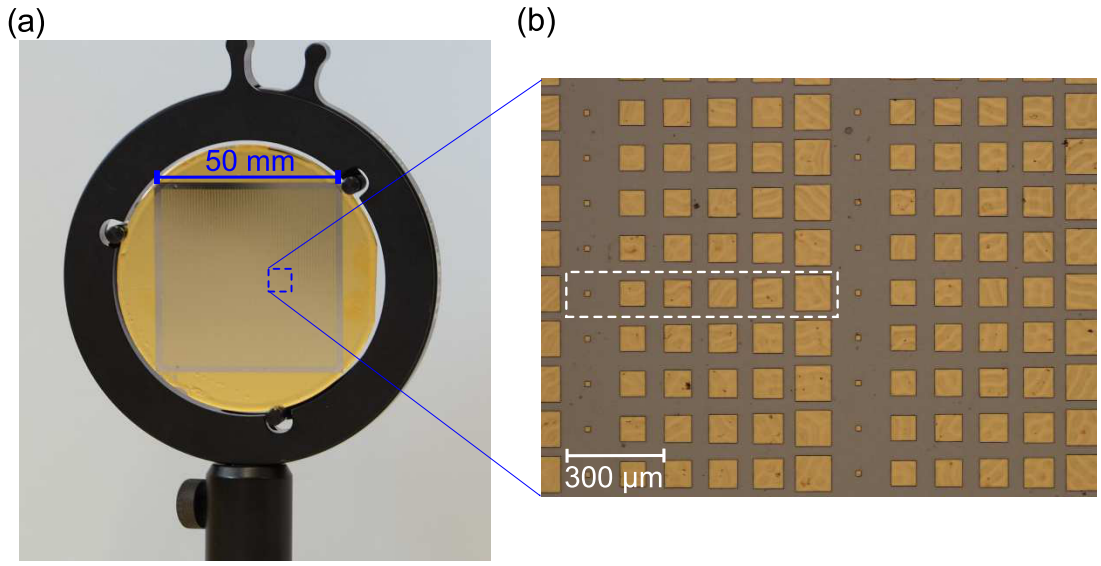

Figure 4.4. Reflectarray prototype. (a) Photograph of the sample. (b) Microscopy image for a small part of the reflectarray. The dashed rectangle encloses one of the sub-arrays.

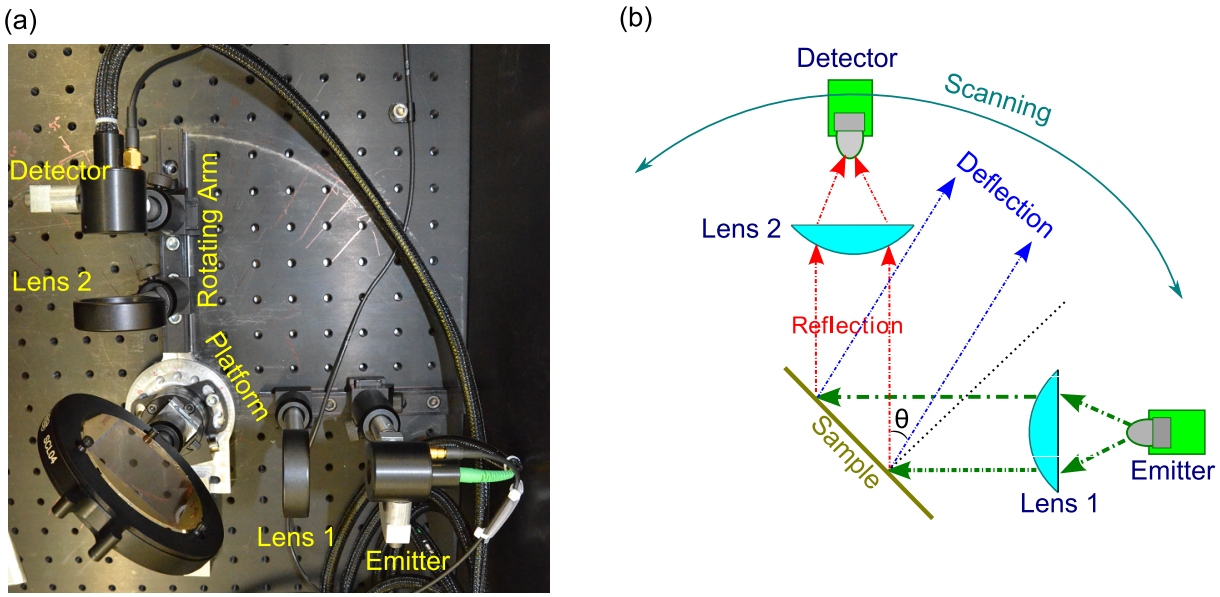

Figure 4.5. Measurement system. (a) Photograph of the measurement system. (b) Corresponding schematic. The beam from the emitter is collimated by Lens 1, and incident on the surface of the sample. Lens 2 concentrates the scattered beam on to the detector. Lens 2 and the detector are fixed on an arm mounted on a rotating platform, allowing a wide angular range to be scanned.

strong reflection is detected, as shown by the pulse and corresponding spectrum in Figs. 4.6(b) and 4.6(d), respectively. The reflection spectrum in Fig. 4.6(d) (red solid line) reveals an obvious notch around 0.93 THz. This shows that considerable energy

around this frequency is deflected off the direction of the specular reflection. The rotating arm is then moved to the expected angle of the deflection, and slightly adjusted for the maximal amplitude. The time-resolved deflection signal is shown in Fig. 4.6(c) and exhibits an oscillation caused by the spectrally selective deflection of the reflectarray. This is confirmed in the deflection spectrum in Fig. 4.6(d) (blue solid line), where a strong deflection peak appears at the frequency corresponding to the strongest notch in the reflection spectrum. Hence the measurement proves that the fabricated terahertz reflectarray has the ability to deflect the incident wave towards the predesigned direction. In order to estimate the performance of the reflectarray, the normalized reflection and deflection are calculated and shown in Fig. 4.6(e), demonstrating that up to nearly 80% of the incident amplitude is deflected around the operational frequency. It is worth noting that the sum of the reflection and deflection energy is less than unity at a wide frequency range. This missing energy is likely to be absorbed by the PDMS substrate or scattered into other directions. For the TE polarisation, the results are given in Figs. 4.7(a)-4.7(e). The measurement results for both polarisations are similar. In both cases, the strong deflection is observed at around 0.93 THz.

The angular radiation patterns of the reflectarray have been measured to characterize the spectral behaviour of the reflected/deflected beams and side lobes. The radiation patterns are measured with an angular resolution of 2° and are represented at different frequencies for both polarisations in Fig. 4.8. At around 0.93 THz, as shown in Fig. 4.8(c), the deflection is strongest, while on the other hand at 0.6 THz, the specular reflection is the strongest. At other frequencies, the patterns show a combination of lobes caused by the Floquet modes arising from the sub-array periodicity. Generally, the performance of the reflectarray for the TM and TE polarisations are similar.

4.4.2 Discussion

Despite a qualitatively satisfying demonstration of the reflectarray operation, there are some discrepancies between the simulated and measured results. The frequency for the maximum deflection is shifted from the designed frequency of 1 THz to the measured 0.93 THz. Meanwhile, the deflection angle also shifts from the expected 21° to the measured 25°. Possible causes have been investigated and are described in the following.

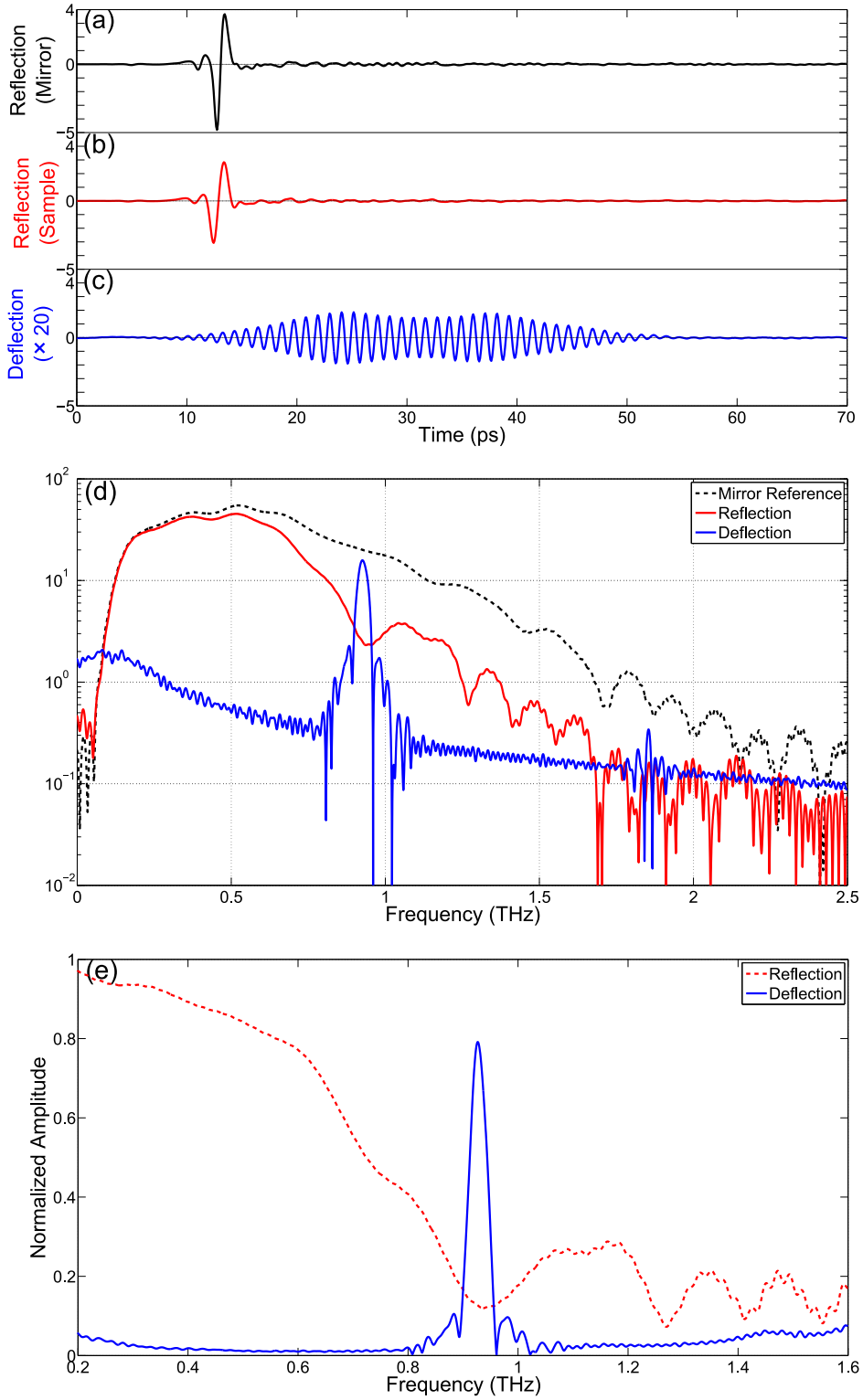

Figure 4.6. Measured pulses and spectra in the TM polarisation. (a) The reference pulse. (b) The specular reflection of the reflectarray sample. (c) The deflection of the reflectarray sample. (d) The spectra of the reference (black dashed line), the reflection (red solid line), and the deflection (blue solid line). (e) The normalized reflection (red dotted line) and deflection (blue solid line) amplitude.

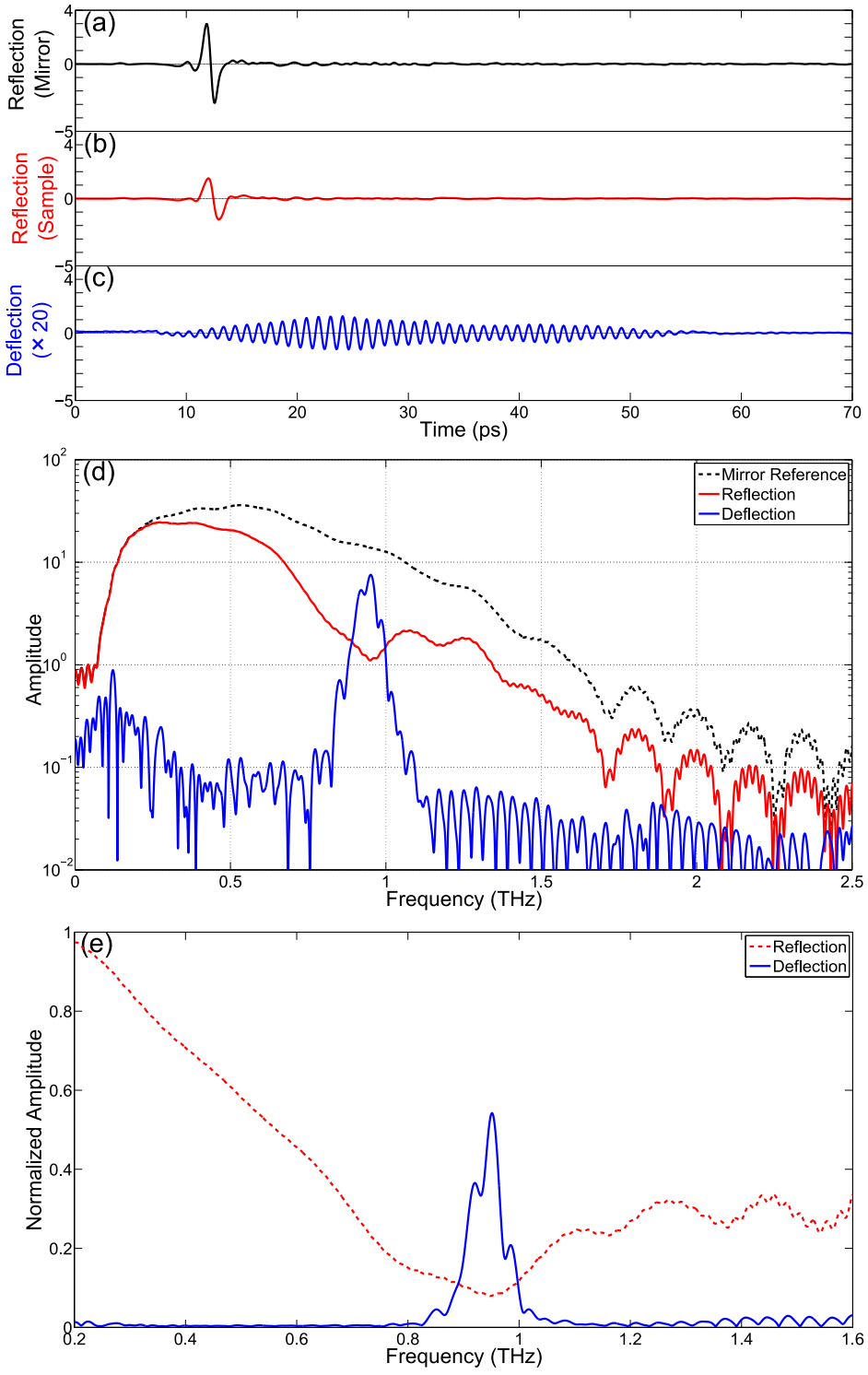

Figure 4.7. Measured pulses and spectra in the TE polarisation. (a) The reference pulse. (b) The specular reflection of the reflectarray sample. (c) The deflection of the reflectarray sample. (d) The spectra of the reference (black dashed line), the reflection (red solid line), and the deflection (blue solid line). (e) The normalized reflection (red dotted line) and deflection (blue solid line) amplitude.

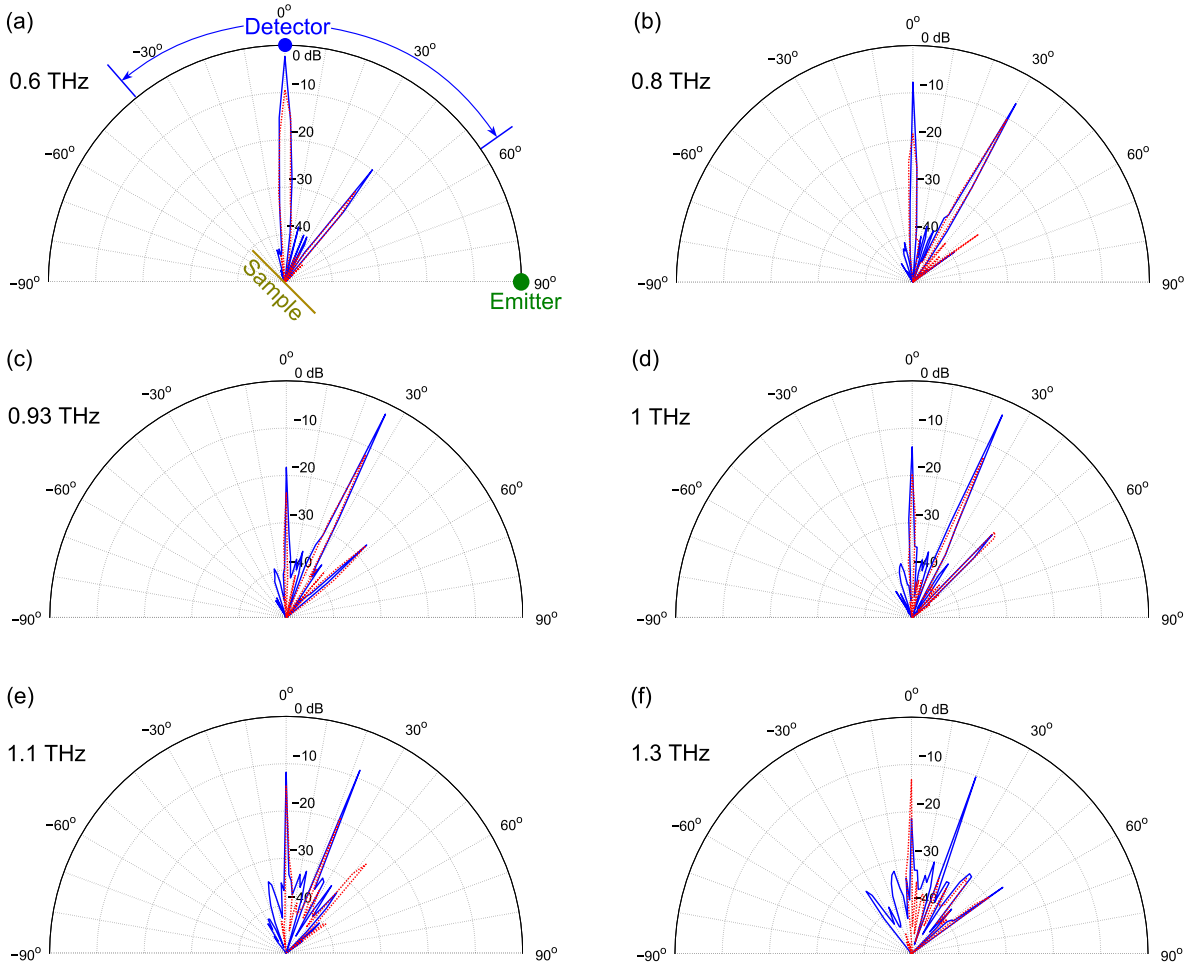

Figure 4.8. Measured radiation pattern at different frequencies in TM polarisation (blue solid line) and TE polarisation (red dotted line) in logarithmic scale. The reflection and deflection always exist as Floquet modes although the intensity varies with frequency. The closer the frequency is to 0.93 THz, the stronger the deflection and the weaker the reflection become, and vice versa.

Fabrication tolerance is the main factor that gives rise to the frequency shift. In order to evaluate the effect from the tolerance, two samples with different substrate thicknesses (15 µm, 17 µm) have been measured. The resulting deflection spectra are shown in Fig. 4.9. It is evident that a variation in the substrate thickness leads to a shift in the frequency for the maximum deflection. For the reflectarray with a substrate thickness of 15 µm investigated in Section 4.4.1, the measured frequency at 0.93 THz where the deflection is strongest decreases from the designed frequency of 1 THz. Consequently, the deflection angle is increased according to the Floquet spatial mode (also called grating lobes) associated with the periodicity of sub-array structures. These Floquet

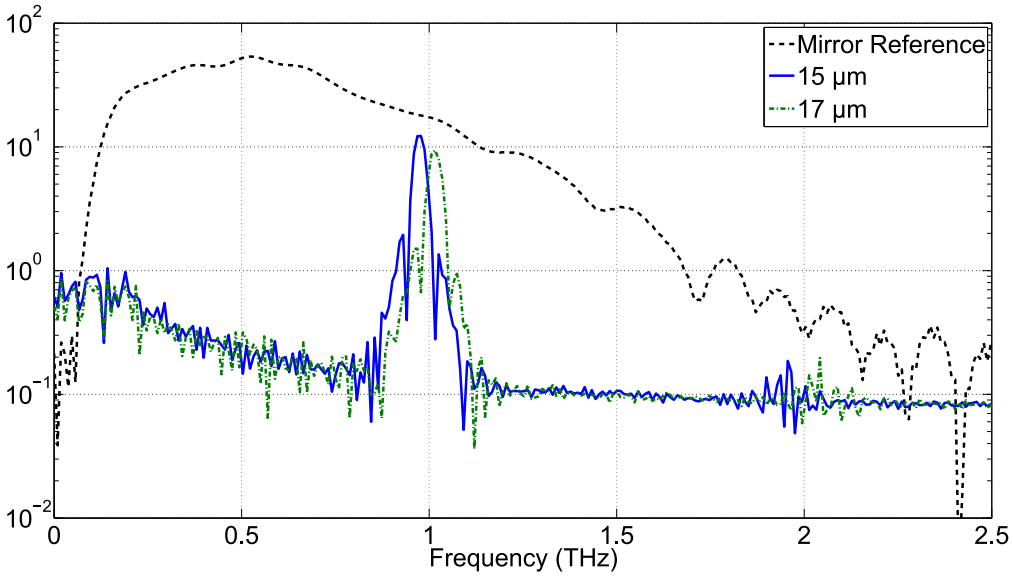

Figure 4.9. Measured deflection spectra for two samples with different substrate thicknesses for the TM polarisation. For the sample with the thickness of 15 μm, the angle for maximum deflection is 25°, while for the 17 μm thick sample, the corresponding deflection angle is 26°.

modes cannot be neglected in arrays for which the inter-spacing of sub-arrays is larger than a half of the wavelength. In the present case, the inter-spacing between adjacent sub-array is 840 μm, or 2.8 times the wavelength at the frequency of operation.

In addition, the experiments are performed at an incident angle of 45° rather than the normal incident angle used in the design step. This difference is another reason that causes the deflection angle to shift from the designed 21° to the experimentally determined 25°. The dependence of the phase response curve on the incident angle has been investigated by Targonski *et al.* (Targonski and Pozar 1994). It is suggested that adopting the phase response of the normally incident wave for the oblique incident wave brings a new tolerance. Particularly, the difference between the practical performance and its theoretical expectation will become significant when the incident angle is larger than 40°. In order to verify this aspect, the reflection coefficients of the uniform infinite patch arrays at 1 THz are simulated for a 45° incidence in both TM and TE polarisations. The obtained phase curves of the reflection coefficients for these cases are shown in Fig. 4.10 and compared to the normal incidence case. As described by Targonski and Pozar (1994), it is observed that the phase responses for the normal and oblique angles of incidence are slightly different. The phase response of the TM-polarised wave is less affected by the off-normal incidence angle compared to the TE-polarised wave,

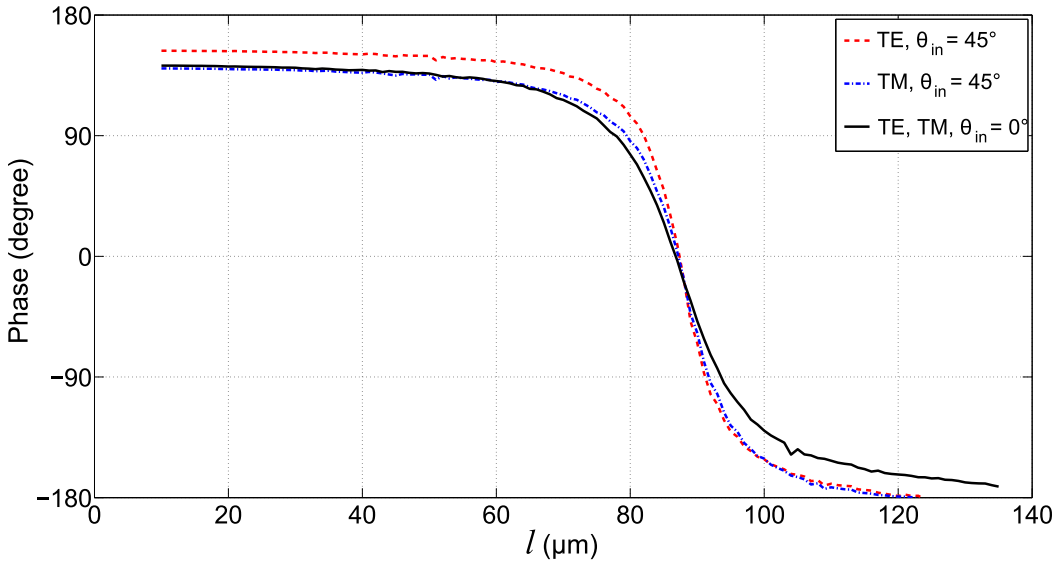

Figure 4.10. Simulated reflection phase responses for 2D uniform infinite patch arrays with the normal and oblique incidences for the TM and TE polarisations at 1 THz. All the dimensions, including the substrate thickness and the unit cell size, are the same with the case of $h = 15\,\mu\text{m}$ given in Fig. 4.2.

which is consistent with the findings of Tsai and Bialkowski (2003). Physically, this phenomenon is caused by an imbalance response of each patch in the TE polarisation, arising from small phase shifts between two opposite edges of the patch when the incident wave is oblique to the surface of the reflectarray. To further explain this phenomenon physically, the simulations of the reflectarray are carried out at the frequency of 0.93 THz for both the TM and TE polarisations with the incident angle of 45°. Instantaneous current density distributions are shown in Fig. 4.11(a) and (b). It can be observed that the current densities under the patches are influenced by a small phase difference between the left and right edges of the patches, introduced by the angle in the incident electric field. For the TE polarisation, this imbalanced response of the patches leads to emergence of a transverse current that degrades the deflection more significantly than in the TM polarisation. This theoretical inference is qualitatively consistent with the measurement of normalized deflection amplitude shown in Figs. 4.6(c) and 4.7(c).

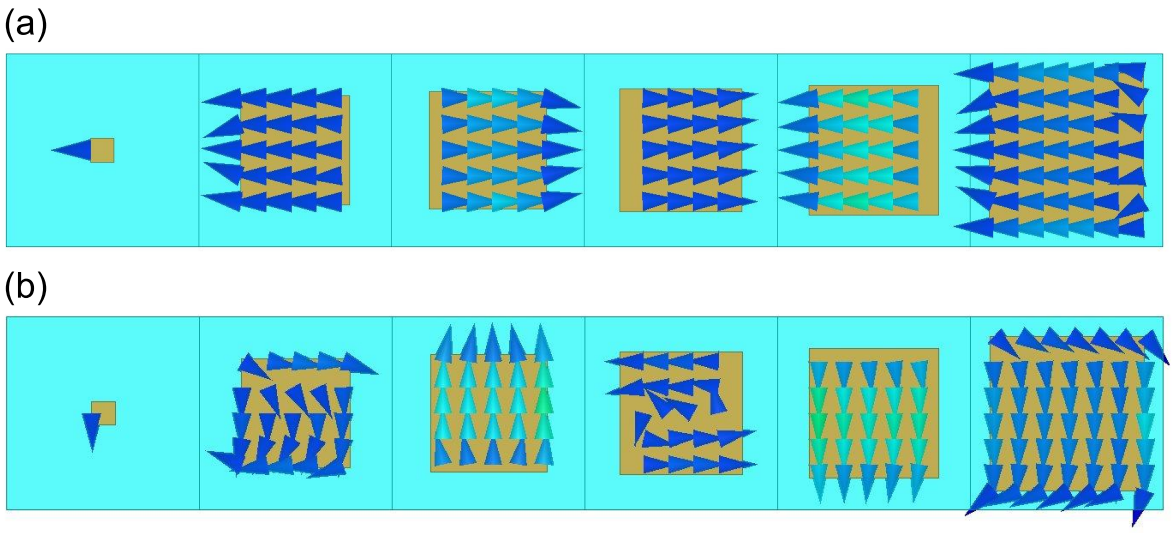

Figure 4.11. Simulated instantaneous current density distributions on the bottom surface of the patches in the reflectarray. (a) TM and (b) TE polarisations with an incidence angle of 45° at 0.93 THz.

4.5 Conclusion

In this chapter, terahertz reflectarrays with metallic patch elements have been proposed. The theoretical design taking into account fabrication tolerances has been verified through simulations and experiments. Prototypes have been fabricated and the measurements have been carried out by using a THz-TDS system. The measurement in both TE and TM polarisations shows that a nonuniform reflectarray can efficiently deflect the terahertz waves towards a predesigned angle at a predefined frequency of operation. The possible factors for a small shift in the operation frequency and in the deflection angle have been investigated. It is suggested that the fabrication tolerance and the dependence on the incidence angle should be taken into consideration in optimizing reflectarrays.

The proposed terahertz reflectarrays gain their properties from the configuration of the periodically arranged patch elements. Hence, the appearance and functionality are close to metamaterials (Chen *et al.* 2011). However, the reflectarrays cannot be considered as terahertz metamaterials since the patch dimensions are in the order of half of the operating wavelength. Thus, the whole arrangement of the reflectarrays cannot be described by effective electromagnetic parameters. In terms of its potential applications, the designed reflectarrays can become useful in various aspects owing to

their capability of manipulating terahertz beams with high efficiency yet low design and fabrication complexity. Their function is not limited to beam deflection, and can be extended to beam steering or shaping in various forms. In addition, active patch-element structures can be used to dynamically configure versatile arrays for advanced beamforming, for example using graphene as reconfigurable elements (Carrasco and Perruisseau-Carrier 2013). In particular, the extension to active reflectarray systems promises the application in the area of short-range terahertz communications.

Chapter 5

Terahertz reflectarrays for polarisation beam splitting

A Reflectarray is designed and demonstrated experimentally for polarisation-dependent beam splitting at 1 THz. This reflective component is composed of two sets of orthogonal strip dipoles arranged into interlaced triangular lattices over a ground plane. By varying the length and width of the dipoles, a polarisation-dependent localized phase change is achieved on reflection, allowing periodic subarrays with a desired progressive phase distribution. Both the simulated field distributions and the measurement results from a fabricated sample verify the validity of the proposed concept. The designed terahertz reflectarray can efficiently separate the two polarisation components of a normally incident wave towards different predesigned directions of $\pm 30^{\circ}$. Furthermore, the measured radiation patterns show excellent polarisation purity, with a cross-polarisation level below -27 dB. The designed reflectarray could be applied as a polarizing beam splitter for polarisation-sensitive terahertz imaging or for emerging terahertz communications.

5.1 Introduction

For centuries, controlling the propagation of light has been one of the intensively researched topics in science and engineering. From conventional optical lenses to the exotic artificially patterned structures of today, scientists and engineers have progressively introduced more degrees of freedom in both theoretical and experimental aspects of beam manipulation for increasingly sophisticated applications (Pendry *et al.* 2006, Schurig *et al.* 2006, Kwon and Werner 2008, Chen *et al.* 2010, Valentine *et al.* 2009, Yang *et al.* 2012, Yu *et al.* 2011, Aieta *et al.* 2012, Monnai *et al.* 2012). Beam splitters with polarisation-dependent properties can play an important role in applications requiring high polarisation purity or polarisation-dependent multiplexing/demultiplexing. In the optical range, coupled plasmonic waveguide arrays (Tai *et al.* 2007), an asymmetrical directional coupler (Guan *et al.* 2013), and a 34-layer polymer thin-film (Yang *et al.* 2011) have been proposed as polarising beam splitters. Further concepts inspired by metamaterials have been introduced for designing or realising beam splitters across different spectral ranges (Rahm *et al.* 2008, Farmahini-Farahani and Mosallaei 2013).

In the terahertz regime, due to lack of suitable naturally birefringent materials and because of high intrinsic material loss, devices that can separate the incident waves with polarisation-dependent properties still remain challenging to realise. Implementations include a magnetically tunable liquid crystal phase grating used for tuning the ratio of the zeroth and first-order diffracted terahertz waves (Lin *et al.* 2008). This fabricated terahertz beam splitter achieved modest efficiency of around 40%, although it was shown to provide high extinction ratio and tunability across a wide frequency range. To improve the efficiency, Berry *et. al.* (Berry and Jarrahi 2012) demonstrated the potential of a subwavelength silver grating fabricated on a high-density polymer substrate for constructing a terahertz polarising beam splitter in a wide frequency band. In (Peralta *et al.* 2009), a metamaterial structure based on circular split rings was used to control the characteristics of transmitted terahertz waves, with effects strongly dependent on the incident polarisation. One aspect worthy to mention here is that these designs mainly focus on polarisation beam-splitting in transmission, with emphasis on frequency tunability. Beam splitting operation in reflection mode remains to the best of our knowledge relatively unexplored.

One feasible pathway for beam splitting in reflection is offered by the concept of reflectarrays. Owing to their high efficiency and flat profile, reflectarrays have been adopted

widely in the microwave and millimetre-wave regions (Huang and Encinar 2008, Tamminen *et al.* 2013b, Tamminen *et al.* 2013a), and implementations have been extended across the electromagnetic spectrum to the terahertz (Nayeri *et al.* 2014, Niu *et al.* 2013, Carrasco and Perruisseau-Carrier 2013) and optical regimes (Memarzadeh and Mosallaei 2011, Pors *et al.* 2011, Zou *et al.* 2013, Yifat *et al.* 2014) with various functionalities such as beam deflection, focussing and beam shaping. Among the versatile functions of reflectarrays, steering reflected waves with polarisation-dependent properties can find applications in areas such as signal transmission, polarisation-sensitive measurements, and discrimination of incident polarisations. For example in the microwave regime, multilayer elements with rectangular patches (Encinar *et al.* 2006) and cross-shaped microstrip loops (Perruisseau-Carrier 2010) have been used as unit cells for constructing dual-polarisation reflectarrays. Those realisations can achieve polarisation-dependent beamforming functions, i.e. to scatter orthogonal polarisation components into different directions. The scaled implementation of similar configurations with stacked multilayer structures in the terahertz and optical ranges is presently very challenging or even impossible to manufacture with the required precision.

In this chapter, a design of a polasizing beam splitter operating at 1 THz is proposed and experimentally validated. The device is based on the reflectarray concept and demonstrates the capability to separate the orthogonal polarisation components of an incident beam and deflect them into different directions. Two sets of orthogonally oriented dipole resonators arranged either loosely or compactly in interlaced triangular lattices are used for composing the unit cell, and the corresponding local reflection response is achieved by varying the length and width of the dipoles. Subarrays are then constructed from the unit cells with the desired progressive phase distributions to respond to incident waves with polarisation-dependent properties. By taking micro-fabrication tolerance into design consideration, the reflectarray with compactly arranged dipoles is then fabricated for experimental validation. Both simulation and measurement are employed to verify the concept and assess the efficiency and polarisation purity of the device.

5.2 Beam splitter with sparsely arranged dipoles

Reflectarrays with polarisation-dependent beam shaping ability can be in principle implemented using different approaches. For example, crossed dipoles with variable

arm lengths (Pozar and Targonski 1998, Li *et al.* 2011) or arrangements of orthogonal linear dipoles with variable dimensions (Farmahini-Farahani and Mosallaei 2013, Perruisseau-Carrier 2010) can be employed. It was however observed that cross-talk between crossed dipoles in a non-uniform array can induce cross-polarised currents on the connected orthogonal arms, thereby degrading the polarisation purity. Therefore, the approach considering interlaced arrays of orthogonal linear dipoles is preferred. In this section, it will be shown that an array with strip dipoles sparsely arranged in an interlaced triangular-lattice can function as a polarisation-dependent terahertz reflectarray.

5.2.1 Unit cell with sparse arrangement

As shown in Fig. 5.1, a unit cell is composed of two sets of orthogonal dipole resonators with a sparse arrangement. Each set of the dipoles corresponds to a particular polarisation. A configuration of two interlaced triangular-lattice arrays is chosen to reduce mutual coupling. The unit cell comprises three layers: dipoles made of gold as the top layer, a PDMS dielectric spacer as a substrate and a platinum ground plane. For the metals, the material parameters used in the previous chapter, i.e. surface impedance $Z_{\text{Au}} = 0.287 + j0.335\ \Omega/\text{sq}$ for gold and $Z_{\text{Pt}} = 0.628 + j0.667\ \Omega/\text{sq}$ for platinum, are adopted here, while PDMS has a relative permittivity 2.35 and loss tangent 0.03 (Khodasevych *et al.* 2012). For operation at 1 THz, the size of the unit cell and the thickness of the PDMS substrate are selected at fixed values $2a = 300\ \mu$m and $h = 20\ \mu$m, respectively. Different phase responses for a particular polarisation can be achieved by varying the length and width of a corresponding dipole. A phase response profile is simulated by using uniform infinite arrays in Ansys HFSS commercial software with

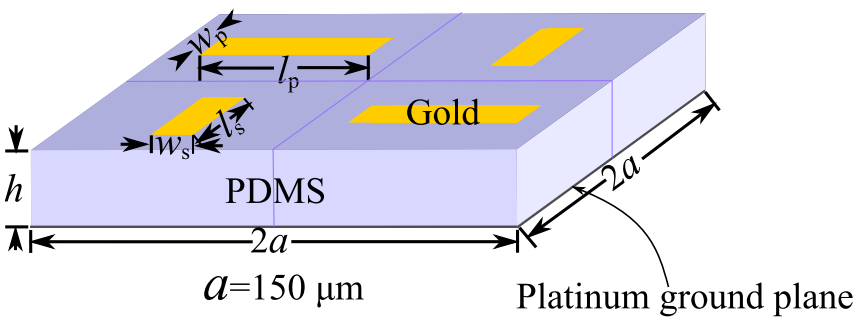

Figure 5.1. A unit cell containing four sparsely arranged dipoles for the polarisation-dependent reflectarray.

master-slave boundary conditions. Based on a numerical analysis, it is confirmed that the effect of a dipole is negligible for the incident wave with polarisation orthogonal to its longitudinal axis. Therefore, in the optimization of the unit cell shown in Fig. 5.1, the dipoles perpendicular to a given polarisation are fixed, while the length and width of the dipoles parallel to the polarisation are varied. In addition, in order to test the effect of the dielectric loss of the spacer on the reflection coefficients, three values of loss tangent, $\tan\delta = 0, 0.03, 0.06$, are applied in the simulation. The numerically resolved reflection phase and magnitude responses as a function of the dipole length for an infinite uniform array are given in Fig. 5.2(a) and (b), respectively. From the simulation results, a phase range of over 300° is obtained, which is sufficient for designing a periodic gradient reflectarray if the progressive phase change is larger than 60°. It is obvious that the loss of the substrate can significantly affect the reflection coefficient for the designed structure. A larger loss tangent leads to a sharper phase change and higher loss, and therefore the performance of the designed reflectarray would be more sensitive to the tolerance in the dimensions.

5.2.2 Design of dual-deflection reflectarray

Based on the phase response data shown in Fig. 5.2(a), a subarray containing two groups each with 6 sparsely arranged dipoles is designed for deflecting an incident wave into two different directions according to the polarisation components. For simplicity of the theoretical design, we assume that the substrate is lossless, and therefore the blue solid line in Fig. 5.2 (a) is used for designing the subarray. At 1 THz, i.e. $\lambda_0 = 300$ μm, a progressive phase change of $\Delta\phi = \pm 60°$ between adjacent dipoles with the same alignment results in a beam deflection of

$$\theta = \arcsin\frac{\Delta\phi\lambda_0}{2\pi a} = \pm 19.5°. \tag{5.1}$$

The layout of the subarray is shown in Fig. 5.3. Taking the fabrication tolerance into account, the micrometer values for the length and the width of each dipole in the subarray are chosen as integers. In order to achieve more accurate phase response of each dipole and thus better performance of the reflectarray, the phase of the surface current on the dipoles are observed during the subarray simulations. Both of the lengths and widths of the dipoles in the subarray are then fine-tuned to achieve the desired gradient phase response. The optimized dimensions of the 12 dipoles are given in Table 5.1.

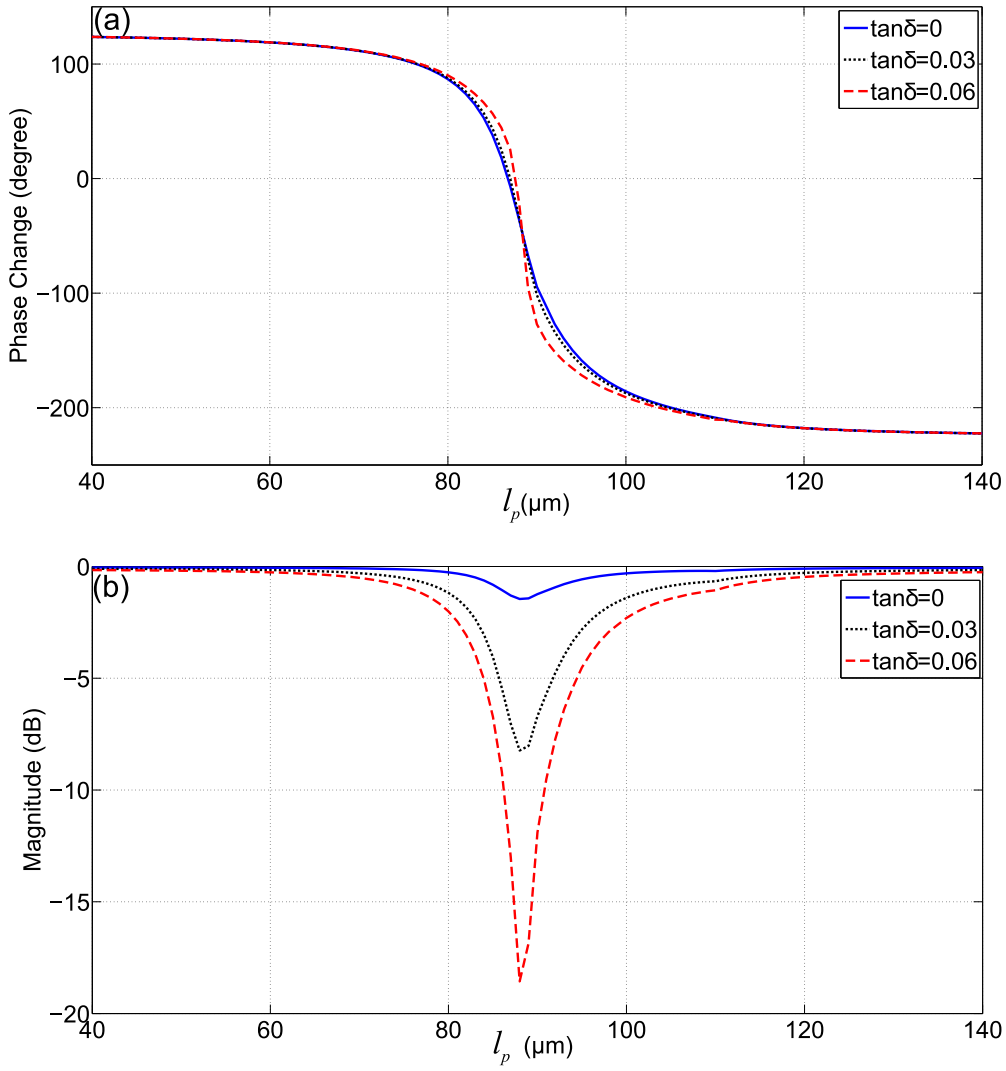

Figure 5.2. Simulated scattering response of the sparsely arranged unit cell. Reflection phase change in degree (a) and magnitude in dB (b) for the structure operating at 1 THz shown in Fig. 5.1 as a function of the length l_p, for a dimension $a = 150$ μm, $h = 20$ μm. For a flat phase curve, the width w_p varies with the length l_p according to the relation $w_p = 32$ μm $+ 0.2\times$ l_p when 40 μm $\leq l_p \leq$ 90 μm, $w_p = 230$ μm $- 2\times$ l_p when 90 μm $\leq l_1 \leq$ 105 μm, $w_p = 20$ μm when 105 μm $\leq l_p \leq$ 140 μm. The loss tangent of the PDMS substrate affects both the phase and magnitude responses.

In designing the reflectarray, possible coupling effects between adjacent dipoles of different orientations have to be taken into account. One property that indicates this aspect is the distribution of the surface current on the strip dipoles. So, it is necessary to observe the distributions of the surface current on the dipoles, as shown in Fig. 5.4 for both the TE and TM incident polarisations (note that the TE and TM polarisation

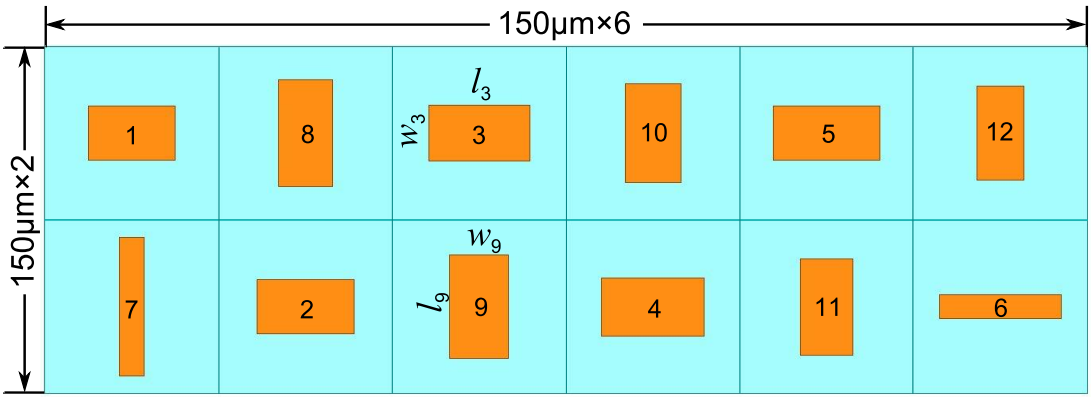

Figure 5.3. Structure of one subarray made of 12 dipoles. The figure is to scale.

Table 5.1. Sizes of the dipoles for the designed subarray. The units are in μm.

Dipole	1	2	3	4	5	6	7	8	9	10	11	12
Length	75	84	87	89	92	105	120	92	89	85	83	81
Width	47	47	48	50	47	21	21	47	51	48	45	40

are defined in the deflection plane). It is clear that the surface currents on the dipoles responding to one specific polarisation are dominant compared to the other polarisation. This further verifies that the effect of the dipoles is negligible for the incident wave with orthogonal polarisation.

The simulated incident plane wave at 1 THz shown in Fig. 5.5(b) is normal to the surface of the reflectarray. The field distributions of the deflected waves for the TE and TM polarisations are demonstrated in Figs. 5.5(a) and (c), respectively. It is clear that the normal incident wave is deflected into the predesigned direction depending on the polarisation. For the TM polarisation, the deflected wavefront is dominant over the specular reflection component in the scattered field. On the other hand, for the TE polarisation, an obvious specular reflection component is observed. The phenomenon has also been observed and discussed by Niu *et al.* (Niu *et al.* 2013). Overall, the results confirm that the designed reflectarray is able to deflect terahertz waves into the two designed different directions, according to the incident polarisation.

For further evaluation of the performance of the designed reflectarray, we consider a reflectarray that contains 168 × 56 subarrays. This corresponds to a sample with a size of 50.4 mm × 50.4 mm, which is sufficient to cover the collimated beam in the measurement. Based on this configuration, the radiation pattern can be numerically obtained (neglecting edge effects) by using Ansys HFSS commercial software as shown

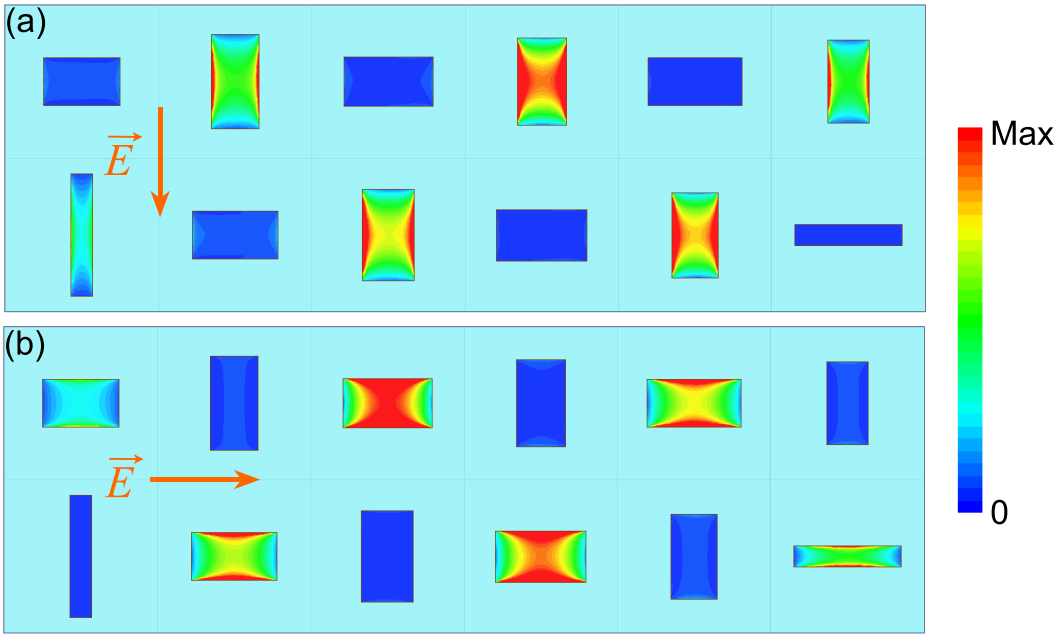

Figure 5.4. Simulated magnitude of the surface current on the dipoles. (a) TE polarisation. (b) TM polarisation. The both images share the same colour scale.

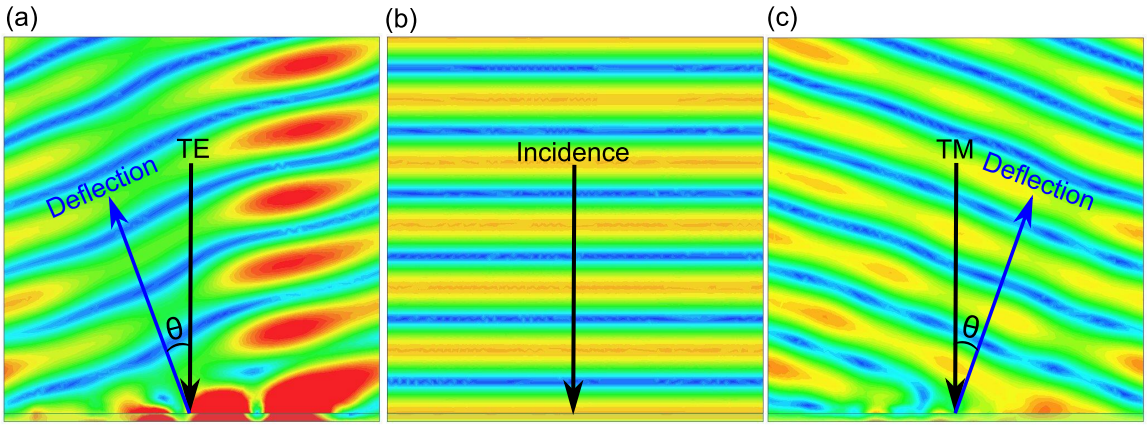

Figure 5.5. Simulated instantaneous scattered field from the reflectarray in TE and TM polarisations at 1 THz. When the incident wave (b) is normal to the surface of the reflectarray, the TE and TM polarised wave are deflected into two different directions with the angles of $\pm 19.5^{\circ}$ as shown in (a) and (c), respectively. All the images share the same colour scale.

in Fig. 5.6. It is obvious that the incident waves with the TE and TM polarisations can be efficiently deflected into two different directions. For the TM polarisation, the intensity in the designed deflection direction is around 20 dB higher than that in the specular reflection, while for the TE polarisation the difference is smaller. The results

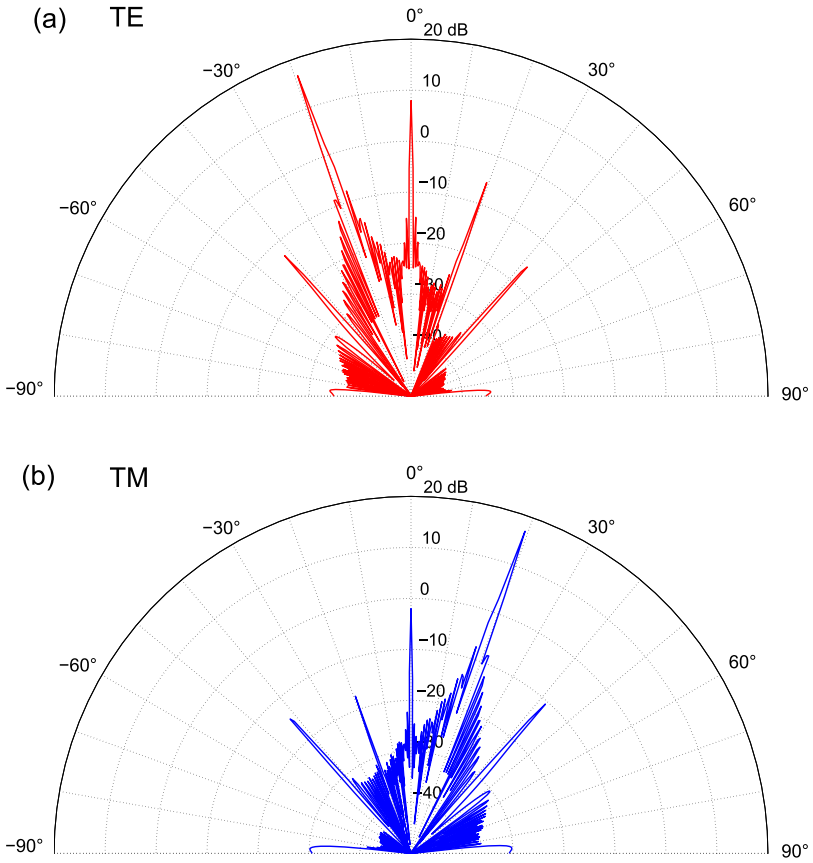

Figure 5.6. Simulated radiation pattern of the reflectarray with sparsely arranged dipoles. The dimension of the reflectarray is 50.4 mm × 50.4 mm. A wave normal to the array with the TE and TM polarisations can be efficiently deflected onto the direction of $-19.5°$ (a) or $+19.5°$ (b), respectively.

further confirm that the designed reflectarray can separate the polarisation components of an incident beam by deflecting them into two different directions in a given plane.

5.2.3 Discussion

For the designed terahertz reflectarray with sparsely arranged dipoles, the simulation results verify that the reflectarray can deflect the incident waves with different polarisations into desired directions. However, it is noted that, to avoid high loss and sharp phase response, the substrate adopted in the design is lossless, which is not realistic. One approach to solve this issue is to improve the layout of the strip dipoles on the top layer for a flatter phase curve and lower loss. In the following section, a layout of unit

cell with compactly arranged dipoles is adopted to realise a terahertz beam splitter with improved efficiency.

5.3 Beam splitter with compactly arranged dipoles

This section introduces the configuration of the reflectarray with compactly arranged dipoles. The unit cell is described first, followed by the design of subarrays with the desired operation as a polarising beam splitter. The designed structure is fabricated, and the corresponding measurement results are obtained through a terahertz time-domain spectroscopy (THz-TDS).

5.3.1 Unit cell with compact arrangement

A unit cell for a uniform reflectarray is shown in Fig. 5.7. The structure is composed of two sets of orthogonal dipole resonators arranged in a compact layout, with each set corresponding to a particular polarisation. The arrangement of the interlaced triangular-lattice is chosen for reducing the mutual coupling between the two sets of dipoles, while a compact layout significantly increases the efficiency of reflection compared to a loose arrangement of dipoles. The parameters of the materials for simulations are the same as used in the previous section. For operation at 1 THz, the size of the unit cell

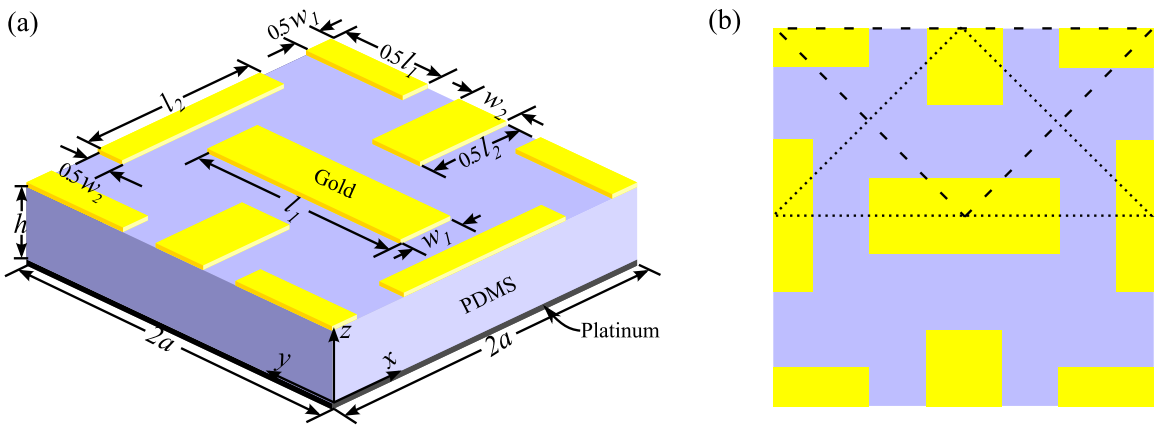

Figure 5.7. Single unit cell of the proposed reflectarray with compact dipoles. Each unit cell contains four dipoles with $a = 100\,\mu\text{m}$ and $h = 20\,\mu\text{m}$. The lengths and widths of the dipoles are varied to obtain a nearly full cycle of phase response. (a) 3D view of the unit cell. (b) Top view of the unit cell indicating the interlaced triangular lattices.

and the thickness of the PDMS substrate are selected at fixed values $2a = 200\,\mu\text{m}$ and $h = 20\,\mu\text{m}$, respectively. Different phase responses for a particular polarisation can be achieved by varying the length and width of the active strip dipoles.

The phase response profile is simulated by using uniform infinite arrays in a commercial software package, Ansys HFSS, with periodic boundary conditions, and Floquet port excitation is applied. Based on numerical analysis, it is first confirmed that the effect of a dipole is negligible for the incident wave with polarisation orthogonal to its axis. Therefore, in optimisation of the unit cell shown in Fig. 5.7, the dipoles perpendicular to a given polarisation are fixed at the dimension of $40\,\mu\text{m} \times 80\,\mu\text{m}$, while the length of the dipoles parallel to the polarisation is varied from $40\,\mu\text{m}$ to $140\,\mu\text{m}$. In order to achieve a smoother phase curve with less stringent tolerances, a strategy based on variation of both length and width is found to be more efficient than variation of length only (Yifat *et al.* 2014). As shown in Fig. 5.8, narrower strip dipoles introduce a wider dynamic phase range but at the cost of a steeper phase change and reduced efficiency around resonance. In contrast, widening the dipoles decreases the dynamic range but smooths the transition of the phase curve around resonance. Based on this trade-off, we strategically adapt the dipole width for a wide enough dynamic range and relatively smooth phase change response for higher efficiency. We start the length variation with the shorter dipoles with a narrow width, to maximize the starting phase. With an increase in the dipole length, the width is linearly increased for a smoother phase response and low absorption around the resonance. After the resonance, the width of the dipoles is gradually decreased with further increasing length for a wider phase range. Away from resonance, the phase response is not sensitive to the width of the dipoles, and therefore a change in the width is not necessary. Based on these considerations, the length $l_{1,2}$ and width $w_{1,2}$ of the gold dipoles are varied according to the piecewise linear function relation:

$$w_{1,2} = \begin{cases} 32\,\mu\text{m} + 0.2\,l_{1,2} & \text{if } 40\,\mu\text{m} \leq l_{1,2} \leq 90\,\mu\text{m}, \\ 230\,\mu\text{m} - 2\,l_{1,2} & \text{if } 90\,\mu\text{m} \leq l_{1,2} \leq 105\,\mu\text{m}, \\ 20\,\mu\text{m} & \text{if } 105\,\mu\text{m} \leq l_{1,2} \leq 140\,\mu\text{m}. \end{cases} \tag{5.2}$$

These linear functions are illustrated as the solid line in Fig. 5.8.

The numerically resolved reflection phase and magnitude responses obtained as a function of the dipole length with the described width variation are given in Figs. 5.9(a) and 5.9(b), respectively. From the results, it is observed that a phase change of over

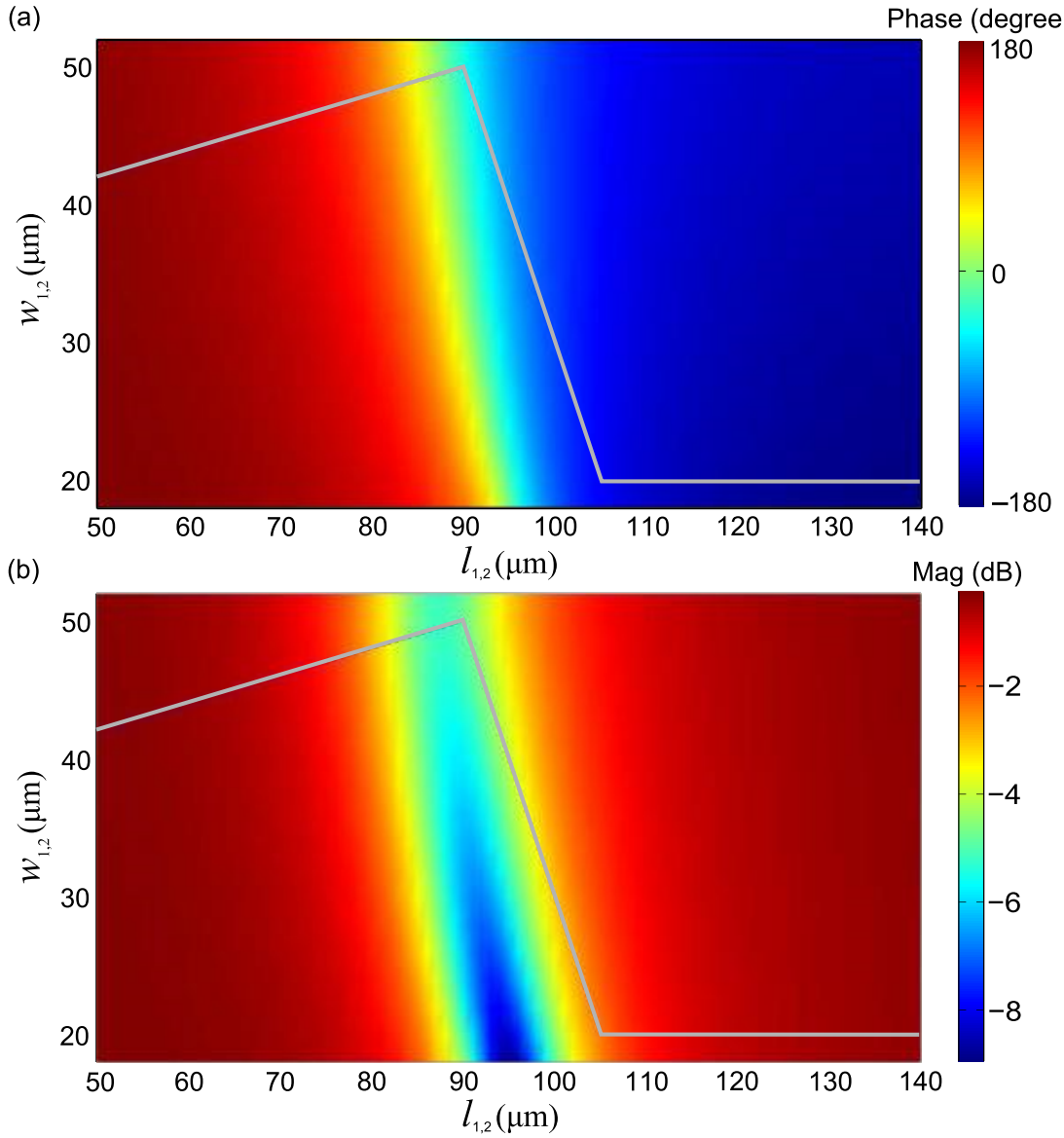

Figure 5.8. Simulated reflection phase and magnitude responses as a function of the dipole length and width. The graphs show the strategy for determining the relation of the length and width of the dipoles to achieve a smooth and wide phase response with high efficiency. The lines correspond to the length and width relation given in Eq. 5.2.

300° is achieved, while the highest loss on resonance is around 5.5 dB for a substrate loss tangent of 0.06. Since narrower strips have lower reflection efficiency on resonance (Fig. 5.9 (b)), the maximum loss on resonance of the dipole is higher than the maximum loss of 1.2 dB observed in the square patch unit cell with similar material properties in Chapter 4. Nevertheless, considering that most dipoles in the reflectarray will be operating detuned from resonance, these results indicate that the proposed structure can

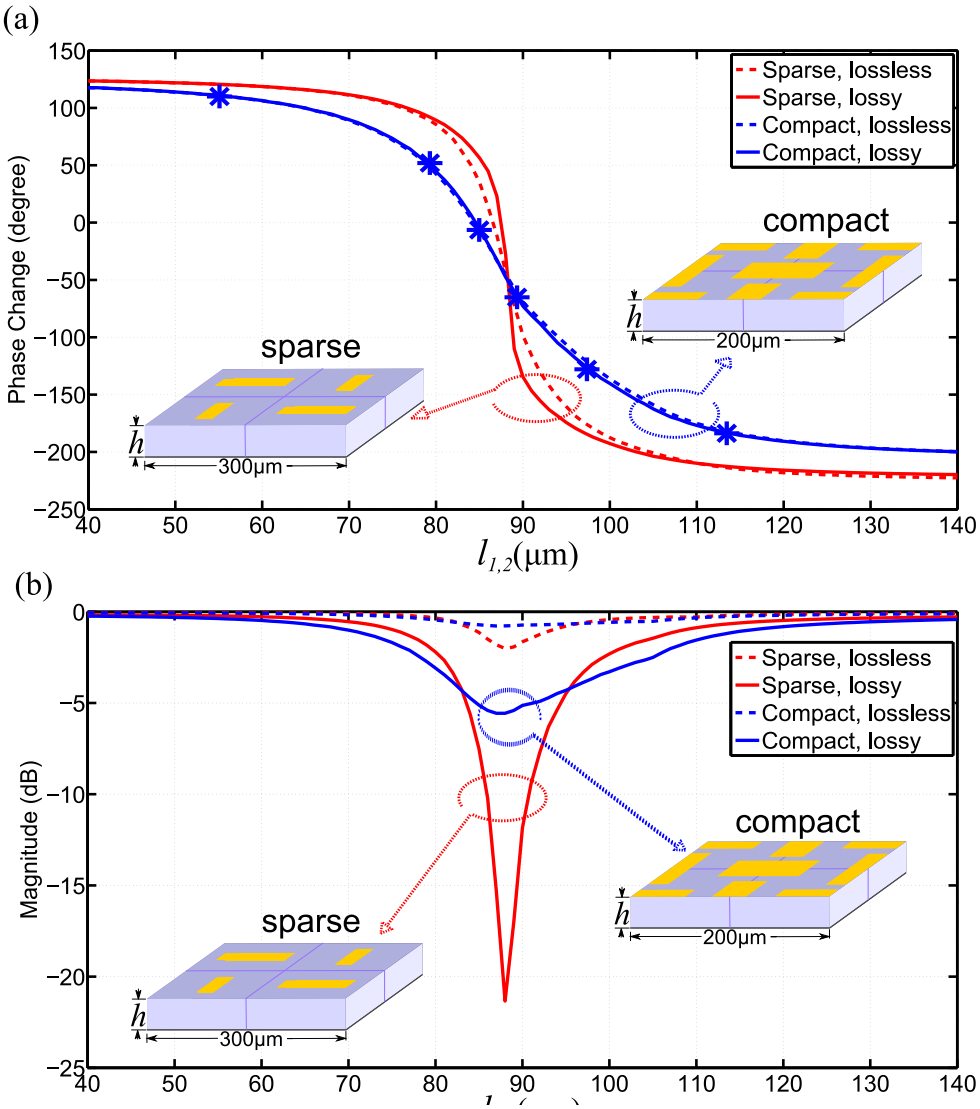

Figure 5.9. Simulated complex reflection coefficients for uniform infinite dipole arrays. Blue dashed and solid lines are for uniform infinite dipole arrays in compact configuration, while the red dashed and solid lines are for sparse configuration. (a) Reflection phase response in degrees. (b) Reflection magnitude in dB at 1 THz as a function of the dipole size. The solid and dashed lines are for configurations with the substrate loss tangent of 0.06 (lossy) and 0 (lossless), respectively. Six points on the phase curve with different widths and lengths indicate the required dipoles for constructing the beam-splitting reflectarray.

offer a sufficient phase range for designing a reflectarray with reasonable reflection efficiency. On the other hand, in order to show that the compact structure can improve the reflection efficiency of the unit cell for the reflectarray, the reflection coefficients with a sparse configuration are displayed in Fig. 5.9 (red dashed lines and solid lines).

Table 5.2. Dimensions of the dipoles for the optimized subarray. The units are in µm.

Dipole	1	2	3	4	5	6	7	8	9	10	11	12
Length	55	75	85	91	100	122	120	97	88	82	76	55
Width	38	48	49	50	30	24	20	34	45	52	48	43

It is obvious that, for the dipoles of the same dimensions with both the lossy or lossless substrates, the compact configuration has a smoother phase response and lower loss than its sparse counterpart. Therefore, the compact configuration have the advantages of relaxing the design tolerance for fabrication and increasing the reflection efficiency of the reflectarray, which verifies that compacting the radiating dipoles is an alternative approach for improving the performance of the reflectarray.

5.3.2 Subarray arrangement for terahertz beam splitting

The phase response data shown as blue solid line in Fig. 5.9(a) is applied for constructing subarrays composed of several unit cells. The full reflectarray will then consist of a periodic arrangement of such identical subarrays. In the present case, subarrays containing two orthogonal sets of dipoles, each composed of 6 elements are designed for deflecting a normally incident wave into two different directions. By following the design procedure presented in Chapter 4, at the operating frequency of 1 THz, i.e. $\lambda_0 = 300\,\mu\text{m}$ and $a = 100\,\mu\text{m}$, a progressive phase change of $\Delta\phi = \pm 60^\circ$ between adjacent dipoles with the same orientation results in a beam deflection of

$$\theta = \arcsin \frac{\Delta\phi\lambda_0}{2\pi a} = \pm 30^\circ, \tag{5.3}$$

where θ is the deflection angle off the specular reflection in the incident plane.

The layout of the subarray obtained from this design procedure is shown in Fig. 5.10. By taking the fabrication tolerance into account, the length and the width of each dipole in the subarray are rounded to the next discrete value in micrometer. Due to different mutual coupling in the uniform and non-uniform arrays, the dimensions of the dipoles for constructing subarrays selected from the phase curve shown in Fig. 5.9(a) require fine tuning to achieve more accurate local phase response in the array. The corresponding optimized dimensions of the 12 dipoles are given in Table 5.2.

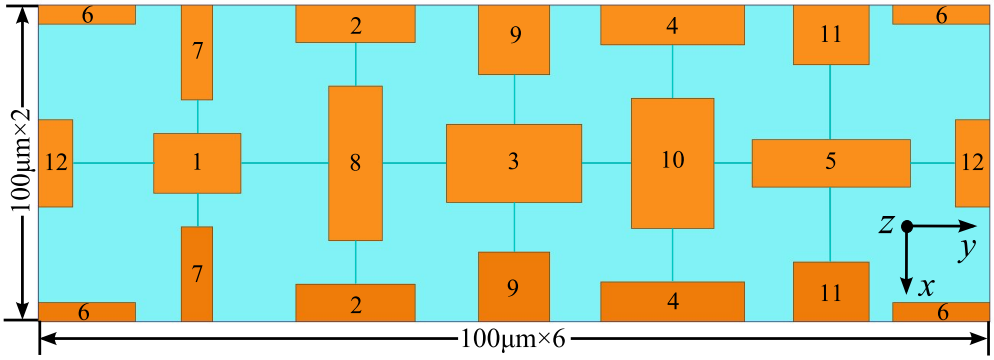

Figure 5.10. Structure of one subarray made of 12 dipoles. The dimensions of the subarray are initially based on the phase response for a uniform array shown in Fig. 5.9. An iterative fine tuning of the dimensions is required to compensate for the variations of actual mutual coupling between dipoles in the non-uniform subarray.

Instantaneous field distributions depicting the response of the reflectarray illuminated by a normally incident plane wave at 1 THz are shown in Fig. 5.11. The incident field is shown in Fig. 5.11(b) whereas the scattered fields for the TE and TM polarisations are demonstrated in Figs. 5.11(a) and 5.11(c), respectively. The scattered fields clearly illustrate that the normally incident plane wave is deflected into predefined directions according to the polarisation. The relatively strong amplitude suggests good efficiency for the deflection. Due to the attenuation and the discrete resolution of the dipoles, the uniformity of the deflected wavefront is slightly degraded. This phenomenon is more obvious for the TE polarisation than for the TM polarisation. Similar observations have been reported in (Niu *et al.* 2013, Tsai and Bialkowski 2003), with a possible cause being the imbalanced response of each dipole in the TE polarisation. It is noteworthy that, if the incident polarisation is 45° in the xy plane, the normally incident beam will be split into two deflected beams of equal power with the sign of the deflection angle being determined according to the linear polarisation component. The magnitudes of the surface current density plotted in Figs. 5.11(d) and 5.11(e) confirm that the two sets of dipoles are selectively excited by the corresponding polarisation.

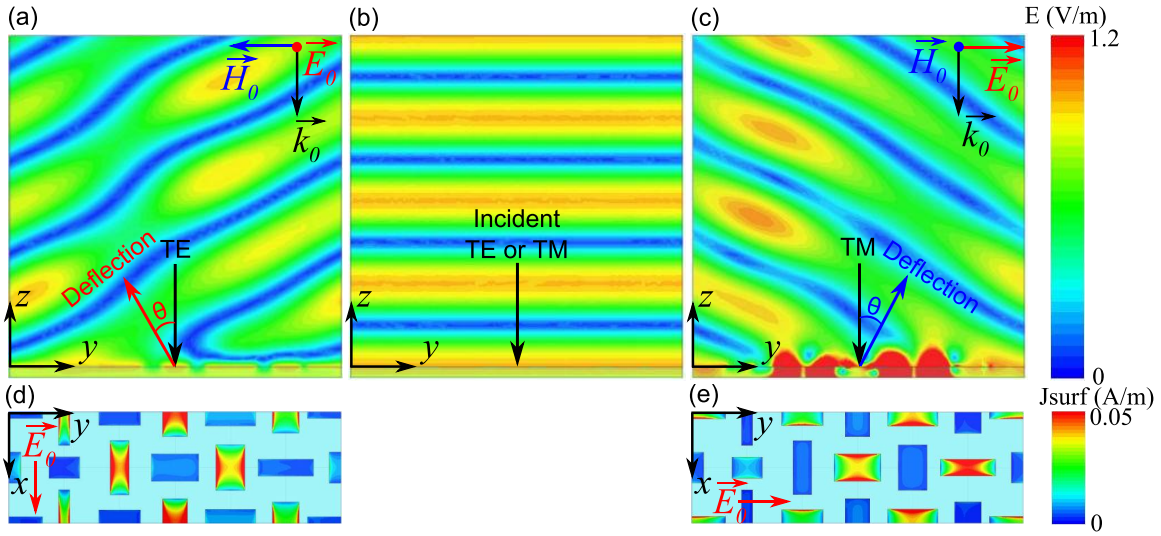

Figure 5.11. Simulated instantaneous incident and scattered field distributions from the reflectarray in TE and TM polarisations at 1 THz. When the incident wave (b) is impinging normally to the surface of the reflectarray, the TE and TM polarised wave are deflected into two different directions with the angles of $-30°$ and $+30°$ as shown in (a) and (c), respectively. The corresponding magnitude of the surface current density on the dipoles is shown in (d) and (e).

5.3.3 Reflectarray fabrication

In order to validate the reflectarray designed for beam splitting, a reflectarray that contains a periodic arrangement of 252×84 subarrays shown in Fig. 5.10 has been fabricated. This corresponds to a total sample size of 50.4 mm $\times$ 50.4 mm, which fits a standard 3 inch wafer and is sufficient to cover a collimated beam in the measurement. The details of the fabrication process and sample are given in this section.

A 3 inch silicon (100) oriented wafer was cleaned with solvents, dried with high purity compressed nitrogen, and coated with the metallic ground plane. The ground plane was composed of a 200 nm platinum thin film, with a 20 nm titanium thin film utilized to promote adhesion to silicon, deposited at room temperature by electron beam evaporation. A two-part, high purity, silicone elastomer — PDMS — was prepared as a mixture of curing agent and pre-polymer in a 1:10 weight ratio (Khodasevych *et al.* 2012). This PDMS is used to define the controlled thickness dielectric layer of 20 µm in the reflectarray. To attain 20 µm, the polymer is spin-coated at 1,950 rpm, with an acceleration of 1,000 rpm/s^2 for a 30 s duration. The layer is then cured at 72°C for 1 h. The attained thickness was verified experimentally by surface profilometry. The metallic dipoles were defined using 200 nm thick gold films, with a 20 nm thick adhesion layer

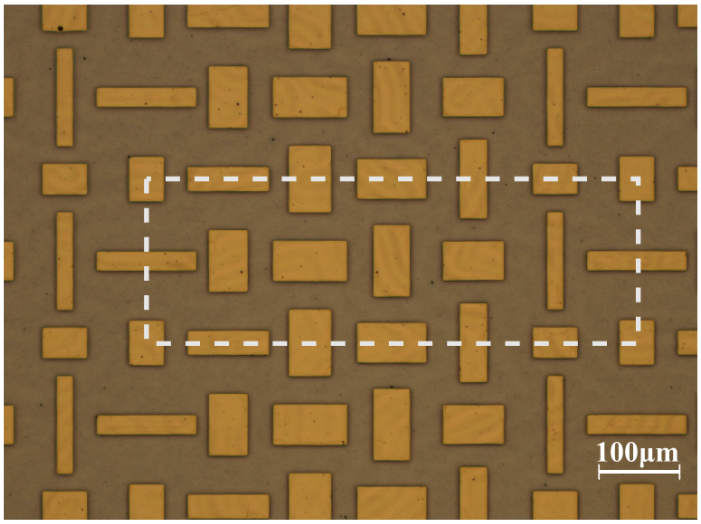

Figure 5.12. Optical micrograph of a small part of the fabricated reflectarray. The dashed rectangle encloses one of the subarrays.

of chromium. This metallic bilayer is patterned using photolithography and wet etching, with the choice of platinum for the ground plane ensuring selectivity. The residual photoresist is cleaned with solvents, in preparation for terahertz measurements. A micrograph of a small region of the final sample is shown in Fig. 5.12, with one subarray highlighted.

5.3.4 Results and discussion

The sample has been measured using a commercial terahertz time-domain spectroscopy (THz-TDS) measurement system, namely, Tera K15 developed by Menlo Systems GmbH. The measurement setup and experimental results are given in this section.

Measurement system

A photograph of the measurement setup is shown in Fig. 5.13(a) with a corresponding schematic representation in Fig. 5.13(b). The two identical lenses with an effective focal length of 54 mm are used for obtaining a collimated beam. The emitter and lens #1 are mounted on a fixed rail. The sample is mounted on a platform with angular scale that can be rotated for adjustment of the incidence angle. Particular care is necessary to ensure that the surface of the sample has its centre located on the rotation axis. A femtosecond optical pulse from a near-infrared laser source is guided by a fibre to the

terahertz emitter. The generated broadband terahertz radiation guided from the emitter is collimated by lens #1 before impinging the reflectarray. The detection part of the system comprises lens #2 that focuses the scattered fields onto the detector. Both of the components are mounted on a rotation arm pivoting around the sample centre point. This arrangement allows convenient scanning the radiation pattern in a wide angular range. For the reference, a gold-coated mirror replaces the reflectarray, and the incident and reflected angles are set to 15°. For each polarisation, two measurements are carried out on the sample. Firstly, the incidence angle is set to 15° for measuring the specular reflection off the reflectarray sample. Secondly, the sample is illuminated at normal incidence in a given polarisation, while the detection arm is rotated to scan the scattered terahertz waves at different angles. In the measurement of the radiation patterns, the scanning ranges for both the TE and TM polarisations are limited to the ranges, $-48°$ to $-22°$ and $22°$ to $48°$, because the minimum clearance between the lens #1 and lens #2 precludes measurements around the specular direction. Measurements are not carried out beyond $48°$ or $-48°$ because the deflection becomes negligible. A measurement angular resolution of $0.5°$ is sufficient for resolving the main features of the deflected beams. For measurements in the other polarisation, both the emitter and detector are rotated by $90°$, and the measurement procedure is repeated. All the measurements of the reflectarray are normalized using the mirror reference to remove any system dependency.

Measurement results

For the TE polarised incident wave, the normalized spectra for specular reflection and $-30°$ deflection are shown in Fig. 5.14(a). A distinct notch at around 1 THz can be observed from the sample specular reflection. This is because considerable energy around this frequency is deflected away from the specular direction. At the predesigned deflection direction of $-30°$, the strong deflection peak appears close to the design frequency of 1 THz as shown in Fig. 5.14(a) with the red solid line. It is observed that, for the TE polarised incident wave, 75% of the incident magnitude is deflected into the designed direction. Similar results are obtained for the TM polarisation, however with the difference that the deflection direction is on the other side of the incident direction. The corresponding measured results are given in Fig. 5.14(b). Strong deflection can be observed at around 1 THz in the designed deflection of $+30°$ with a deflection magnitude of around 80%, thus showing slightly higher deflection efficiency compared to the TE polarisation.

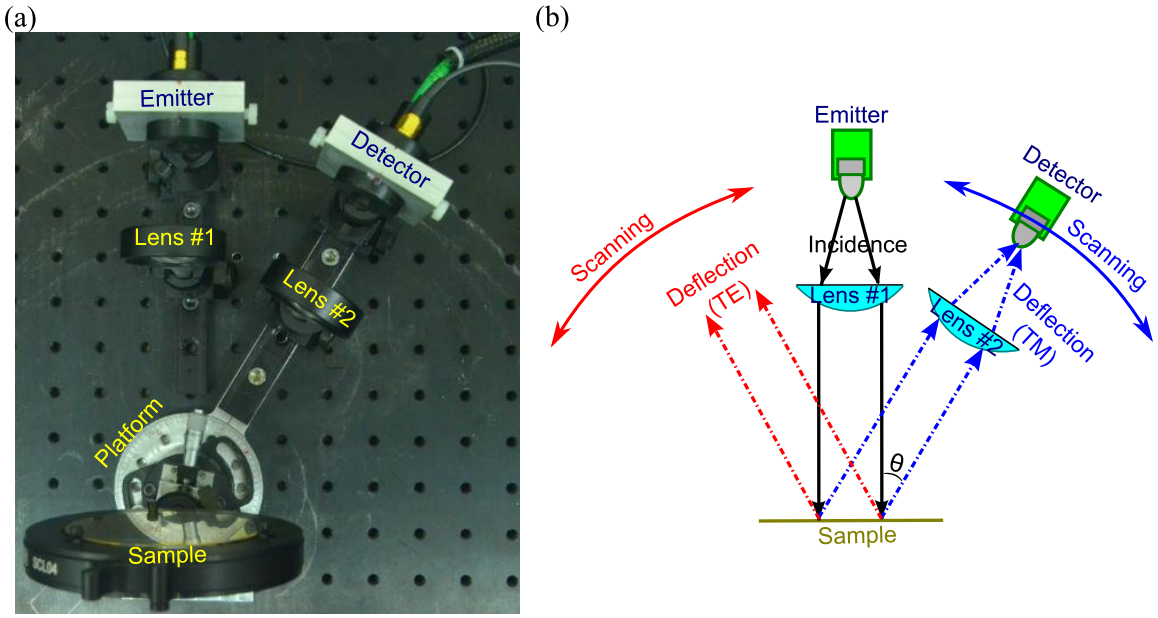

Figure 5.13. Measurement system. (a) Photograph of the measurement system. (b) Corresponding schematic. The beam from the emitter is collimated by lens #1, and incident on the surface of the sample. Lens #2 collects and focuses the scattered wave onto the detector. Lens #2 and the detector are fixed on a rotating arm pivoting around the location of the sample center. This arrangement allows a wide angular range to be scanned.

In order to characterize the angular behaviour of the deflected beams for normal incidence, the radiation patterns of the reflectarray for both of the TE and TM polarisations are simulated and measured as shown in Fig. 5.15. In the HFSS simulations, the radiation pattern of the TE and TM polarisations can be numerically obtained using an approach based on the array factor, but neglecting edge effects. The results shown in Figs. 5.15(a) and 5.15(b) demonstrate the predicted polarisation-dependent deflections. A specular reflection component, i.e. a feed image lobe (Almajali *et al.* 2014), exists but is around 10 dB lower than the maximum deflection. This specular component can also be interpreted as imperfectly suppressed zeroth-order spatial harmonics associated with the subarray periodicity. The measured radiation patterns at 1 THz are given in Figs. 5.15(c) and 5.15(d) for the TE (red line) and TM (blue line) polarisations, respectively. Because of different excitations, plane waves for simulations and Gaussian beams for measurements, wider deflection beams and lower side lobes are observed in measured radiation patterns when compared with the simulated patterns. The measured cross-polarised components caused by grating lobes in the deflected

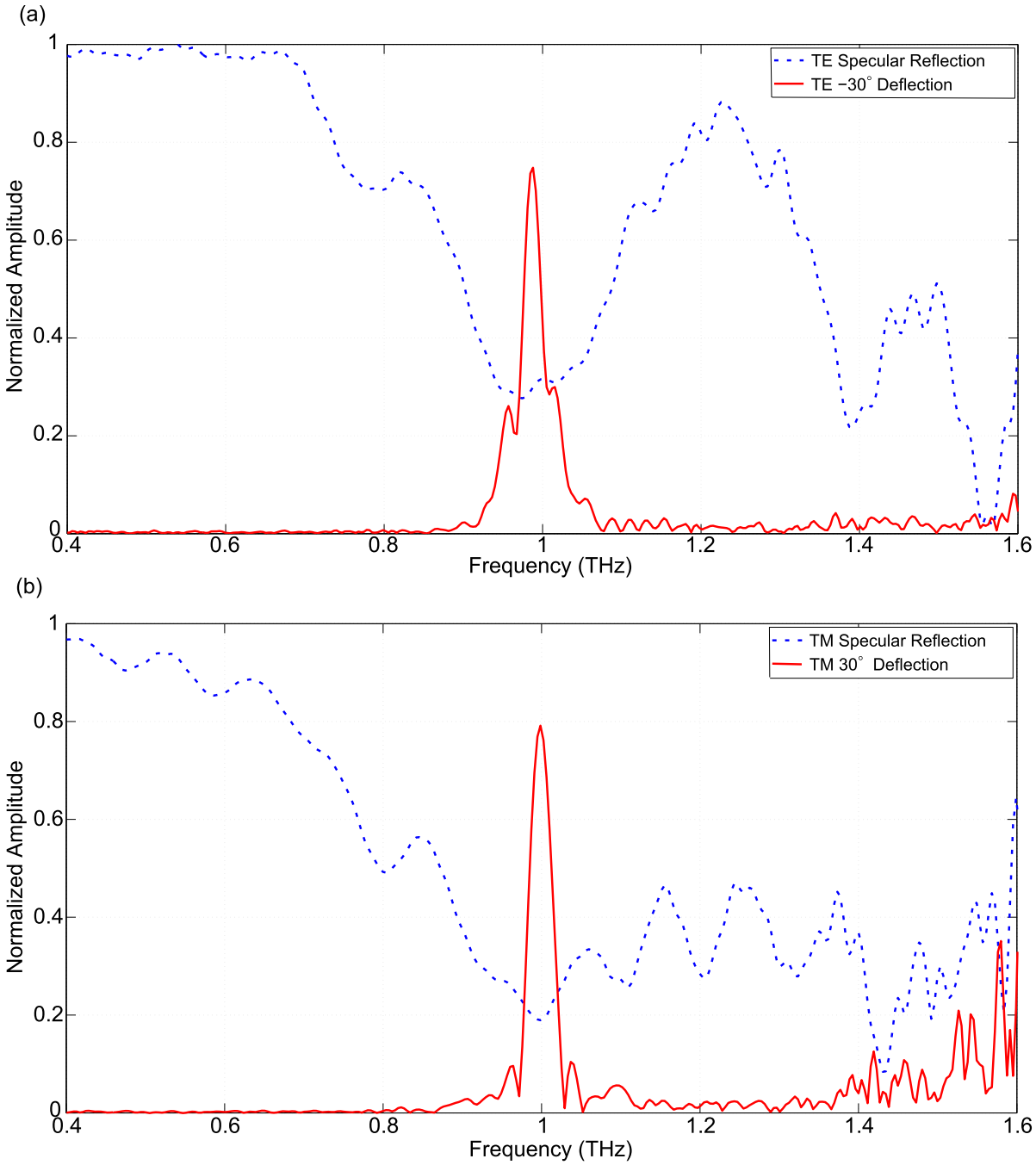

Figure 5.14. Measured normalized amplitude spectra for specular reflection (blue dashed line) and deflection (red solid line). The 15° incident waves with TE (a) and TM (b) polarisations are specularly reflected and distinct notches at around 1 THz are observed in the spectra, whereas the normally incident TE and TM waves are efficiently deflected into $-30°$ and $+30°$, respectively.

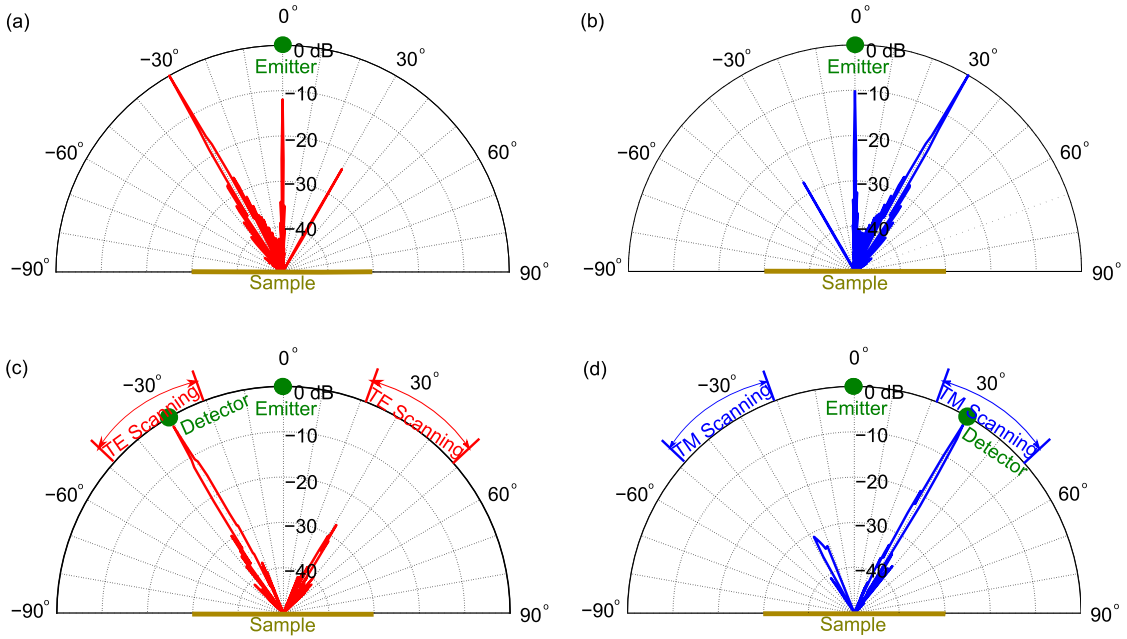

Figure 5.15. Radiation patterns at 1 THz for TE and TM polarised incident waves on a logarithmic scale. The normally incident wave with the TE or TM polarisation can be efficiently deflected into the direction of $-30°$ or $+30°$. (a) and (b) Simulated radiation patterns for the TE and TM polarised incident plane wave, respectively. (c) and (d) Measured results for the TE and TM polarised incident Gaussian beam, respectively.

beams are -27 dB for the TE polarisation and -29 dB for the TM polarisation. However, it is noted that those values are most likely limited by the measurement system dynamic range.

As for the spectral characteristics of the reflectarray, the normalized scattered wave amplitude is shown in Fig. 5.16. The magnitude is plotted in linear scale as a function of frequency and scan angle. It is again demonstrated that the strongest deflection takes place around the specified frequency in the designed directions for both of the TE and TM polarisations. Off the optimum, the deflection efficiency degrades gradually. Away from the predesigned main lobes for both the TE and TM polarisations, grating lobes introduced by the periodic configuration in subarrays are apparent in Fig. 5.16 beyond 1.4 THz.

The above measurement results demonstrate promising prospects for the designed reflectarray for terahertz beam splitting. However, there are two aspects that could be improved for further enhancing the performance of the reflectarray. Firstly, the angle

for the maximum deflection amplitude of the TE and TM polarised incident waves shifts from the designed $\mp 30^\circ$ at 1 THz to measured -28° at 1.04 THz and $+29^\circ$ at 1.03 THz, respectively. This slight disparity is caused by fabrication tolerance. In particular, the substrate thickness of the fabricated sample has been estimated to be 17 µm, rather than the target thickness of 20 µm. The fabrication tolerance moves the frequency for the maximum deflection slightly off the designed optimal frequency, which translates in a shift of the angle for the maximum deflections, i.e. through the phenomenon of beam squint with frequency (Targonski and Pozar 1996). Secondly, the deflection efficiency for the TE and TM polarisations could be improved by using dielectric substrates with lower loss tangent.

5.4 Reflectarray for asymmetric beam splitting

In this section, a subarray is constructed from multiple unit cells with dipoles arranged in the compact layout to create two asymmetric progressive phase distributions to respond to the TE and TM polarised incident waves. Numerical results for the near- and far-field distributions of the reflectarray demonstrate that the proposed structure can separate the polarisation components of an incident beam by deflecting them into two different directions, i.e. -48.6° and 30°, in plane.

Based on the phase response data of the compactly arranged dipoles shown in Fig. 5.9(a) (blue solid line), two different progressive phase changes of -90° for the TE wave and $+60^\circ$ for the TM wave between adjacent dipoles with the same orientation are chosen. This results in a deflection of the incident wave into two different directions. The deflection angle θ off the specular reflection can be calculated according to the Eq. 5.3. With the required parameters, the selected progressive phase changes will result in a beam deflection of -48.6° and $+30^\circ$ for the TE and TM polarisations, respectively. The corresponding sizes of the dipoles for the required phase changes are selected from the simulated phase curve. For a subarray, 4 dipoles are required to cover one cycle for the TE polarisation while 6 dipoles are required to cover one cycle for the TM polarisation. Therefore, the total number of dipoles for constructing the whole subarray is the twice of least common multiple of 4 and 6, i.e. $2 \times \mathrm{LCM}(4, 6) = 24$. The layout of the subarray composed of 24 dipoles divided into two groups is configured as shown in Fig. 5.17(a). The field distributions of the deflected wave at 1 THz for the TE and TM polarisations are demonstrated in Figs. 5.17(b) and 5.17(c), respectively. The scattered

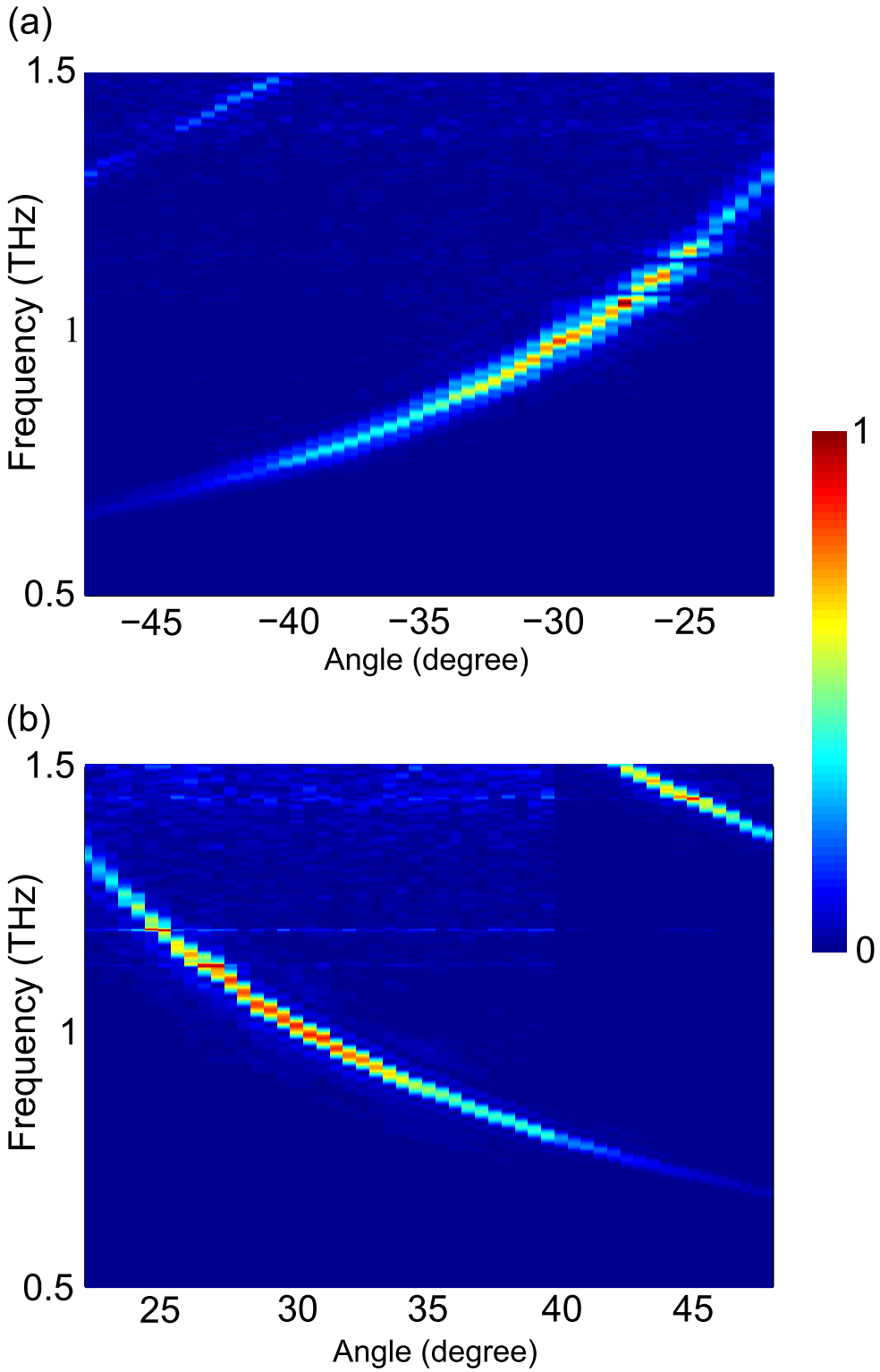

Figure 5.16. Normalized deflection magnitudes in linear scale as a function of the frequency and scan angle for TE (a) and TM (b) polarisations by measurements.

fields clearly illustrate that the normally incident plane wave is predominantly deflected into the predefined directions according to the incident polarisation. In order to demonstrate the ability of a finite reflectarray for beam splitting with asymmetric deflections, a reflectarray that contains 42 × 252 subarrays in periodic arrangement is considered. This corresponds to a total sample size of 50.4 mm × 50.4 mm. Based on this configuration, the radiation pattern for the total reflected electrical field can be numerically obtained (neglecting edge effects) using Ansys HFSS as shown in Fig. 5.18. It is confirmed that the designed reflectarray can separate the polarisation components of an incident beam into two different desired directions in a given plane with a polarisation purity of -20 dB and -25 dB for the TE and TM waves, respectively. Due to the asymmetric beam deflections, the detrimental effect from the grating lobes associated with cross-polarisation can be reduced.

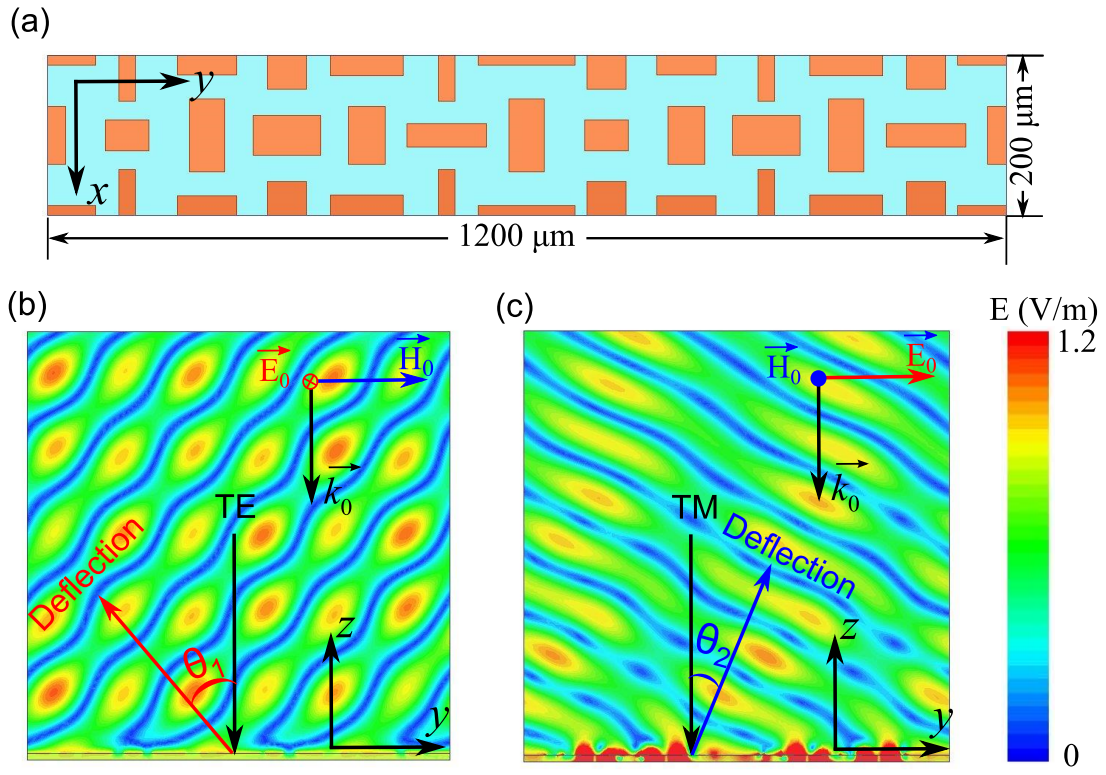

Figure 5.17. Reflectarray for asymmetric beam splitting. (a) Structure of one sub-array made of 24 dipoles; (b) and (c) simulated instantaneous scattered field distributions from the reflectarray at 1 THz for the TE and TM polarisations, respectively. For the normally incident plane wave with the TE and TM polarisations, the reflectarray can deflected them into two different directions with the angles of $\theta_1 = 48.6°$ and $\theta_2 = 30°$, respectively.

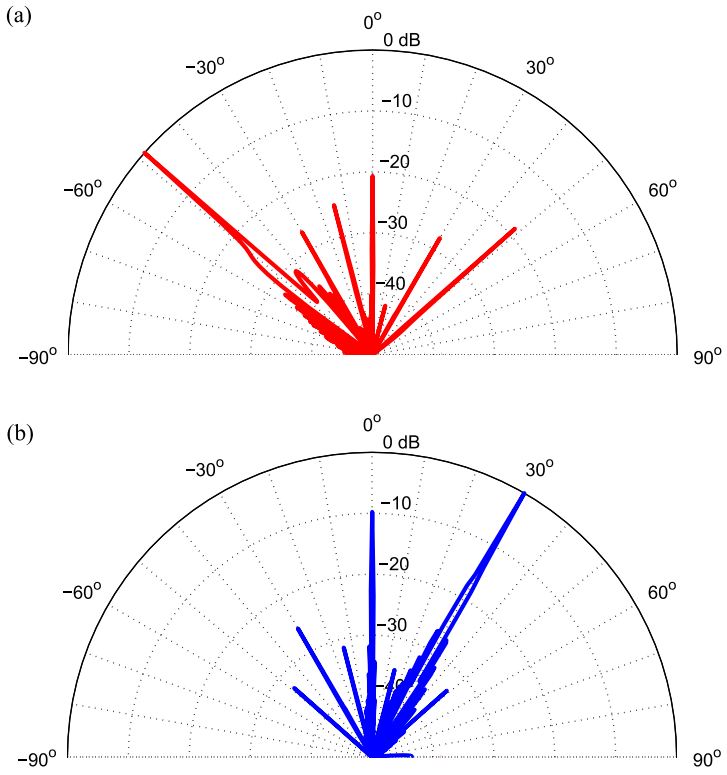

Figure 5.18. Simulated radiation patterns. The periodic reflectarray is composed of the subarray shown in Fig. 5.17(a) with a total size of 50.4 mm × 50.4 mm for the TE (a) and TM (b) polarised incident plane waves.

5.5 Conclusion

Terahertz reflectarrays with orthogonal strip dipoles in an interlaced triangular-lattice configuration have been proposed and designed for operation as a polarisation beam splitter. It has been first demonstrated that, compared with a reflectarray with sparsely arranged dipoles, a reflectarray with compact layout exhibits improved efficiency. Additionally, it offers relaxed tolerances, making it more feasible to fabricate and more amenable to practical applications. The performance of the fabricated prototype with the compact layout has been measured with a THz-TDS system. Both the simulation and measurement results successfully verify that the designed reflectarray can efficiently deflect the incident waves into different directions depending on the incident linear polarisation with an efficiency of over 60% and polarisation purity of at least -27 dB. For higher deflection efficiency, a lower loss material could be applied as the substrate. As the reflectarray construction is based on resonant elements, the -3 dB bandwidth of the designed beam splitter is limited at about 3% in the present case. The

limited bandwidth behaviour of the terahertz beam splitter could be improved by considering multi-layer approaches developed in the microwave regime (Encinar 2001). As an extension of the concept, a reflectarray for bidirectional deflection with asymmetric progressive phase profiles has been proposed and simulated. The simulation results have successfully verified that the reflectarray can efficiently and asymmetrically deflect the incident waves with high polarisation purity into different directions depending on the incident linear polarisation. These reflectarrays could be applied as optical components for polarisation discrimination or as polarisation demultiplexers for terahertz communications.

Chapter 6

Polarisation-dependent wire-grid reflectarray for terahertz waves

A thin-film polarisation-dependent reflectarray based on patterned metallic wire grids is realised at 1 THz. Unlike conventional reflectarrays with resonant elements and a solid metal ground, parallel narrow metal strips with uniform spacing are employed in this design to construct both the radiation elements and the ground plane. For each radiation element, a certain number of thin strips with an identical length are grouped to effectively form a patch resonator with equivalent performance. The ground plane is made of continuous metallic strips, similar to conventional wire-grid polarisers. The structure can deflect incident waves with the polarisation parallel to the strips into a designed direction, and transmit the orthogonal polarisation component. Measured radiation patterns show reasonable deflection efficiency and high polarisation discrimination. Utilizing this flexible device approach, similar reflectarray designs can be realised for conformal mounting onto surfaces of cylindrical or spherical devices for terahertz imaging and communications.

6.1 Introduction

Owing to the advantages of a flat profile and high efficiency, reflectarrays have been widely implemented across the electromagnetic spectrum (Huang and Encinar 2008), from microwave (Carrasco *et al.* 2013a, Bayraktar *et al.* 2012), millimetre-wave (Hu *et al.* 2008, Nayeri *et al.* 2014), terahertz (Carrasco *et al.* 2013b, Huang *et al.* 2014, Grady *et al.* 2013) to optics (Ahmadi *et al.* 2010, Zou *et al.* 2013, Yifat *et al.* 2014, Carrasco *et al.* 2015). As reviewed in Chapter 3, a typical reflectarray is composed of three layers: a top layer with resonant elements arranged periodically with a beam-forming phase distribution, a dielectric spacer, and a metal ground plane. As one of the possible functions of a reflectarray, waves incident on its surface can be deflected into an off-specular direction, as demonstrated in Chapter 4. Because of the presence of a full metal ground plane, the incident electric field can only be re-radiated backwards into free space after interacting with the reflectarray. In some applications such as beam splitting and polarisation-sensitive beam forming, structures that can either reflect or transmit incident beams with polarisation dependence are necessary for manipulating wavefronts of the propagating fields. Thin-film wire grid is an attractive alternative for designing structures with the characteristic of polarisation-dependent transmission. With the development of nanolithographic manufacturability, wire grids have been widely applied for constructing compact and planar polarisers in different frequency ranges (Ekinci *et al.* 2006, Wu *et al.* 2013, Weber *et al.* 2014). A wire-grid efficiently transmits the electric field perpendicular to the wires and reflects the other polarisation component parallel to the wires with high extinction ratios of transmission and reflection over a wide incident angle and frequency range, provided that the wavelength of the incident light is much larger than the period of the grid. Based on this characteristic, it is possible to use the patterned grating structures as the radiating elements to construct an array that can reflectively deflect one polarisation and transmit the other polarisation with high efficiency.

In this chapter, a terahertz reflectarray using patterned double-layer metallic wire-grid geometry is proposed to realise two polarisation-dependent functions: (i) reflective deflection for the incident polarisation parallel to the grid and (ii) normal transmission for the orthogonal polarisation—therefore it can be considered as a combination of a reflectarray and a wire-grid polariser. This reflectarray structure is fabricated on a free-standing flexible polymer substrate. Hence the structure is flexible and stretchable,

and it can be conformed onto curved surfaces to achieve a desired radiation pattern provided that the radius of the curved surface is electrically large.

6.2 Unit cell with metallic wire grids

A schematic diagram of the unit cell and the layout for the proposed reflectarray is given in Fig. 6.1. The array is composed of periodically arranged identical subarrays. Each subarray contains a certain number of subwavelength unit cells, and each cell is made of a resonant element on the ground plane with a flexible polymer polydimethylsiloxane (PDMS) (Khodasevych *et al.* 2012) as a dielectric spacer. This individual resonant element is formed by grouping thin gold strips together in a square shape, while the ground plane is made of continuous gold strips. All the gold strips for both the top and bottom layers have a width of 5 μm, and are uniformly arranged with an inter-strip spacing of 5 μm. The size of the unit cell is fixed at $a = 140\,\mu\text{m}$ and the thickness of the PDMS dielectric layer is $h = 20\,\mu\text{m}$. To improve the structural strength, a supporting layer of PDMS with a thickness of 100 μm is included under the ground plane. For clarity, this layer is not included in Fig. 6.1.

The proposed unit cell shown in Fig. 6.1(a) is simulated with the commercial software package, Ansys HFSS. A plane-wave excitation with a Floquet port and master-slave boundary conditions is applied for investigating the phase and magnitude responses of the unit cell in a uniform array. At 1 THz, the surface impedance of gold (Lucyszyn 2007) obtained from a Drude model is $Z_{\text{Au}} = 0.287 + 0.335j\,\Omega/\text{sq}$. The relative permittivity and loss tangent of PDMS (Khodasevych *et al.* 2012) adopted from independent measurement are $\epsilon_r = 2.35$ and $\tan\delta = 0.06$, respectively. For incident waves with a polarisation parallel to the strips, denoted as the TE polarisation, the structure performs as a reflectarray. Here, each group of thin strips on the top layer behaves as polarisation-dependent equivalent of a patch resonator. When the length of the equivalent square patch is varied from 20 μm to 135 μm, the number of strips discretely increases from 2 to 14, as obtained by rounding the value of $l/10$ to the next integer. Over this length variation, a reflection phase range of over 300° is achieved for the TE polarisation with acceptable efficiency, as shown in Fig. 6.2. The highest reflection loss of about -5 dB takes place at the resonance size of the wire-grid patch, for a length l of around 81 μm. For the excitation with the TM polarisation (also shown in Fig. 6.2), regardless of the wire-grid patch size, the transmission amplitude and phase remain

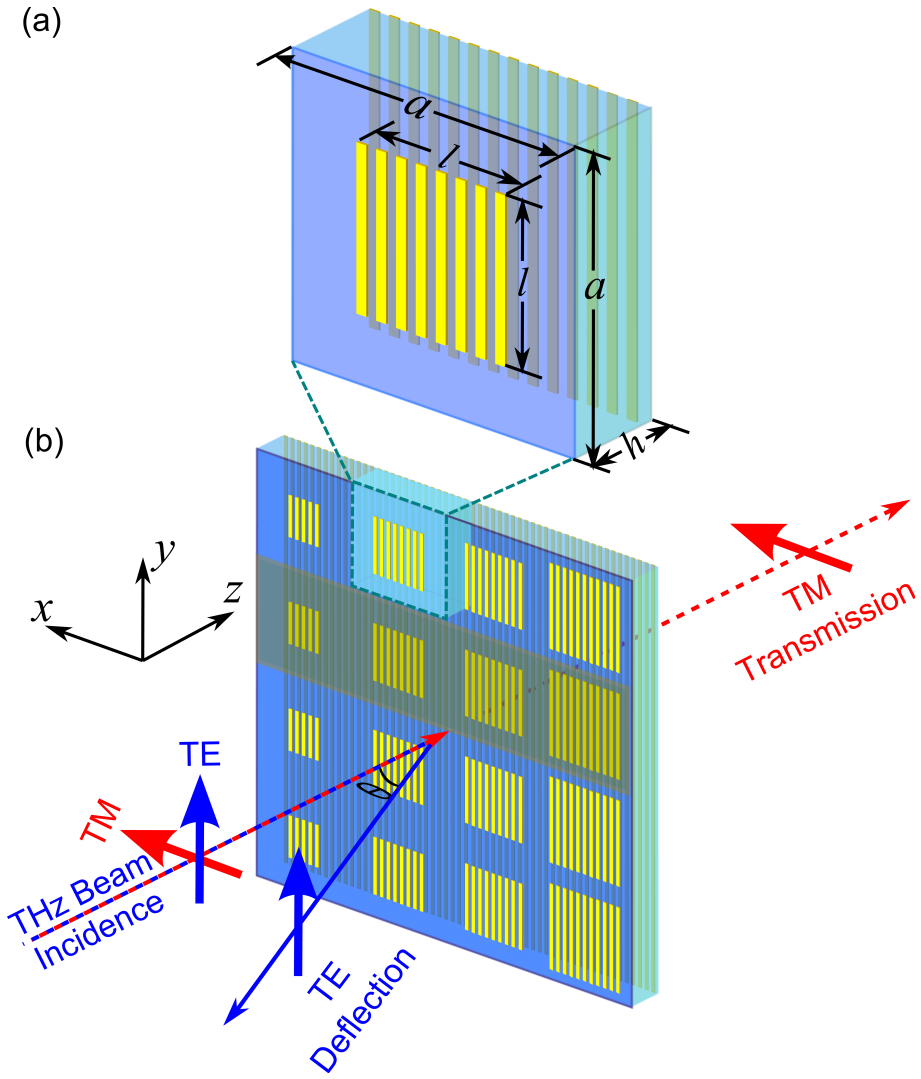

Figure 6.1. Schematic diagram of the unit cell and the layout of the reflectarray. Each radiating element is composed of metal strips to form a polarisation-dependent patch resonator, and the ground plane is made of a metallic wire grid. The strips for both the radiating element and the ground plane have the same width of 5 µm, and the gap between the adjacent strips is 5 µm. (a) The unit cell with a width of $a = 140\,\mu\text{m}$ and a thickness of $h = 20\,\mu\text{m}$. (b) A part of the reflectarray showing 4 subarrays with each subarray being composed of 4 unit cells with different sizes of radiating elements. The shaded zone specifies one of the subarrays. The polarisation-dependent functions are indicated with blue and red arrows.

nearly constant, with a small loss introduced by the dielectric PDMS substrate. Importantly, the device is not affected by polarisation conversion. As a consequence, the transmitted energy of less than -26 dB for the TE polarisation and the reflected energy

of around -11 dB for the TM polarisation are insignificant, and are not presented in Fig. 6.2.

At terahertz frequencies, the dissipation loss in metals caused by finite conductivity and the dispersion with frequency require a more realistic metal model than PEC to describe their performance. For comparison, the radiating element together with the ground plane in Fig. 6.1 is simulated with both the PEC and Drude models, and the corresponding magnitude and phase responses are given in Fig. 6.3. The phase responses available from both models are almost the same. However, the magnitude responses are remarkably different. The PEC model gives the magnitude that is more than 1 dB higher compared with the Drude model at the resonance size. This means the loss as a result of the finite conductivity has to be taken into account in the terahertz design.

For comparison, the reflection phase and magnitude responses of equivalent resonators realised with solid patches and single dipoles with a width of 5 μm, both on a grating ground plane, are also displayed in Fig. 6.4. The wire-grid patch offers similar phase and magnitude responses as those of the solid patch for the TE polarisation. However, for the TM polarisation, the solid patch has much lower transmission efficiency that reduces from -0.4 dB to -10 dB when the patch size increases from 20 μm to 135 μm (this result is not included in Fig. 6.4). On the other hand, the phase curve of the single dipole resonator has a remarkably steep slope and significantly higher loss due to a high-Q resonance. Therefore, using the wire-grid patch resonator as radiating elements combines the advantages of high efficiency of the patch (for the TE polarisation) with the polarisation dependence of the dipole.

6.3 Design of the subarray

As a proof of concept, a polarisation-dependent reflectarray is designed to deflect a normally incident TE polarisation into a predefined direction while transmitting the TM polarisation. For simplicity, the array is constructed as periodic arrangement in subarrays, designed based on the phase response of the unit cell as shown in Fig. 6.2. The deflection angle θ is determined by the progressive phase change of adjacent wire-grid patches according to the formula

$$\theta = \arcsin\left(\frac{\lambda_0}{d}\right) = \arcsin\left(\frac{\Delta\phi\lambda_0}{2\pi a}\right), \tag{6.1}$$

where λ_0 is the operation wavelength, $d = 2\pi a/\Delta\phi$ the size of the subarray, $\Delta\phi$ the progressive phase change between adjacent cells, and a the size of the unit cell. The

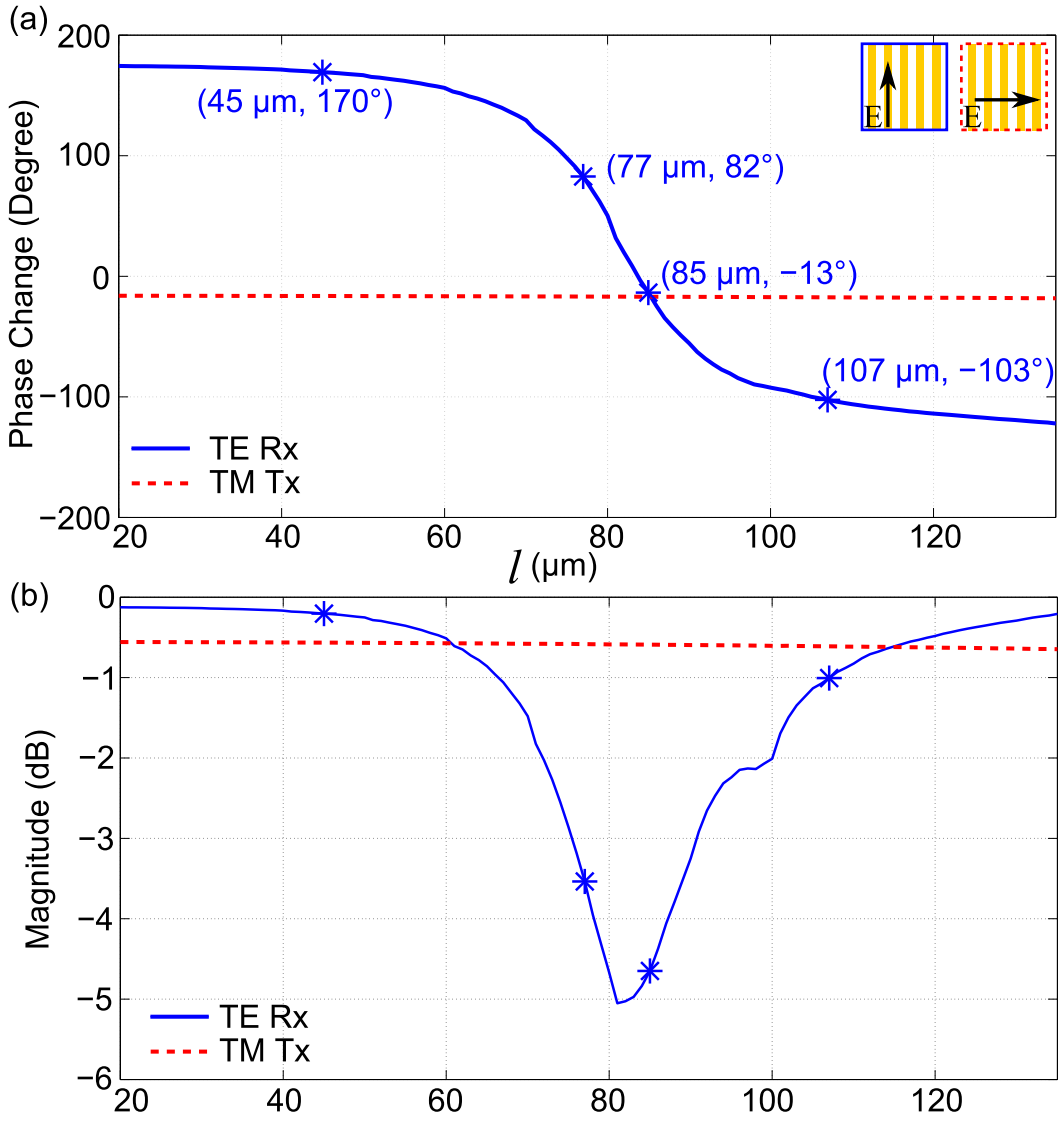

Figure 6.2. Simulated phase and magnitude responses of the proposed unit cell with thin-film wire-grid patch for both the TE and TM polarised incident waves. (a) Phase response, and (b) magnitude response. The marks $*$ on the phase and magnitude curves indicate the selected radiating elements for defining a subarray that completes one full phase cycle.

value of $\Delta\phi$ can be chosen arbitrarily. In this chapter, we choose $\Delta\phi = \pi/2$ so that a complete phase cycle of 2π is achieved with subarrays of 4 elements. Therefore, the length of the subarray is given by $d = 4a = 560\,\mu\text{m}$ to achieve a deflection angle of $\theta = 32.4^\circ$ at 1 THz. The size and corresponding phase and amplitude responses of the 4 elements are marked in Fig. 6.2(a). It is noted that the fabrication tolerance demands the lengths of the strips for the radiating elements to be rounded to discrete values

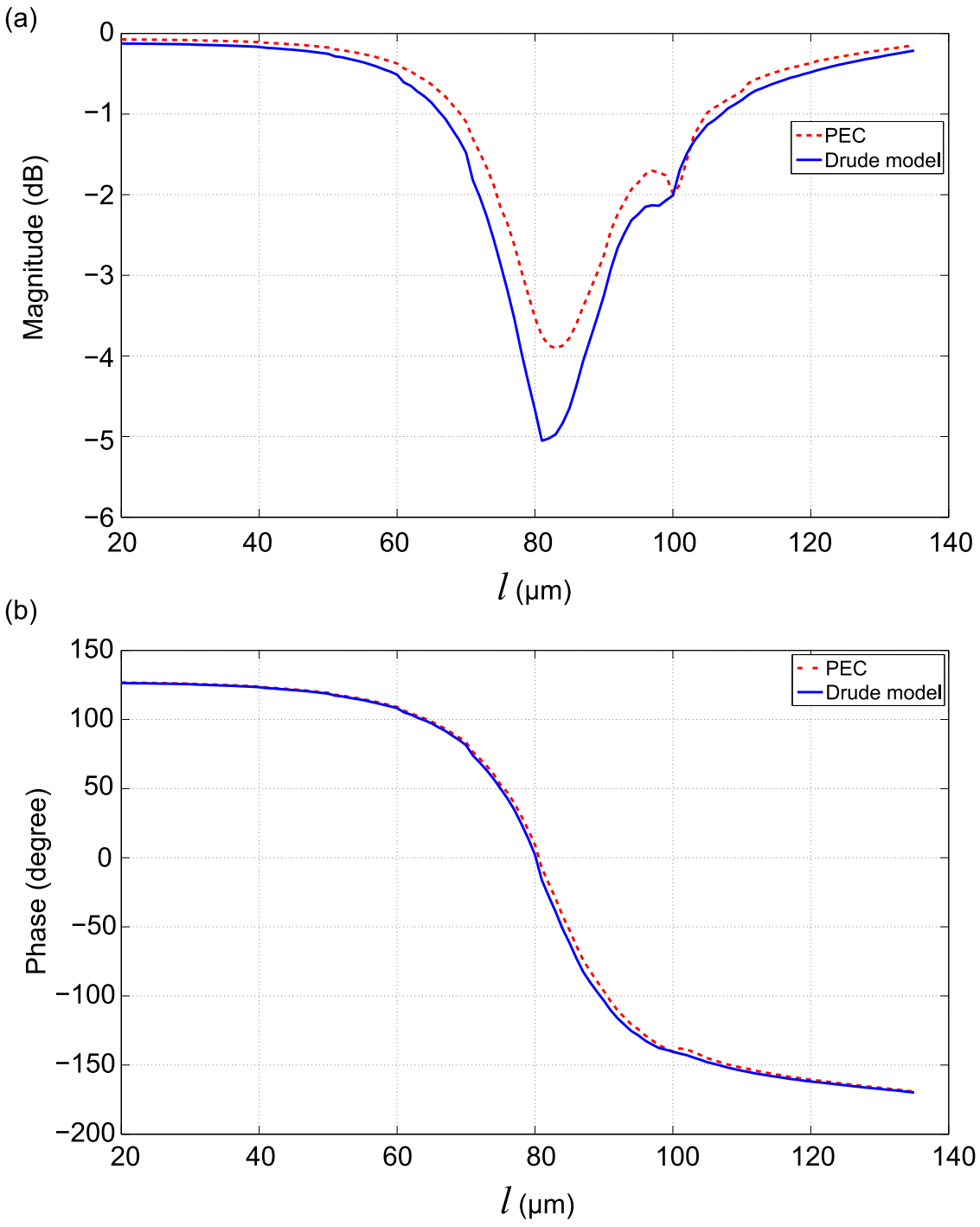

Figure 6.3. Simulated magnitude and phase responses of the radiating element together with the ground plane in Fig. 6.1 with both the PEC and Drude models. (a) Simulated reflection magnitude and (b) phase responses for 2D uniform infinite arrays with radiating resonators made of grids grouped in a square shape and griding ground plane for TE polarisation at 1 THz.

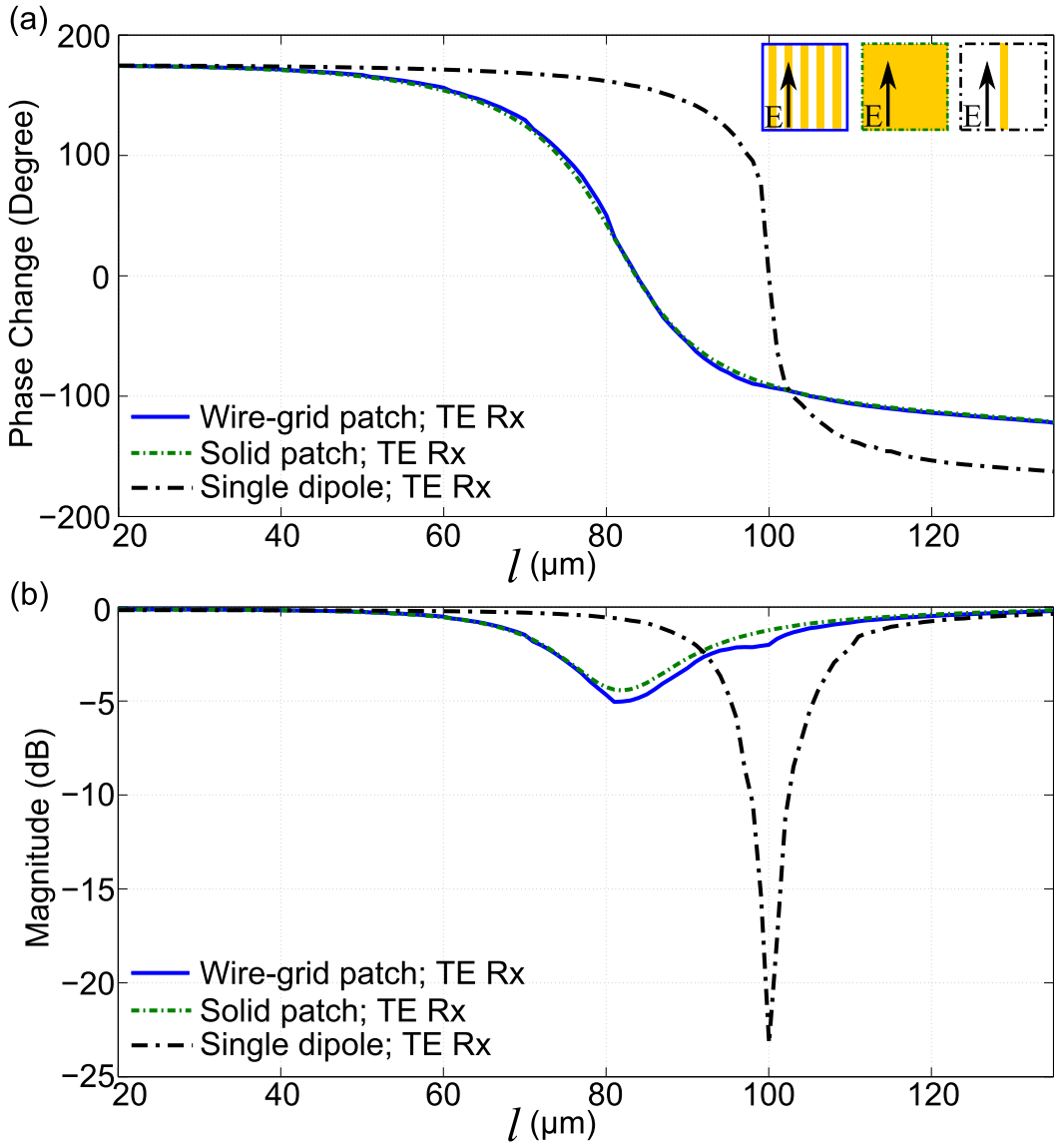

Figure 6.4. Simulated phase and magnitude responses of the unit cell with wire-grid patch, solid patch and single dipole for both the TE polarised incident waves. (a) Phase response, and (b) magnitude response.

in microns, and thus, small phase inaccuracies can be expected particularly where the phase response is highly sensitive to a change in the wire-grid patch length i.e. in the section of the phase curve with a steep slope.

The simulated scattered field distributions for the TE and TM polarised plane wave excitations are demonstrated in Fig. 6.5(a) and (b), respectively. When the normally incident plane wave is polarised in the direction parallel to the strips (TE), the designed structure functions as a reflectarray deflecting the incident waves into the predesigned direction $\theta = 32.4^\circ$ off the direction of specular reflection. From Fig. 6.5(a), the energy

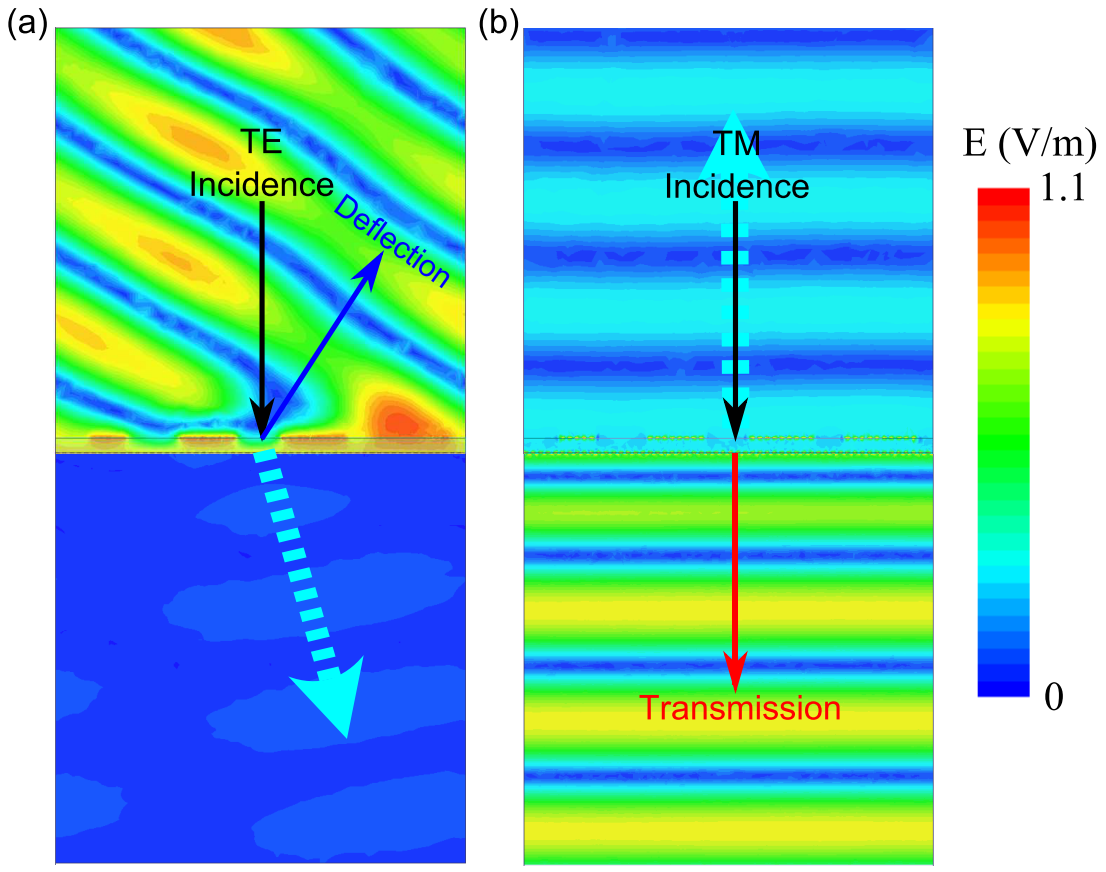

Figure 6.5. Simulated instantaneous scattered fields from the reflectarray at 1 THz. (a) The TE polarisation. (b) The TM polarisation.

leaking to the other side of the structure is relatively small. For the plane wave with polarisation perpendicular to the strips (TM), the structure allows transmission with minimal attenuation caused by the dielectric dissipation and reflection losses.

6.4 Measurement and results

The designed reflectarray has been fabricated for validation of the proposed functionality. The optical micrographs of a small area in Fig. 6.6 show the details of the gold wire-grid patches and the wire-grid ground plane. The entire sample has a size of 50.4 mm × 50.4 mm and contains 90 × 360 periodically arranged subarrays. The sample is measured with a terahertz time-domain spectroscopy (THz-TDS) system, Tera K15 developed by Menlo Systems GmbH. The schematic diagram for the measurement setup is show in Fig. 6.7. The front surface of the sample is located at the centre of the scanning circle, and faces the direction of 0°. The emitter antenna is fixed on the circle at 0°, and the emitted terahertz beam is collimated by Lens 1 before impinging

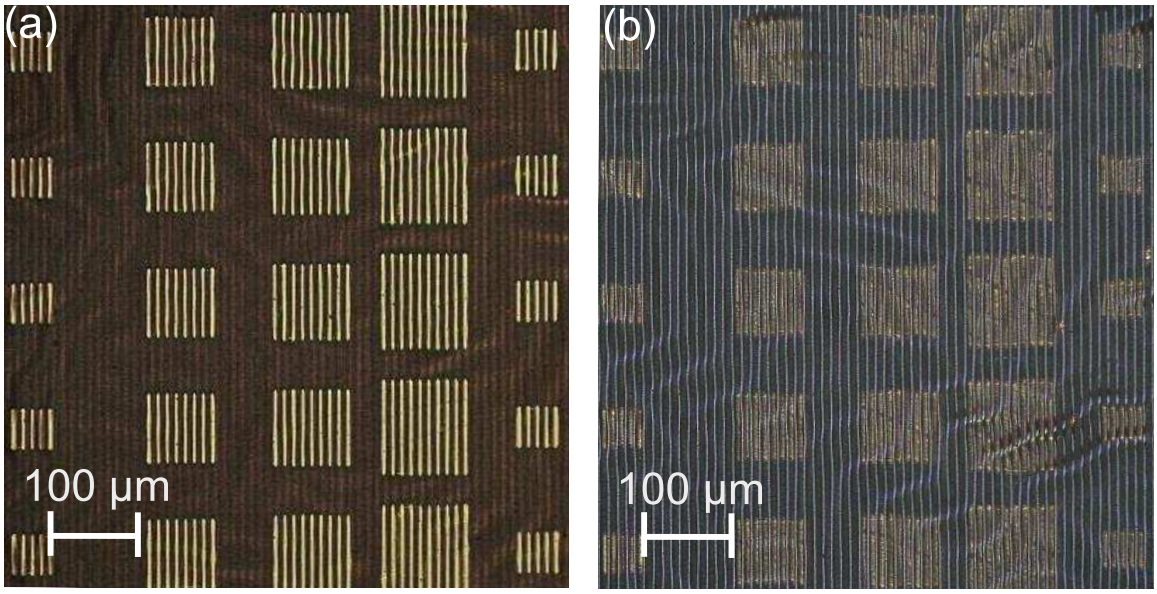

Figure 6.6. Optical micrographs of a part of the fabricated sample. (a) The gold wire-grid patches of several subarrays located on the front side of the sample. (b) Back side showing the gold wire-grid ground plane (through a 100 µm thick layer of PDMS).

on the sample. Lens 2 collects and focuses the scattered radiation into the detector, and the detector antenna is automatically rotated at a fixed radius from the sample, taking a THz-TDS measurement every 0.5° to establish a radiation pattern. The minimum clearance between the emitter and the detector is 25°. Three measurement configurations are necessary to characterize the sample. The first two configurations are set to collect the radiation patterns around the sample for normal incidence in the TE and TM polarisations. Because of the blind zone around the emitter, a third configuration is necessary to measure the specular reflection for the TE wave, which is achieved by rotating the sample with an angle of 20° while the emitter remains positioned at 0°. All the measurements are normalized using the air reference in transmission to remove system dependency.

For the normally incident beam, the measured normalized radiation patterns at the design frequency of 1 THz are presented in Fig. 6.8. When the polarisation of the excitation is parallel to the wire-grid strips, the maximum deflection at the angle of 33° is observed with an efficiency of −4.1 dB and a polarisation purity of at least −30 dB, as shown with the blue solid line. In contrast, the TM wave orthogonal to the strips is primarily transmitted through the sample with a normalized maximum amplitude of −2.2 dB as shown by the red dotted line in Fig. 6.8. In addition, the spectral characteristics of the reflectarray for normal incidence are demonstrated in Fig. 6.9 where the

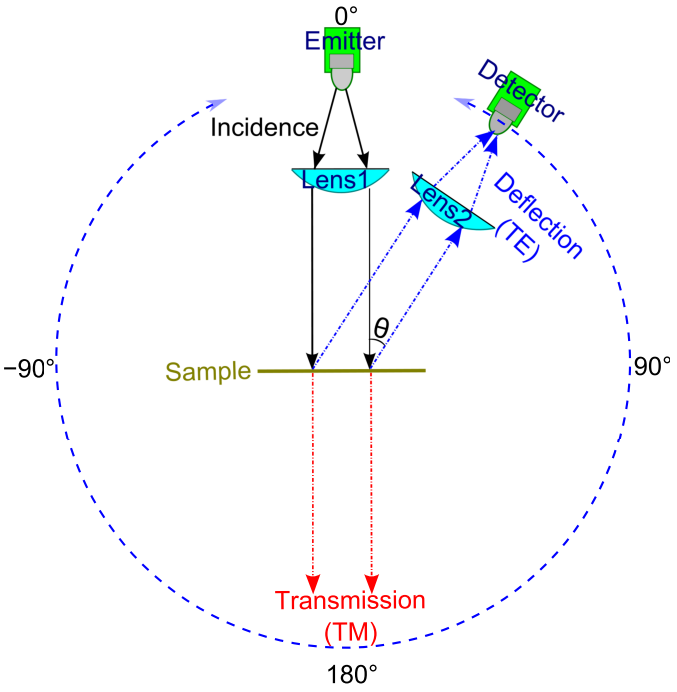

Figure 6.7. Schematic diagram for the THz-TDS measurement setup. The beam from the emitter at 0° is collimated by Lens 1, and incident on the front side of the sample located at the centre of the circle. Lens 2 collects and focuses the scattered wave onto the detector pivoting around the location of the sample centre in the clockwise direction from 25° to −25°. This arrangement allows an angular range of 310° to be scanned.

normalized magnitude is plotted in logarithmic scale as a function of frequency and scan angle. For the TE polarisation as illustrated in Fig. 6.9(a), a strong deflection appears around the specified frequency in the designed direction. Above and below the optimal frequency of 1 THz, the deflection efficiency degrades progressively. The deflection angle reduces with an increase in the operation frequency, i.e. as expected from the phenomenon of beam squint with frequency (Targonski and Pozar 1996). In addition to the main deflection lobe, minor lobes are observed in the forward and backward directions as a result of diffraction from the periodic configuration in subarrays. The corresponding results for the TM excitation are given in Fig. 6.9(b). For this polarisation, the array is almost transparent to the incident waves in the measurable frequency range. The transmission magnitude is slightly reduced because of the reflection and dissipation losses. Small grating lobes with amplitude below −30 dB can be observed.

In the case of the TE obliquely incident excitation with an angle of 20°, the radiation pattern at the targeted frequency of 1 THz and the scattered field around the sample at different frequencies are demonstrated in Fig. 6.10(a) and Fig. 6.10(b), respectively. At

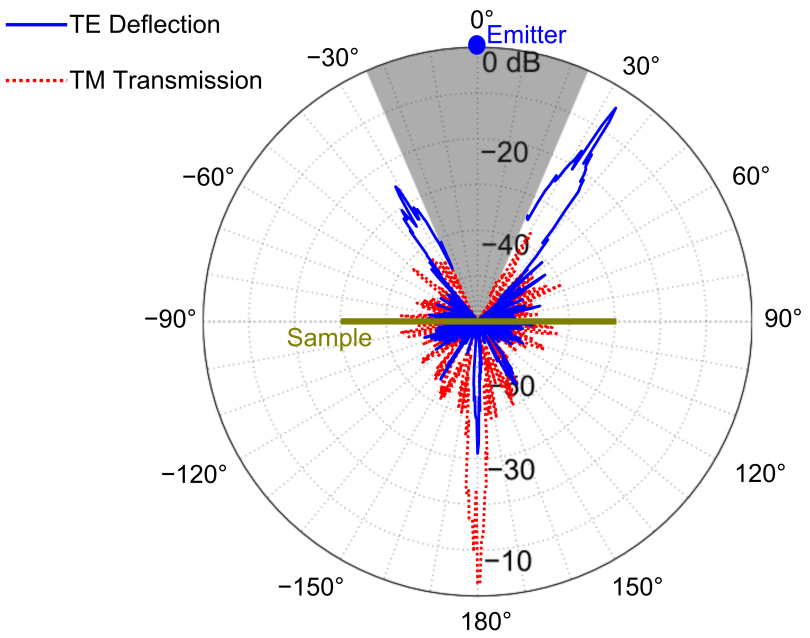

Figure 6.8. Measured normalized radiation patterns for normal incidence. Radiation patterns at 1 THz for the TE (blue solid line) and TM (red dotted line) polarised waves on a logarithmic scale. The emitter antenna is located at 0°, and the collimated broadband terahertz beam normally impinges on the surface of the sample. The detector scans the angular range clockwise from 25° to −25° with an angular resolution of 0.5°. The minimum clearance between the emitter and the detector is 25°, and the angular clearance range is indicated by the grey zone.

1 THz, the maximum deflection takes place at the off-normal angle of 61.5°, which is consistent with the theoretical expectation according to the formula (Yu *et al.* 2011)

$$\sin\theta_r = \sin\theta_i + \lambda_0/d, \tag{6.2}$$

where $\theta_i = 20°$ is the angle of incidence and θ_r corresponds to the deflection angle with respect to the normal. The calculated angle for the deflection is $\theta_r = 61.4°$. Therefore the angle between the emitter and the detector for the maximum deflection should be $\theta_r + \theta_i = 81.4°$. In terms of power, the deflection magnitude is larger than the specular reflection magnitude by 12 dB. The spectral performance of the sample with the oblique TE polarised incident wave is shown in Fig. 6.10(b). In the frequency range lower than 0.8 THz, the sample can be regarded as a mirror and the incident beams is mostly reflected into the specular direction. At higher frequencies, the deflection becomes dominant, and then reaches the maximum around the desired direction at 1 THz. At frequencies above 1 THz, the main deflection lobe attenuates gradually while the specular reflection becomes stronger.

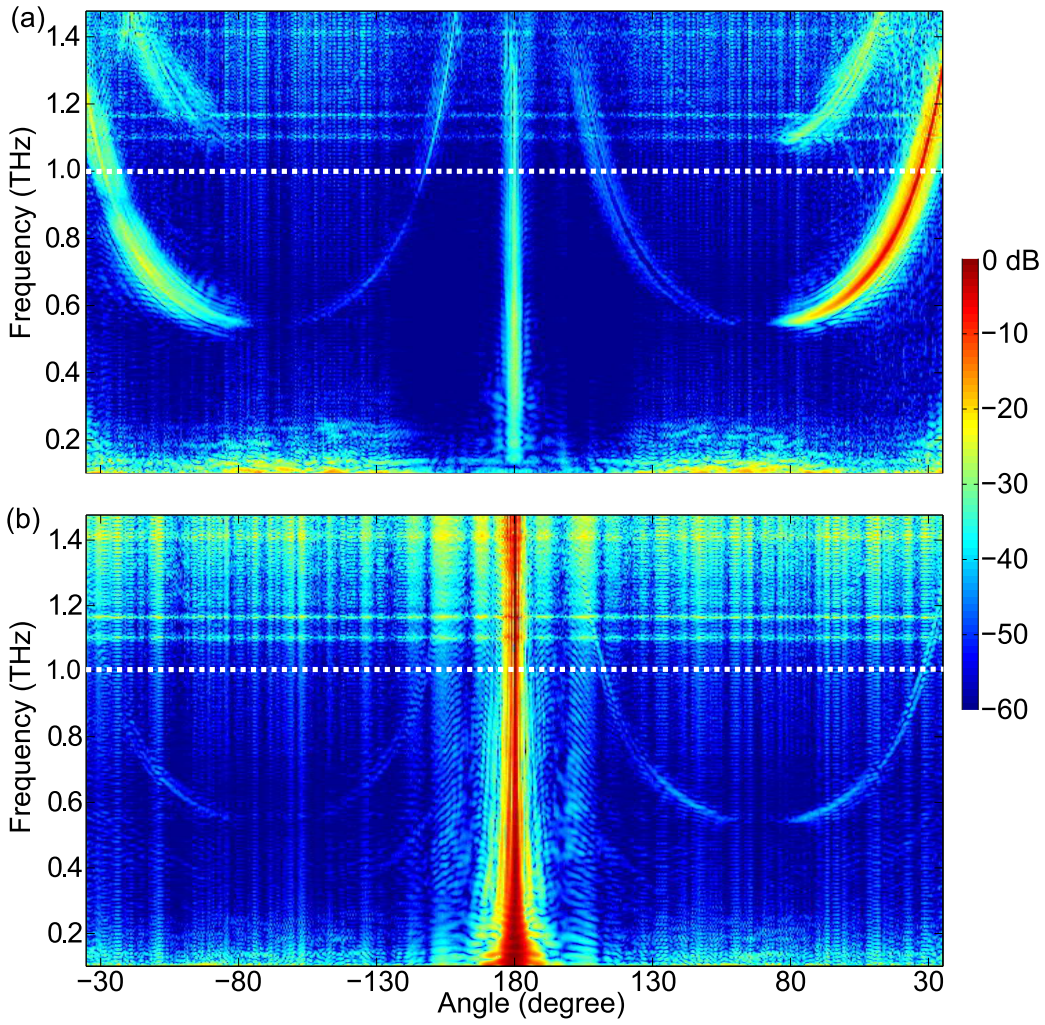

Figure 6.9. Measured colormap for radiation characteristics. Normalized scattered field as a function of the frequency and scan angle for the (a) TE and (b) TM polarisation. White dotted lines at 1 THz in (a) and (b) correspond to the radiation patterns for the TE and TM polarisations, respectively, shown in Fig. 6.8.

As the structure is stretchable, the function of beam steering can be achieved by mechanically stretching the reflectarray within a certain range. In the case of stretchable/flexible implementation, the thickness of the PDMS substrate and the geometry of the resonators will be changed, and correspondingly the phase behaviour of each radiating element will shift away from the predesigned values. This variation of the phase response will lead to distortion of the deflected main beam such as widened beamwidth and decreased directivity and gain. Additionally, the size of the subarray will also be changed because of stretching, and therefore the deflection direction of the main beam will change accordingly. We have tested the performance of the

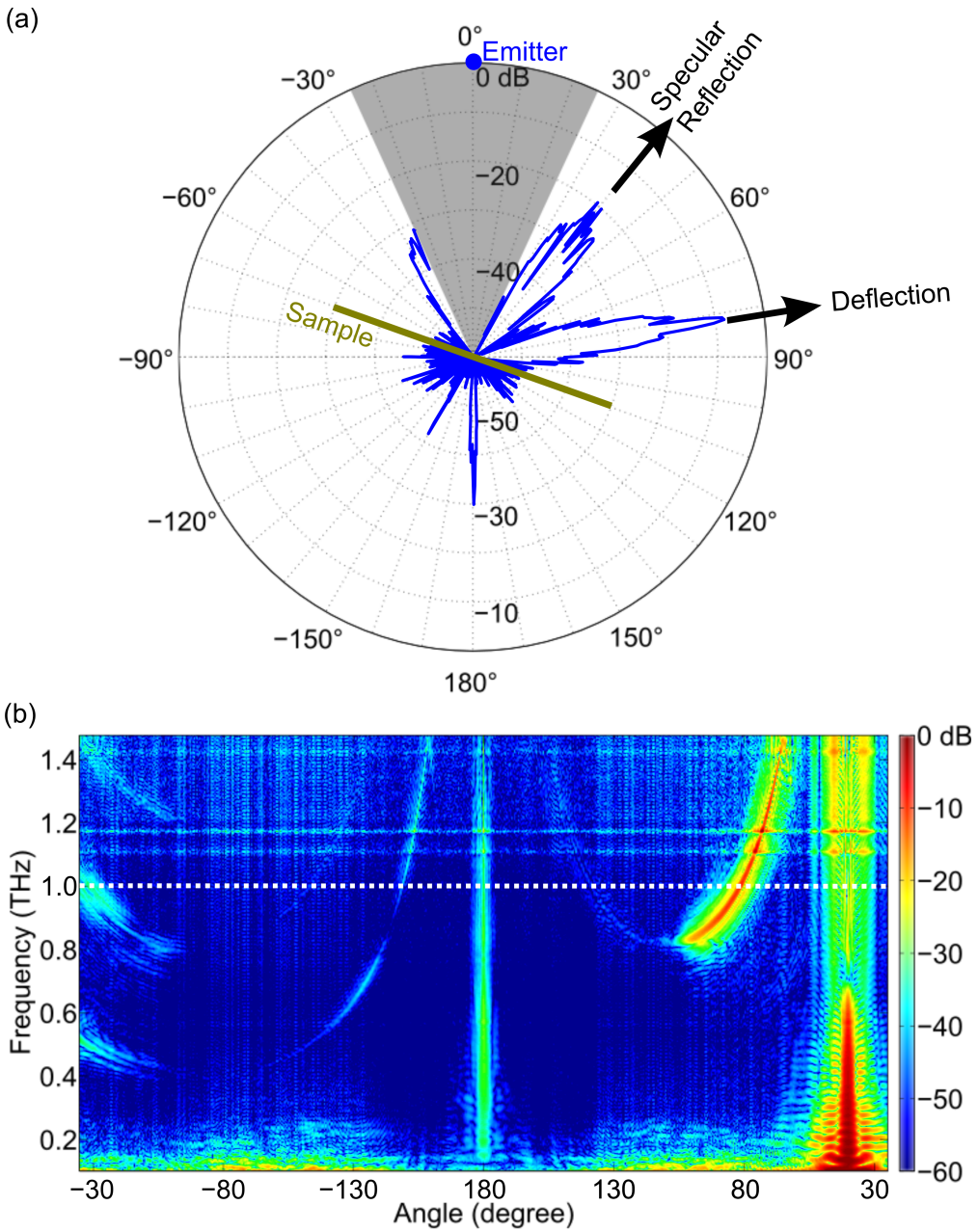

Figure 6.10. Measured normalized radiation patterns for oblique incidence. Reflectarray response for the TE excitation with an oblique incident angle of 20° on a logarithmic scale. The emitter antenna is located at 0°, and the normal vector of the sample is toward 20°. (a) Radiation pattern at 1 THz. The grey zone indicates the angular clearance. (b) Normalized scattered field as a function of the frequency and scan angle. White dotted line at 1 THz corresponds to the radiation pattern in (a).

proposed reflectarray stretched by about 20% in the x direction. The preliminary measured radiation pattern shown in Fig. 6.11 indicates that the main lobe decreased and

moved away from the designed direction of 32.4° to an angle smaller than 25° (beyond the measurable angular range), while the gating lobes significantly increased. If a frequency-dependent linear phase response is achieved from broadband radiating resonators such as single-layered multi-resonant dipoles, beam steering with high performance can be achieved with the design concept demonstrated in this work. Owing to the flexible characteristics, the reflectarray can be conformally mounted onto a device with slightly curved surface to have a similar radiation pattern with a slight reduction in gain (Nayeri *et al.* 2011). Because the pattern of each radiating element is normal to the local surface, the beamwidth of the conformal reflectarray is expected to be wider than its planar counterpart. For an improved design with no reduction of performance for curved surfaces, sophisticated phase synthesis approaches can be adopted (Josefsson and Persson 2006).

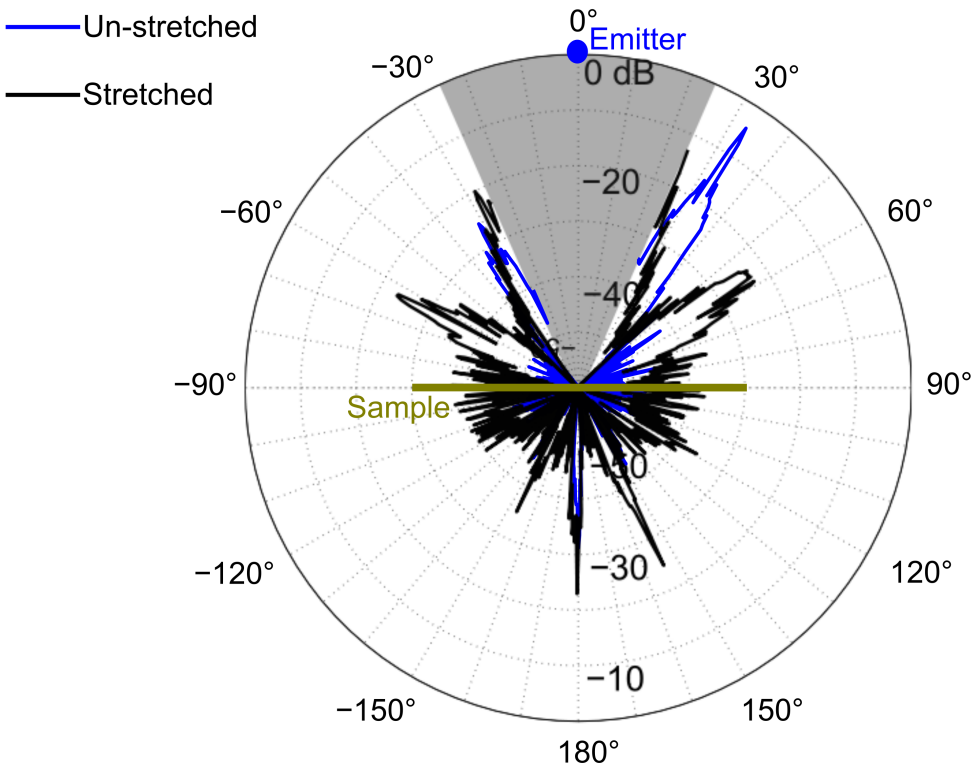

Figure 6.11. Measured normalized radiation patterns of the reflectarray with about 20% (black line) and without (blue line) stretching at 1 THz for the TE polarised waves.

6.5 Conclusion

In conclusion, the concept of reflectarray based on the metallic wire-grid configuration has been numerically and experimentally validated in the terahertz regime. The combined polarisation-dependent functions of reflective deflection and transmission are realised by the same structure. In the TE mode, a deflection efficiency of -4.1 dB is achieved. On the other hand, the TM waves can be transmitted through the reflectarray with a minimal change in amplitude. We note a small shift in the micro-fabricated wire-grid patches as a result of the mask preparation. Despite that imperfection, the sample still performs as expected, which further confirms the robustness of the design. Owing to the flexible characteristics, similar reflectarray configurations can be designed to be conformally mounted onto devices with an uneven surface (Yi *et al.* 2014). In addition, the proposed concept of reflectarray can be extended to polarisation-dependent reflective and transmissive deflection (Padilla *et al.* 2010, Memarzadeh and Mosallaei 2011, Lau and Hum 2012, Pfeiffer and Grbic 2013) by adding more layers of resonant elements onto the backside of the sample.

Chapter 7

Broadband reflectarray with parallel elliptical dipoles

A Resonant element consisting of three parallel elliptical dipoles is proposed for the design of a broadband reflectarray at 1 THz. The phase response of the proposed radiating element is reasonably linear over a wide frequency range. A subarray composed of 4 radiating elements with a progressive phase change is configured to deflect a normally incident plane wave into a predesigned direction. The numerically simulated field distributions and radiation patterns at different frequencies in the terahertz range demonstrate that the designed reflectarray can perform as expected in a wide frequency band.

7.1 Introduction

As illustrated in the previous chapters, reflectarray antennas combine the advantages of high efficiency of reflectors and flat profile of phase arrays. Without a complicated feeding network, various accurate contour beam shapes with low loss have been formed by reflectarrays across the electromagnetic spectrum (Huang and Encinar 2008, Gianvittorio and Rahmat-Samii 2006, Carrasco *et al.* 2013b, Niu *et al.* 2014c, Nayeri *et al.* 2014, Zou *et al.* 2013, Yang *et al.* 2014). Despite these advantages, the inherent characteristic of narrow bandwidth is associated with most reflectarray configurations. Primarily, two factors determine the bandwidth of reflectarrays: the bandwidth of the radiating elements and the differential spatial phase delay resulting from different path lengths from the feed to each element (Huang and Encinar 2008). For an ideal plane wave or a collimated beam excitation as commonly used at terahertz frequencies, only the first factor determines the bandwidth performance of the reflectarray, and typically limits the fractional bandwidth to around 5%. As shown in Fig. 7.1(a), the phase response of a typical narrow-band radiating element does not linearly change with the variation of a geometrical dimension at an operation frequency, while the phase response curves at different frequencies are not parallel to each other. For an ideal case, broadband means that the phase response as a function of one geometrical dimension of the radiating resonator is perfectly linear. When the operation frequency deviates from the designed value, the phase curves have a constant gradient to the variation of the frequency in a wide range, i.e. curves are parallel to each other as shown in Fig. 7.1(b). In practical design, many techniques have been developed to achieve nearly linear phase response to overcome the bandwidth limitation of the radiating elements, such as using a thick substrate, stacked patches in a multilayered configuration (Encinar 2001, Encinar and Zornoza 2003), and multi-loops with different shapes in a single layer (Chaharmir *et al.* 2009, Chaharmir *et al.* 2010). The method of using thick substrate reduces the phase range of the radiating element while multilayered structures are very challenging for fabrication particularly at high frequencies beyond the millimetre-wave range. A strategy of multi-resonant dipoles arranged in a single layer with a linear phase response can be adopted to the design of broadband reflectarrays, as demonstrated in the microwave range (Li *et al.* 2009, Florencio *et al.* 2014).

In the present chapter, a new type of unit cell with three parallel elliptical dipoles is presented and numerically validated for constructing a broadband reflectarray operating in the terahertz range. A preliminary design employs the configuration of the

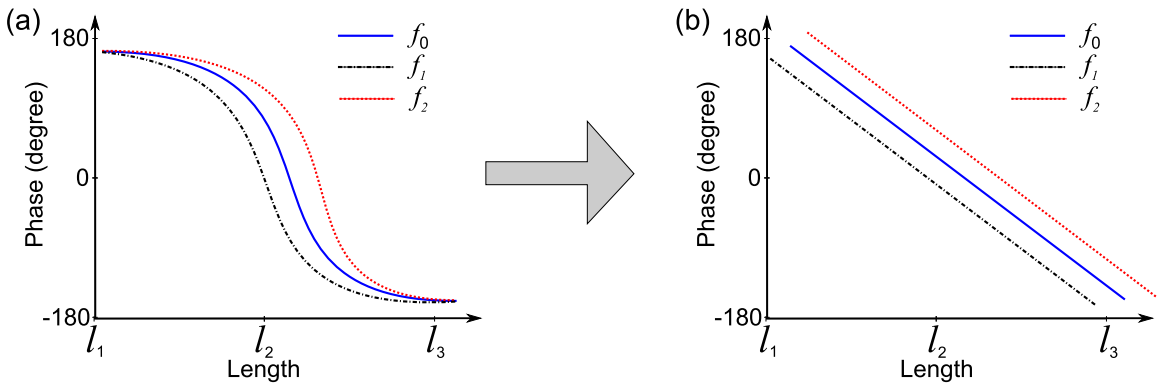

Figure 7.1. Schematic showing the phase characteristic of a reflectarray with broad bandwidth. (a) Nonlinear phase responses of a narrow-band radiating element. (b) Linear phase curves parallel to each other at different frequencies indicate that the radiating element can be used to configure a broadband reflectarray.

three elliptical dipoles with a fixed length ratio. With the proposed radiating element, a smooth and nearly linear phase response with acceptable loss and an adequate phase range covering over 300° is achieved. A subarray is then configured based on these elements, and the simulated field distributions and radiation patterns of a deflecting reflectarray are verified at different frequencies. In order to further improve the performance of the proposed structure, in the second design, lengths of these three parallel elliptical dipoles are not fixed but vary independently, and a phase response profile is obtained based on the simulation with variation of the lengths of the central and side dipoles. This phase response profile offers a constant phase gradient over a wide frequency range. Correspondingly, the performance of the reflectarray is improved, which is verified by numerical simulations.

7.2 The preliminary broadband design

Owing to the multi-resonance effect, a much linear phase response have been achieved by using three parallel rectangular dipoles, i.e. a main dipole and two parasitic dipoles (Li *et al.* 2009). Inspired by this work and considering the inherent broadband characteristic of elliptical dipoles comparing to rectangular dipoles, Li *et al.*'s design can be improved by replacing the rectangular dipoles with elliptical dipoles for a better performance (Niu *et al.* 2015b). Numerical investigation of the proposed radiating element and a wideband reflectarray is given in the following subsections.

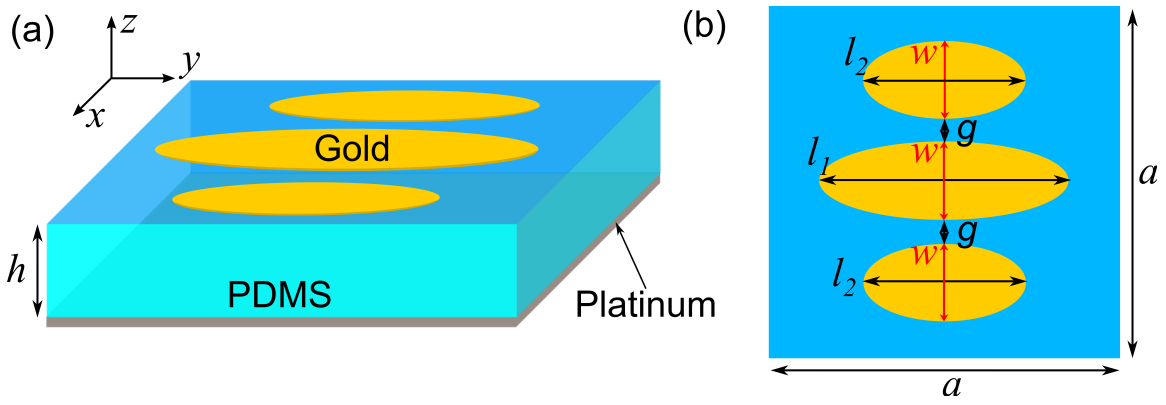

Figure 7.2. Schematic diagram of the radiating element with 3 parallel elliptical dipoles. (a) Perspective view and (b) top view of the unit cell. The dimensions are $a = 140\,\mu\text{m}$, $h = 40\,\mu\text{m}$, minor axis of the elliptical dipoles $w = 30\,\mu\text{m}$, the ratio of major axes $r = l_2/l_1 = 0.65$, and the gap $g = 10\,\mu\text{m}$.

7.2.1 Analysis of the unit cell

The structure of the proposed unit cell for broadband reflectarray is shown in Fig. 7.2. A set of three parallel elliptical gold dipoles is located on the top layer as the radiating element, and a substrate made of polydimethylsiloxane (PDMS) plays the role of the dielectric spacer while the bottom ground plane is made of platinum. The parameters of these materials for simulation at 1 THz are: surface impedance of gold $Z_{\text{Au}} = 0.287 + j0.335\,\Omega/\text{sq}$, surface impedance of platinum $Z_{\text{Pt}} = 0.628 + j0.667\,\Omega/\text{sq}$, the relative permittivity and loss tangent of PDMS $\epsilon_r = 2.35$ and $\tan\delta = 0.06$, respectively. To simplify the design process, the three elliptical dipoles are set to have the same minor axis lengths of $w = 30\,\mu\text{m}$, and the ratio of the side to central dipole lengths is fixed at $r = l_2/l_1 = 0.65$ (Li *et al.* 2009) while the gap between the neighbour dipoles is set to $g = 10\,\mu\text{m}$. For the incident wave polarised in the y direction parallel to the major axes of the dipoles, different phase responses can be achieved by varying the dipole length. With these conditions, the simulated phase and magnitude responses of a infinite uniform array is obtained as a function of the length l_1 as shown in Fig. 7.3. A reasonably linear phase response with slow variation and sufficient range of over 300° is achieved with an acceptable reflection efficiency for the proposed radiating element. Furthermore, in comparison to their counterpart rectangular dipoles, the elliptical dipoles show a relatively lower loss while the rectangular dipoles provides a wider phase range. The higher loss of the rectangular dipoles is caused by the stronger multi-resonance response and mutual coupling between the dipoles. Within

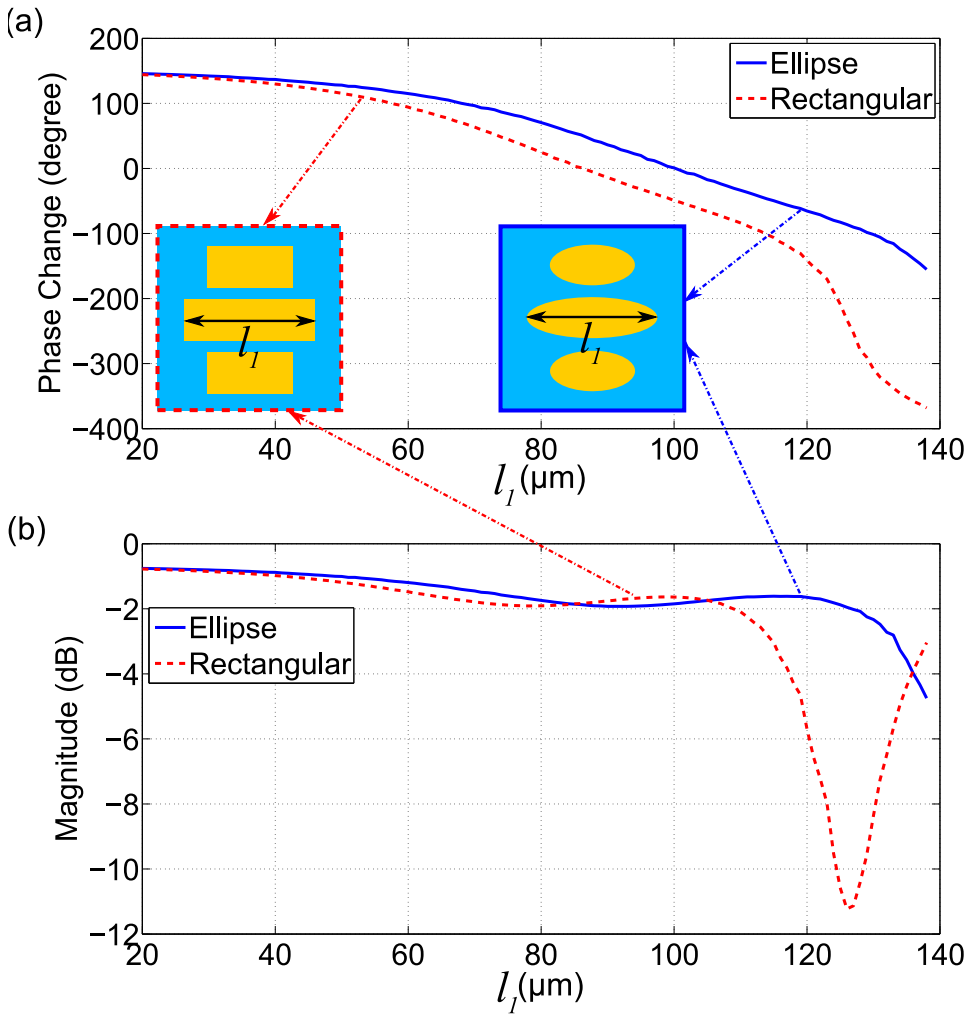

Figure 7.3. Simulated reflection response for the structure shown in Fig. 7.2 at 1 THz as a function of the length l_1. (a) Phase response and (b) magnitude response of the element with elliptical dipoles (blue solid line) and rectangular dipoles (red dashed line). The length and width of the rectangular dipoles are the same to the lengths of the major and minor axes of the elliptical dipoles, respectively. It is noted that the side dipoles maintain the aspect ratio $r = l_2/l_1 = 0.65$.

a wide enough phase range of over 300°, the element with elliptical dipoles offers the possibility of configuring a broadband reflectarray to achieve a higher efficiency.

In addition, the performance of the unit cell with three elliptical dipoles at different frequencies is studied and the corresponding results are given in Fig. 7.4. When the operation frequency deviates ±10% (corresponding to 20% functional bandwidth) from the designed 1 THz, i.e. 0.9 THz at the lower side and 1.1 THz at the higher side, the phase curves remain nearly linear, and are almost parallel to each other except for a diverging behaviour at 1.1 THz when the dipole length is longer than 125 μm. The steep slope of

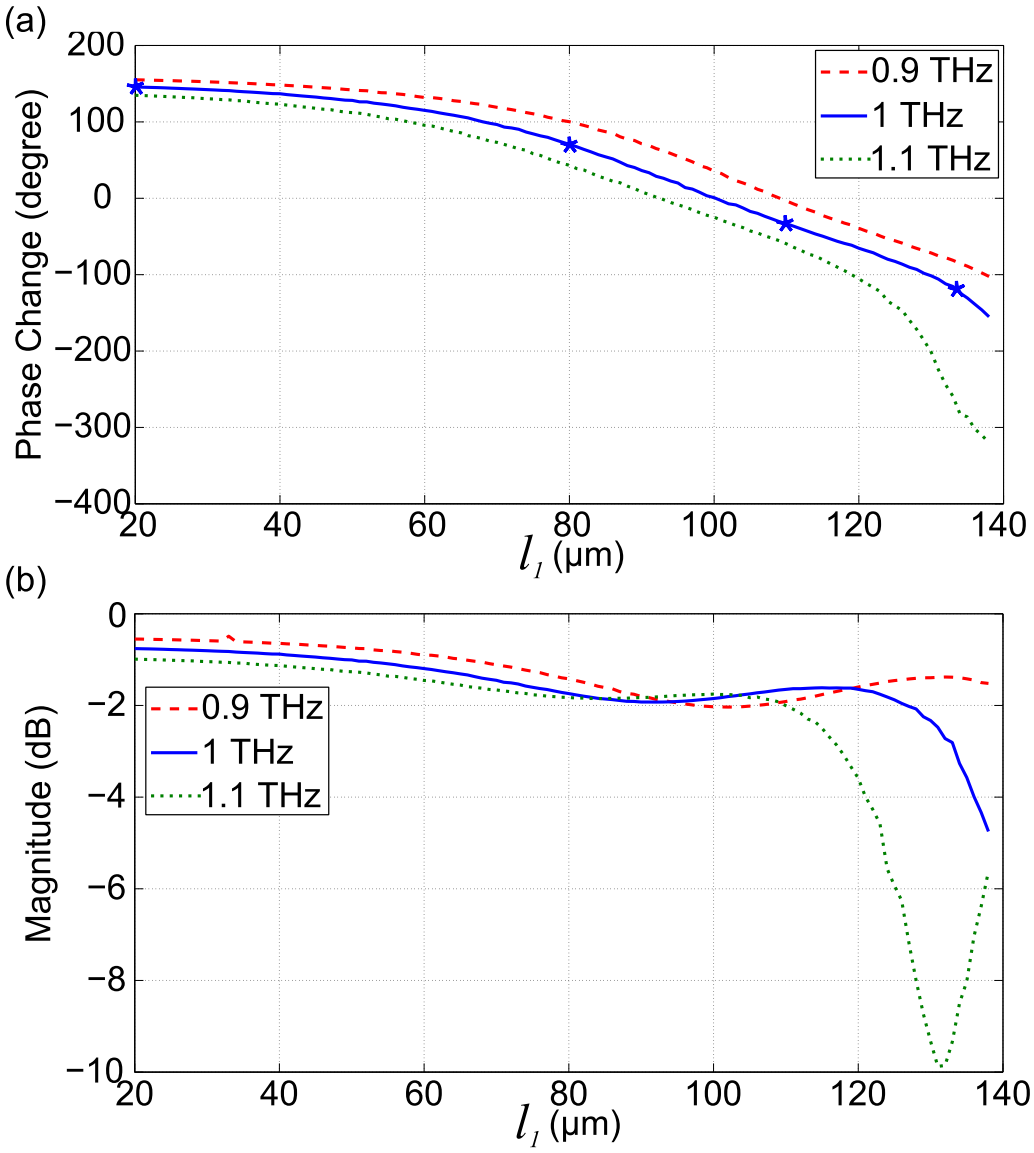

Figure 7.4. Simulated reflection response of the unit cell with the elliptical dipoles at different frequencies as a function of the length l_1. The 4 blue marks on the phase curve for 1 THz indicate the selected dipole lengths to define a subarray that completes one full cycle phase change.

the phase curve for $l_1 > 125$ μm at 1.1 THz is caused by a strong multiresonance of the three dipoles, which is confirmed by the corresponding magnitude curve in Fig. 7.4(b). Nevertheless, from this result, it is promising to design a reflectarray with a desired bandwidth close to 20%.

7.2.2 Design and performance of the reflectarray

As a proof-of-concept, a reflectarray with a progressive phase ramp is designed for deflection of the beam to a predefined direction. A subarray with 4 radiating elements is configured according to the phase response shown in Fig. 7.4 at 1 THz, and the deflection angle for the TM polarised (along the y axis) normal incidence is therefore designed at 32.4° according to the formula

$$\theta = \arcsin\left(\frac{\Delta\phi\lambda_0}{2\pi a}\right), \tag{7.1}$$

where $\Delta\phi = 90°$ is the progressive phase change for the subarray with 4 elements and $\lambda = 300\,\mu\text{m}$, $a = 140\,\mu\text{m}$. The layout of the subarray is shown in Fig. 7.5(d), where the dipole lengths l_1 are 20 µm, 80 µm, 109 µm and 135 µm from left to right. The simulated scattered field distributions at 1 THz is demonstrated in Fig. 7.5(b), and the corresponding radiation pattern for a sample with 360 × 90 subarrays (equivalent to the total array dimensions of 50.4 mm × 50.4 mm) is given in Fig. 7.5(e) (blue solid line). It is clear that the normally incident plane wave is predominantly deflected into the predefined direction. In order to verify the bandwidth of the reflectarray, simulation results at different frequencies are also presented. It is found that the reflectarray can maintain acceptable performance within the frequency range from 0.85 THz to 1.06 THz. The simulated scattered field distributions at these two frequencies are given in Fig. 7.5(a) (0.85 THz) and Fig. 7.5(c) (1.06 THz) while the radiation patterns are represented in Fig. 7.5(e) with the red dashed line for 0.85 THz and green dotted line for 1.06 THz. The flat wavefronts and the radiation pattern with over 10 dB difference between the main deflection lobe and the maximum side lobe (including specular reflection) indicate that the designed terahertz reflectarray can efficiently deflect the TM polarised normally incident waves. Scanning of the deflection angle is observed with frequency due to the phenomenon of beam squint (Targonski and Pozar 1996). When the frequency increased up over 1.1 THz, the first side lobe increases to the level that is almost equal to the main lobe, while the specular reflections dominate the scattered field at the frequencies lower than 0.85 THz.

7.3 Improved design

For the structure shown in Fig. 7.2, it is possible to achieve a more linear phase response with a 360° phase range if the major axis lengths of the central and the side

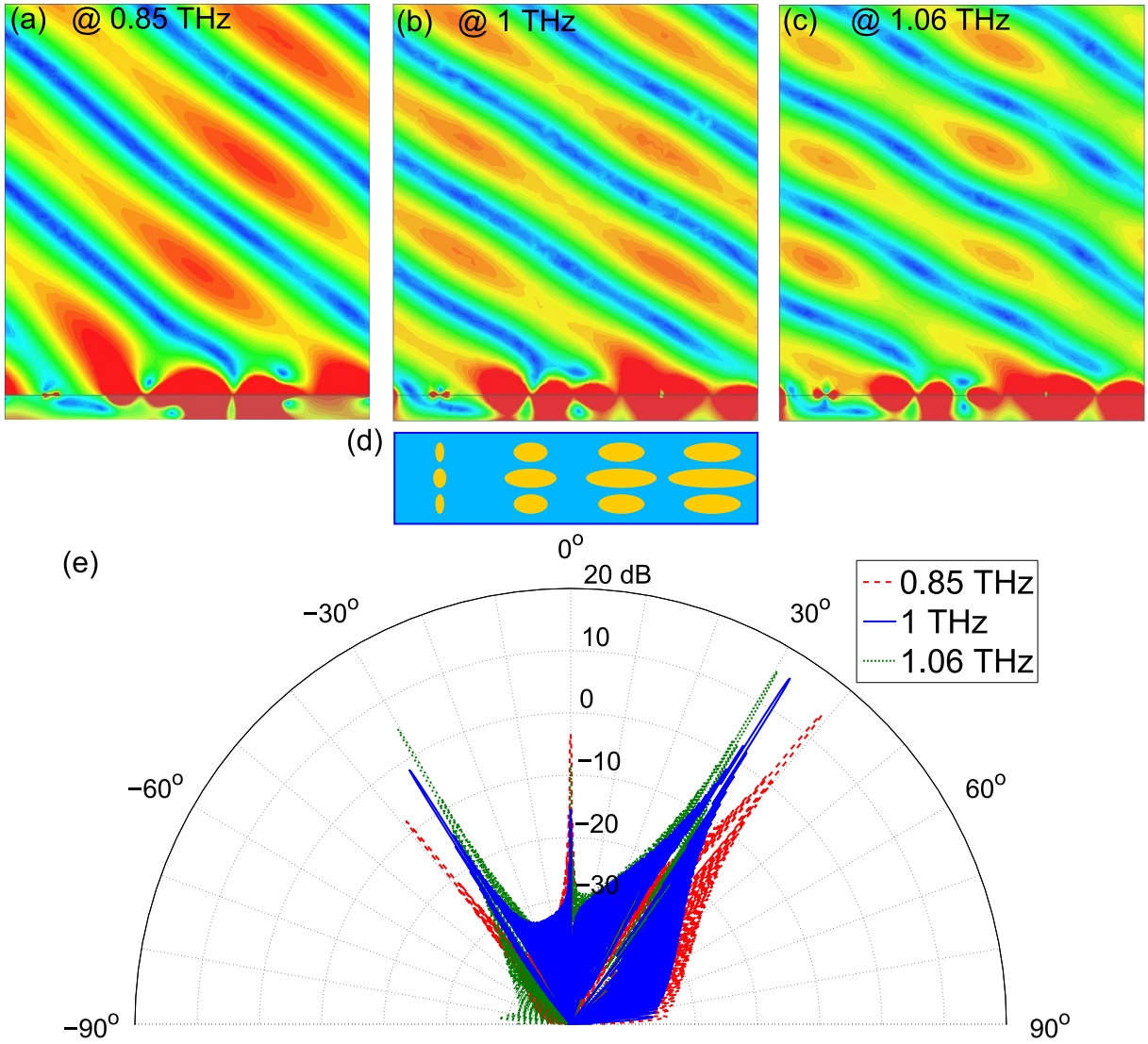

Figure 7.5. Simulated instantaneous scattered field distributions and radiation patterns of the designed broadband reflectarray at different frequencies with the TM incident plane waves. (a), (b) and (c) the scattered fields of the 2D infinite reflectarray composed of the subarray (d) at 0.85 THz, 1 THz and 1.06 THz, respectively. (e) The simulated radiation patterns of the sample with 90×360 subarrays at 0.85 THz (red dashed line), 1 THz (blue solid line) and 1.06 THz (green dotted line).

dipoles vary independently. In this section, the dimensions of the unit cell and the minor axis lengths of the three elliptical dipoles are set the same as in the previous design. However, the major axis lengths l_1 and l_2 are independently varied for a more linear and smoother phase response. The unit cell is optimized first, followed by the numerically simulated performance of the designed broadband reflectarray.

7.3.1 Optimization of the radiating element

The main design of the radiating element shown in Fig. 7.2 is untouched, i.e. the size of the element $a = 140\,\mu m$ and $h = 40\,\mu m$, as well as the minor axis lengths of $w = 30\,\mu m$ and the gap of $g = 10\,\mu m$ between the neighbor elliptical dipoles. Here the major axis lengths of the centre dipole l_1 and of the side dipoles l_2 are varied independently. For the incident wave polarised in the y axis direction (corresponding to the TM polarisation with the E field component parallel to the major axes of the dipoles), the phase and magnitude response profiles are obtained by simulations with periodic boundary conditions and Floquet port excitation at 1 THz. As shown in Fig. 7.6, when the length of the side dipoles l_2 is smaller than $90\,\mu m$ while the length of the central dipole l_1 increases from $20\,\mu m$ to $138\,\mu m$, the resonance is mainly induced by the central dipole and a phase range over 250° can be achieved by varying the length of the central dipole. However, when l_2 increases to a value within the range between $90\,\mu m$ and $110\,\mu m$, the resonance is dominated by the length of the side dipoles. Especially, when l_2 increases over $120\,\mu m$, multi-resonance of the three dipoles happens, and the strong resonance leads to steep phase gradients and high resonance losses, which are illustrated by the navy blue areas in Figs. 7.6(a) and (b), respectively. For l_2 larger than $110\,\mu m$, variation of l_1 has little effect on the phase responses of the radiating element.

Based on the phase and magnitude response profiles shown in Fig. 7.6, a linear phase curve with a reasonable loss can be obtained in such a way that the phase change linearly decreases from the maximum value as the function of the central dipole length l_1. In this strategy, in order to avoid the high loss caused by multi-resonance of the three dipoles, the length of the side dipoles l_2 is chosen to be smaller than $90\,\mu m$. From the phase map illustrated in Fig. 7.6(a), it can be found that, with an linear increase in the dipole length l_1, the phase value is decreased with a nearly constant gradient provided that the length of the side dipoles l_2 varies as the function of l_1 according to the piecewise linear function relation:

$$l_2 = \begin{cases} 2l_1 - 14\,\mu m & \text{if } 20\,\mu m \le l_1 \le 32\,\mu m, \\ l_1 + 18\,\mu m & \text{if } 32\,\mu m \le l_1 \le 44\,\mu m, \\ l_1/2 + 40\,\mu m & \text{if } 44\,\mu m \le l_1 \le 100\,\mu m, \\ 90\,\mu m & \text{if } 100\,\mu m \le l_{1,2} \le 138\,\mu m. \end{cases} \tag{7.2}$$

These linear functions are illustrated as the solid lines in Fig. 7.6. With this varying relation, the numerically resolved reflection phase and magnitude response curves as the

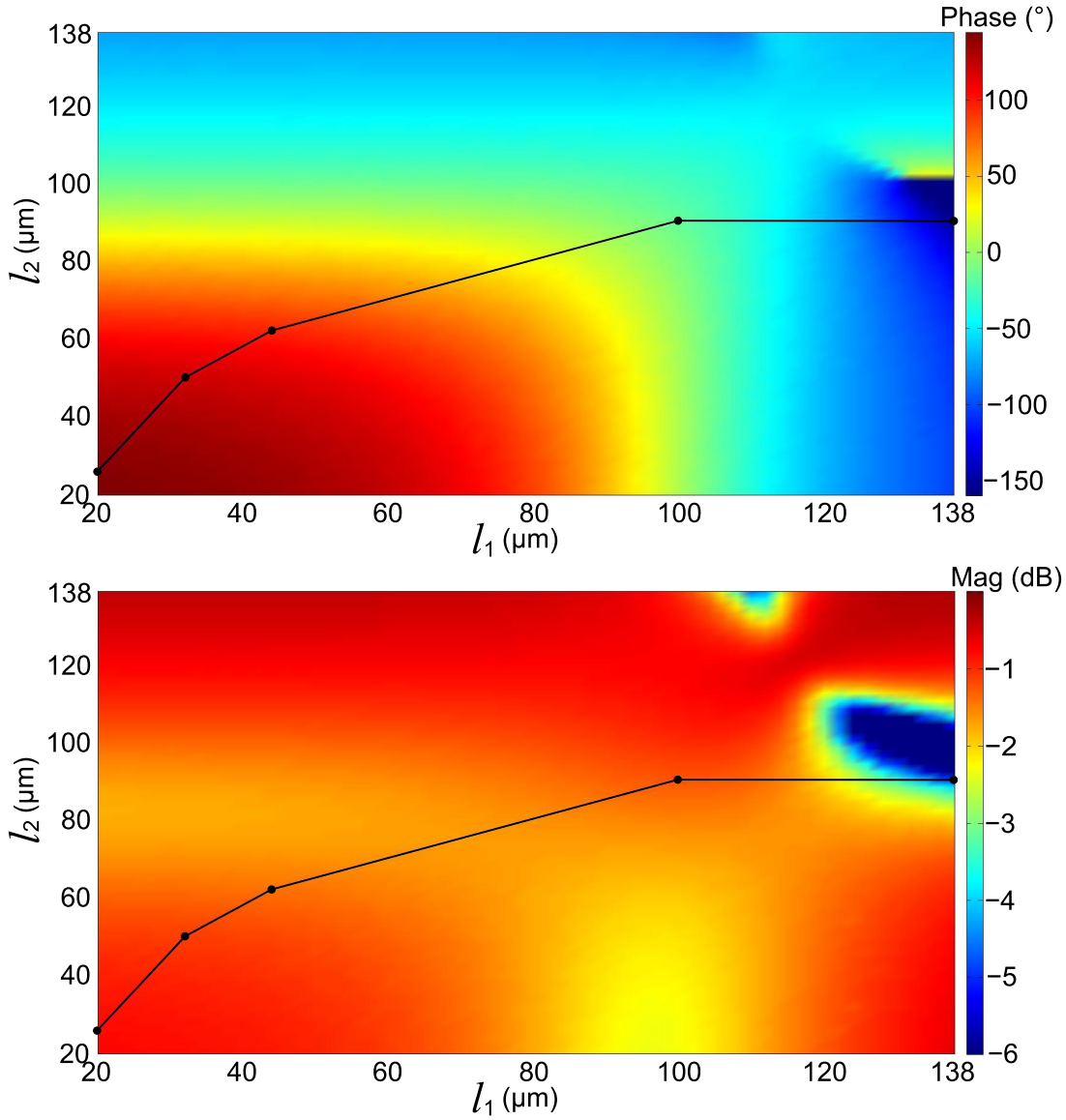

Figure 7.6. Simulated phase and magnitude response profiles of the unit cell for the TM polarisation at 1 THz. (a) Phase and (b) magnitude response for the radiating element shown in Fig. 7.2 as a function of the lengths of the central dipole l_1 and the side dipoles l_2. The graphs show the selected lengths of the dipoles to achieve a smooth and wide phase response with high efficiency. The lines correspond to the relation given in Eq. 7.2.

function of the central dipole length l_1 are given in Figs. 7.7(a) and (b) with solid blue lines, respectively. From the results, it is observed that a nearly linear phase change of over 300° is achieved, while the highest loss on resonance is around 4.8 dB at 1 THz. Comparing to the phase curve of the three parallel dipoles with the fixed length ratio shown in Fig. 7.3, the optimized design with the length relation described by Eq. 7.2 significantly improves the phase response performance while the magnitude response

remains similar, which means that a broadband reflectarray with improved performance can be expected. In order to verify the performance of the unit cell in terms of bandwidth, simulations at different frequencies are taken on the same structure, and the corresponding results are shown in Fig. 7.7. When the operation frequency deviates from the designed 1 THz to 0.85 THz at the lower side and 1.05 THz at the higher side, the phase curves remain nearly linear, and are almost parallel to each other. From this result, a reflectarray with a desired bandwidth of 20% can be designed.

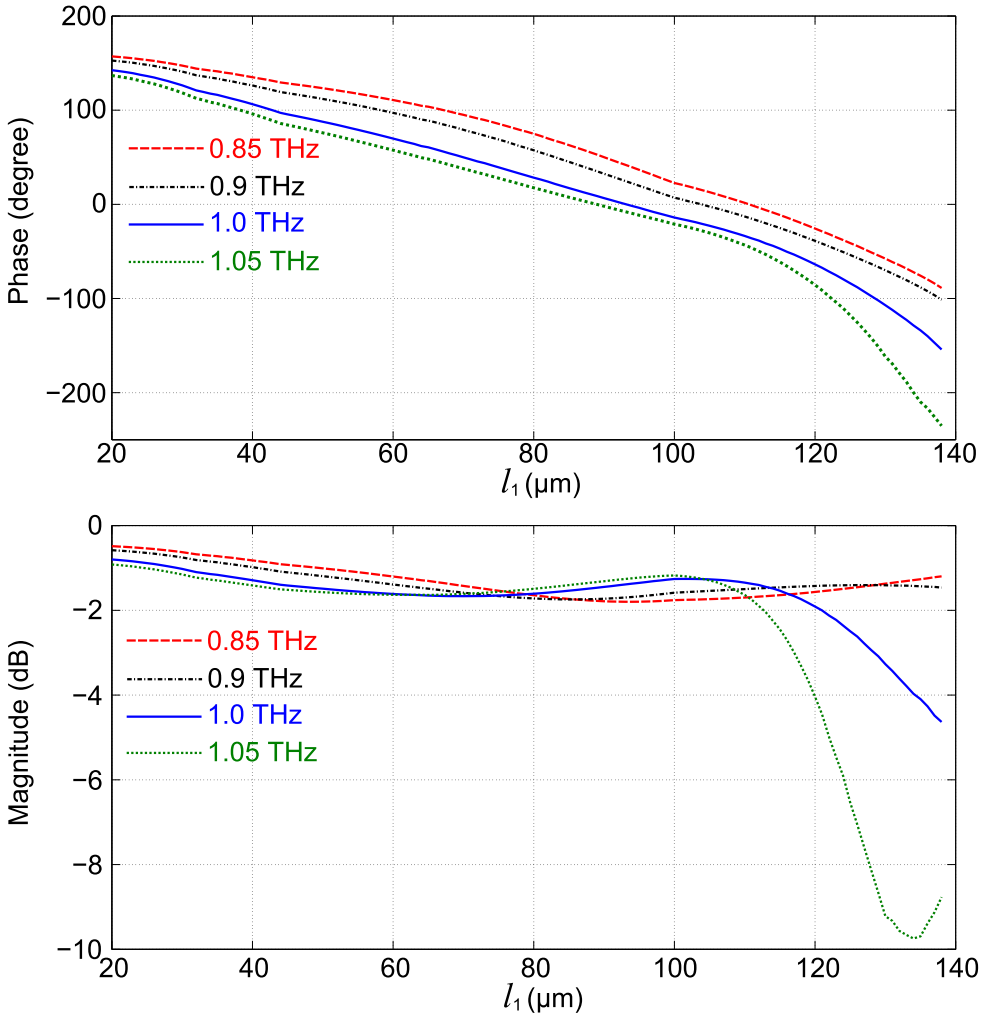

Figure 7.7. Simulated complex reflection coefficients for uniform infinite array at different frequencies. (a) Reflection phase response in degrees. (b) Reflection magnitude in dB as a function of the length of the central dipole l_1.

Table 7.1. Dimensions of the elliptical dipoles for the optimized subarray. The units are in μm.

Element	1	2	3	4
l_1 (Central dipole)	22	70	113	134
l_2 (Side dipoles)	30	75	90	90

7.3.2 Performance of the broadband reflectarray

Based on the phase curve shown in Fig. 7.7, a subarray composed of 4 elements with a progressive phase change of 90° is configured. The lengths of the central and side elliptical dipoles for each elements are given in Table 7.1. It is noted that the side elliptical dipoles can be longer than the central dipole. With the periodic boundary conditions, the simulated instantaneous scattered field distributions depicting the response of the broadband reflectarray illuminated by a normally incident plane wave at three different frequencies are demonstrated in Fig. 7.8. At the designed frequency of 1 THz, the incident plane wave is strongly deflected into the designed direction of 32.4° with flat wavefronts. When the operation frequency deviates from 1 THz to a frequency range from 0.85 THz to 1.05 THz, the scattered field distributions still clearly show that the incident plane waves with the TM polarisation can be efficiently deflected into the directions off the specular reflection. The simulated radiation patterns of the reflectarray consisted of 360 × 90 subarrays at 0.85 THz, 1 THz and 1.05 THz are given in Fig. 7.9. From the radiation patterns, it is obvious that the major deflection lobe in the tested frequency range is maintained at a stable level when the operation frequency is varied. The results further verify that the designed reflectarray can efficiently deflect the incident plane wave into a direction away from the specular direction in a bandwith at least of 20%. Moreover, comparing to the preliminary reflectarray design presented in the previous section (Sec. 7.2), the improved design holds the potential of broader bandwidth and higher efficiency. Because of the phenomenon of beam squint, the deflection scans in a angular range with variation in operation frequency. This phenomenon can be either used for beam scanning controlled by frequency (Rodrigo *et al.* 2013, Li *et al.* 2014) or eliminated by using offset feedings (Targonski and Pozar 1996, Almajali *et al.* 2013).

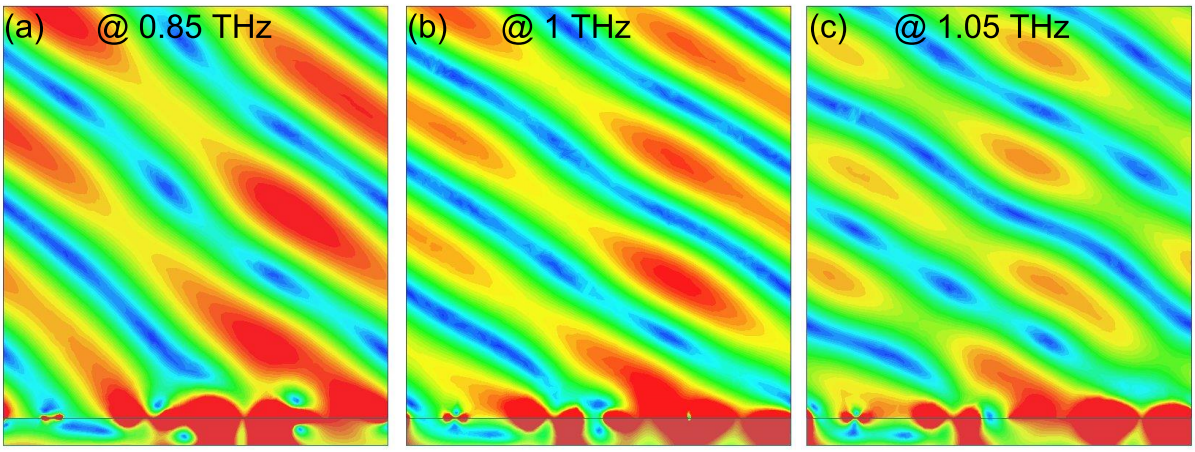

Figure 7.8. Simulated instantaneous scattered field distributions of the optimized broadband reflectarray at different frequencies for TM incident plane waves. (a), (b) and (c) the scattered fields of the 2D infinite reflectarray composed of the subarrays at 0.85 THz, 1 THz and 1.05 THz, respectively.

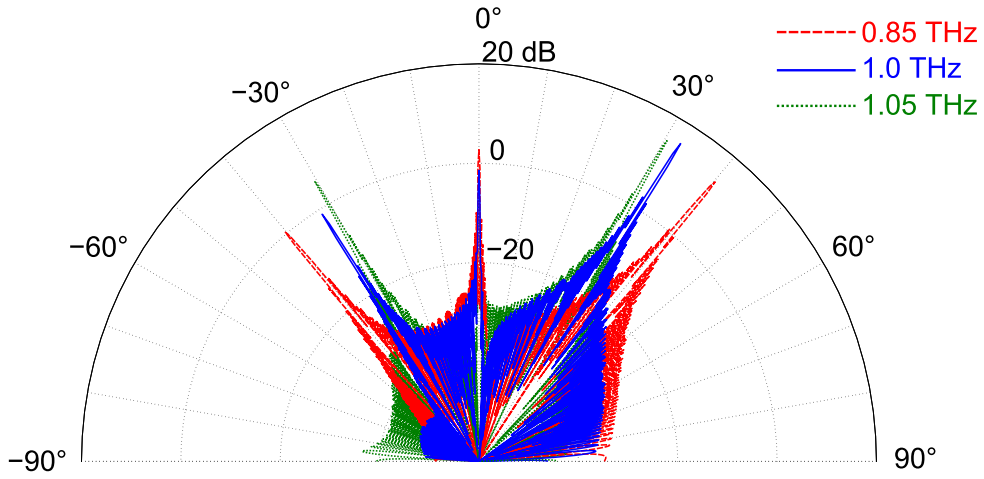

Figure 7.9. Simulated radiation patterns of the optimized broadband reflectarray at different frequencies with the TM incident plane waves. The simulated radiation patterns of the sample with 90×360 subarrays at 0.85 THz (red dashed line), 1 THz (blue solid line) and 1.05 THz (green dotted line).

7.4 Conclusion

A resonant element with three parallel elliptical dipoles has been proposed for designing a broadband terahertz reflectarray. The reflection response of the unit cell and the performance of the reflectarray have been observed through simulations. Comparing with its counterpart with three parallel rectangular dipoles, the radiating element with three parallel elliptical dipoles proposed here shows a similarly linear phase response, but lower average loss within the same phase range. Furthermore, an optimised design

has been obtained by varying the length of the central and side dipole independently. The simulated phase and magnitude responses show that the optimized structures can offer a more linear phase curve. Therefore the reflectarray is expected to operate with higher efficiency. The scattered field distributions and the radiation patterns of the reflectarray confirm that the proposed structure can offer a fractional bandwidth of over 20% with a 10 dB difference between the main deflection and the maximum sidelobes for the TM incident polarisation. The simulated 3 dB bandwidth for the maximum gain for the main deflection is even broader than 20%. For example, at 1.1 THz, the deflection gain drops by 2.5 dB, but the maximum side lobe is 8 dB lower than the main deflection and the scattered wavefront does not appear very flat anymore. The definition of the bandwidth with 10 dB difference between the main deflection and the maximum side lobe, as chosen in the present work, is thus in this case stricter than 3 dB bandwidth for the maximum gain for the main deflection. The observed beam squint suggests an application of terahertz beam scanning controlled by the operation frequency. For other applications requiring a fixed deflection direction regardless of the operation frequency, beam squint can be undermined or even eliminated by using offset feedings. As an extension, the orthogonal triangular lattice arrangement demonstrated in Chapter 5 can be used to make the reflectarray work for the both polarisations at a wide frequency range.

The experimental validation of the reflectarrays presented in previous chapters of the thesis gives good confidence that the measurement results will match the predictions from simulations.

Chapter 8

Thesis summary and conclusions

THIS chapter summarises and concludes the work in this thesis. Chapters 1 to 3 have reviewed materials that cover background of terahertz radiation, techniques for terahertz beamforming, and fundamental theories for designing reflectarrays. Chapters 4 to 7 have described the original contributions to the design and realisation of reflectarrays for terahertz beam deflection, beam splitting, and broadband operation.

8.1 Thesis conclusion

With unique capabilities, terahertz radiation has attracted research interests in numerous areas such as ultra-broadband indoor wireless communications, high-resolution imaging and high-sensitivity stand-off detection. With the gradual maturation of terahertz solid-state sources and detectors, terahertz beamforming components with compact profile and high efficiency are becoming increasingly indispensable for extending terahertz systems to broader application areas. Various techniques of diffraction gratings, leaky-wave antennas, phased arrays, and reflectarrays have been proposed for terahertz beamforming. Periodic and chirped diffraction gratings can be used for both transmissive and reflective beamforming in the region around broadside, while waves radiated from a leaky-wave antenna can be patterned in a wide angular range extending from back end-fire through broadside to front end-fire. Phased arrays integrated with programmable phase shifters theoretically hold great potential for arbitrarily controlling beamforming. However, unaffordable losses and strict fabrication tolerance have challenged the development of these beamforming techniques in the terahertz regime. On the other hand, the concept of reflectarray which bypasses the complicated feeding network has been proposed to form a desired far-field radiation pattern based on reradiating resonators at a desired terahertz frequency.

The aim of this thesis was to design and realise terahertz reflectarrays based on conventional metal-substrate resonance for forming various desired radiation patterns in far-field. In this thesis it has been demonstrated that advanced micro-scale manufacturability with strict tolerances can be utilised for fabricating reflectarrays with high design versatility towards functional terahertz beamforming. The following provides a summary and conclusions on the original contributions and results of three major parts of the thesis.

8.1.1 Part I: Terahertz reflectarrays for beam deflection

The first major part of the thesis contains Chapter 4 that involves the design and realisation of a reflectarray with gold square patch resonators for terahertz beam deflection.

Background: Reflectarrays have been successfully applied in the microwave regime due to their advantages of flat profile and high efficiency. In the terahertz frequency range, the concept of reflectarray is a promising alternative for designing beamforming components for terahertz communication and imaging systems. However, challenges

in manufacturability of samples with micro-scale cells and measurement of the sample with terahertz systems have up to date hindered the development of reflectarrays in this rapidly evolving frequency range. It is worthy to verify that the methodology of designing reflectarrays based on the conventional metal-substrate resonance can be adapted and extended in the terahertz regime. Furthermore, it is necessary to confirm that the THz-TDS system can be used to measure the radiation characteristics of a reflectarray.

Methodology: By adopting a similar design principle for designing reflectarrays as in the microwave frequency range, micro-scale square gold patch resonators mounted on a dielectric spacer are employed as the radiating elements for constructing a terahertz reflectarray. The chosen function of the demonstrated reflectarray is to efficiently deflect the incident beams into a predesigned direction away from specular reflection with polarisation independence. At 1 THz, the metal used for radiating resonators and ground plane is described with the surface impedance from a Drude model. By varying the size of the square patch, the numerically resolved phase response with a wide enough phase range can be obtained for designing a subarray with a wrapped progressive phase distribution. The reflectarray with the periodically arranged subarrays has been configured and then fabricated.

Results: The simulated field distributions of subarrays and the measured radiation patterns of the fabricated prototype have demonstrated that the designed reflectarray can efficiently deflect the normal incident waves with the TE and TM polarisations into the same predesigned direction with high polarisation purity at the predefined operation frequency. The slight deviation of the measurement results from the theoretical expectations suggests that the fabrication tolerance and the dependence on the incident angle should be taken into consideration in optimising reflectarrays. In addition, due to an imbalance response of each patch in the TE polarisation, the deflection efficiency for the TE polarised waves is slightly lower than that for the TM polarisation.

Original contribution: For the first time, a beam-deflection reflectarray with micro-scale metal radiating resonators has been realised in the terahertz regime with experimental validation performed with a THz-TDS system. Specific technological challenges in micro-scale manufacturability and unconventional measurement setup have been addressed in the realisation and verification of the functional terahertz reflectarray. These aspects represent novel contributions in the terahertz and antenna communities. The potential reflectarray function is not limited to the demonstrated beam

deflection, but also can be extended to various versatile beamforming applications owing to the capability of manipulating terahertz beams with high efficiency yet low design and fabrication complexity. This work opens the possibility of realising terahertz reflectarrays with a conventional operation principle based on metal-substrate resonance. From this stage, various reflectarrays with versatile design strategies can be expected for functional terahertz beamforming.

8.1.2 Part II: Terahertz reflectarrays for beam splitting

The second major part of the thesis encompasses Chapter 5 and 6 that focus on the design and realisation of reflectarrays for terahertz beam splitting.

Background: Splitting beams with polarisation-dependent properties is an important functionality in applications requiring high polarisation purity or polarisation-dependent multiplexing/demultiplexing. In the terahertz regime, due to lack of suitable naturally birefringent materials and because of high intrinsic material loss, devices that can split the incident waves with polarisation-dependent properties still remain challenging to realise. Reflectarrays with high deflection efficiency offer the possibility of beam splitting for the terahertz radiation, where the directions of the split beams can be controlled by tailoring the dimensions of each radiating element configured by a specific strategy.

Methodology: The capability of reflectarray to split the incident waves either by reflectively deflecting the orthogonal incident components backwards into two different directions or by reflectively deflecting one polarisation component and normally transmitting the other orthogonal component has been demonstrated. For bidirectional reflective deflections, two sets of orthogonal strip dipoles arranged into interlaced triangular lattices over a solid full ground plane have been employed. By independently configuring the dimensions of the dipoles of each set, deflection directions for the TE and TM polarised beams can be arbitrarily controlled. For the functionality combining the reflective deflection and the normal transmission, thin-film wire grids have been introduced in the design for both the radiating resonators and the ground plane. With this strategy, the structure reflectively deflects the polarisation component parallel to the strips into the predesigned direction, and normally transmits the other polarisation that orthogonal to the strips.

Results: The reflectarrays designed with the both strategies have been numerically simulated and then experimentally measured. At the designed operation frequency, the prototype for bidirectional reflective deflection was shown to exhibit around 80% deflection magnitude for the TM polarisation, and 75% the TE polarisation, the two polarisations being designed with opposite deflection directions. A similar function of terahertz beam splitting has been achieved by a second reflectarray composed of thin-film wire grids. For this sample, the TE polarised waves are reflectively deflected backwards to a predesigned angle while the TM polarised waves are normally transmitted through the structure with high efficiency. These two samples were demonstrated to exhibit polarisation-dependent beam splitting with a high polarisation purity.

Original contribution: For the first time, the functionality of beam splitting is achieved by using single-layered reflectarrays in the terahertz regime. The interlaced triangular lattice of the orthogonally arranged strip dipoles functioning as radiating elements is one highlight of the design of the bidirectional deflection reflectarray, while the novelty of the reflectarray made of thin-film wire grids is to achieve the combined functionality of deflective reflectarray and transmissive polariser. The first design expands possible functions that reflectarrays can achieve, and the design strategy can be extended to other frequency ranges for beam splitting. The second reflectarray creatively uses a layer of continuous wire grid rather than the conventional solid full metal as its ground plane. The continuous wire grid functions as a reflective ground plane for one polarisation and a wire-grid polariser for the other orthogonal polarisation, which have never been demonstrated before in a reflectarray configuration. The design strategy with wire grids for both radiating resonator and ground plane, along with the presence of the stretchable substrate, makes conformal applications and beam steering by mechanical stretching a real possibility. This novel design concept can be adopted to other frequency ranges for polarisation sensitive beamforming and conformal antenna applications. The two reflectarrays hold the potential for constructing components for polarisation discrimination and polarisation demultiplexing for terahertz communications. A common limitation of these two designs is the narrow bandwidth, and it is also the intrinsic drawback of reflectarrays. Multi-layered structures have been demonstrated for broadband operation. However, this is not suitable for terahertz reflectarrays due to challenges in layer-alignment during fabrication. The strategy of single layer radiating element with several parallel resonators based on multi-resonance can be an alternative for broadening bandwidth in the terahertz regime. This anticipation has been numerically verified in the next contribution.

8.1.3 Part III: Design of a broadband terahertz reflectarray

In terms of the broadband design of the reflectarrays, the third major part of the thesis referring to Chapter 7 proposes a novel structure for terahertz reflectarrays offering a bandwidth of over 20%.

Background: Despite the advantages of compact structure and high efficiency, most reflectarray configurations suffer the inherent drawback of narrow bandwidth. Primarily, for an ideal plane wave or a collimated beam excitation as commonly used at terahertz frequencies, the bandwidth of the radiating elements determines the bandwidth performance of the reflectarray. Multi-layered structures have been used for broadening the bandwidth of the radiating elements. However, such stacked structures are very challenging for fabrication at high frequencies beyond the millimetre-wave range. The strategy utilizing multi-resonance of several dipoles arranged on a single layer is a feasible alternative for designing broadband reflectarrays at terahertz frequencies.

Methodology: Three parallel elliptical dipoles arranged on a single layer have been employed to achieve a broadband reflectarray for terahertz radiation. The lengths of these three dipoles are varied independently for obtaining a smooth and linear phase response with respect to the length of the central dipole, and therefore a broadband reflectarray can be designed based on this particular phase response. For the incident polarisation parallel to the orientation of the dipoles, the reflectarray can deflect the incident wave into a predesigned angle away the specular deflection. For the other polarisation component, the structure performs as a mirror.

Results: The designed structure has been numerically validated. By optimizing the length relations between the central and side dipoles, the simulated phase response for the TM polarisation shows a constant gradient with respect to the length variation of the central dipole at the designed operation frequency. When the operation frequency deviates from the designed value in a range of 20% around the nominal design frequency, the phase response remains linear and nearly parallel to the original design curve. The simulated field distributions and radiation patterns of the reflectarray have further verified that the designed structure dramatically improves the bandwidth to over 20% with high efficiency.

Original contribution: Parallel elliptical dipoles on a single layer are for the first time employed to improve the bandwidth of the reflectarray by utilizing the characteristic

of the multi-resonance between the dipoles. Unlike the approach using parallel rectangular dipoles with fixed length ratio, the length of the three elliptical dipoles have been varied independently, and the linear phase response has been extracted from the 2D phase profile. It has been proved that this strategy can significantly improve the bandwidth performance of the reflectarray. This strategy for broadband operation definitely can be extended to other frequency ranges and be integrated with any other radiating resonators of reflectarrays. For instance, the patch wire-grid radiating resonators for the reflectarray in the second contribution can be improved to be broadband by replacing each grating patches by three grating elliptical dipoles. Such a design can realise a broadband reflectarray that combines the polarisation-sensitive functionalities of reflective-deflection reflectarray and transmissive polariser.

8.2 Future work

All the terahertz reflectarrays presented in this thesis are built with passive radiating elements. The passive structures mean straightforward design and easy fabrication but inflexible functionality. In the applications involving active beam steering, reflectarrays with active or reconfigurable radiating elements are required. As a complement and extension of this thesis, the following objectives are the future work.

Experimental realisation of the broadband reflectarray

The broadband reflectarray with thin-film wire-grid configuration has been numerically validated with the promise of a fractional bandwidth reaching 20% with high efficiency. It is now necessary to fabricate the sample for experimental verification. Furthermore, the configuration with wire grids for flexible and stretchable structure can be adopted into the design of the broadband reflectarray, i.e., elliptical dipoles realised as wire-grids can be designed as broadband radiating resonators, together with a wire-grid ground plane. This would allow to form a conformal and stretchable broadband reflectarray.

Single-layered terahertz reflectarrays

Conventionally, a reflectarray is made of three layers: radiating resonators as the top layer, dielectric layer as the spacer and a full metal ground plane. The scattered phase

shift of each element is generated by the resonance between the metal and the dielectric. To fabricate such a stack-layered structure in the terahertz frequency range, processes of depositing, spinning, and coating are involved. Passive reflectarrays could be realised only by a layer of metal with resonant cavities. For instance, a solid metal block with drilled cylindrical holes or truncated coaxial holes can be used to achieve different phase responses by varying the depths of the hole, and therefore a single-layer full metal reflectarray composed of drilled holes with different depths could be realised. This will be the object of future investigations.

Active reflectarrays for terahertz beam steering

Reconfigurable structures for constructing reflectarrays can be achieved by introducing specific materials or components which properties can be tuned by applying external bias. For example, the conductivity of graphene can be efficiently and dynamically controlled via an external bias electric field. Based on this unique electrical property, terahertz reflectarrays with tunable graphene reflective cells have been postulated for reconfigurable-beam reflectarrays. Further materials that can offer thermally or electrically transformable properties include liquid crystal (LC), vanadium dioxide (VO_2), Ti_2O_3, and so on. These materials can be applied for reflectarrays, and a bias network for electronically tuning material properties is necessary. By changing the properties of the tunable materials, the phase response of each unit cell can be changed, and a reasonable beam steering range can be achieved with an appropriately designed structure.

8.3 Concluding statement

The terahertz reflectarrays based on metallic resonators demonstrated in this thesis offer a type of compact-profile and high-efficiency components with versatile beamforming functionality in the terahertz regime. By introducing these advanced reflectarrays into various terahertz systems, the development and commercialisation of terahertz technologies can be accelerated. Terahertz indoor wireless communications with high data rate can adopt reflectarray antennas in the ceiling or in corners of the room, supporting the aspirations towards a terahertz very-high throughput indoor wireless local area networks (WLAN) system. Similarly, specific astronomical applications of terahertz spectroscopy can benefit from such high-efficiency components. For the stand-off terahertz scanning and imaging technologies, the demonstrated reflectarrays can

be integrated into the corresponding devices for improving detection sensitivity and image resolution. This implementation will bring innovations into various application areas of medicine, pharmaceutics, or biology.

References

ABBOTT-D. (2000). Directions in terahertz technology, *IEEE 22nd Annual GaAs IC Symposium*, pp. 263–266.

AHMADI-A., GHADARGHADR-S., AND MOSALLAEI-H. (2010). An optical reflectarray nanoantenna: The concept and design, *Optics Express*, **18**(1), pp. 123–133.

AIETA-F., GENEVET-P., YU-N., KATS-M. A., GABURRO-Z., AND CAPASSO-F. (2012). Out-of-plane reflection and refraction of light by anisotropic optical antenna metasurfaces with phase discontinuities, *Nano Letters*, **12**(3), pp. 1702–1706.

AKYILDIZ-I. F., JORNET-J. M., AND HAN-C. (2014). Terahertz band: Next frontier for wireless communications, *Physical Communication*, **12**, pp. 16–32.

ALMAJALI-E., MCNAMARA-D., SHAKER-J., AND CHAHARMIR-M. R. (2013). Beam squint suppression in offset-fed reflectarrays, *IEEE Antennas and Wireless Propagation Letters*, **12**, pp. 587–590.

ALMAJALI-E., MCNAMARA-D., SHAKER-J., AND CHAHARMIR-M. R. (2014). Feed image lobes in offset-fed reflectarrays: diagnosis and solution, *IEEE Transactions on Antennas and Propagation*, **62**(1), pp. 216–227.

BAHL-I. J., AND BHARTIA-P. (1980). *Microstrip antennas*, Artech house.

BALANIS-C. (1982). *Antenna theory: analysis and design*, Harper & Row New York.

BALANIS-C. A. (1989). *Advanced engineering electromagnetics*, Vol. 20, Wiley New York.

BAYRAKTAR-O., CIVI-O. A., AND AKIN-T. (2012). Beam switching reflectarray monolithically integrated with rf mems switches, *IEEE Transactions on Antennas and Propagation*, **60**(2), pp. 854–862.

BERRY-C. W., AND JARRAHI-M. (2012). Broadband terahertz polarizing beam splitter on a polymer substrate, *Journal of Infrared, Millimeter, and Terahertz Waves*, **33**(2), pp. 127–130.

BERRY-C. W., HASHEMI-M. R., PREU-S., LU-H., GOSSARD-A. C., AND JARRAHI-M. (2014). High power terahertz generation using 1550 nm plasmonic photomixers, *Applied Physics Letters*, **105**(1), p. 011121.

BERRY-D., MALECH-R., AND KENNEDY-W. (1963). The reflectarray antenna, *IEEE Transactions on Antennas and Propagation*, **11**(6), pp. 645–651.

BIRD-T. S., WEILY-A. R., AND HANHAM-S. M. (2008). Antennas for future very-high throughput wireless lans, *IEEE International Symposium on Antennas and Propagation Society AP-S*, pp. 1–4.

BLANCHARD-P., GREENAWAY-A., HARVEY-A., AND WEBSTER-K. (1999). Coherent optical beam forming with passive millimeter-wave arrays, *Journal of Lightwave Technology*, **17**(3), p. 418.

BOOSKE-J. H. (2008). Plasma physics and related challenges of millimeter-wave-to-terahertz and high power microwave generationa), *Physics of Plasmas (1994-present)*, **15**(5), p. 055502.

BOOSKE-J. H., DOBBS-R. J., JOYE-C. D., KORY-C. L., NEIL-G. R., PARK-G.-S., PARK-J., AND TEMKIN-R. J. (2011). Vacuum electronic high power terahertz sources, *IEEE Transactions on Terahertz Science and Technology*, **1**(1), pp. 54–75.

BRUNNER-F. D., KWON-O.-P., KWON-S.-J., JAZBINSEK-M., SCHNEIDER-A., AND GŘNTER-P. (2008). A hydrogen-bonded organic nonlinear optical crystal for high-efficiency terahertz generation and detection, *Optics Express*, **16**(21), pp. 16496–16508.

CARRASCO-E., AND PERRUISSEAU-CARRIER-J. (2013). Reflectarray antenna at terahertz using graphene, *IEEE Antennas and Wireless Propagation Letters*, **12**, pp. 253–256.

CARRASCO-E., BARBA-M., AND ENCINAR-J. (2012). X-band reflectarray antenna with switching-beam using pin diodes and gathered elements, *IEEE Transactions on Antennas and Propagation*, **60**(12), pp. 5700–5708.

CARRASCO-E., BARBA-M., ENCINAR-J. A., ARREBOLA-M., ROSSI-F., AND FRENI-A. (2013a). Design, manufacture and test of a low-cost shaped-beam reflectarray using a single layer of varying-sized printed dipoles, *IEEE Transactions on Antennas and Propagation*, **61**(6), pp. 3077–3085.

CARRASCO-E., TAMAGNONE-M., AND PERRUISSEAU-CARRIER-J. (2013b). Tunable graphene reflective cells for thz reflectarrays and generalized law of reflection, *Applied Physics Letters*, **102**(10), pp. 104103–104103.

CARRASCO-E., TAMAGNONE-M., MOSIG-J. R., LOW-T., AND PERRUISSEAU-CARRIER-J. (2015). Gate-controlled mid-infrared light bending with aperiodic graphene nanoribbons array, *Nanotechnology*, **26**, p. 134002.

CHAHARMIR-M. R., SHAKER-J., GAGNON-N., AND LEE-D. (2010). Design of broadband, single layer dual-band large reflectarray using multi open loop elements, *IEEE Transactions on Antennas and Propagation*, **58**(9), pp. 2875–2883.

CHAHARMIR-M., SHAKER-J., AND LEGAY-H. (2009). Broadband design of a single layer large reflectarray using multi cross loop elements, *IEEE Transactions on Antennas and Propagation*, **57**(10), pp. 3363–3366.

CHATTOPADHYAY-G. (2011). Technology, capabilities, and performance of low power terahertz sources, *IEEE Transactions on Terahertz Science and Technology*, **1**(1), pp. 33–53.

CHATZAKIS-I., TASSIN-P., LUO-L., SHEN-N.-H., ZHANG-L., WANG-J., KOSCHNY-T., AND SOUKOULIS-C. M. (2013). One-and two-dimensional photo-imprinted diffraction gratings for manipulating terahertz waves, *Applied Physics Letters*, **103**(4), p. 043101.

CHEN-C.-Y., HSIEH-C.-F., LIN-Y.-F., PAN-R.-P., AND PAN-C.-L. (2004). Magnetically tunable room-temperature 2 pi liquid crystal terahertz phase shifter, *Optics Express*, **12**(12), pp. 2625–2630.

CHEN-H., CHAN-C., AND SHENG-P. (2010). Transformation optics and metamaterials, *Nature Materials*, **9**(5), pp. 387–396.

CHEN-H.-T., O'HARA-J. F., AZAD-A. K., AND TAYLOR-A. J. (2011). Manipulation of terahertz radiation using metamaterials, *Laser & Photonics Reviews*, **5**(4), pp. 513–533.

CHEN-P.-Y., ARGYROPOULOS-C., AND ALU-A. (2013). Terahertz antenna phase shifters using integrally-gated graphene transmission-lines, *IEEE Transactions on Antennas and Propagation*, **61**(4), pp. 1528–1537.

CHURCHLEY-D., LYNCH-R. J., LIPPERT-F., EDER-J. S. O., ALTON-J., AND GONZALEZ-CABEZAS-C. (2011). Terahertz pulsed imaging study to assess remineralization of artificial caries lesions, *Journal of biomedical optics*, **16**(2), pp. 026001–026001.

CLOUGH-B., DAI-J., AND ZHANG-X.-C. (2012). Laser air photonics: beyond the terahertz gap, *Materials Today*, **15**(1), pp. 50–58.

COSTLEY-A., HURSEY-K., NEILL-G., AND WARD-J. (1977). Free-standing fine-wire grids: their manufacture, performance, and use at millimeter and submillimeter wavelengths, *JOSA*, **67**(7), pp. 979–981.

DEIBEL-J. A., ESCARRA-M. D., AND MITTLEMAN-D. M. (2005). Photoconductive terahertz antenna with radial symmetry, *Conference on Lasers and Electro-Optics*, Optical Society of America, p. JWB23.

DE MAAGT-P. (2007). Terahertz technology for space and earth applications, *2007 IEEE International Workshop on Antenna Technology: Small Antennas, Novel EM Structures and Materials, and Applications (iWAT)*, pp. 111–115.

DENG-L., TENG-J., ZHANG-L., WU-Q., LIU-H., ZHANG-X., AND CHUA-S. (2012). Extremely high extinction ratio terahertz broadband polarizer using bilayer subwavelength metal wire-grid structure, *Applied Physics Letters*, **101**(1), p. 011101.

DREYHAUPT-A., WINNERL-S., DEKORSY-T., AND HELM-M. (2005). High-intensity terahertz radiation from a microstructured large-area photoconductor, *Applied Physics Letters*, **86**(12), p. 121114.

EKINCI-Y., SOLAK-H. H., DAVID-C., AND SIGG-H. (2006). Bilayer al wire-grids as broadband and high-performance polarizers, *Optics Express*, **14**(6), pp. 2323–2334.

ELLIOTT-R., AND GILLESPIE-E. (1983). Ieee standard definitions of terms for antennas, *IEEE Transactions on Antennas and Propagation*, **31**(6), pp. 1–29.

ENCINAR-J. (2001). Design of two-layer printed reflectarrays using patches of variable size, *IEEE Transactions on Antennas and Propagation*, **49**(10), pp. 1403–1410.

ENCINAR-J. (2010). Recent advances in reflectarray antennas, *IEEE Proceedings of the Fourth European Conference on Antennas and Propagation (EuCAP)*, pp. 1–6.

ENCINAR-J. A., AND ZORNOZA-J. A. (2003). Broadband design of three-layer printed reflectarrays, *IEEE Transactions on Antennas and Propagation*, **51**(7), pp. 1662–1664.

ENCINAR-J. A., DATASHVILI-L. S., ZORNOZA-J. A., ARREBOLA-M., SIERRA-CASTAÑER-M., BESADA-SANMARTÍN-J. L., BAIER-H., AND LEGAY-H. (2006). Dual-polarization dual-coverage reflectarray for space applications, *IEEE Transactions on Antennas and Propagation*, **54**(10), pp. 2827–2837.

ESQUIUS-MOROTE-M., GOMEZ-DIAZ-J. S., AND PERRUISSEAU-CARRIER-J. (2014). Sinusoidally modulated graphene leaky-wave antenna for electronic beamscanning at thz, *IEEE Transactions on Terahertz Science and Technology*, **4**(1), pp. 116–122.

FALKOVSKY-L., AND PERSHOGUBA-S. (2007). Optical far-infrared properties of a graphene monolayer and multilayer, *Physical Review B*, **76**(15), p. 153410.

FARMAHINI-FARAHANI-M., AND MOSALLAEI-H. (2013). Birefringent reflectarray metasurface for beam engineering in infrared, *Optics Letters*, **38**(4), pp. 462–464.

FEDERICI-J. F., SCHULKIN-B., HUANG-F., GARY-D., BARAT-R., OLIVEIRA-F., AND ZIMDARS-D. (2005). Thz imaging and sensing for security applications—explosives, weapons and drugs, *Semiconductor Science and Technology*, **20**(7), p. S266.

FERGUSON-B., AND ZHANG-X. (2002). Materials for terahertz science and technology, *Nature Materials*, **1**(1), pp. 26–33.

FITCH-M., AND OSIANDER-R. (2004). Terahertz waves for communications and sensing, *Johns Hopkins APL Technical Digest*, **25**(4), pp. 348–355.

FITZGERALD-A. J., PICKWELL-MACPHERSON-E., AND WALLACE-V. P. (2014). Use of finite difference time domain simulations and debye theory for modelling the terahertz reflection response of normal and tumour breast tissue, *PLoS ONE 9(7): e99291. doi:10.1371/journal.pone.0099291.*

FITZGERALD-A. J., PINDER-S., PURUSHOTHAM-A. D., O'KELLY-P., ASHWORTH-P. C., AND WALLACE-V. P. (2012). Classification of terahertz-pulsed imaging data from excised breast tissue, *Journal of Biomedical Optics*, **17**(1), p. 016005.

FLORENCIO-R., BOIX-R. R., CARRASCO-E., ENCINAR-J. A., BARBA-M., AND PÉREZ-PALOMINO-G. (2014). Broadband reflectarrays made of cells with three coplanar parallel dipoles, *Microwave and Optical Technology Letters*, **56**(3), pp. 748–753.

FROBERG-N., HU-B., ZHANG-X., AND AUSTON-D. (1992). Terahertz radiation from a photoconducting antenna array, *IEEE Journal of Quantum Electronics*, **28**(10), pp. 2291–2301.

GHADARGHADR-S., HAO-Z., AND MOSALLAEI-H. (2009). Plasmonic array nanoantennas on layered substrates: modeling and radiation characteristics, *Optics Express*, **17**(21), pp. 18556–18570.

GIANVITTORIO-J., AND RAHMAT-SAMII-Y. (2006). Reconfigurable patch antennas for steerable reflectarray applications, *IEEE Transactions on Antennas and Propagation*, **54**(5), pp. 1388–1392.

GINN-J., LAIL-B., ALDA-J., AND BOREMAN-G. (2008). Planar infrared binary phase reflectarray, *Optics Letters*, **33**(8), pp. 779–781.

GRADY-N. K., HEYES-J. E., CHOWDHURY-D. R., ZENG-Y., REITEN-M. T., AZAD-A. K., TAYLOR-A. J., DALVIT-D. A., AND CHEN-H.-T. (2013). Terahertz metamaterials for linear polarization conversion and anomalous refraction, *Science*, **340**(6138), pp. 1304–1307.

GRANT-P., LAFRAMBOISE-S., DUDEK-R., GRAF-M., BEZINGER-A., AND LIU-H. (2009). Terahertz free space communications demonstration with quantum cascade laser and quantum well photodetector, *Electronics Letters*, **45**(18), pp. 952–954.

GUAN-X., WU-H., SHI-Y., WOSINSKI-L., AND DAI-D. (2013). Ultracompact and broadband polarization beam splitter utilizing the evanescent coupling between a hybrid plasmonic waveguide and a silicon nanowire, *Optics Letters*, **38**(16), pp. 3005–3008.

HAN-P., CHO-G., AND ZHANG-X.-C. (2000). Time-domain transillumination of biological tissues with terahertz pulses, *Optics Letters*, **25**(4), pp. 242–244.

HANSEN-R. C. (2009). *Phased array antennas*, Vol. 213, John Wiley & Sons.

HASANI-H., KAMYAB-M., AND MIRKAMALI-A. (2010). Broadband reflectarray antenna incorporating disk elements with attached phase-delay lines, *IEEE Antennas and Wireless Propagation Letters*, **9**, pp. 156–158.

HUANG-J., AND ENCINAR-J. (2008). *Reflectarray antenna*, Wiley Online Library.

HUANG-J., AND POGORZELSKI-R. J. (1998). A ka-band microstrip reflectarray with elements having variable rotation angles, *IEEE Transactions on Antennas and Propagation*, **46**(5), pp. 650–656.

HUANG-Z., PARK-H., PARROTT-E. P., CHAN-H. P., AND PICKWELL-MACPHERSON-E. (2013). Robust thin-film wire-grid thz polarizer fabricated via a low-cost approach, *IEEE Photonics Technology Letters*, **25**(1), pp. 81–84.

HUANG-Z., PARROTT-E. P., PARK-H., CHAN-H. P., AND PICKWELL-MACPHERSON-E. (2014). High extinction ratio and low transmission loss thin-film terahertz polarizer with a tunable bilayer metal wire-grid structure, *Optics Letters*, **39**(4), pp. 793–796.

HÜBERS-H.-W., SEMENOV-A., RICHTER-H., AND BÖTTGER-U. (2007). Terahertz imaging system for stand-off detection of threats, *Defense and Security Symposium*, International Society for Optics and Photonics, p. 65490A.

HU-W., CAHILL-R., ENCINAR-J., DICKIE-R., GAMBLE-H., FUSCO-V., AND GRANT-N. (2008). Design and measurement of reconfigurable millimeter wave reflectarray cells with nematic liquid crystal, *IEEE Transactions on Antennas and Propagation*, **56**(10), pp. 3112–3117.

ISLAM-M., AND KOCH-M. (2006). Terahertz patch antenna arrays for indoor communications, *Int. Conference on Next-Generation Wireless Systems (Dhaka, Bangladesh)*.

JACKSON-D. R., AND OLINER-A. A. (2008). Leaky-wave antennas, *Modern Antenna Handbook*, **1**, pp. 325–368.

JACOB-M., PRIEBE-S., KURNER-T., JASTROW-C., KLEINE-OSTMANN-T., AND SCHRADER-T. (2009). An overview of ongoing activities in the field of channel modeling, spectrum allocation and standardization for mm-wave and thz indoor communications, *IEEE GLOBECOM Workshops*, pp. 1–6.

JAVOR-R., WU-X., AND CHANG-K. (1995). Design and performance of a microstrip reflectarray antenna, *IEEE Transactions on Antennas and Propagation*, **43**(9), pp. 932–939.

JEDLICKA-R., POE-M., AND CARVER-K. (1981). Measured mutual coupling between microstrip antennas, *Antennas and Propagation, IEEE Transactions on*, **29**(1), pp. 147–149.

JEPSEN-P. U., AND KEIDING-S. (1995). Radiation patterns from lens-coupled terahertz antennas, *Optics Letters*, **20**(8), pp. 807–809.

JOSEFSSON-L., AND PERSSON-P. (2006). *Conformal Array Antenna Theory and Design*, John Wiley & Sons.

JUAREZ-J. C., DWIVEDI-A., HAMMONS-A. R., JONES-S. D., WEERACKODY-V., AND NICHOLS-R. A. (2006). Free-space optical communications for next-generation military networks, *Communications Magazine, IEEE*, **44**(11), pp. 46–51.

KAWASE-K., OGAWA-Y., WATANABE-Y., AND INOUE-H. (2003). Non-destructive terahertz imaging of illicit drugs using spectral fingerprints, *Optics Express*, **11**(20), pp. 2549–2554.

KHODASEVYCH-I., SHAH-C., SRIRAM-S., BHASKARAN-M., WITHAYACHUMNANKUL-W., UNG-B., LIN-H., ROWE-W., ABBOTT-D., AND MITCHELL-A. (2012). Elastomeric silicone substrates for terahertz fishnet metamaterials, *Applied Physics Letters*, **100**(6), pp. 061101–061101.

KLEINE-OSTMANN-T., AND NAGATSUMA-T. (2011). A review on terahertz communications research, *Journal of Infrared, Millimeter, and Terahertz Waves*, **32**(2), pp. 143–171.

KWON-D.-H., AND WERNER-D. H. (2008). Polarization splitter and polarization rotator designs based on transformation optics, *Optics Express*, **16**(23), pp. 18731–18738.

LAU-J. Y., AND HUM-S. V. (2012). Reconfigurable transmitarray design approaches for beamforming applications, *IEEE Transactions on Antennas and Propagation*, **60**(12), pp. 5679–5689.

LEE-S. H., CHOI-J., KIM-H.-D., CHOI-H., AND MIN-B. (2013). Ultrafast refractive index control of a terahertz graphene metamaterial, *Scientific Reports*, **3**, p. 2135.

LI-H., WANG-B.-Z., AND DU-P. (2007). Novel broadband reflectarray antenna with windmill-shaped elements for millimeter-wave application, *International Journal of Infrared and Millimeter Waves*, **28**(5), pp. 339–344.

LI-L., CHEN-Q., YUAN-Q., SAWAYA-K., MARUYAMA-T., FURUNO-T., AND UEBAYASHI-S. (2009). Novel broadband planar reflectarray with parasitic dipoles for wireless communication applications, *IEEE Antennas and Wireless Propagation Letters*, **8**, pp. 881–885.

LI-L., CHEN-Q., YUAN-Q., SAWAYA-K., MARUYAMA-T., FURUNO-T., AND UEBAYASHI-S. (2011). Frequency selective reflectarray using crossed-dipole elements with square loops for wireless communication applications, *IEEE Transactions on Antennas and Propagation*, **59**(1), pp. 89–99.

LIN-C.-J., LI-Y.-T., HSIEH-C.-F., PAN-R.-P., AND PAN-C.-L. (2008). Manipulating terahertz wave by a magnetically tunable liquid crystal phase grating, *Optics Express*, **16**(5), pp. 2995–3001.

LI-Y. B., WAN-X., CAI-B. G., CHENG-Q., AND CUI-T. J. (2014). Frequency-controls of electromagnetic multi-beam scanning by metasurfaces, *Scientific Reports*, **4**, p. 06921.

LLOMBART-N., CHATTOPADHYAY-G., SKALARE-A., AND MEHDI-I. (2011). Novel terahertz antenna based on a silicon lens fed by a leaky wave enhanced waveguide, *IEEE Transactions on Antennas and Propagation*, **59**(6), pp. 2160–2168.

LUCYSZYN-S. (2007). Evaluating surface impedance models for terahertz frequencies at room temperature, *The Plan Index Enquiry and Retrieval System (PIERS) Online*, **3**(4), pp. 554–559.

MAILLOUX-R. J. (1994). Phased array antenna handbook, *Boston, MA: Artech House, 1994.*

MAKI-K., SHIBUYA-T., OTANI-C., SUIZU-K., AND KAWASE-K. (2009). Terahertz beam steering via tilted-phase difference-frequency mixing, *Applied Physics Express*, **2**(2), p. 022301.

MALAGISI-C. (1978). Microstrip disc element reflect array, *EASCON'78; Electronics and Aerospace Systems Convention*, Vol. 1, pp. 186–192.

MATSUURA-S., TANI-M., AND SAKAI-K. (1997). Generation of coherent terahertz radiation by photomixing in dipole photoconductive antennas, *Applied Physics Letters*, **70**(5), pp. 559–561.

MEMARZADEH-B., AND MOSALLAEI-H. (2011). Array of planar plasmonic scatterers functioning as light concentrator, *Optics Letters*, **36**(13), pp. 2569–2571.

MITTLEMAN-D., GUPTA-M., NEELAMANI-R., BARANIUK-R., RUDD-J., AND KOCH-M. (1999). Recent advances in terahertz imaging, *Applied Physics B*, **68**(6), pp. 1085–1094.

MITTLEMAN-D., JACOBSEN-R., AND NUSS-M. (1996). T-ray imaging, *IEEE Journal of Selected Topics in Quantum Electronics*, **2**(3), pp. 679–692.

MONNAI-Y., ALTMANN-K., JANSEN-C., HILLMER-H., KOCH-M., AND SHINODA-H. (2013). Terahertz beam steering and variable focusing using programmable diffraction gratings, *Optics Express*, **21**(2), pp. 2347–2354.

MONNAI-Y., VIERECK-V., HILLMER-H., ALTMANN-K., JANSEN-C., KOCH-M., AND SHINODA-H. (2012). Terahertz beam steering using structured mems surfaces for networked wireless sensing, *IEEE Ninth International Conference on Networked Sensing Systems (INSS)*, pp. 1–3.

NAGATSUMA-T., HORIGUCHI-S., MINAMIKATA-Y., YOSHIMIZU-Y., HISATAKE-S., KUWANO-S., YOSHIMOTO-N., TERADA-J., AND TAKAHASHI-H. (2013). Terahertz wireless communications based on photonics technologies, *Optics Express*, **21**(20), pp. 23736–23747.

NAYERI-P., LIANG-M., GARCÍA-R. S., TUO-M., YANG-F., GEHM-M., XIN-H., AND ELSHERBENI-A. (2014). 3d printed dielectric reflectarrays: low-cost high-gain antennas at sub-millimeter waves, *IEEE Transactions on Antennas and Propagation*, **62**, pp. 2000–2008.

NAYERI-P., LIANG-M., SABORY-GARCIA-R., TUO-M., YANG-F., GEHM-M., XIN-H., AND ELSHERBENI-A. (2013). High gain dielectric reflectarray antennas for thz applications, *2013 IEEE International Symposium on Antennas and Propagation Society (APSURSI)*, pp. 1124–1125.

NAYERI-P., YANG-F., AND ELSHERBENI-A. Z. (2011). Radiation characteristics of conformal reflectarray antennas, *IEEE International Symposium on Antennas and Propagation (APSURSI)*, pp. 365–368.

NISHIZAWA-J.-I., SASAKI-T., SUTO-K., YAMADA-T., TANABE-T., TANNO-T., SAWAI-T., AND MIURA-Y. (2005). Thz imaging of nucleobases and cancerous tissue using a gap thz-wave generator, *Optics Communications*, **244**(1), pp. 469–474.

NIU-T., UPADHYAY-A., WITHAYACHUMNANKUL-W., HEADLAND-D., ABBOTT-D., BHASKARAN-M., SRIRAM-S., AND FUMEAUX-C. (2015a). Polarization-dependent thin-film wire-grid reflectarray for terahertz waves, *Applied Physics Letters*, **107**(3), p. 031111.

NIU-T., WITHAYACHUMNANKUL-W., ABBOTT-D., AND FUMEAUX-C. (2014a). Design of polarization-dependent reflectarray for terahertz waves, *2014 IEEE International Workshop on Antenna Technology: Small Antennas, Novel EM Structures and Materials, and Applications (iWAT)*, pp. 205–207.

NIU-T., WITHAYACHUMNANKUL-W., ABBOTT-D., AND FUMEAUX-C. (2014b). Terahertz reflectarray for bidirectional beam splitting, *IEEE 39th International Conference on Infrared, Millimeter, and Terahertz waves (IRMMW-THz)*, pp. 1–2.

NIU-T., WITHAYACHUMNANKUL-W., AND FUMEAUX-C. (2015b). Terahertz broadband reflectarray with parallel elliptical dipoles, *2015 IEEE 4th Asia-Pacific Conference on Antennas and Propagation (APCAP)*, pp. 102–104.

NIU-T., WITHAYACHUMNANKUL-W., UNG-B., MENEKSE-H., BHASKARAN-M., SRIRAM-S., AND FUMEAUX-C. (2012). Design and implementation of terahertz reflectarray, *IEEE Infrared, Millimeter, and Terahertz Waves (IRMMW-THz), 2012 37th International Conference on*, pp. 1–2.

NIU-T., WITHAYACHUMNANKUL-W., UNG-B. S.-Y., MENEKSE-H., BHASKARAN-M., SRIRAM-S., AND FUMEAUX-C. (2013). Experimental demonstration of reflectarray antennas at terahertz frequencies, *Optics Express*, **21**(3), pp. 2875–2889.

NIU-T., WITHAYACHUMNANKUL-W., UPADHYAY-A., GUTRUF-P., ABBOTT-D., BHASKARAN-M., SRIRAM-S., AND FUMEAUX-C. (2014c). Terahertz reflectarray as a polarizing beam splitter, *Optics Express*, **22**(13), pp. 16148–16160.

O'HARA-J., AVERITT-R., AND TAYLOR-A. (2004). Terahertz surface plasmon polariton coupling on metallic gratings, *Optics Express*, **12**(25), pp. 6397–6402.

OLINER-A. A., AND JACKSON-D. R. (1993). Leaky-wave antennas, *Antenna Engineering Handbook*, **4**, p. 12.

PADILLA-P., MUÑOZ-ACEVEDO-A., SIERRA-CASTAÑER-M., AND SIERRA-PÉREZ-M. (2010). Electronically reconfigurable transmitarray at ku band for microwave applications, *IEEE Transactions on Antennas and Propagation*, **58**(8), pp. 2571–2579.

PARK-J.-H., YU-C.-J., KIM-J., CHUNG-S.-Y., AND LEE-S.-D. (2003). Concept of a liquid-crystal polarization beamsplitter based on binary phase gratings, *Applied Physics Letters*, **83**(10), pp. 1918–1920.

PAWAR-A. Y., SONAWANE-D. D., ERANDE-K. B., AND DERLE-D. V. (2013). Terahertz technology and its applications, *Drug Invention Today*, **5**(2), pp. 157–163.

PENDRY-J. B., SCHURIG-D., AND SMITH-D. R. (2006). Controlling electromagnetic fields, *Science*, **312**(5781), pp. 1780–1782.

PERALTA-X. G., SMIRNOVA-E. I., AZAD-A. K., CHEN-H.-T., TAYLOR-A. J., BRENER-I., AND O'HARA-J. F. (2009). Metamaterials for thz polarimetric devices, *Optics Express*, **17**(2), pp. 773–783.

PEREZ-PALOMINO-G., BAINE-P., DICKIE-R., BAIN-M., ENCINAR-J. A., CAHILL-R., BARBA-M., AND TOSO-G. (2013). Design and experimental validation of liquid crystal-based reconfigurable reflectarray elements with improved bandwidth in f-band, *IEEE Transactions on Antennas and Propagation*, **61**(4), pp. 1704–1713.

PERRUISSEAU-CARRIER-J. (2010). Dual-polarized and polarization-flexible reflective cells with dynamic phase control, *IEEE Transactions on Antennas and Propagation*, **58**(5), pp. 1494–1502.

PERRUISSEAU-CARRIER-J., BONGARD-F., GOLUBOVIC-NICIFOROVIC-R., TORRES-SÁNCHEZ-R., AND MOSIG-J. R. (2010). Contributions to the modeling and design of reconfigurable reflecting cells embedding discrete control elements, *IEEE Transactions on Microwave Theory and Techniques*, **58**(6), pp. 1621–1628.

PFEIFFER-C., AND GRBIC-A. (2013). Millimeter-wave transmitarrays for wavefront and polarization control, *IEEE Transactions on Microwave Theory and Techniques*, **61**(12), pp. 4407–4417.

PHELAN-H. R. (1977). Spiraphase reflectarray for multitarget radar, *Microwave Journal*, **20**, p. 67.

PICKWELL-E., WALLACE-V. P., COLE-B. E., ALI-S., LONGBOTTOM-C., LYNCH-R. J., AND PEPPER-M. (2007). A comparison of terahertz pulsed imaging with transmission microradiography for depth measurement of enamel demineralisation in vitro, *Caries Research*, **41**(1), pp. 49–55.

PORS-A., NIELSEN-M. G., VALLE-G. D., WILLATZEN-M., ALBREKTSEN-O., AND BOZHEVOLNYI-S. I. (2011). Plasmonic metamaterial wave retarders in reflection by orthogonally oriented detuned electrical dipoles, *Optics Letters*, **36**(9), pp. 1626–1628.

POZAR-D., AND METZLER-T. (1993). Analysis of a reflectarray antenna using microstrip patches of variable size, *Electronics Letters*, **29**(8), pp. 657–658.

POZAR-D. M., AND TARGONSKI-S. D. (1998). A microstrip reflectarray using crossed dipoles, *IEEE International Symposium on Antennas and Propagation Society*, Vol. 2, pp. 1008–1011.

RAHM-M., CUMMER-S. A., SCHURIG-D., PENDRY-J. B., AND SMITH-D. R. (2008). Optical design of reflectionless complex media by finite embedded coordinate transformations, *Physical Review Letters*, **100**(6), p. 063903.

ROBIN-T., BOUYE-C., AND COCHARD-J. (2014). Terahertz applications: trends and challenges, *SPIE OPTO*, International Society for Optics and Photonics, pp. 898512–898512.

RODRIGO-D., JOFRE-L., AND PERRUISSEAU-CARRIER-J. (2013). A frequency reconfigurable cell for beam-scanning reflectarrays, *IEEE International Symposium on Antennas and Propagation Society (APSURSI)*, pp. 1666–1667.

SAYIDMARIE-K. H., AND BIALKOWSKI-M. E. (2008). Broadband microstrip reflectarray formed by double circular ring elements, *IEEE 17th International Conference on Microwaves, Radar and Wireless Communications, MIKON 2008*, pp. 1–4.

SCHERGER-B., REUTER-M., SCHELLER-M., ALTMANN-K., VIEWEG-N., DABROWSKI-R., DEIBEL-J. A., AND KOCH-M. (2012). Discrete terahertz beam steering with an electrically controlled liquid crystal device, *Journal of Infrared, Millimeter, and Terahertz Waves*, **33**(11), pp. 1117–1122.

SCHERMER-R. T., BUCHOLTZ-F., AND VILLARRUEL-C. A. (2011). Continuously-tunable microwave photonic true-time-delay based on a fiber-coupled beam deflector and diffraction grating, *Optics Express*, **19**(6), pp. 5371–5378.

SCHURIG-D., MOCK-J., JUSTICE-B., CUMMER-S., PENDRY-J., STARR-A., AND SMITH-D. (2006). Metamaterial electromagnetic cloak at microwave frequencies, *Science*, **314**(5801), pp. 977–980.

SIEGEL-P. (2002). Terahertz technology, *IEEE Transactions on Microwave Theory and Techniques*, **50**(3), pp. 910–928.

SIEGEL-P. H. (2007). Thz instruments for space, *IEEE Transactions on Antennas and Propagation*, **55**(11), pp. 2957–2965.

SONG-H.-J., AND NAGATSUMA-T. (2011). Present and future of terahertz communications, *IEEE Transactions on Terahertz Science and Technology*, **1**(1), pp. 256–263.

SQUIRES-A., CONSTABLE-E., AND LEWIS-R. (2014). 3d printed terahertz diffraction gratings and lenses, *Journal of Infrared, Millimeter, and Terahertz Waves*, **36**(1), pp. 72–80.

STOLAREK-M., YAVORSKIY-D., KOTYŃSKI-R., ZAPATA RODRÍGUEZ-C. J., ŁUSAKOWSKI-J., AND SZOPLIK-T. (2013). Asymmetric transmission of terahertz radiation through a double grating, *Optics Letters*, **38**(6), pp. 839–841.

SUN-J., TIMURDOGAN-E., YAACOBI-A., HOSSEINI-E. S., AND WATTS-M. R. (2013). Large-scale nanophotonic phased array, *Nature*, **493**(7431), pp. 195–199.

TAI-C.-Y., CHANG-S. H., AND CHIU-T. (2007). Design and analysis of an ultra-compact and ultra-wideband polarization beam splitter based on coupled plasmonic waveguide arrays, *IEEE Photonics Technology Letters*, **19**(19), pp. 1448–1450.

TAMAGNONE-M., GOMEZ-DIAZ-J., MOSIG-J., AND PERRUISSEAU-CARRIER-J. (2012). Analysis and design of terahertz antennas based on plasmonic resonant graphene sheets, *Journal of Applied Physics*, **112**(11), p. 114915.

TAMMINEN-A., ALA-LAURINAHO-J., MÄKELÄ-S., GOMES-MARTINS-D., HÄKLI-J., KOIVISTO-P., RANTAKARI-P., SÄILY-J., TUOVINEN-R., AND LUUKANEN-A. R. (2013a). Near-field measurements of submillimeter-wave reflectarrays, *SPIE Defense, Security, and Sensing*, International Society for Optics and Photonics, p. 871506.

TAMMINEN-A., MAKELA-S., ALA-LAURINAHO-J., HAKLI-J., KOIVISTO-P., RANTAKARI-P., SAILY-J., LUUKANEN-A., AND RAISANEN-A. V. (2013b). Reflectarray design for 120-ghz radar application: measurement results, *IEEE Transactions on Antennas and Propagation*, **61**(10), pp. 5036–5047.

TARGONSKI-S., AND POZAR-D. (1994). Analysis and design of a microstrip reflectarray using patches of variable size, *IEEE International Symposium on Antennas and Propagation Society AP-S. Digest*, Vol. 3, pp. 1820–1823.

TARGONSKI-S., AND POZAR-D. (1996). Minimization of beam squint in microstrip reflectarrays using an offset feed, *IEEE International Symposium on Antennas and Propagation Society AP-S. Digest*, Vol. 2, pp. 1326–1329.

TAVALLAEE-A. A., WILLIAMS-B. S., HON-P. W., ITOH-T., AND CHEN-Q.-S. (2011). Terahertz quantum-cascade laser with active leaky-wave antenna, *Applied Physics Letters*, **99**(14), p. 141115.

TAYLOR-Z. D., SINGH-R. S., BENNETT-D. B., TEWARI-P., KEALEY-C. P., BAJWA-N., CULJAT-M. O., STOJADINOVIC-A., LEE-H., AND HUBSCHMAN-J. (2011). Thz medical imaging: in vivo hydration sensing, *IEEE Transactions on Terahertz Science and Technology*, **1**(1), pp. 201–219.

TONOUCHI-M. (2007). Cutting-edge terahertz technology, *Nature Photonics*, **1**(2), pp. 97–105.

TSAI-F., AND BIALKOWSKI-M. (2003). Designing a 161-element ku-band microstrip reflectarray of variable size patches using an equivalent unit cell waveguide approach, *IEEE Transactions on Antennas and Propagation*, **51**(10), pp. 2953–2962.

UEMATSU-K., MAKI-K., AND OTANI-C. (2012). Terahertz beam steering using interference of femtosecond optical pulses, *Optics Express*, **20**(20), pp. 22914–22921.

VALENTINE-J., LI-J., ZENTGRAF-T., BARTAL-G., AND ZHANG-X. (2009). An optical cloak made of dielectrics, *Nature Materials*, **8**(7), pp. 568–571.

WALLACE-V., FITZGERALD-A., SHANKAR-S., FLANAGAN-N., PYE-R., CLUFF-J., AND ARNONE-D. (2004). Terahertz pulsed imaging of basal cell carcinoma ex vivo and in vivo, *British Journal of Dermatology*, **151**(2), pp. 424–432.

WEBER-T., KROKER-S., KÄSEBIER-T., KLEY-E.-B., AND TÜNNERMANN-A. (2014). Silicon wire grid polarizer for ultraviolet applications, *Applied Optics*, **53**(34), pp. 8140–8144.

WEG-C. A., VON SPIEGEL-W., HILS-B., LÖFFLER-T., HENNEBERGER-R., ZIMMERMANN-R., AND ROSKOS-H. (2008). Fast active thz camera with range detection by frequency modulation, *IEEE 33rd International Conference on Infrared, Millimeter and Terahertz Waves (IRMMW-THz)*, pp. 1–3.

WISE-S., QUETSCHKE-V., DESHPANDE-A., MUELLER-G., REITZE-D., TANNER-D., WHITING-B., CHEN-Y., TÜNNERMANN-A., AND KLEY-E. (2005). Phase effects in the diffraction of light: beyond the grating equation, *Physical Review Letters*, **95**(1), p. 013901.

WITHAYACHUMNANKUL-W., FISCHER-B. M., AND ABBOTT-D. (2008). Numerical removal of water vapour effects from terahertz time-domain spectroscopy measurements, *Proceedings of the Royal Society A: Mathematical, Physical and Engineering Science*, **464**(2097), pp. 2435–2456.

WOODWARD-R., WALLACE-V., ARNONE-D., LINFIELD-E., AND PEPPER-M. (2003). Terahertz pulsed imaging of skin cancer in the time and frequency domain, *Journal of Biological Physics*, **29**(2), pp. 257–259.

WU-B. K., CHENG-Y. J., DJERAFI-T., AND HONG-W. (2012). Substrate-integrated millimeter-wave and terahertz antenna technology, *Proceedings of the IEEE*, **100**(7), pp. 2219–2232.

WU-C.-L., SUNG-C.-K., YAO-P.-H., AND CHEN-C.-H. (2013). Sub-15 nm linewidth gratings using roll-to-roll nanoimprinting and plasma trimming to fabricate flexible wire-grid polarizers with low colour shift, *Nanotechnology*, **24**(26), p. 265301.

XU-F., WU-K., AND ZHANG-X. (2010). Periodic leaky-wave antenna for millimeter wave applications based on substrate integrated waveguide, *IEEE Transactions on Antennas and Propagation*, **58**(2), pp. 340–347.

YAMADA-I., TAKANO-K., HANGYO-M., SAITO-M., AND WATANABE-W. (2009). Terahertz wire-grid polarizers with micrometer-pitch al gratings, *Optics Letters*, **34**(3), pp. 274–276.

YANG-F., MEI-Z. L., JIN-T. Y., AND CUI-T. J. (2012). Dc electric invisibility cloak, *Physical Review Letters*, **109**(5), p. 053902.

YANG-K., LONG-X., HUANG-Y., AND WU-S. (2011). Design and fabrication of ultra-high precision thin-film polarizing beam splitter, *Optics Communications*, **284**(19), pp. 4650–4653.

YANG-Y., WANG-W., MOITRA-P., KRAVCHENKO-I. I., BRIGGS-D. P., AND VALENTINE-J. (2014). Dielectric meta-reflectarray for broadband linear polarization conversion and optical vortex generation, *Nano Letters*, **14**(3), pp. 1394–1399.

YARDIMCI-N. T., YANG-S.-H., BERRY-C. W., AND JARRAHI-M. (2015). High-power terahertz generation using large-area plasmonic photoconductive emitters, *IEEE Transactions on Terahertz Science and Technology*, **5**(2), pp. 223–229.

YIFAT-Y., EITAN-M., ILUZ-Z., HANEIN-Y., BOAG-A., AND SCHEUER-J. (2014). Highly efficient and broadband wide-angle holography using patch-dipole nanoantenna reflectarrays, *Nano Letters*, **14**(5), pp. 2485–2490.

YI-M., LEE-W., AND SO-J. (2014). Design of cylindrically conformed metal reflectarray antennas for millimetre-wave applications, *Electronics Letters*, **50**(20), pp. 1409–1410.

YOSHIDA-H., OGAWA-Y., KAWAI-Y., HAYASHI-S., HAYASHI-A., OTANI-C., KATO-E., MIYAMARU-F., AND KAWASE-K. (2007). Terahertz sensing method for protein detection using a thin metallic mesh, *Applied Physics Letters*, **91**, p. 253901.

YU-N., GENEVET-P., KATS-M. A., AIETA-F., TETIENNE-J.-P., CAPASSO-F., AND GABURRO-Z. (2011). Light propagation with phase discontinuities: generalized laws of reflection and refraction, *Science*, **334**(6054), pp. 333–337.

ZINOV'EV-N. N., SUDWORTH-C. D., BERRY-E., STRAFFORD-S. M., WOOD-D. J., CARMICHAEL-F. A., MILES-R. E., SMITH-M. A., AND CHAMBERLAIN-J. (2003). Identification of tooth abnormalities using terahertz imaging and spectroscopy, *European Conference on Biomedical Optics*, Vol. 5141, Optical Society of America, pp. 196–201.

ZOU-L., WITHAYACHUMNANKUL-W., SHAH-C., MITCHELL-A., BHASKARAN-M., SRIRAM-S., AND FUMEAUX-C. (2013). Dielectric resonator nanoantennas at visible frequencies, *Optics Express*, **21**(1), pp. 1344–1352.